On the Interface Interaction between Cobalt Phthalocyanines and Molybdenum Disulfide

Dissertation

der Mathematisch-Naturwissenschaftlichen Fakultät

der Eberhard Karls Universität Tübingen

zur Erlangung des Grades eines

Doktors der Naturwissenschaften

(Dr. rer. nat.)

vorgelegt von

Philipp Haizmann

aus Freudenstadt

Tübingen

2026

Gedruckt mit Genehmigung der Mathematisch-Naturwissenschaftlichen Fakultät der Eberhard Karls Universität Tübingen.

Tag der mündlichen Qualifikation:	21.04.2026
Dekan:	Prof. Dr. Thilo Stehle
1. Berichterstatter/-in:	Prof. Dr. Marcus Scheele
2. Berichterstatter/-in:	Prof. Dr. Reinhold Fink

This dissertation was prepared in the time from August 2020 to March 2024 in the group of Prof. Dr. Marcus Scheele at the Institute for Physical and Theoretical Chemistry at the Eberhard Karls University Tübingen.

„The interface is where the action is.“ – Jacob Nissim Israelachvili

This page was intentionally left blank.

Abstract

This dissertation examines the interfacial interactions between cobalt phthalocyanines and molybdenum disulfide (MoS_2), focusing on their potential for tailoring optoelectronic properties in advanced semiconductor devices. Motivated by the versatility of transition metal dichalcogenides (TMDCs) in applications such as field-effect transistors, photovoltaics, and flexible electronics, this study explores how molecular functionalization impacts electronic structures and interfacial dynamics.

The research utilizes advanced spectroscopic techniques such as photoelectron spectroscopy (PES), X-ray absorption spectroscopy (XAS), and angle-resolved photoelectron spectroscopy (ARPES). These methods reveal that CoPc and its perfluorinated derivative, hexadecafluoro cobalt phthalocyanine ($CoPcF_{16}$), exhibit distinct interfacial behaviors. CoPc induces significant n-type doping in MoS_2, characterized by band bending and a surface dipole shift, whereas $CoPcF_{16}$ promotes p-type doping through a bandgap state near the valence band maximum. Additionally, the molecular orientation of cobalt phthalocyanines on MoS_2 substrates diverges based on the numbers of substrate layers: on monolayers of MoS_2 the phthalocyanines show a tilted orientation, contrasting with flat-lying configurations on bulk (multiple layers) MoS_2 substrates.

These findings offer insights into the design of organic-inorganic heterostructures, advancing the understanding of doping mechanisms and molecular orientation effects for organic-inorganic heterostructures. The work also contributes to the European “Coupled Organic Inorganic Nanostructures for Fast, Light-induced Data Processing” (COINFLIP) project, funded by the European Research Council, which seeks to develop ultra-fast optical switches and novel material architectures, positioning these results as foundational for next-generation optoelectronic applications.

Deutsche Zusammenfassung

Diese Dissertation untersucht die Wechselwirkungen an der Grenzfläche zwischen Cobalt-Phthalocyaninen und Molybdändisulfid (MoS_2), wobei der Schwerpunkt auf der Möglichkeit liegt, die optoelektronischen Eigenschaften für den Einsatz Halbleitergeräten zu optimieren. Motiviert durch die Vielseitigkeit von Übergangsmetall-Dichalkogeniden (TMDCs) in Anwendungen wie Feldeffekttransistoren, Photovoltaik und flexibler Elektronik untersucht die Arbeit, wie molekulare Funktionalisierungen elektronische Strukturen und Grenzflächendynamiken beeinflussen.

Die Forschung nutzt fortschrittliche spektroskopische Techniken wie die Photoelektronenspektroskopie (PES), die Röntgenabsorptionsspektroskopie (XAS) und die winkelaufgelöste Photoelektronenspektroskopie (ARPES). Diese Untersuchungen zeigen, dass CoPc und sein perfluoriertes Derivat Cobalt-Hexadecafluorphthalocyanin ($CoPcF_{16}$) unterschiedliche Grenzflächenverhalten aufweisen. CoPc bewirkt eine signifikante n-Dotierung in MoS_2, gekennzeichnet durch Bandverbiegung und eine Verschiebung des Oberflächendipols, während $CoPcF_{16}$ eine p-Dotierung durch einen Bandlückenzustand nahe dem Valenzbandmaximum hervorruft. Darüber hinaus unterscheidet sich die molekulare Orientierung von Cobalt-Phthalocyaninen auf MoS_2-Substraten je nach Schichtdicke: auf MoS_2 Monolagen zeigen die Phthalocyanine eine geneigte Orientierung im Gegensatz zu flachliegenden Konfigurationen auf bulk (viele Lagen) MoS_2 Substraten.

Diese Erkenntnisse können neue Möglichkeiten bezüglich des Designs organisch-anorganischer Heterostrukturen ermöglichen und vertiefen das Verständnis von Dotierungsmechanismen und molekularen Orientierungseffekten bei organischen-anorganischen Heterostrukturen. Die Arbeit trägt zudem zum europäischen „Coupled Organic Inorganic Nanostructures for Fast, Light-induced Data Processing“ (COINFLIP) Projekt des Europäischen Forschungsrates bei, das darauf abzielt, ultraschnelle optische Schalter und neuartige Materialarchitekturen zu entwickeln, und dem Ziel diese Ergebnisse als Grundlage für nächste Generationen optoelektronischer Anwendungen zu nutzen.

This page was intentionally left blank.

Table of Content

1 Introduction

1.1 Motivation

Semiconductor devices are crucial in the Information Age. Silicon-based field-effect transistors form the backbone of the logic circuits that drive our computing technology. Additionally, semiconductors are essential in modern communication technologies, which increasingly depend on photon-based data transmission through optical fibers. These materials are key for both the generation of photons from electrical charge carriers and the detection of photons, effectively converting light into electronic signals.

The research on semiconductor materials used for photon generation, modulation, and detection is a central focus of our work. In addition to the synthesis of new materials, we place significant emphasis on their analytical examination using advanced methods and cutting-edge equipment.

Given the limitations of pure semiconductor materials in fabricating complex components, researchers have turned to heteromaterials, including silicon doped with elements like phosphorus and boron. In this research, an alternative approach involves constructing heterostructures by integrating organic molecules with semiconductor materials. By precisely controlling synthesis conditions, semiconductor quantum dots can be produced, each encased in a well-defined organic shell. Quantum dots are nanoscale semiconductor particles that exhibit unique optical and electronic properties due to their size, often leading to quantum confinement effects. These properties include size-dependent emission wavelengths which leads to the possibility to fine tune light emission, making them valuable in various applications such as light-emitting diodes (LEDs) and in general display technologies. Subsequent modification of this ligand shell can enhance the quantum dots stability and improve their photon emission efficiency, making them particularly suitable for LED applications.

In addition, semiconductor heterostructures can be formed by depositing molecules on pure semiconductor surfaces. Studying these materials demands advanced measurement techniques to uncover fundamental phenomena, which in turn informs the development of new synthesis strategies and material compositions.

This work is part of the ERC-funded project COINFLIP, an acronym for "Coupled Organic Inorganic Nanostructures for Fast, Light-Induced Data Processing." The

project aims to develop optical switches with ultra-fast response times in the range of a few picoseconds. In addition to exploring new device design approaches, the project also involves fundamental research on novel materials. The latter was the primary motivation behind this work.

1.2 Objective and Outline of this Thesis

The aim of this work is to investigate the interface between a transition metal dichalcogenide and phthalocyanines using photoelectron spectroscopy. The initial chapters are intended to establish a foundation for the discussions in the subsequent sections. The first chapter focus is on the properties of transition metal dichalcogenides, particularly noting that characteristics such as electrical conductivity and band gaps can vary significantly based on crystal structure and layer count. Many of these variations can be studied using PES. Following this, an introduction to the phthalocyanines used in this research is given. It is crucial to understand the impact of possible modifications to the phthalocyanines that result from further chemical functionalization. Moreover, due to the planar structure of these molecules, X-ray absorption spectroscopy can provide insights into the orientation of the molecules on different surfaces. Since the orientation of organic molecules in a film can greatly affect their electronic properties, this aspect is explored in depth. The discussion on theoretical fundamentals concludes with an examination of the interfacial interactions between an inorganic semiconductor and an organic semiconductor layer. A key tool for describing these interactions is energy-level alignment, which aids in understanding doping effects through interfacial interactions in relation to the Fermi level position. Related to this PES can be used to investigate phenomena such as band bending at surfaces or interfaces, which can be represented in an energy-level alignment diagram. As mentioned, the majority of the research focused on exploring the potential of these semiconductor systems using photoelectron spectroscopy. Given the close connection between material research and the methodology in this work, and since the methodology is detailed in various textbooks, the necessary foundations for understanding the data are integrated into the material-specific chapters. The chapters following the theoretical background are dedicated to the publications that form the basis of this cumulative dissertation.

The different phases of molybdenum disulfide (MoS_2), namely the semiconducting 2H phase and the metallic 1T phase, were studied in colloidal MoS_2 nanosheets and

nanoplatelets. As described in the theoretical section, photoelectron measurements can distinguish between these two phases based on the position of the Fermi level. It is crucial to describe the collected data using a physical model, and through physically meaningful fits, it is possible to deconvolute the signals and derive quantitative insights into the phase composition.

The next chapter discusses the interfacial interaction between cobalt phthalocyanine (CoPc) as well as the perfluorinated cobalt phthalocyanine ($CoPcF_{16}$) moiety and MoS_2. Significant differences were observed in the comparison between CoPc and $CoPcF_{16}$. Both molecules were able to influence the electronic structure of MoS_2. CoPc led to n-doping of MoS_2, whereas $CoPcF_{16}$ resulted in p-doping, or more precisely, a reduction of n-doping in the n-type MoS_2. The mechanisms derived from the measurements were quite different. In the case of CoPc, band bending and a pronounced surface dipole were observed, while $CoPcF_{16}$ induced a charge transfer leading to a new state within the bandgap. ARPES measurements, conducted at the LowDosePES endstation at the BESSY II electron storage ring, were particularly useful for this investigation.

The final chapter, based on the publications, focuses on the orientation of CoPc molecular films on the surface of few-layer to monolayer MoS_2. The fundamental question was whether the flat-lying molecular orientation observed on bulk materials also exists on these substrates. To address this, thin samples were prepared by top-down exfoliation from the same bulk crystals used in the BESSY experiments, aiming to obtain samples containing both many-layer and few-layer to monolayer MoS_2 regions. This was successful, but such samples are only a few micrometers in size, requiring microscopy techniques for investigation. To maintain comparability with previous work and since XAS is necessary, photoemission electron microscopy (PEEM) was chosen as the method. This technique also requires synchrotron radiation. A suitable endstation with a PEEM setup is the WERA endstation at the Karlsruhe Institute of Technology (KIT) Light Source in Karlsruhe. The investigations revealed that the orientation on thin MoS_2 regions differs significantly from that found on bulk material, exhibiting an orientation at a significant angle from the surface rather than the flat orientation, placing it between the edge-on and face-on configurations.

In the concluding chapter 5, other works that do not focus on the molybdenum disulfide/cobalt phthalocyanine system, but in which I made significant contributions,

are presented. A major part of this chapter is dedicated to work on cesium lead halide perovskite quantum dots. My expertise in photoelectron spectroscopy allowed me to contribute to a deeper understanding of the influence of ligand shells and the stability of these systems. Additionally, this chapter includes work that resulted from beamtime at BESSY II.

2 Theoretical Foundation and Methodology

2.1 Introduction to Molybdenum Disulfide

Ultra-thin materials, which have become significant in the development of new electronic devices, have garnered increasing research interest following the discovery of graphene. Graphene is defined as a single layer of graphite, a carbon modification like diamond, comprising multiple layers of graphene where carbon atoms are arranged in a hexagonal pattern through sp^2 hybridization. Graphene is renowned for its exceptional properties, including extremely high charge carrier mobility and a unique band structure that enables the existence of massless Dirac fermions.[9] However, graphene is considered a zero-bandgap semiconductor, which poses a challenge for the development of modern semiconductor devices that require a bandgap to function effectively.

Despite this limitation, graphene research has catalyzed the exploration of other promising low-dimensional semiconductor materials. Layered crystals, such as graphite, have seen renewed interest, leading to increased focus on transition metal dichalcogenides (TMDCs). Among these, molybdenum disulfide (MoS_2) has emerged as the most intensively studied, and it is the primary focus of this work. **Figure 1** illustrates a diagram showing the number of publications related to 2D materials, specifically graphene and MoS_2, based on a search on the citation network webofscience.com (as of January 4, 2024) using the keywords "Graphene" and "MoS2." The data clearly show that, after a brief delay, the annual number of publications on MoS_2 has increased substantially compared to those on graphene. The earlier interest in MoS_2 is largely due to its use as a lubricant.

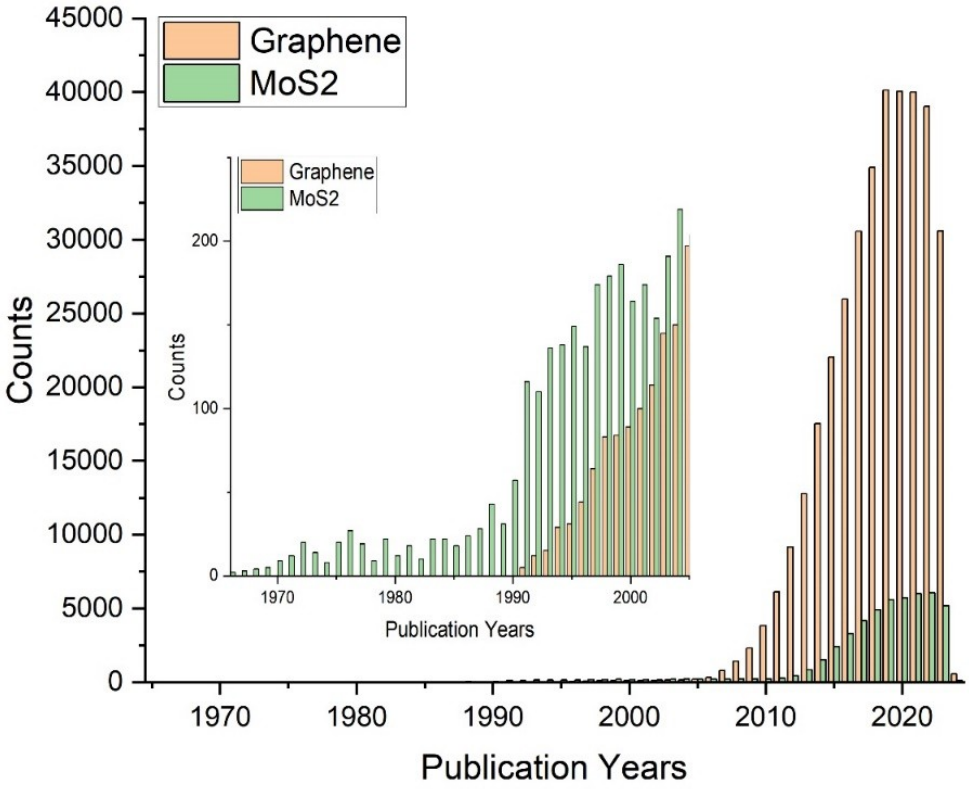

Figure 1 Diagram illustrates the number of publications focused on the 2D materials graphene and MoS_2. This data was retrieved from a Web of Science search (as of January 4, 2024) using the keywords "Graphene" and "MoS2".

Structure

Transition metal dichalcogenides (TMDCs) generally have the chemical formula MX_2 with one transition metal M and two chalcogenides X. **Figure 2** schematically illustrates the crystal structure of TMDCs. The commonly studied TMDCs typically contain the transition metals molybdenum (Mo) or tungsten (W). These transition metals form layers which are sandwiched between chalcogens, elements from group 16, typically sulfur (S), selenium (Se), or tellurium (Te). The transition metals and chalcogens are covalently bonded and form a layer by them self, often referred to as monolayer. In bulk crystals, the individual monolayers interact through van der Waals forces.[10] The thickness of a single layer (monolayer) is approximately 0.6 to 0.7 nm.[11-14]

Most TMDCs are semiconductors; however, depending on the number of d-electrons in the transition metal and the polytype, which will be discussed in more detail later, some TMDCs can exhibit metallic or semi metallic characteristics. Since this work focuses on MoS_2, the following discussion of crystal structure and its resulting properties will be limited to this specific TMDC.

MoS_2 exists in three polytypes, namely 1T, 2H, and 3R. The differences between these polytypes arise from two structural variations, the different polymorphs (trigonal prismatic and the octahedral coordination of the central transition metal) and the stacking sequence of the layers. First, the relative orientation of the chalcogen atoms to the transition metals differs. **Figure 3** illustrates the two different coordination geometries: the transition metal can be either trigonal prismatic or octahedral coordinated by the chalcogenide. Not shown in the figure is the rhombohedral coordination, which lies between these two extremes.

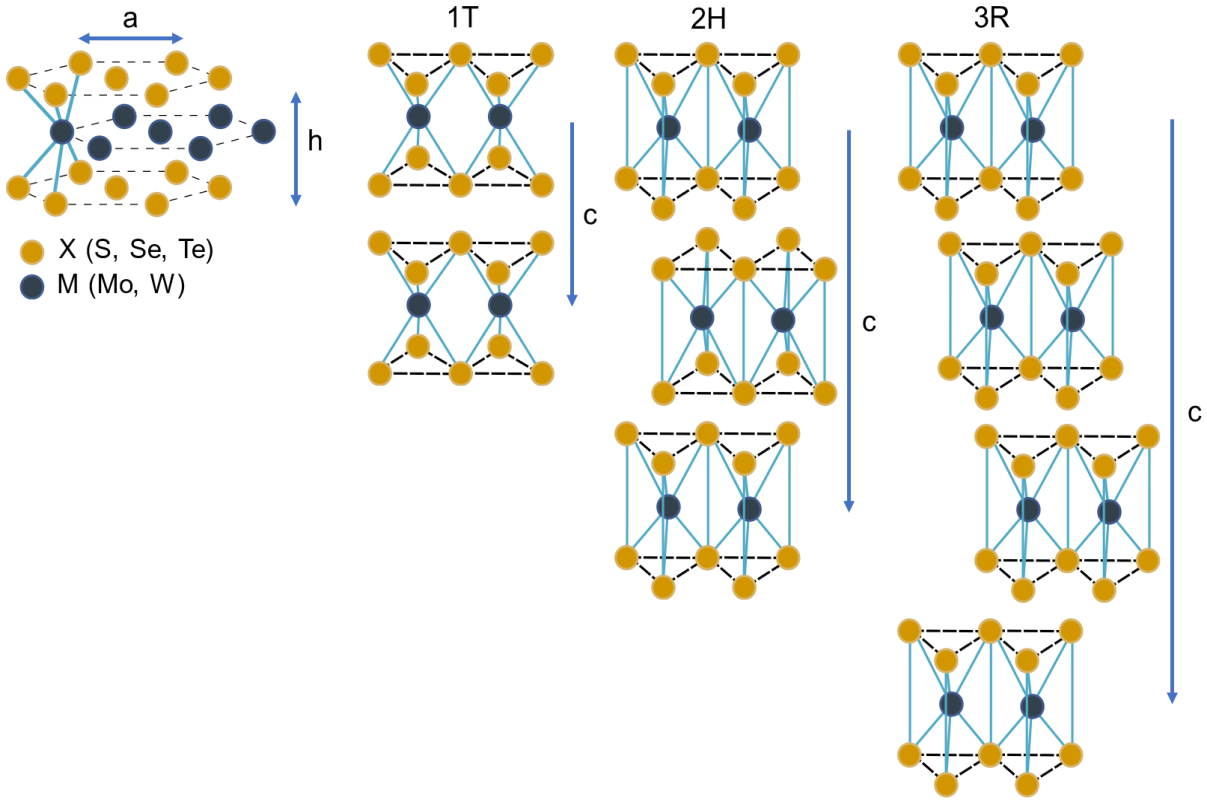

Figure 2 Schematic representation of the crystal structure of transition metal dichalcogenides and the polytypes 1T, 2H, and 3R phases.

In addition to the coordination of chalcogens around the transition metal, the polytypes also differ in their unit cells. This distinction is encoded in the names of the individual polytypes and is also shown in **Figure 2**. In the 1T phase, characterized by octahedral coordination, the unit cell consists of a single monolayer. In the 2H phase (trigonal prismatic, hexagonal), the unit cell contains two layers, while in the 3R phase (rhombohedral), the unit cell includes three layers. For 2H MoS_2, which is the material most commonly used in this work, the lattice constants are a = b = 3.160 Å and c = 12.294 Å.[15]

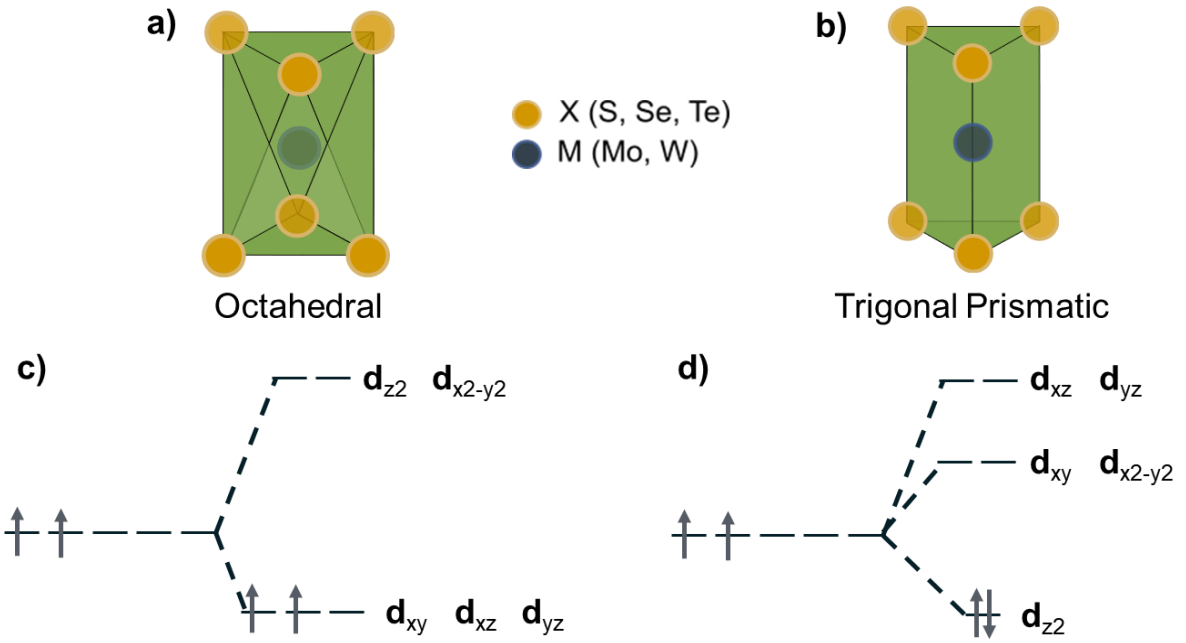

Figure 3 (**a**) and (**b**) illustrate the octahedral and trigonal prismatic coordination of transition metals in TMDCs, respectively. (**c**) and (**d**) show the resulting crystal field splitting, including the electron occupancy for the case of Mo^{4+}.

The 1T and 2H phases are the most frequently discussed in literature, while the 3R phase, though less technically relevant, can occur naturally. When examining the physical differences in properties arising from the different chalcogen coordination around the transition metals, it is useful to consider the crystal field splitting. In the octahedral coordination, the d orbitals experience splitting where the d_{xy}, d_{xz}, and d_{yz} orbitals are lowered in energy compared to the degenerate starting situation, while the d_{z2} and d_{x2-y2} orbitals are raised in energy. In contrast, for trigonal prismatic coordination, only the d_{z2} orbital is significantly lowered in energy, with the other orbitals being raised, as illustrated in **Figure 3**.

In MoS_2, molybdenum is in the +4 oxidation state. Upon filling the orbitals, it becomes apparent that in the trigonal prismatic coordination, the d_{z2} orbital is fully occupied, while the other orbitals remain unoccupied. In the octahedral coordination, the two electrons occupy the d_{xy}, d_{xz}, and d_{yz} orbitals. This difference explains why the 1T phase of MoS_2 exhibits metallic behavior, whereas the 2H phase has semiconducting properties. Thermodynamically, the 2H phase of MoS_2 is the more stable form. In Chapter 3.1, colloidal MoS_2 is examined, showing that under specific synthesis conditions, colloidal metallic MoS_2 can be produced as the kinetic product of the reaction. However, altering reaction parameters such as time, temperature, and precursor concentration results in the formation of only the thermodynamically more stable 2H-MoS_2.

Band Structure

To understand the electronic properties of MoS_2, I first briefly explain the construction of its Brillouin zone. The high-symmetry points of the first Brillouin zone are crucial for the analysis of ARPES data discussed in Chapter 3.2 and serve as reference points in band diagrams, which are used to study electronic transitions in semiconductor materials.

Figure 4 illustrates the crystal structure from a top-down view, including the lattice vectors. The second part of the figure shows the corresponding reciprocal lattice along with the reciprocal lattice vectors. I focus on the two-dimensional perspective because the measurement technique used in Chapter 3.2, with constant excitation energy, maps the momentum of the photoelectrons only in the k_x and k_y planes.

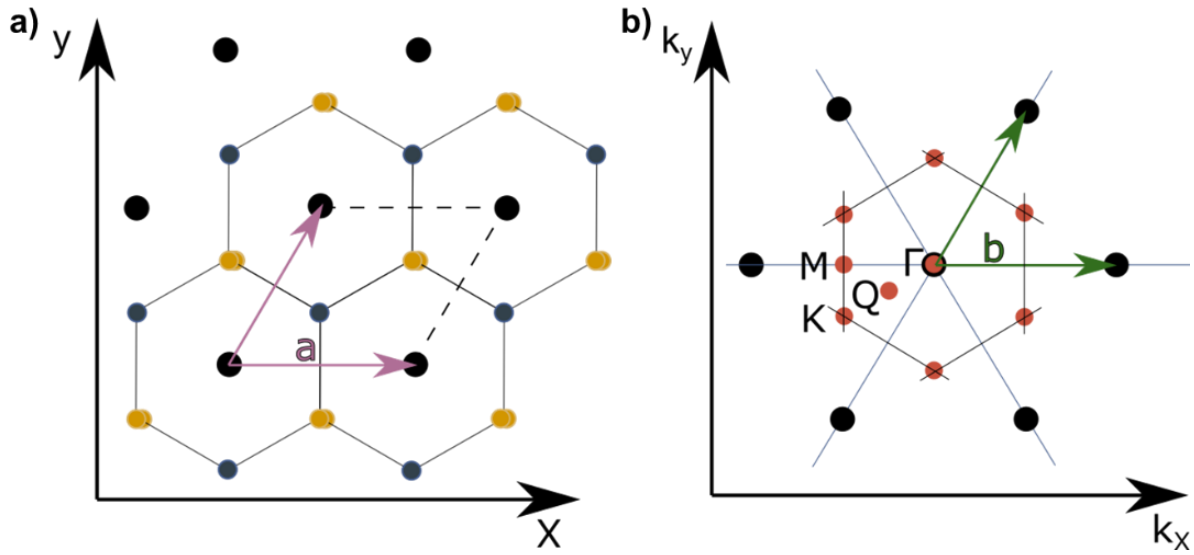

Figure 4 Construction of the hexagonal Brillouin zone from the crystal structure. (**a**) Shows the hexagonal crystal structure with lattice constant a from a top-down view. (**b**) Constructed first Brillouin zone with reciprocal lattice constant b and high-symmetry points Γ, M, K, and Q.

In the two-dimensional analysis of the hexagonal lattice in 2H-MoS_2, with the unit vectors in real space denoted as $\hat{x}$ and $\hat{y}$, the lattice vectors are:

$$\overrightarrow{a_1} = \frac{a}{2}\left(\sqrt{3}\,\hat{x} + \hat{y}\right)$$
$$\overrightarrow{a_2} = \frac{a}{2}\left(-\sqrt{3}\,\hat{x} + \hat{y}\right) \qquad (1)$$

In the reciprocal space, the reciprocal lattice vectors, with the reciprocal unit vectors $\widehat{k_x}$ and $\widehat{k_y}$, are given by:

$$\overrightarrow{b_1} = \frac{2\pi}{a}\left(\frac{\sqrt{3}}{3}\,\widehat{k_x} + \widehat{k_y}\right)$$
$$\overrightarrow{b_2} = \frac{2\pi}{a}\left(-\frac{\sqrt{3}}{3}\,\widehat{k_x} + \widehat{k_y}\right) \qquad (2)$$

After constructing the reciprocal lattice, the Brillouin zone can be determined. To do this, lines are drawn through all points of the lattice, and the intersection points reveal the high-symmetry points. The construction of the Brillouin zone is analogous to the construction of the Wigner-Seitz cell, but in reciprocal space.

From the geometric analysis of the Brillouin zone, the distances between the points ΓM, ΓK (which is the same as KK), and MK are given by:

$$\Gamma M = \frac{\overrightarrow{b_1}}{2} = \frac{2\pi}{\sqrt{3}\,a}$$
$$\Gamma K = KK = \frac{4\pi}{3a} \qquad (3)$$
$$MK = \frac{2\pi}{3a}$$

In MoS_2, with a lattice constant of 3.162 Å, this results in distances of 1.147 Å^{-1}for ΓM, 1.325 Å^{-1} for ΓK, and 0.663 Å^{-1} for MK.

A key aspect of the energy dispersion in MoS_2 is the transition from an indirect to a direct semiconductor when the number of layers is reduced to a single monolayer. As mentioned earlier, bulk MoS_2 is an indirect semiconductor. **Figure 5** shows the band structure calculated using density functional theory (DFT) for bulk MoS_2, as well as for bilayer and monolayer MoS_2.

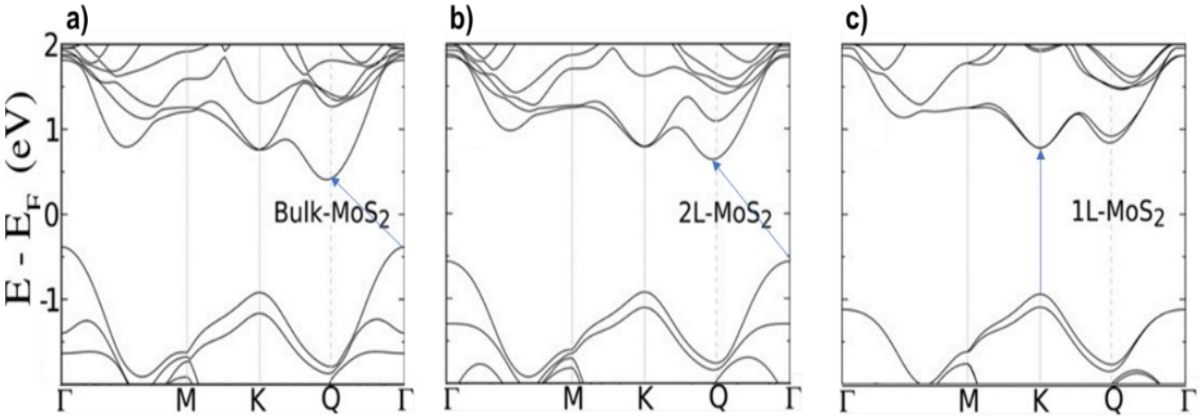

Figure 5 Band structure of MoS_2 from DFT calculations with varying layer numbers for (**a**) bulk MoS_2, (**b**) bilayer MoS_2, and (**c**) monolayer MoS_2. (Figure adapted and slightly modified with permission from Ref.[4])

In this work, the valence band of bulk MoS_2 was directly measured using ARPES at the LowDosePES endstation at the BESSY II electron storage ring in Berlin (see Chapter 3.2), and it reflects the structure predicted by the DFT calculations in **Figure 5 a**.[4] The DFT calculations clearly demonstrate the shift from an indirect semiconductor, where the valence band maximum occurs at the Γ-point (center of the Brillouin zone, see **Figure 4 b**) and the conduction band minimum at the Q-point (midway between Γ and K, see **Figure 4 b**), to a direct semiconductor, with the

transition occurring at the K-point (corners of the hexagonal Brillouin zone, see **Figure 4 b**).

This transition has significant effects on for the photoluminescence (PL) of MoS_2. First, there is a substantial increase in PL intensity when moving from a bilayer to a monolayer, corresponding to the shift from an indirect to a direct semiconductor transition. Additionally, a blue shift can be observed as the number of layers decreases, which is attributed to the widening of the bandgap. In Chapter 3.3, the study of the orientation of cobalt phthalocyanines on MoS_2 samples with different layer counts is discussed. PL measurements were part of this study to characterize exfoliated monolayers of MoS_2.

2.2 Introduction to cobalt phthalocyanine

A significant portion of this work focuses on the investigation of heterostructures composed of an inorganic semiconductor, molybdenum disulfide (MoS_2) as introduced in the previous chapter, and an organic molecule, cobalt phthalocyanine (CoPc). CoPc belongs to the class of transition metal phthalocyanines, which are carbon and nitrogen-based molecules that form an extended conjugated macrocyclic π-system.[16, 17] In **Figure 6**, the general structural formula of phthalocyanines, specifically cobalt phthalocyanine and its perfluorinated derivative, is shown. The figure highlights all chemically inequivalent nitrogen and carbon atoms.

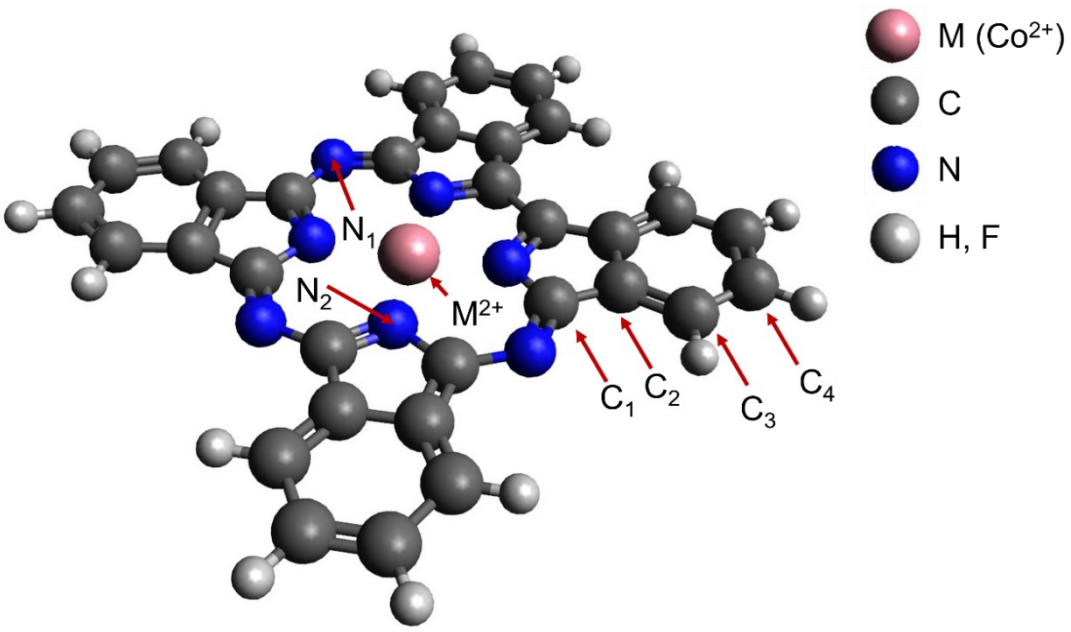

Figure 6 General structural formula of phthalocyanines, specifically cobalt phthalocyanine and its perfluorinated derivative. All chemically inequivalent nitrogen and carbon atoms are highlighted.

The general structure of transition metal phthalocyanines can be described as a transition metal ion (M^{2+}) coordinated by four pyrrole nitrogen atoms (labeled as N_2 in **Figure 6**). These pyrrole groups are connected by four bridging aza nitrogen atoms (N_1).

Regarding the investigation of phthalocyanines, it is important to emphasize again that the carbon atoms in these molecules are chemically inequivalent and can therefore be distinguished using X-ray photoelectron spectroscopy (XPS).[18] This distinguishability

becomes even more pronounced when leveraging one of the key advantages of phthalocyanines: their wide range of chemical versatility. For example, the hydrogen atoms can be substituted with fluorine. In the non-fluorinated form, it is challenging to distinguish the carbon atoms bridging the pyrrole unit and the phenyl unit (C_2) from the phenyl carbons (C_3 and C_4) in terms of the chemical shifts in the **C***1s* region of the XPS spectrum. Therefore, in the fit models used to deconvolute the **C***1s* peaks for the heterostructures of MoS_2 and phthalocyanines discussed in Chapter 3.2, no distinction was made between the bridging (C_2) and aromatic carbons (C_3 and C_4).[19]

This situation changes when the hydrogen atoms are substituted with fluorine. In this case, there are significant differences in the chemical environment, and due to the highly electronegative fluorine, the binding energy of photoelectrons emitted from the core levels of the carbon atoms (C_3 and C_4) increases by more than 2 eV compared to the non-fluorinated phthalocyanine.

Furthermore, fluorination impacts additional properties of phthalocyanines. It has been observed that fluorination influences the optical bandgap. UV-Vis absorption studies (see **Figure S13** in Appendix B) showed a slightly reduced bandgap of approximately 0.1 eV. Beyond the bandgap, electronic properties such as the ionization energy of organic molecules are also crucial when studying interactions between organic molecules and semiconductor materials. This property can be determined using PES, and as demonstrated in Chapter 3.2, the ionization energy of non-fluorinated CoPc differs from that of fluorinated $CoPcF_{16}$ by more than 1 eV. These specific material properties play a pivotal role in the study of energy-level alignment in organic-inorganic semiconductor heterostructures, as discussed in Chapter 3.2.

In addition to the ability to modify peripheral groups, the choice of the transition metal offers another degree of freedom. This work focused on cobalt phthalocyanines. In CoPc, cobalt is in the +2 oxidation state, with 7 valence electrons distributed among the five Co *d*-orbitals. These d-orbitals differ in their spatial orientation and are categorized as d_{z2}, d_{x2-y2}, d_{xy}, d_{yz}, and d_{xz}. Phthalocyanines possess several C_4 and C_2 rotational axes, as well as a horizontal mirror plane, which places them in the D_{4h} point group. The coordination of the transition metal causes the energetically degenerate orbitals to split. **Figure 7** illustrates the respective orbitals along with their symmetries and electron occupancy for Co(II).

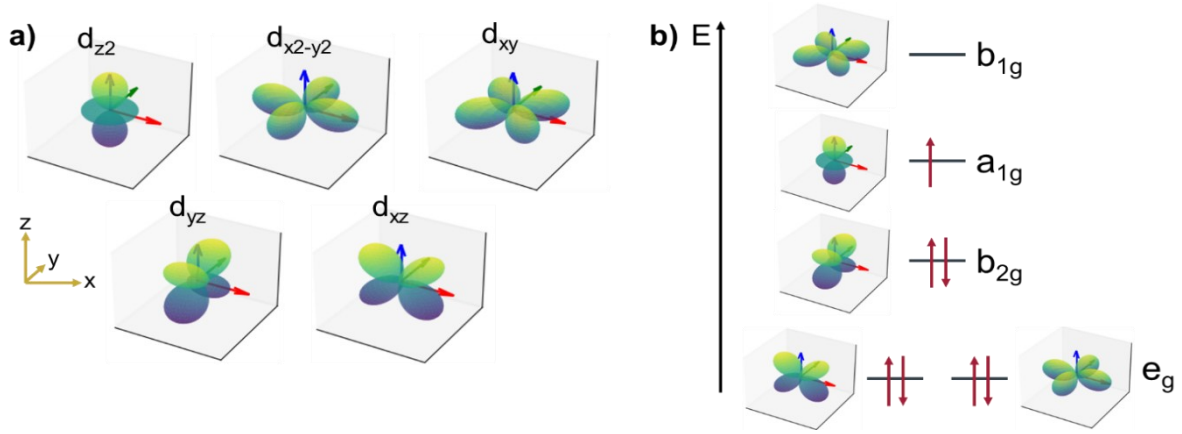

Figure 7 (a) Schematic representation of the d-orbitals and their notation based on spatial orientation. (b) Lifting of the energetic degeneracy of the orbitals in the ligand field of phthalocyanine with D4h symmetry.

The order of orbital splitting, based on density functional theory (DFT) calculations, has been a topic of considerable debate, as two possible configurations appeared plausible. However, the configuration shown in **Figure 7 b** was confirmed through X-ray absorption experiments.[20] In this work, X-ray absorption spectroscopy (XAS) experiments were also conducted, forming the basis of the investigations in Chapter 3.2 and Chapter 3.3. These experiments revealed p-d transitions, described in detail later in Chapter 2.4, that exhibit angular dependence. This is due to absorption processes occurring in the unoccupied b_{1g} orbitals within the molecular plane and the a_{1g} orbitals orthogonal to the molecular plane. With cobalt as the central atom, these studies enable the investigation of the orientation of molecules on the surface as well as the possible formation of covalent bonds, which could block certain absorption transitions.

Although the d-orbitals of the central transition metal can contribute states within the highest occupied molecular orbital (HOMO) and the lowest unoccupied molecular orbital (LUMO) gap, DFT results for CoPc suggest only a moderate interaction, resulting in limited perturbation of the frontier orbital energies. This allows for a reasonable comparison with related systems such as copper phthalocyanine (CuPc). Similarly, fluorination does not alter the order or shape of the wavefunctions, but as previously mentioned, it does affect the energy levels.[21] **Figure 8 a-c** displays the wavefunctions of the HOMO and the degenerate LUMOs for CuPc. As shown by DFT

calculations for other phthalocyanines, the wavefunctions for the CoPc and $CoPcF_{16}$ investigated in this work are analogous (see **Figure 8 g**).

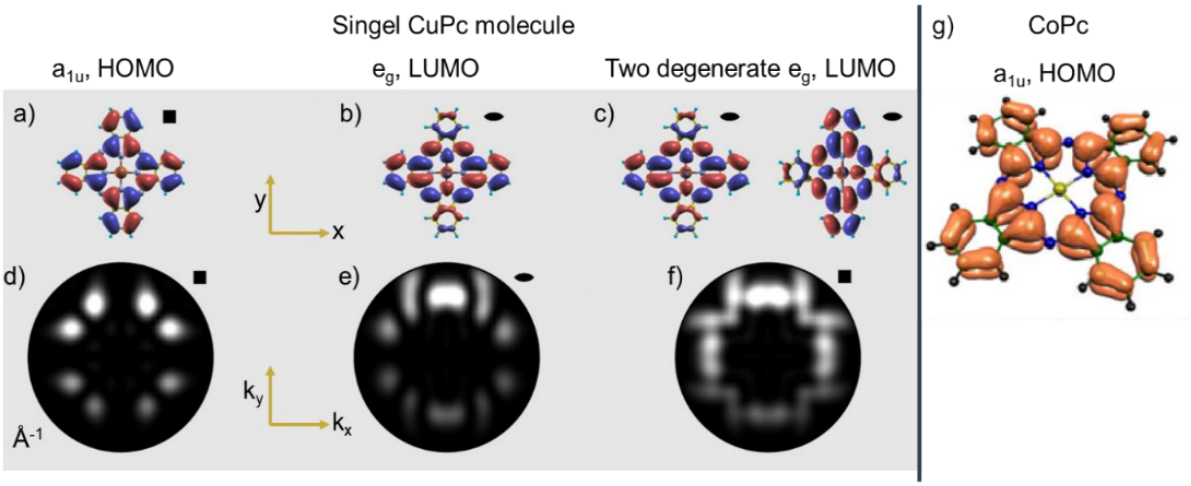

Figure 8 (**a-c**) Display the calculated HOMO and LUMO wavefunctions of CuPc and (**d-f**) the corresponding momentum maps in reciprocal space. (Figure adapted and slightly modified with permission from Ref.[5]) In (**g**), the wavefunction of the HOMO specifically calculated for CoPc is shown. (Figure adapted and slightly modified with permission from Ref.[7])

Figure 8 d–f shows the calculated momentum maps of the HOMO and LUMOs. These momentum distributions can be directly measured using angle-resolved photoelectron spectroscopy (ARPES). In this work, similar angle resolved photoelectron emission measurements were conducted in Chapter 3.2 and are central to the discussion on the potential charge transfer processes at the interface between CoPc and $CoPcF_{16}$ with MoS_2.

2.3 Photoelectron Spectroscopy

Photoelectron Spectroscopy (PES) is an analytical technique that, as the name suggests, utilizes the interaction of light with matter to obtain information about the occupied electronic states in a material. The method is based on the photoelectric effect, which was experimentally discovered in 1887 by Heinrich Hertz and Wilhelm Hallwachs, and for its theoretical explanation, Albert Einstein was awarded the Nobel Prize in Physics in 1921.

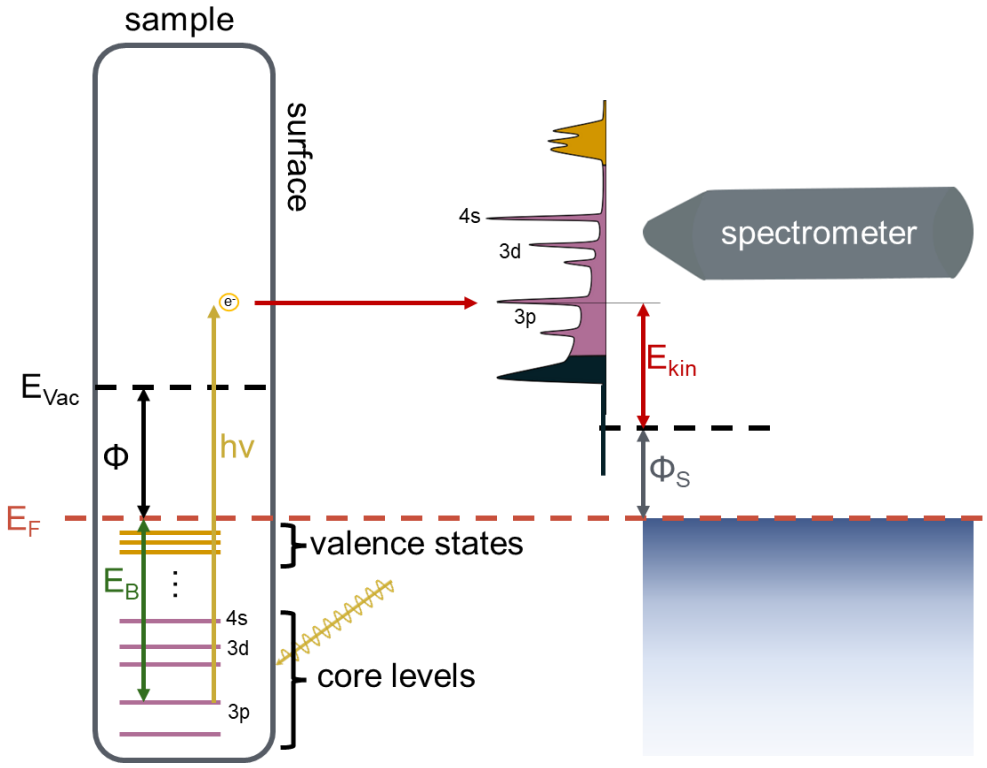

Figure 9 Schematic illustration of a Photoelectron Spectroscopy (PES) measurement, indicating all relevant electronic states and the corresponding measurement parameters.

In **Figure 9**, the measurement principle is illustrated. Light, specifically photons with energy $h\nu$, strikes the surface of a sample. If the energy of the incoming photons is sufficiently high, an electron that was previously bound in a state with a specific binding energy (E_B) can be excited above the vacuum level (E_{Vac}) and becomes free in the vacuum. The vacuum level is defined as the energy of an electron at rest in the vacuum, far from any surface. In the context of photoelectron spectroscopy (PES), however, the relevant quantity is the local vacuum level near the surface, which reflects

the energy an electron needs to overcome the surface potential barrier, including the effects of surface dipoles. It serves as a reference for determining the work function and binding energies of electronic states.[22] The work function (Φ), which is, in the first approximation, a material-specific constant, but it also depends on the surface properties. The quantity measured in PES is the kinetic energy (E_{kin}) of the photoelectrons, which depends on the excitation energy, the binding energy, and the work function. This relationship and the underlying equation form the fundamental equation of photoelectron spectroscopy.

$$E_{kin} = h\nu - E_B - \Phi_S \qquad (4)$$

In a photoelectron spectrometer, the sample and the electron analyzer are typically in electrical contact, which results in alignment of their Fermi levels. The Fermi level thus serves as a common reference point for energy measurements. Depending on the choice of energy axis, spectra can be plotted either as a function of binding energy and therefore referenced to the Fermi level or as a function of kinetic energy and be referenced to the vacuum level. In the former case, the Fermi level is set to 0 eV, whereas in the latter, it corresponds to the excitation energy minus the analyzer work function. As illustrated in **Figure 9**, the measured kinetic energy of a photoelectron is lower than the energy difference between the initial state (e.g., a core level) and the Fermi level. This discrepancy arises because the photoelectron must also overcome the work function of the analyzer to be detected. The analyzer work function is not necessarily equal to that of the sample and must be determined via calibration. This is commonly done by measuring the binding energy of a well-known core level, such as the Au $4f_{7/2}$ level of a clean gold reference, which has a well-established binding energy of 84.0 eV. The energy scale of the spectrometer is then adjusted accordingly.

Notation

In this work, references to specific element-specific binding energies of emitted photoelectrons are frequently made. As mentioned earlier, for instance, in the case of the Au *4f* core level, spectroscopic notation is used. This notation follows a scheme where the element symbol corresponding to the nucleus is listed first, followed by the principal quantum number (n) and the azimuthal quantum number (l), which is represented by the corresponding letters (s, p, d, f). When spin-orbit coupling occurs,

resulting in a change in orbital energy, it is indicated by adding the total angular momentum quantum number (j) as an index.

In addition to the notation for the main peaks in XPS spectra, electrons emitted from secondary processes are also detected. These are electrons that result from the Auger effect and are therefore called Auger electrons. The Auger process will be explained in more detail in subsequent sections, but it is important to note here that Auger electrons are labeled differently, using X-ray notation. X-ray absorption also utilizes this notation. For example, in Chapters 3.2 and 3.3, different absorption edges of CoPc and $CoPcF_{16}$ on MoS_2 are examined, with particular focus on the Co L_2 and Co L_3 edges.

Quantum number				**Atomic notation**	**X-ray notation**
n	**l**	**s**	**j**		
1	0	1/2	1/2	*1s*	K
2	0	1/2	1/2	2s	L_1
2	1	1/2	1/2	$2p_{1/2}$	L_2
2	1	1/2	3/2	$2p_{3/2}$	L_3
3	0	1/2	1/2	3s	M_1
3	1	1/2	1/2	$3p_{1/2}$	M_2
3	1	1/2	3/2	$3p_{3/2}$	M_3
3	2	1/2	3/2	$3d_{3/2}$	M_4
3	2	1/2	5/2	$3d_{5/2}$	M_5

Photoelectron Spectra

Based on the XPS spectra measured in the studies, the following sections will explain the detected signals and their physical background. The spectrum shown in **Figure 10 a** was recorded using the in-house spectrometer and presents an overview spectrum measured on a molybdenum disulfide crystal, which was cleaved in ultra-high vacuum (UHV). In a subsequent measurement series, $CoPcF_{16}$ was deposited on the crystal using molecular beam epitaxy. The detailed setup of the spectrometer, including the monochromatized Al K_α (1486.6 eV) photon source, is described in Chapter 2.5.1.

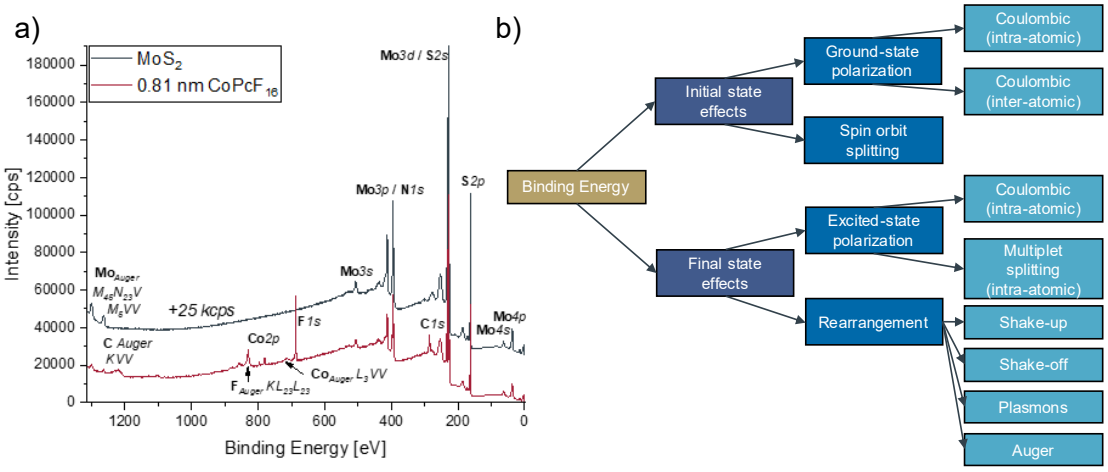

Figure 10 (**a**) XPS spectrum of MoS_2 and MoS_2 after deposition with $CoPcF_{16}$. (**b**) Schematic illustration of the effects influencing the detected binding energy (sketch adapted from Ref.[1])

In **Figure 10 a**, several peaks can be observed, each corresponding to orbitals of the respective atoms. For the physical description of the binding energy, a PES experiment must be considered as a many-body problem. The initial state is a system with N electrons. After the removal of one electron, the system is left with N-1 electrons, which represents the final state. The total energy of the system is then described by the equation:

$$E_{tot}(N) + h\nu = E_{tot}(N-1) + E_{kin} + \Phi \qquad (5)$$

where $E_{tot}(N)$ is the energy of the system with N electrons, $E_{tot}(N-1)$ is the energy of the system with $N-1$ electrons, $h\nu$ is the photon energy, and Φ is the work function.

This equation captures the essence of the energy required to remove an electron from the system and reflects the complexity of the many-body interactions involved.

Taking Equation (6) into account, the binding energy E_B is given by the energy difference between the ionized final state and the initial state of the system:

$$E_B = E_{tot}(N-1) - E_{tot}(N) \qquad (7)$$

This expression represents the energy required to remove an electron from the system, reflecting the difference in total energy between the ionized state (with $N-1$ electrons) and the initial state (with N electrons).

This problem can be solved using the Hartree-Fock method under the assumption that the removal of an electron from a specific orbital k does not affect the remaining orbitals. In this context, the binding energy of an electron in a particular orbital is equal to the negative of its orbital energy. This conclusion is known as Koopmans' theorem.

$$E_B(k) = -\varepsilon_k \quad (8)$$

In experiments, the measured binding energy is typically lower than the value predicted by the negative orbital energy. This discrepancy arises from various effects, which are summarized in the diagram in **Figure 10 b**. These effects can generally be categorized into initial-state and final-state effects.

Initial-state effects include the bonds that an atom forms. In the diagram (**Figure 10 b**), these are collectively referred to as ground-state polarization. These can be further subdivided into intra-atomic and inter-atomic effects. For example, in the **C***1s* spectra of cobalt phthalocyanine, we observe different signals for the chemically nonequivalent carbon atoms. Although chemical bonding involves valence electrons, all other electrons, including core electrons, experience changes in charge density.

An example of inter-atomic Coulomb effects and their influence on the detected binding energy is found in Chapter 5.1, where cesium lead halide perovskites were investigated. Under X-ray irradiation, a contraction of the ionic lattice was observed. This example clearly shows how changes in atomic distances, in this case, ions, affect the potential on individual atoms, thereby altering the measured binding energy of the electrons. This change in potential can be calculated using the Madelung potential, as demonstrated in the work discussed in Chapter 5.1.

Additionally, in the spectrum shown in **Figure 10 a**, it can be observed that all signals, except those from photoelectrons detected from s-orbitals, split into doublets. This phenomenon is due to an initial-state effect known as spin-orbit coupling (also referred to as spin-orbit splitting). This effect occurs because a spinning electron creates a magnetic field that interacts with the magnetic field generated by the electron's motion around the nucleus. Since the orbital on which the electron moves around the nucleus is defined by the azimuthal quantum number l, and an electron can have two spin orientations, two possible configurations arise, described by the so-called total angular momentum quantum number j:

$$j = l \pm s \quad (9)$$

where l is the orbital angular momentum and s is the electron spin quantum number. This spin-orbit coupling leads to the observed splitting of the spectral lines in the XPS spectra.

As seen in **Figure 10 a**, the magnitude of the spin-orbit splitting varies for each element and each orbital under consideration. This variation occurs because the spin-orbit coupling constant (a) depends on both the atomic number (Z) and the distance of the electron from the nucleus (r). Specifically, the spin-orbit coupling strength increases with higher atomic numbers and decreases with greater distances of the electron from the nucleus. This dependency explains why heavier elements, or electrons in orbitals closer to the nucleus, exhibit larger spin-orbit splitting compared to lighter elements or electrons in more distant orbitals.

$$a = \frac{\mathrm{Ze}^2 \mu_0 \hbar^2}{8\pi m_e^2 r^3} \quad (10)$$

The expectation value for $\frac{1}{r^3}$ is given as:[23]

$$\langle \frac{1}{r^3} \rangle = \frac{Z^3}{a_B^3 n^3 l(l+\frac{1}{2})(l+1)} \quad (11)$$

Upon substitution, it becomes clear that the appearance of spin-orbit components in the experiment, as expected, depends on the atomic number, specifically with a Z^4 dependency, and on the azimuthal quantum number with a dependency of $\frac{1}{l(l+\frac{1}{2})(l+1)}$.

This is nicely illustrated by the example of molybdenum *3p* and *3d* orbitals, where the splitting of the *3p* orbital (with $l = 1$) is significantly larger than that of the *3d* orbital (with $l = 2$).

In addition to the initial-state effects discussed so far, XPS spectra also display additional features that arise because of the photoemission process. As illustrated schematically in **Figure 10 b**, these are referred to as final-state effects. The corresponding physical mechanisms are depicted in **Figure 11**.

Figure 11 a shows multiplet splitting, which is observed in this work and discussed in Chapter 3.2. In particular, the **Co***2p* signals exhibit significant broadening. As shown in

Chapter 2.2 (**Figure 7**), Co^{2+} has unpaired electrons in the *3d* shell. After photoemission from a *2p* orbital, the resulting core hole interacts with the open-shell *3d* electrons. The overlap of the core and valence wave functions leads to an intra-atomic Coulomb interaction, which splits the final state into several energy levels. This multiplet structure arises from the vector coupling of the angular momenta of the *2p* and *3d* electrons and manifests as broadening or even well-resolved sub-peaks in the XPS spectrum.

Another class of final-state effects involves electronic rearrangement processes. One such process, observed in the **Co***1s* spectra of CoPc and $CoPcF_{16}$ molecules and included in the fitting model described in Chapter 3.2, is the so-called shake-up process. Here, in addition to the photoemission event, a second electron undergoes a non-radiative excitation, commonly a HOMO–LUMO transition in organic molecules. This results in satellite peaks at higher binding energies (or lower kinetic energies) relative to the main photoemission line, as illustrated in **Figure 11 b**. The energy difference between the main line and the satellite reflects the energy of the accompanying excitation.

A different type of energy loss structure is observed in the spectra of MoS_2 and is attributed to interactions with collective electron excitations, known as plasmons. As shown in **Figure 10 a**, plasmon loss features appear as regularly spaced replicas of the main Mo and S core levels, each separated by the plasmon energy. These structures result from the quantized nature of plasmons and typically exhibit decreasing intensity with increasing energy loss.

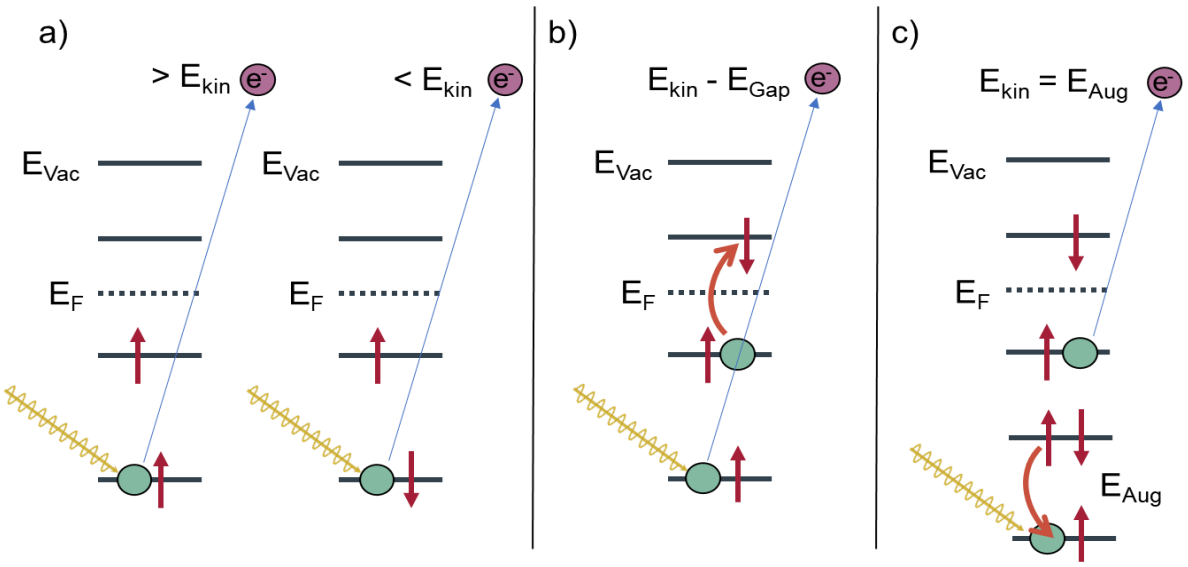

Figure 11 Schematics illustrating the occurrence of loss structures alongside the main signals in core-level XPS spectra. (**a**) Multiplet effects due to interactions with unpaired valence electrons. (**b**) Shake-up processes caused by simultaneous excitation of HOMO-LUMO transitions. (**c**) Auger process resulting from the filling of a hole state created by photoemission.

Further possible final-state decay channel is the Auger process, shown in **Figure 11 c**. In this process, a higher-lying electron fills the core hole created by photoemission, and the excess energy is transferred to a second electron, which is subsequently emitted. The kinetic energy of the Auger electron corresponds to the difference in binding energies of the involved electronic levels and is, in contrast to photoemission, largely independent of the excitation energy. As a result, Auger electrons appear at fixed kinetic energies. When spectra are plotted as a function of binding energy (using Equation (4)), their apparent position depends on the excitation energy. Therefore, particular care must be taken in experiments using tunable photon energies, such as synchrotron-based measurements, to avoid overlap between Auger peaks and core-level photoemission signals.

Auger transitions are denoted using X-ray notation. For example, a carbon Auger signal observed after phthalocyanine deposition would be labeled C_{KVV}. The first letter (K) refers to the initial core hole (*1s* level), the second (V) to the orbital from which an electron fills the core hole (in this case, a valence state), and the third (V) to the orbital from which the emitted Auger electron originates.

The equation shown earlier (Equation (4)) is only valid for primary electrons that leave the sample, providing direct information about the energy levels of core and valence electrons. However, electrons moving through a material are subject to inelastic scattering processes. Inelastic scattering results in a loss of kinetic energy and, consequently, the detection of secondary electrons in the spectrum. These secondary electrons contribute to the typical background observed in photoelectron spectra, a topic that will be discussed in greater detail later.

Also a characteristic feature in a photoelectron spectrum is the secondary electron cutoff (SECO). It marks the lowest kinetic energy at which photoelectrons can still escape from the sample into the vacuum. Since electrons must overcome the material's work function to be emitted, any electron with a kinetic energy lower than this threshold relative to the vacuum level cannot contribute to the detected spectrum. This leads to a sharp drop in intensity, known as the SECO. Determining the exact position of this cutoff is essential in photoelectron spectroscopy, as it enables the accurate determination of the work function. A more detailed discussion will follow in later chapters.

So far, I have focused on the kinetic energy of the detected photoelectrons. To understand the measured intensity, i.e., the number of photoelectrons detected at a given kinetic energy, the following section introduces the three-step model of photoemission, originally proposed by Berglund and Spicer.[24] This phenomenological model provides an intuitive framework for describing the photoemission process from solids and is widely used in the interpretation of XPS data.

The three steps are:

1. Photoexcitation of electrons within the bulk of the material
2. Transport to the sample surface
3. Escape of the electrons into the vacuum

While simplified, this model captures the essential physical processes that determine the photoemission yield and lineshape.

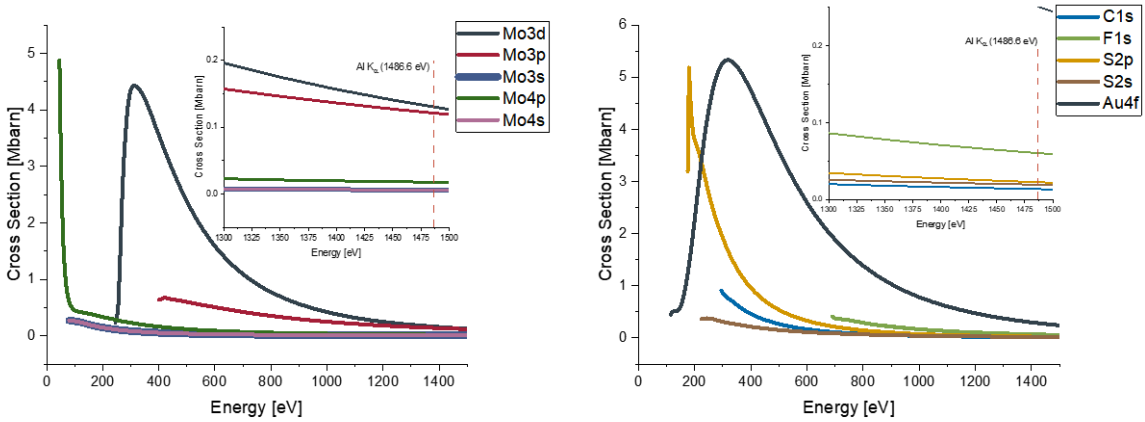

Figure 12 Photoionization Cross Sections for different materials and orbitals used in this work taken from Yeh and Lindau.[3] The inlays show a magnified selection in the vicinity of the Al Kα (1486.6 eV) excitation, marked by a vertical line.

The excitation of photoelectrons and the corresponding probability can be described by Fermi's golden rule. For practical purposes, particularly in the analysis of XPS spectra, photoionization cross sections are of significant importance. In **Figure 10 a**, one can observe that the signals from molybdenum appear with varying intensities. This difference is due to the different photoionization cross sections of the individual orbitals, as shown in **Figure 12**. For quantitative analysis of the signals, the photoionization cross sections must be considered when comparing the areas of the peaks, as was done to elucidate the reaction mechanism discussed in Chapter 5.1.

In general, the choice of substrate for the perovskite studies conducted in Chapters 5.1, 5.2, and 5.3 can also be justified based on the photoionization cross sections. One challenge in these studies was the suppression of charging effects, which occur when, after photoionization, not enough electrons flow back to return the system to its relaxed initial state. As exemplified in **Figure 12** with the **Au***4f* level, several gold core orbitals, especially **Au***4f*, exhibit a relatively high photoionization cross section under Al Kα excitation. As a result of the efficient photoionization, the number of secondary electrons, produced through scattering processes as will be further discussed, is also very high. This large number of secondary electrons can help suppress charging effects in less conductive materials. Therefore, gold-coated silicon wafers were used for the investigation of perovskite samples, which, in addition to facilitating the preparation of monolayers of perovskite nanocrystals, effectively eliminated charging.

The second step in the three-step model is the transport of electrons to the sample surface. During this process, inelastic collisions can occur, reducing the kinetic energy of the electrons. These lower-energy electrons contribute to the typical background seen in XPS spectra. In **Figure 10 a**, one can clearly see how the background exhibits a step-like increase following the main peaks. These step profiles are accounted for in fitting by using a Shirley background. An important parameter that highlights the surface sensitivity of PES experiments is the inelastic mean free path (λ, IMFP) of the electrons in the solid. One of the earliest attempts to predict this was made by Seah and Dench, [25] which resulted in the so-called universal curve for the mean free path.

$$\lambda(E_{kin}) = \frac{143}{E_{kin}} + 0.054 \cdot \sqrt{E_{kin}} \qquad (12)$$

This approach is purely empirical. The work by Seah and Dench further revealed that the IMFP differs between inorganic and organic solids. The formula developed for organic materials has served as the basis for the determination of film thicknesses using XPS, which will be explained later. This formula also includes the density (ρ) of the respective material:

$$\lambda(E_{kin}) = \frac{\frac{49}{E_{kin}^2} + 0.11\sqrt{E_{kin}}}{\rho} \qquad (13)$$

In this work, the model of Seah and Dench was frequently used to calculate the inelastic mean free path (IMFP), for example to estimate the number of deposited layers of CoPc and $CoPcF_{16}$. However, in Chapter 3.2 , which discusses the interaction of cobalt phthalocyanines with MoS_2 bulk crystals, it is shown that the surface and subsurface interactions differ significantly between the fluorinated and non-fluorinated derivatives. What is then demonstrated in the aforementioned chapter, these findings are based on synchrotron experiments that allowed for systematic variation of the excitation energy and, consequently, for a depth-resolved analysis via the energy-dependent IMFP. Therefore, more recent methods for determining the IMFP were employed in this context. The theoretical determination of the IMFP remains an active area of research, with ongoing efforts to incorporate additional physical parameters into the calculation models. Two commonly used approaches incorporate the free-electron plasmon energy (E_p), which depends on the number of valence electrons (N_V), the density (ρ), and the molar mass (M). Another important parameter, particularly for

insulators and semiconductors, is the bandgap (E_g). This approach is based on the work of Tanuma, Powell, and Penn, known as the TPP-2M equation.[26] The IMFP (λ) is calculated using the following relationship:

$$\lambda(E_{kin}) = \frac{E_{kin}}{E_p^2[\beta \cdot \ln(\gamma E_{kin}) - \left(\frac{C}{E_{kin}}\right) + \left(\frac{D}{E_{kin}^2}\right)} \quad (14)$$

with

$$E_p = 28.8 \cdot \left(\frac{N_V \rho}{M}\right)^{\frac{1}{2}} \quad (15)$$

$$\beta = -0.10 + \frac{0.944}{\left(E_p^2 + E_g^2\right)^{\frac{1}{2}}} + 0.069\rho^{0.1} \quad (16)$$

$$\gamma = 0.191\rho^{-0.5} \quad (17)$$

$$C = 1.97 - 0.91U \quad (18)$$

$$D = 53.4 - 20.8U \quad (19)$$

$$U = \frac{N_V \rho}{M} = \frac{E_p^2}{829.4} \quad (20)$$

Seah also extended his original formula.[27] The extended formula, known as the S1 equation, models the system based on the molar mass (M), the density (ρ), the number of different types of atoms (i) in the solid, their atomic numbers (Z), and the bandgap (E_g):

$$\lambda(E_{kin}) = \frac{(4 + 0.44Z^{0.5} + 0.104E_{kin}^{0.872})\alpha^{1.7}}{(Z^{0.3} * (1 - 0.02E_g)} \quad (21)$$

With the atomic numbers (Z):

$$Z = \frac{\sum i \cdot Z_i}{\sum i} \quad (22)$$

and

$$\alpha = \frac{10^{21} M}{\rho N_A \sum i} \quad (23)$$

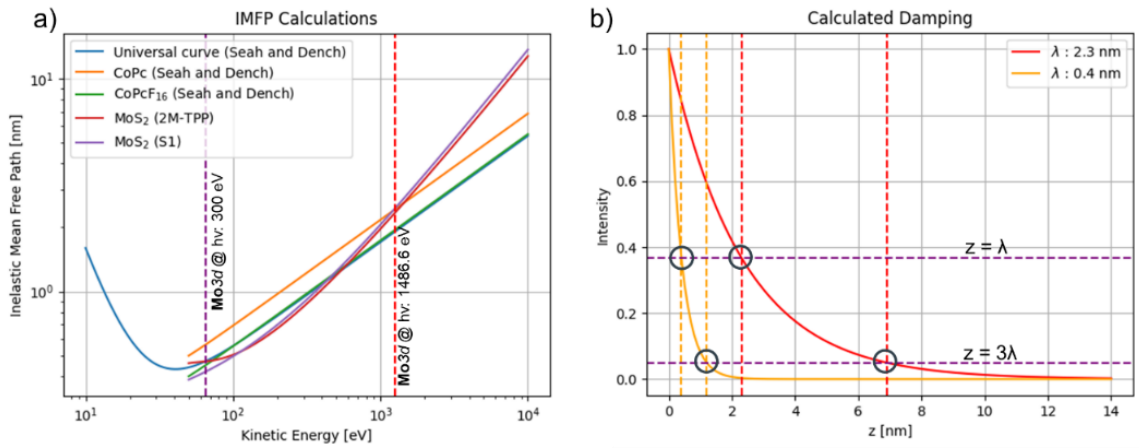

Figure 13 (a) IMFP calculated for different materials used in this work and with different equations. (b) Calculated damping dependent on different IMFP values for **Mo***3d* with different excitation energies.

As mentioned, the IMFP is the reason why PES experiments are surface-sensitive. In **Figure 13 a**, the IMFPs for the materials used in this work are calculated and plotted based on the previously discussed formulas. While X-rays can penetrate deeply into a sample, the detected photoelectrons in XPS experiments originate from only a few tens of angstroms beneath the surface, depending on their kinetic energy. **Figure 13 b** illustrates the attenuation of intensity as a function of depth (z) and the IMFP, using the **Mo***3d* signals as an example. Two different IMFPs are considered, corresponding to excitation with Al Kα radiation (1486.6 eV) and with synchrotron radiation at 300 eV, as was done in Chapter 3.2.

For these two excitation energies, the kinetic energies of the photoelectrons from the **Mo***3d* levels are approximately 1252 eV and 65.5 eV, respectively. The attenuation of intensity as a function of sample depth is described by the Lambert-Beer law:

$$I = I_0 \cdot e^{-\frac{z}{\lambda}} \qquad (24)$$

where I is the intensity at depth z, I_0 is the initial intensity at the surface, and λ is the IMFP. This relationship shows how the signal decreases exponentially with increasing depth, emphasizing the surface sensitivity of PES, particularly for lower kinetic energies where the IMFP is shorter.

As a result, when z equals λ, only about 37% of the photoelectrons emitted from that depth have not experienced inelastic scattering. At a depth of 3λ, which is considered

the information depth in PES experiments, approximately 95% of the emitted photoelectrons have already undergone inelastic scattering.

The final step in the three-step model is the emission of photoelectrons from the sample surface.

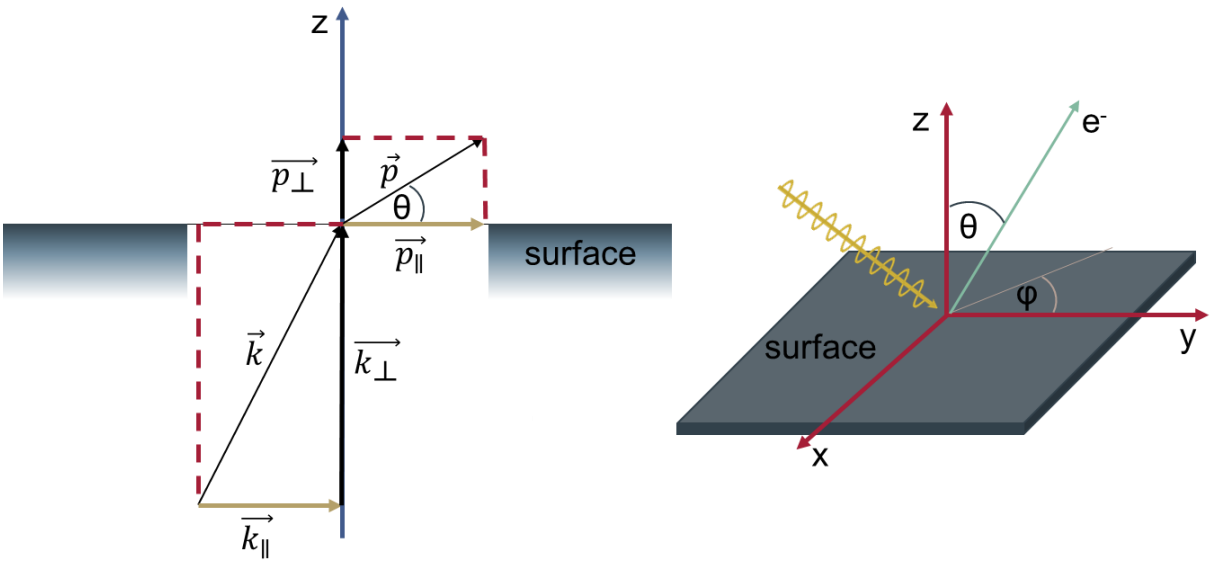

Figure 14 Schematic illustration of the relevant angles and momenta involved in a photoelectron spectroscopy experiment.

A photoelectron emitted from a solid not only possesses kinetic energy, which depends on its binding energy, but also a momentum (p), which is related to its crystal momentum (k). It is important to note that momentum is conserved parallel to the surface, but not orthogonal to it, due to the symmetry breaking at the surface. In most PES experiments, such as those conducted with the laboratory spectrometer used in this work, the momentum information is lost because the measurement integrates over all photoelectrons with the same kinetic energy. However, by using different detectors, such as the Angle-Resolved Time-of-Flight (ARTOF) detector at the LowDosePES endstation at BESSY II, which was used in Chapter 3.2, it is possible to directly map the valence band structure of two-dimensional systems using the momentum information.

With the angles shown in **Figure 14**, the relationship between the measured momentum of the electron and the crystal momentum is given by:

$$k_x = p_x = \frac{1}{\hbar}\sqrt{2m_e E_{kin}}sin\theta cos\varphi \quad (25)$$

$$k_y = p_y = \frac{1}{\hbar}\sqrt{2m_e E_{kin}}sin\theta sin\varphi \quad (26)$$

Determination of film thickness by XPS

An important parameter for studying interactions in this work is the determination of the film thickness of organic molecules on surfaces. Generally, systems composed of organic molecules and transition metal dichalcogenides were fabricated using Molecular Beam Epitaxy (MBE). The film thicknesses were initially estimated by determining the evaporation rates using a quartz crystal microbalance, allowing for the deposition of defined layers based on the deposition times. However, the film thickness after deposition was also determined using XPS measurements.

For this purpose, it is assumed that the new layer causes an attenuation of the substrate signals. As previously mentioned, the intensity of the substrate signal depends on the IMFP and, something that has been neglected so far, on the geometry of the sample relative to the analyzer. This aspect has been neglected up until now because, in a typical experimental setup, the sample surface is oriented perpendicular to the analyzer, resulting in an intensity dependency proportional to $cos\theta$, which equals 1 for this orientation.

The attenuation of the substrate signal due to the overlayer can be described by the following equation:

$$I_S = I_{S,0} \cdot e^{-\frac{d}{\lambda \cdot cos\theta}} \quad (27)$$

The intensity for an infinite overlayer would be:

$$I_D = I_{D,\infty} \cdot \left(1 - e^{-\frac{d}{\lambda \cdot cos\theta}}\right) \quad (28)$$

By calculating the ratios of the measured substrate and coating signals and solving for the layer thickness (d), the following equation is obtained:

$$d = \lambda \cdot cos\theta \cdot \ln\left(1 + \frac{I_D \cdot I_{S,0}}{I_S \cdot I_{D,\infty}}\right) \quad (29)$$

Here, I_S and I_D are directly accessible through the integration of the respective signals in the spectrum. Since this is not the case for $I_{S,0}$ and $I_{D,\infty}$ the emitters per volume are

determined and substituted accordingly. Sensitivity factors of the respective signals must also be taken into account. Furthermore, the stoichiometric factors of the respective atoms in the volume are crucial. This results in the formula that was used for calculating the layer thicknesses in this study:

$$d = \lambda \cdot cos\theta \cdot \ln\left(1 + \left(\frac{x_S \cdot I_D \cdot \sigma_S \cdot \frac{\rho_S}{M_S}}{x_D \cdot I_S \cdot \sigma_D \cdot \frac{\rho_D}{M_D}}\right)\right) \quad (30)$$

UPS

In ultraviolet photoelectron spectroscopy (UPS) using 21.2 eV (He I) or 40.8 eV (He II) photons, the kinetic energy of the emitted photoelectrons typically falls into the range where the inelastic mean free path (IMFP) is near its minimum (see **Figure 13**) Although the IMFP depends primarily on the kinetic energy of the electrons rather than the photon energy, this regime enables surface-sensitive measurements. Furthermore, the photoionization cross-sections for certain orbitals, particularly **C***2p* and **C***2s* states, are significantly higher at UV photon energies than in X-ray photoelectron spectroscopy (XPS) (see **Figure 12**). This makes UPS especially suitable for probing the valence electronic structure. Material properties accessible via UPS include the work function (Ω, derived from the secondary electron cutoff, SECO), as well as the valence band maximum (VBM) in semiconductors or the highest occupied molecular orbitals (HOMO) in organic molecules.

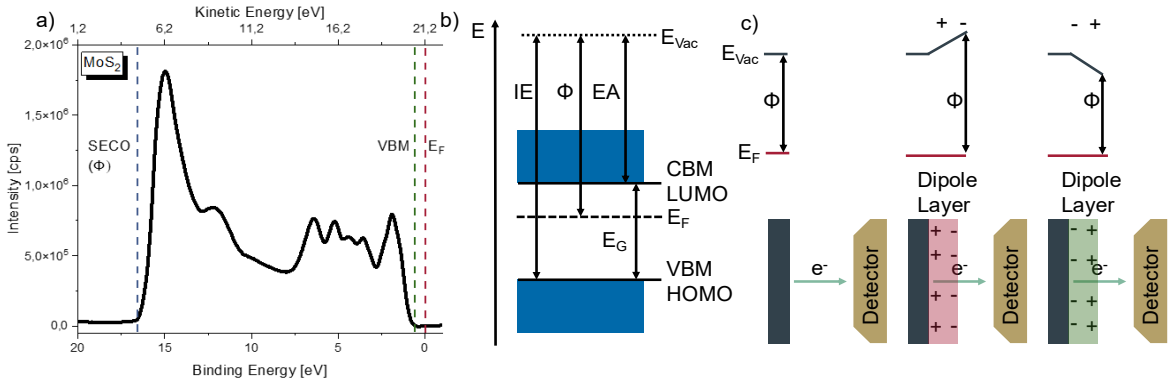

Figure 15 (**a**) UPS spectra of MoS_2. Material properties like the work function, which is related to the SECO, and the VBM relative to the Fermi-Level can be extracted. (**b**) Band structure sketch of a semiconductor with material related values like ionization energie (IE), work function (Φ), electron affinity (EA), valence band maximum (VBM) or highest occupied molecular orbital (HOMO), conduction band minimum (CBM) or lowest unoccupied molecular orbital (LUMO), band gap (E_g) and Fermi-Level (E_F). (**c**) Influence of the formation of a dipole layer on the work function.

In **Figure 15 a**, a UPS spectrum of MoS_2 is shown. The binding energy and the kinetic energy of the measured photoelectrons are plotted. **Figure 15 b** illustrates the typical material properties of semiconductors that can largely be measured by UPS. These properties include the position of the vacuum level, which is the energy of an electron in free space near the surface of a material and serves as a reference for energy measurements. The work function represents the amount of energy required to move an electron from the solid into a vacuum and depends on both the material and its surface. Ionization energy refers to the energy needed to remove the most weakly bound electron from an atom. Electron affinity measures the energy change when an electron is added to an atom, indicating its tendency to attract electrons. [22, 28]

Particularly in the studies on perovskite nanocrystals (NCs) discussed in Chapters 5.1, 5.2, and 5.3, the influence of ligands on the NCs was investigated. Of particular interest was the extent to which the ligands affect surface dipoles and the resulting impact on the stability of the NCs. **Figure 15 c** sketches this relationship, showing that the work function of a system is highly dependent on the surface dipole, which can be modified by ligands depending on the orientation of the dipoles.

2.4 X-ray Absorption Spectroscopy

Like Photoelectron Spectroscopy (PES), X-ray Absorption Spectroscopy (XAS) is a surface-sensitive spectroscopic technique. In XAS, electrons, typically from core levels, are excited to unoccupied states by X-ray radiation. In the PES experiments discussed earlier, photons with discrete energies were used for excitation. In contrast, XAS requires a tunable energy source, making synchrotron radiation necessary for XAS experiments. In this work, the information obtained from XAS experiments was primarily used to study molecular orientations and electronic properties. Generally, however, absorption experiments can also provide insights into the structure and order of a sample. This is achieved by analyzing different regions of the absorption spectrum, which are distinguished by their distance from the so-called absorption edge, the abrupt increase in absorption due to transitions at a specific photon energy.

In the studies conducted for this work, particular emphasis was placed on analyzing the signals near the absorption edge. In this work, XAS is used synonymously with the term NEXAFS (Near Edge X-ray Absorption Fine Structure), which is also commonly used in literature.

When a sample is irradiated with photons whose energy corresponds to the energy difference between an occupied and an unoccupied electronic state, a resonant excitation can occur. This process results in a characteristic absorption edge in the spectrum. Importantly, these unoccupied states can lie either below or above the vacuum level, depending on whether the excitation leads to a bound final state, such as a conduction band or a lowest unoccupied molecular orbital (LUMO), or to ionization. The detection method depends on the specific experimental setup and will be discussed in the following chapter in relation to the detectors used. In general, absorption can be measured directly by monitoring the transmitted X-ray intensity, like other spectroscopic methods. However, for the samples investigated in this work, direct transmission measurements are not feasible. Therefore, indirect detection techniques are employed.

In total electron yield (TEY), all electrons released in subsequent processes following excitation are measured. Another method is based on fluorescence. When a hole state remains after absorption, it can be filled during relaxation, with the energy difference compensated by the emission of a photon.

Again, the intensity of a transition can be described by Fermi's Golden Rule. The probability of a transition from an initial state i (with wave function Ψ_i) to a final state f (with wave function Ψ_f) is given by:

$$w_{if} = \frac{2\pi}{\hbar}\rho_f(E)\left|\langle\Psi_\mathrm{f}\left|\,\widehat{H}\,\right|\Psi_i\rangle\right|^2 \qquad (31)$$

Here, $\widehat{H}$ represents the time-dependent perturbation introduced by the incident radiation. Within the dipole approximation, valid because the photon wavelength is much larger than interatomic distances, this perturbation is given by the scalar product of the electric field vector $\vec{E}$ and the transition dipole moment $\vec{\mu}$. For linearly polarized light, $\vec{E}$ can be treated as a constant factor and taken outside the matrix element, yielding:

$$w_{if} = \frac{2\pi}{\hbar}\rho_f(E)\left|\vec{E}\langle\Psi_\mathrm{f}\left|\,\vec{\mu}\,\right|\Psi_i\rangle\right|^2 \qquad (32)$$

In Chapter 3.3 the angular dependence of X-ray absorption was utilized to investigate the orientation of CoPc and $CoPcF_{16}$ molecules on MoS_2 surfaces. **Figure 16** illustrates this relationship schematically for molecules oriented parallel and perpendicular to the substrate surface, along with the expected angular dependence of the π-resonance intensity. In the simplified vector model, the absorption intensity depends on the angle θ between the electric field vector and the molecular orbital of interest, often described by:

$$I \propto \cos^2\theta \qquad (33)$$

However, this expression is a simplified case. A more accurate description considers the polarization state of the incident light and the geometry of the experiment. As derived by Stöhr[29] and others, the angular dependence for linearly polarized light can be expressed as:

$$I = A[P(\sin^2\cdot\alpha\cdot\sin^2\cdot\theta + 2\cdot\cos^2\cdot\alpha\cdot\cos^2\theta) + (1-P)\cdot sin^2\cdot\alpha] \qquad (34)$$

Here, α is the angle between the molecular axis and the surface normal, θ is the incident angle of the light relative to the surface, and P is the degree of linear polarization. Additionally, experiments such as X-ray Magnetic Circular Dichroism (XMCD) employ circularly polarized light and probe different aspects of the electronic and magnetic structure, which are not captured by the simple vector model.

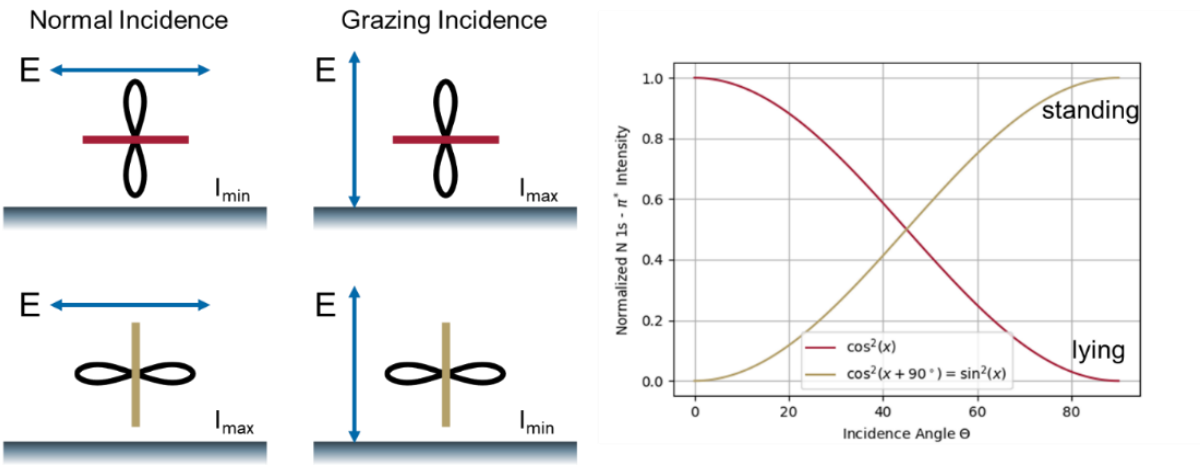

Figure 16 Schematic representation of the molecular orientation of planar conjugated molecules, such as the phthalocyanines used in this work, in both lying and standing configurations. Additionally, the alignment of the electric field vector is illustrated for both grazing and normal incidence. The schematic simplifies the representation by showing a p_z-orbital for the unoccupied π* orbitals. In addition, the dependence of intensity on the angle of incidence is depicted for the two configurations. These represent the standing and lying orientations of the molecules.

2.5 Measurement Setups

Since inelastic scattering processes lead to losses in the kinetic energy of photoelectrons, it is essential that PES experiments are conducted under ultra-high vacuum conditions. Although the principle of photoelectron spectroscopy was known long before the development of measurement systems, its technical realization only became possible with the advent of ultra-high vacuum systems. The quality of a vacuum is categorized into rough vacuum (300 – 1 mbar), fine vacuum (1 – 10^{-3} mbar), high vacuum (10^{-3} – 10^{-7} mbar), and ultra-high vacuum (10^{-7} – 10^{-12} mbar). PES systems typically operate at around 10^{-10} mbar, which is achieved using turbo molecular pumps, preceded by backing pump (often diaphragm pumps). PES systems are commonly constructed with multiple chambers, each equipped with separate forepumps and turbo pumps, and each chamber can be isolated from the others by valves. **Figure 17** shows schematic representations of the systems used in this work, which differ in their functionality, particularly in the type of detector employed.

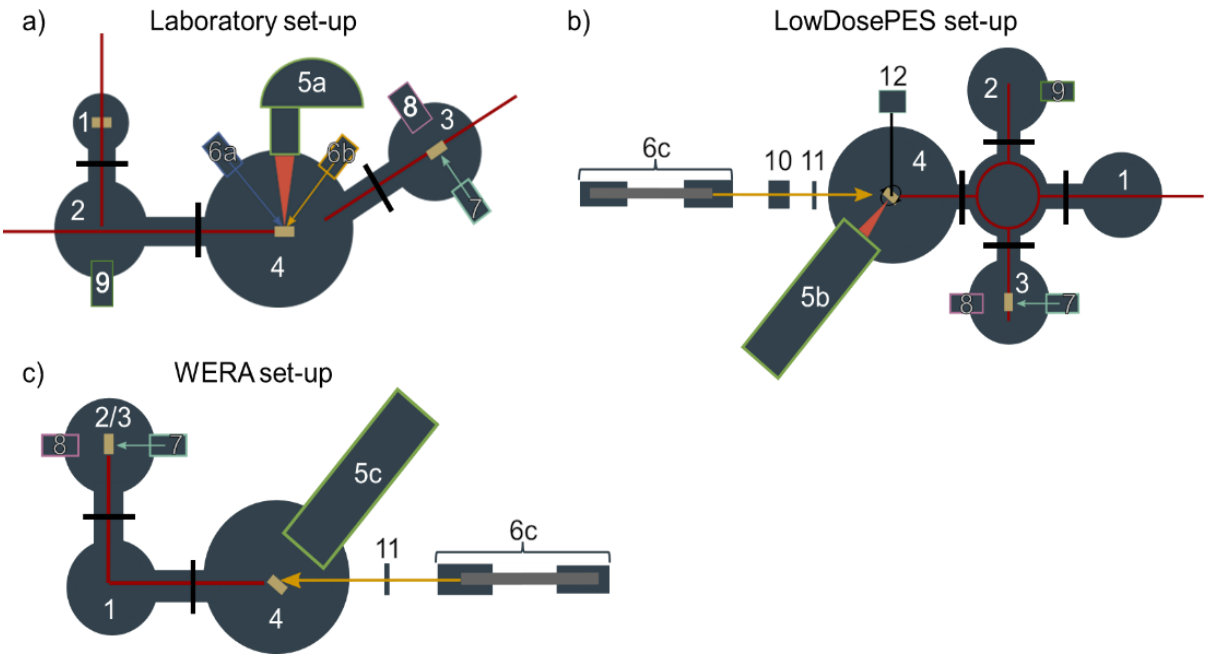

Figure 17 Schematic representations of the measurement systems used in this work. In (**a**), the laboratory spectrometer is shown. In (**b**) and (**c**), the endstations at the synchrotron beamlines BESSY II, the LowDosePES endstation, and the WERA endstation at KARA are depicted, respectively. The assignment of the respective components can be found in **Table 1**.

Table 1 Assignment of the respective numbers shown in **Figure 17**. Each number is assigned the respective function of the measurement setups.

Number	Function	
1	Load-Lock	
2	Preparation Chaimber	
3	Organic Preparation Chaimber	
4	Main Chaimber	
5	a	Hemispherical Detector
	b	Angle Resolved Time of Flight Detector
	c	Photoelectron Microscope
6	a	He-UV Source
	b	Monochrmated Al Kα Source
	c	Dipole and Monochromator
7	Evaporator	
8	Quartz crystal microbalance	
9	Sputter-Gun	
10	Chopper	
11	Mesh	
12	Electrometer	

2.5.1 Laboratory spectrometer

The spectrometer most frequently used in this work is schematically depicted in **Figure 17 a**. For XPS experiments, monochromatic Al K_α radiation (1486.6 eV) can be utilized as the photon source, while for UPS (Ultraviolet Photoelectron Spectroscopy) experiments, He I (21.2 eV) and He II (40.8 eV) radiation can be employed. X-ray radiation is generated by bombarding an aluminum anode with electrons emitted from a hot cathode. These electrons are accelerated by a strong electric field of several kV, leading to the ejection of electrons from the inner K-shell of aluminum atoms. When these vacancies are filled by electrons from higher shells, energy is released as photons corresponding to the energy difference between the shells. Since multiple transitions are possible, it is advantageous to monochromatize the emitted radiation. Therefore, the laboratory spectrometer is equipped with a monochromator, an optical crystal that, by satisfying the Bragg condition, produces monochromatic X-ray radiation.

For ultraviolet photoelectron spectroscopy (UPS), a helium gas discharge lamp is used as the photon source. In the gas discharge, neutral helium atoms (He^0) are excited by electron impact. When these excited states relax, photons are emitted corresponding to transitions into the singlet ground state (1^1S), which is the lowest energy level of the helium atom. The most prominent transition in neutral helium is the $2^1P \rightarrow 1^1S$ transition at 21.2 eV, known as the He I α line. Higher excited states can also decay into the ground state, giving rise to the He I β ($3^1P \rightarrow 1^1S$, 23.1 eV) and He I γ ($4^1P \rightarrow 1^1S$, 23.7 eV) lines, which have lower intensities due to their lower transition probabilities. In the laboratory setup, non-monochromatic UV radiation is used, which means that satellites resulting from excitation with He I β and He I γ radiation appear in the UPS spectrum and must be removed during post-processing. These satellites can be particularly disruptive when determining the valence band maximum (VBM) or the highest occupied molecular orbitals (HOMO). To mitigate this, it is advisable to use He II excitation. In this case, singly ionized helium atoms (He^+), which are hydrogen-like, emit photons during electronic relaxation. The most intense line is the $2p \rightarrow 1s$ transition at 40.8 eV (He II α), with higher transitions such as He II β (48.4 eV) and He II γ (51.0 eV) occurring with lower intensities. Since the satellites from He II emission appear at significantly higher energies, they are generally less disruptive for the analysis of electronic states close to the Fermi level. The relative intensity of He I and

He II lines can be tuned by adjusting the helium gas pressure in the discharge lamp. Lower pressures favor the formation of He^+ and thus enhance He II emission. Additionally, increasing the filament current raises the electron density and promotes both excitation and ionization, providing another means of increasing He II intensity. This approach was also applied for the He II spectra recorded in this work.

A hemispherical analyzer is employed for detecting photoelectrons. In this type of detector, electrons emitted from the sample surface are focused and collected using electrostatic lenses. The hemispherical analyzer consists of two concentric hemispheres, with an electric field applied between them. This electric field guides the electrons along a specific trajectory based on their kinetic energy. The path an electron takes through the analyzer is determined by its kinetic energy and the strength of the electric field. Only electrons with a specific kinetic energy are able to reach the detector at the end of this trajectory, while electrons with different energies are deflected and do not reach the detector.

The pass energy in a hemispherical analyzer is directly related to the voltage applied between the hemispheres. This pass energy dictates which electrons are allowed to pass through the analyzer and reach the detector, thereby influencing both the resolution and intensity of the detected signal. Higher pass energy increases signal intensity but reduces resolution, whereas lower pass energy enhances resolution at the expense of signal intensity. The selection of pass energy is therefore critical in optimizing the balance between resolution and signal strength for a given experiment.

2.5.2 ARPES at LowDosePES

The LowDosePES endstation is a measurement station located at BESSY II, a synchrotron facility operated by the Helmholtz-Zentrum Berlin. In simple terms, synchrotron light is generated when electrons, moving at nearly the speed of light, are forced into a circular trajectory by magnetic fields. This change in direction is equivalent to acceleration, which, in the case of charged particles like electrons, results in the emission of photons, commonly referred to as synchrotron radiation (or bremsstrahlung). The deflection of the electrons can be achieved through various configurations of magnets. At the LowDosePES endstation, the radiation is produced by deflecting the electrons with dipole magnets.

The electrons, or more precisely, individual electron packets (known as electron bunches), circulate in a storage ring with a defined spacing between them. A unique feature of BESSY II is the distribution of these electron bunches within the ring, referred to as the "fill pattern." **Figure 18 a** illustrates the fill pattern of the storage ring. Synchrotron radiation covers a broad spectral range, and for specific experiments, photons of the desired energy can be selected using a monochromator.

A key feature of the LowDosePES endstation at BESSY II is the availability of an angle-resolved time-of-flight (ToF) detector. For precise ToF measurements of photoelectrons, it is essential to know the arrival time of the exciting photon pulse with high accuracy. While the timing is inherently defined by the synchrotron’s electron bunch structure, a mechanical chopper wheel (as shown in **Figure 17 b** (10)) is employed at the endstation to isolate the single bunch from the full fill pattern. As illustrated in **Figure 18 b**, this ensures that only photons from a well-defined single bunch reach the sample, enabling accurate time-of-flight referencing for the emitted photoelectrons.

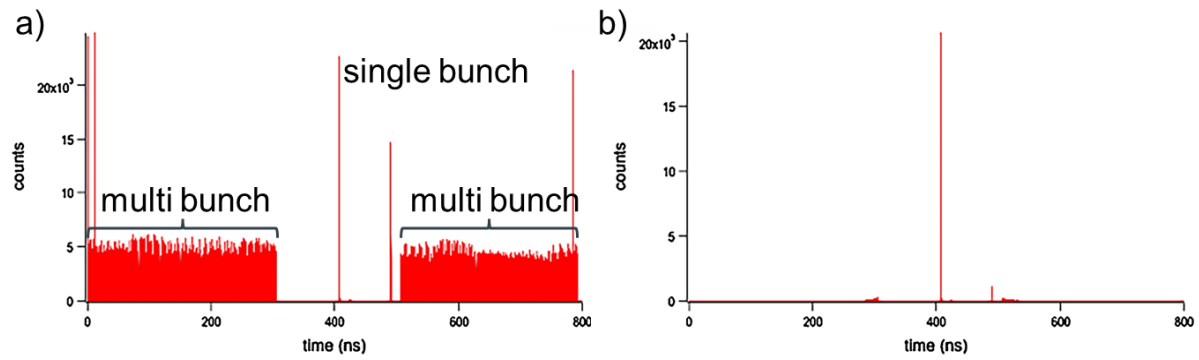

Figure 18 (**a**) Fill pattern of the electron storage ring at BESSY II. (**b**) Extracted single bunch after passing through the copper of the LowDosePES endstation. (Figure adapted and slightly modified with permission from Ref.[30] .)

The flight time (t) is determined by the event of excitation and detection within the analyzer and, in a simple approximation, depends on the length of the detector (L), the kinetic energy of the electron (E_k), and the mass of the electron (m_e) as follows:

$$t = \frac{L}{\sqrt{\frac{2E_k}{m_e}}} \qquad (35)$$

This detection principle allows the kinetic energy of emitted photoelectrons to be measured, which enables the use of this detector type for XPS experiments. More importantly for this study, it also permits the analysis of the photoelectron momentum. By measuring the emission angle with the two-dimensional detector array, the momentum components parallel to the sample surface can be determined. The parallel momentum vector is calculated from the x and y components as follows:

$$k_{\parallel} = \sqrt{k_x^2 + k_y^2} \qquad (36)$$

Using the x and y components:

$$k_x = \frac{m_e}{\hbar} v_x = \frac{m_e}{\hbar} \frac{x}{t} \qquad (37)$$

$$k_y = \frac{m_e}{\hbar} v_y = \frac{m_e}{\hbar} \frac{y}{t} \qquad (38)$$

XPS experiments which include angular information and can therefore determine momentum as described are referred to as Angle-Resolved Photoemission Spectroscopy (ARPES). These experiments were particularly utilized in the study presented in Chapter 3.2. To accurately determine the experimental parameters for

semiconductor materials, it is beneficial to be familiar with the Brillouin zone and the distances between high-symmetry points. At the ARTOF detector of the LowDosePES, various settings can be adjusted with respect to the magnetic lenses. Among these, the acceptance angle of the detector can be modified. A typical value, which was also used in the measurements in Chapter 3.2, is 30°. Assuming that the maximum kinetic energy of the photoelectrons is equal to the excitation energy, the following equation can be derived:

$$k_{\parallel} = sin\theta \sqrt{\frac{2m_e \cdot E_{kin}}{\hbar^2}} \qquad (39)$$

This allows the estimation of the maximum mappable reciprocal space. In the study presented in 3.2, an excitation energy was used that did not allow the entire Brillouin zone to be mapped. When selecting experimental parameters, the advantages and disadvantages must always be carefully weighed. As mentioned, a higher excitation energy enables a larger portion of the Brillouin zone to be mapped. However, higher excitation energies come with certain drawbacks. Typically, the energy resolution decreases at higher excitation energies. Detection becomes less sensitive to minor changes in the energy distribution, which complicates the distinction of fine spectral features. Additionally, the higher kinetic energies result in increased electron scattering, which can impair the angular resolution of the detector. This makes it more challenging to precisely determine the momentum distribution in reciprocal space.

The LowDosePES endstation is equipped with a rotatable sample holder. In the case of MoS_2 and its hexagonal lattice structure, we were able to use lower excitation energies to maximize resolution while still capturing the entire (or half of the) Brillouin zone, which, due to symmetry considerations, is sufficient. By rotating the sample relative to the excitation source, all high-symmetry points could still be mapped. As a result, the high-symmetry point Γ is not located at the center, as might be expected, but rather shifted towards the edge. This configuration, however, enables the detection of features from the K points.

For the investigation of planar molecules, which is particularly relevant in Chapter 3.3, X-ray Absorption Spectroscopy (XAS) can be employed. The LowDosePES endstation is equipped with a rotatable sample holder. The synchrotron radiation is polarized and can be specifically adjusted by varying the angle of incidence relative to the sample

surface, allowing the determination of the molecular orientation on the surface. In the case of molecules such as cobalt phthalocyanines, which have a planar structure, two extreme orientations are typically distinguished: the face-on and edge-on orientation.

Figure 19 shows a schematic representation of the sample orientation relative to the electric field vector of the incoming synchrotron radiation. In this work, (a) corresponds to normal incidence (90°), where the X-ray beam is perpendicular to the sample surface. Configuration (b) represents an intermediate geometry often referred to as 45° incidence, which probes both in-plane and out-of-plane orbitals to a similar extent. Configuration (c) corresponds to grazing incidence, ideally at 0°, where the electric field vector lies nearly parallel to the molecular plane. However, due to experimental constraints, a fixed angle of 20° was used for grazing incidence measurements. This relatively large angle was chosen to ensure sufficient photon flux on the sample and to avoid shadowing effects caused by the sample holder geometry.

In the face-on orientation, the molecular plane is parallel to the sample surface. In this case, the π* orbitals, which are oriented perpendicular to the molecular plane, are most strongly excited at a low angle of incidence (grazing incidence, close to 0°), as shown in **Figure 19 c**. At a high angle of incidence (normal incidence, 90°), the contribution to the excitation of the π* states is minimal because the electric field of the polarized light is parallel to the surface and, therefore, does not effectively interact with the π* orbitals.

In the edge-on orientation, on the other hand, the molecular plane is nearly perpendicular to the sample surface. Here, a low angle of incidence (grazing incidence) results in minimal excitation of the π* orbitals, while at a high angle of incidence (normal incidence), as shown in **Figure 19 a**, a maximum excitation of the π* orbitals is observed. The difference in intensity between these two extremes allows for the unambiguous determination of the preferred molecular orientation.

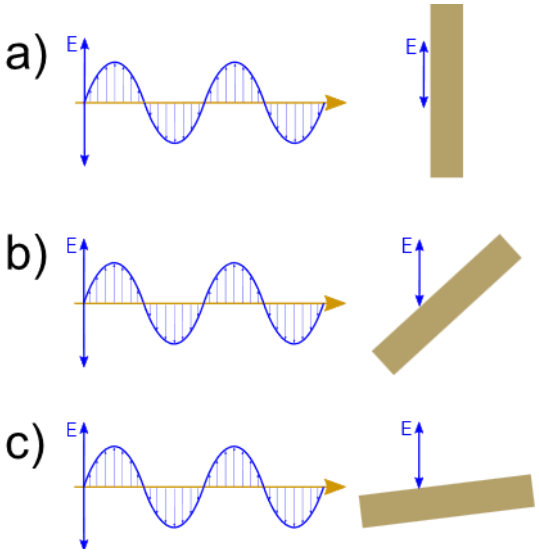

Figure 19 Schematic illustration of the relative position of the sample with respect to the electric field vector. In this work, (**a**) is referred to as a normal incidence or 90° where the X-ray beam is perpendicular to the sample surface, (**b**) as a normal incident at 45°, and (**c**) as a grazing incident, which would ideally correspond to 0°. However, due to practical limitations, an orientation of 20° was used in this study.

2.5.3 PEEM at WERA

Particularly for the investigation of very small structures, such as the MoS_2 monolayer flakes described in Chapter 3.3, microscopic analysis methods are required. The WERA endstation is a facility at the KIT Light Source in Karlsruhe. The WERA endstation, like the previously discussed BESSY, is located at a synchrotron source with an electron storage ring at the Karlsruhe Research Accelerator (KARA). The generation of synchrotron radiation at this endstation is like that at the LowDosePES. The WERA endstation was chosen for the mentioned investigation of MoS_2 monolayers as it is equipped with a Photoemission Electron Microscope (PEEM). The following section describes the operating principle and the evaluation of the obtained data.

As with the previously described methods based on the photoelectric effect, a PEEM experiment also involves the excitation of electrons using ionizing radiation. The free electrons at the surface are accelerated toward the detector by a strong electric field, essentially being “extracted” from the surface. The unique feature of a PEEM is that the electrons are directed onto the detector through imaging magnetic lenses in such a way that their spatial origin on the sample surface is preserved.

A Photoemission Electron Microscope (PEEM) utilizes the photoelectric effect to create images of the electronic emission distribution on surfaces with high lateral resolution. The surface of a sample is irradiated with high-energy radiation, such as synchrotron radiation. The emitted electrons are then accelerated through a strong electric field established between the sample surface and the so-called extractor.

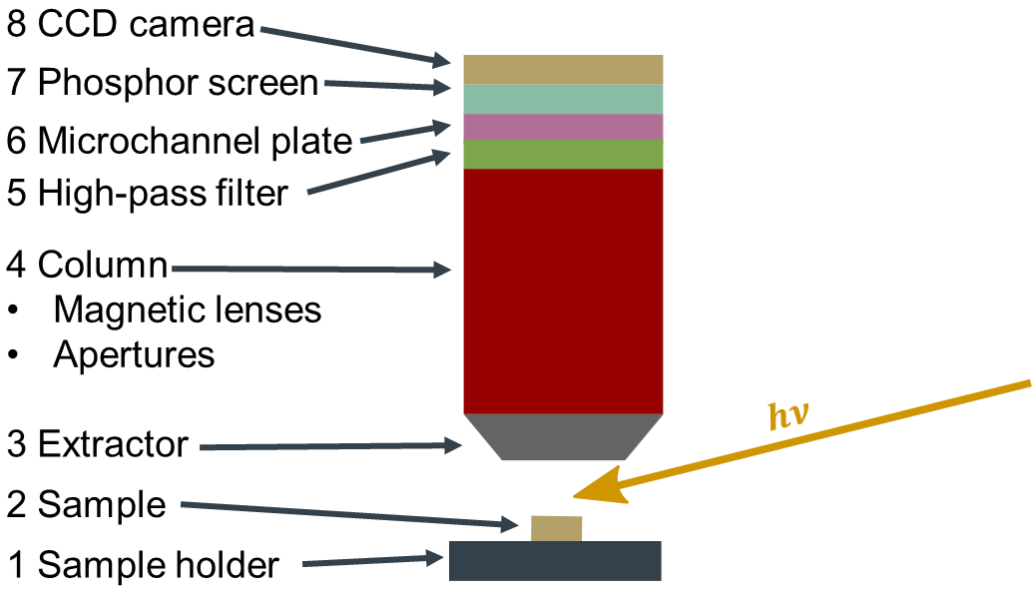

Figure 20 Schematic diagram of the PEEM, consisting of a sample holder (1) that holds the sample (2) at a defined distance from the extractor (3). The emitted electrons are directed through a column (4), which contains imaging magnetic lenses and apertures, onto a microchannel plate (6) and are made visible by a phosphorescent screen (7). Images of the phosphorescent screen are then captured using a CCD camera (8). For certain experiments, such as XPS measurements, the detected electrons must be filtered by energy, which can be achieved using a high-pass filter (5).

In **Figure 20**, this setup is depicted in detail: The sample holder (1) precisely positions the sample (2) within the beam path, and the extractor (3) draws the emitted electrons away from the surface. The column (4) contains the optical elements responsible for lateral focusing and magnification. For X-ray Photoelectron Spectroscopy (XPS) measurements, a bandpass filter (5) is often employed to select electrons based on their kinetic energy, thus extracting spectral information. The filtered electrons are then further amplified by the microchannel plate (6) and projected onto the screen (7), where the image is captured by the CCD camera (8).

The use of a high-pass filter (5) is crucial for XPS measurements performed with PEEM. This filter allows the detection of all emitted electrons above a defined kinetic energy threshold. It collects all electrons while blocking those below the energy threshold, which does not imply that specific energy ranges are directly selected.

Instead, the filter enables integration of the electrons above the set threshold into the image, leading to abrupt changes in the overall intensity when varying the energy filter threshold.

A complete XPS spectrum is generated by systematically varying the filter threshold, which leads to a rapid increase in detected electrons and image intensity as the threshold reaches a specific orbital energetic region. These sudden shifts reflect the binding energy positions and offer insights into the different electronic states within the material.

To generate a complete XPS spectrum from the acquired PEEM data, the derivative of the image intensity as a function of the filter threshold is typically calculated. This derivative makes the abrupt intensity changes more apparent and helps to clearly identify the characteristic binding energies of the electrons. In practice, this evaluation is often performed using image processing software such as Fiji, in combination with the FeatureJ package, which provides tools for precise image intensity differentiation. Applying the derivative function results in a detailed XPS spectrum that provides spectral information for each image pixel, thereby enabling correlated analysis of chemical states and surface topography.

Flat-field and dark-field measurements are essential to minimize systematic errors in PEEM imaging and ensure reliable quantification of the electron signals.

Flat-field measurements: These are performed to correct for imaging inhomogeneities caused by the optical elements in the column (4) or the amplification characteristics of the microchannel plate (6). A homogeneous electron signal is used to generate a reference image, which serves as a correction matrix. The generation of a homogeneous electron signal is achieved by overexposing the microchannel plate, pushing it into saturation. This allows variations in signal intensity that do not originate from the sample to be accounted for.

Dark-field measurements: These are carried out with the electron source turned off to determine the baseline noise of the detection system (including the CCD camera system). Since the system always exhibits some noise, the dark-field image is subtracted from the actual measurement images. This is particularly important in experiments with weak signals to optimize the signal-to-noise ratio and enable a clear analysis of the electronic states.

By combining flat-field and dark-field corrections, the image quality is significantly improved, which is especially necessary for measurements with high lateral resolution and sensitive materials to obtain quantitative results. For the evaluation of the measurement data, image processing software such as Fiji, as previously mentioned, can be utilized.

3 Publications

3.1 Untangling the Intertwined: Metallic to Semiconducting Phase Transition of Colloidal MoS_2 Nanoplatelets and Nanosheets

André Niebur,[,1,2] Aljoscha Söll,[*,1] Philipp Haizmann,[3] Onno Strolka,[1,2,3] Dominik Rudolph,[1,2] Kevin Tran,[4,5] Franz Renz,[4,5] André Philipp Fauendorf,[6] Jens Hübner,[5,6] Heiko Peisert,[3] Marcus Scheele[3] and Jannika Lauth[#,1,2,3,5]*

[1] Institute of Physical Chemistry and Electrochemistry, Leibniz University Hannover, Callinstr. 3a, D-30167 Hannover, Germany

[2] Cluster of Excellence PhoenixD (Photonics, Optics, and Engineering – Innovation Across Disciplines), Hannover, Germany

[3] Institute of Physical and Theoretical Chemistry, University of Tübingen, Auf der Morgenstelle 18, D-72076 Tübingen, Germany

[4] Institute of Inorganic Chemistry, Leibniz University Hannover, Callinstr. 9, D-30167 Hannover, Germany

[5] Laboratory of Nano and Quantum Engineering (LNQE), Leibniz University Hannover, Schneiderberg 39, D-30167 Hannover, Germany

[6] Institute of Solid State Physics, Leibniz University Hannover, Appelstr. 2, D-30167 Hannover, Germany

[*] Equal contribution

[#] Jannika.lauth@uni-tuebingen.de

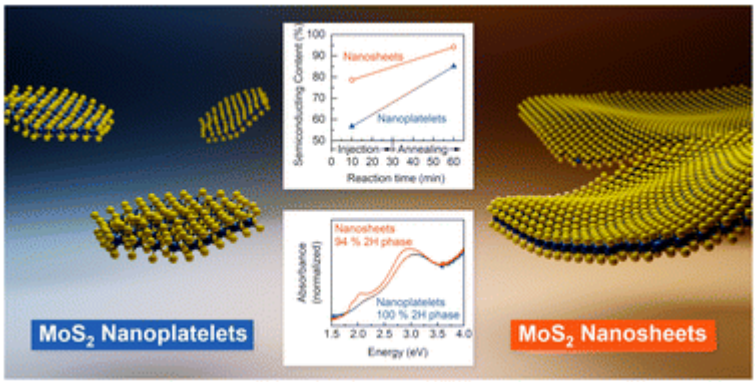

3.1.1 Abstract

2D semiconducting transition metal dichalcogenides (TMDCs) are highly promising materials for future spin- and valleytronic applications and exhibit an ultrafast response to external (optical) stimuli which is essential for optoelectronics. Colloidal nanochemistry on the other hand is an emerging alternative for the synthesis of 2D TMDC nanosheet (NS) ensembles, allowing for the control of the reaction via tunable precursor and ligand chemistry. Up to now, wet-chemical colloidal syntheses yielded intertwined/agglomerated NSs with a large lateral size. Here, we show a synthesis method for 2D mono- and bilayer MoS_2 nanoplatelets with a particularly small lateral size (NPLs, 7.4 nm ± 2.2 nm) and MoS_2 NSs (22 nm ± 9 nm) as a reference by adjusting the molybdenum precursor concentration in the reaction. We find that in colloidal 2D MoS2 syntheses initially a mixture of the stable semiconducting and the metastable metallic crystal phase is formed. 2D MoS_2 NPLs and NSs then both undergo a full transformation to the semiconducting crystal phase by the end of the reaction, which we quantify by X-ray photoelectron spectroscopy. Phase pure semiconducting MoS_2 NPLs with a lateral size approaching the MoS_2 exciton Bohr radius exhibit strong additional lateral confinement, leading to a drastically shortened decay of the A and B exciton which is characterized by ultrafast transient absorption spectroscopy. Our findings represent an important step for utilizing colloidal TMDCs, for example small MoS_2 NPLs represent an excellent starting point for the growth of heterostructures for future colloidal photonics.

3.1.2 Introduction

Ultrathin 2D TMDCs exhibit exciting photophysics and are highly interesting for innovative optoelectronics. Their potential in excitonic devices, silicon-free photovoltaics and as single-photon emitters[31, 32] foreshadows their impact in future photonics. This work is focused on the layered group-VI TMDC molybdenum disulfide MoS_2 which shows exciton physics that are uniquely attributed to this subgroup and ranging from localized excitons over biexcitons to different trion species.[33, 34] Generally, the high exciton binding energies of several hundreds of meV render 2D TMDCs suitable for studying excitons at room temperature.[35] For example, a recent study on colloidal 2D MoS_2 describes the mechanisms responsible for charge-carrier relaxation after photoexcitation in the structures without cooling the samples to cryogenic temperatures.[36] The authors find that excitons in colloidal MoS_2 decay *via* hole capture by midgap states and subsequent trapping of excited electrons. Typically, strongly bound excitons in TMDCs lead to high quantum yields and narrow emission,[37-40] making the materials interesting for room temperature single photon emission. Due to a strong spin-orbit coupling and the lack of inversion symmetry, group VI TMDCs exhibit band-splitting, which causes a spin-dependent occupation of the bands and consequently spin-dependent excitons (A and B excitons).[41] This is applied and investigated in the field of spin- and valley-tronics since electrons have an additional degree of freedom in TMDCs.[42] For example, valleytronic TMDC transistors have been realized using the valley degree of freedom and hence don´t rely on charge carrier transport as in contrast to conventional counterparts based on silicon.[43]

Recently, the lateral size of 2D TMDCs has received increasing attention in catalytic and photonic research.[44, 45] On the one hand, the influence of edge states increases for small lateral sizes of 2D TMDC layers. While these states are found in the band gap and are essential for catalysis,[46-49] they also suppress photoluminescence (PL) by non-radiative recombination in the structures.[50] On the other hand, the wave functions of the electron and hole are affected by a growing quantum confinement in 2D MoS_2 with decreasing lateral dimension. This leads to an increase of the band gap and the electron-hole overlap of the excitons.[51-53]

Since the lateral size of the 2D MoS_2 plays a key role for associated material properties, we study laterally smaller MoS_2 nanoplatelets (NPLs, 7.4 nm ± 2.2 nm) and laterally bigger MoS_2 nanosheets (NSs). NPLs are ultrathin TMDCs at which the effects

described above have to be taken into account. For NSs, the lateral sizes are large (22 nm ± 9 nm) so that these effects are negligible.

(Liquid phase) exfoliation and chemical vapor deposition are well understood methods used to obtain ultrathin TMDC layers.[54-60] Here, we focus on a bottom-up colloidal chemistry route as emerging synthesis method for 2D TMDC NPLs and NSs which offers control over the synthesis product by adjustable precursor and ligand chemistry.[40, 61] The starting point of recent TMDC syntheses is the work of Mahler *et al.* on few-layered WS_2 NSs.[62] The authors used WCl_6 and CS_2 for the reaction and their method yielded WS_2 NSs by adding the precursors to oleylamine at 320 °C *via* slow injection over 30 min. Syntheses adapted to MoS_2 nanosheets typically make use of $MoCl_5$,[61, 63] or molybdenum(II) acetate ($[Mo(Ac)_2]_2$)[44] as the transition metal precursor and elemental sulfur, CS_2 or thioacetamide (TAA) as sulfur precursor. Both, CS_2 and thioacetamide are more reactive than elemental sulfur, but they are also highly volatile at reaction temperatures exceeding 300 °C and are carcinogenic or mutagenic. Zhou and Zhang *et al.* were able to synthesize MoS_2 NSs with lateral sizes of 20 – 40 nm by altering the sulfur to molybdenum ratio of the precursors.[44] They used ($[Mo(Ac)_2]_2$) and TAA as precursors and catalyzed the hydrogen evolution reaction efficiently and durably with the synthesized MoS_2 NSs. Using a design of experiment approach, Pippia *et al.* studied the parameters of a MoS_2 synthesis, optimized the yield of monolayers and were able to obtain NSs that exhibited photoluminescence when sandwiched between hBN layers.[61] With $MoCl_5$ and elemental sulfur as precursors, they found an optimal reaction temperature of 290 °C and an optimum sulfur to molybdenum ratio of 20.5, confirming an excess of sulfur to reduce vacancies at the edges and within the NSs. Alongside these efforts, various studies on single precursor syntheses have been investigated. Savjani *et al.* compared xanthate and dithiocarbamate complexes as precursors and presented a hot-injection thermolysis of $[Mo_2O_2S_2(S_2COEt)_2]$.[64] The rapid injection led to small MoS_2 NPLs (<11 nm) which were used in supercapacitor electrodes. Pang *et al.* reported $[(NH_4)_2MoS_4]$ as a single precursor decomposing at 280 °C and obtained few-layer roselike MoS_2 NSs.[65]

Here we use the combination of a molybdenum and sulfur precursor for the reaction, as this ensures the sulfur excess required and allows for the reactivity of the two precursors to be adjusted independently. The molybdenum precursor $MoCl_5$ is dispersed in a 10 : 1 mixture of oleylamine (OlAm) and oleic acid (OA) forming an acid-

base equilibrium.[66] OA acts as a ligand and helps to improve the colloidal stability of the MoS_2 NSs and NPLs. Elemental sulfur is dissolved in OlAm and activated by hexamethyldisilazane (HMDS) at 320 °C, which leads to the *in situ* formation of highly reactive S_4N_4 rings.[67] When the molybdenum precursor is injected over the course of 30 min into the sulfur solution, colloidal NPLs and NSs begin to grow. With this approach, we can tune the intrinsic properties of colloidal 2D MoS_2 NPLs and NSs including the lateral size, and the crystal phase.[40, 68, 69] A TMDC monolayer is composed of an atomic transition metal layer sandwiched between two layers of chalcogen atoms with the two stacking patterns shown in **Figure 21**. The 2H phase is thermodynamically stable, semiconducting and the allotrope of interest for optical applications.[70, 71] The 1T phase, on the other hand, is metallic, metastable, and typically distorted.[72] The 1T´ phase, a distorted variant of the 1T phase, is semi metallic, metastable and was recently reported in high phase purity obtained *via* colloidal synthesis.[73] Wet-chemical TMDC research is focusing increasingly on the respective crystal phases and their formation, *e.g.* during the synthesis of MoS_2, WS_2 and $MoSe_2$, WSe_2 NSs.[61, 62, 69, 73, 74] However, the mechanism by which the individual crystal phases are controlled and formed during the synthesis up to now lacks systematic description. In order to unlock the potential of colloidal synthesis methods for TMDCs we focus on two critical properties of 2D MoS_2 NSs here: the crystal phase and the morphology which we control by variation of the reaction time and concentration of the molybdenum metal precursor. A short reaction time leads to laterally small NPLs that are subsequently annealed to obtain phase pure semiconducting MoS_2 NPLs. We investigate the size-dependent optical properties of MoS_2 NPLs and NSs by steady-state and ultrafast transient spectroscopy experiments and find that small NPLs lack the A excitonic feature in both, steady-state and transient absorption spectroscopy (TAS) The B exciton in small NPLs decays by a single process, whereas in larger NSs a two-step process is observed.[36] Our results demonstrate the versatility of colloidal 2D MoS_2 for the first time, while also making a broad range of lateral sizes accessible with a single synthesis protocol. Additionally we show for the first time that the charge carrier dynamics in semiconducting 2D MoS_2 structures critically depend on their lateral size. This dependence has not been observed before and is a promising way to tailor the behavior of excitons in colloidal MoS_2. By this synthetic approach, control over the electronic and excitonic properties

of colloidal MoS_2 NPLs and NSs is gained which will help to utilize them in upcoming applications in the fields of photonics and catalysis.

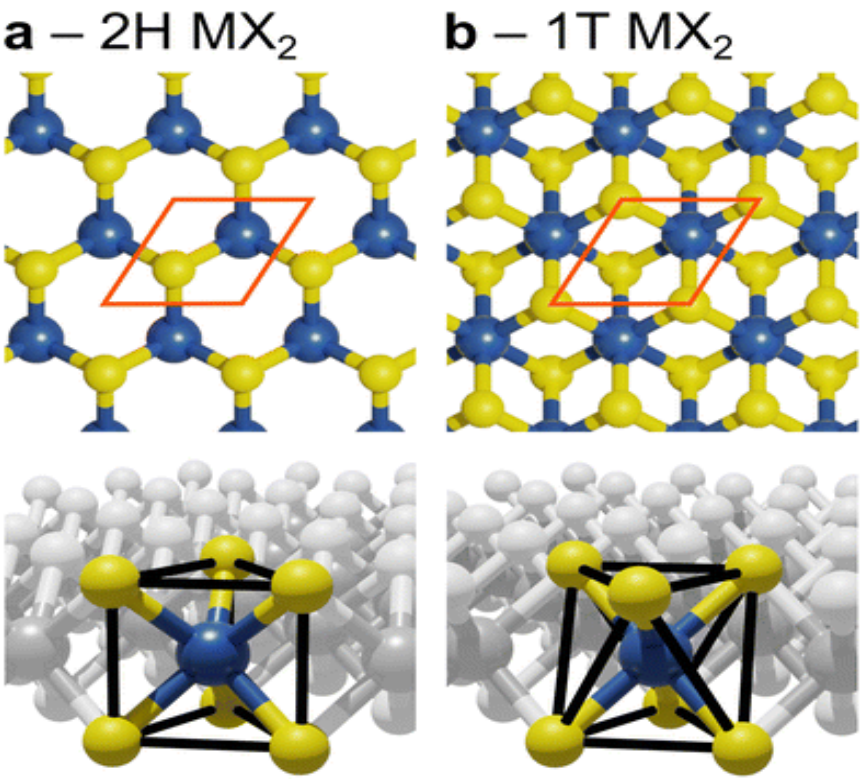

Figure 21 MX_2 TMDC monolayers with unit cells (orange): (a) typically obtained semiconducting 2H phase with transition metal (M, blue) surrounded by sic chalcogen atoms in a trigonal-prismatic coordination (X, yellow) while in (b) an octahedral coordination of the transition metal atoms by the chalcogen atoms in the metallic 1T phase is shown.

3.1.3 Experimental

Chemicals

Oleylamine (OlAm, 70%, technical grade), sulfur (99.98%) and oleic acid (OA, ≥99%) were acquired from Sigma-Aldrich. OlAm was degassed under oil pump vacuum and stirring for 6 h at 160 °C. Subsequently, OlAm was stored under nitrogen. All other chemicals were used as received without further purification and stored under nitrogen. Molybdenum(V) chloride ($MoCl_5$, 99%), and hexane (anhydrous) were purchased from Alfa Aesar. 1,1,1,3,3,3-Hexamethyldisilazane (HMDS, 98%) was purchased from Acros Organics. $MoCl_5$ and HMDS were kept at -25 °C inside a nitrogen filled glovebox.

MoS_2 nanoplatelet and nanosheet synthesis

A MoCl5 precursor solution with different concentrations (10 mM, 38 mM and 240 mM) was prepared by mixing $MoCl_5$ with OA and OlAm (V_{OA} : V_{OlAm} = 1 : 10) inside the glovebox and by stirring the mixture for 48 h at room temperature in a closed vial. In a three-neck flask, 87.5 mg (2.73 mmol) elemental sulfur and 17 mL OlAm were mixed inside the glovebox. The flask was subsequently connected to a Schlenk-line outside of the glovebox for degassing under oil pump vacuum and stirred at 85 °C for 30 min. During this step, the sulfur dissolved completely. The flask was then set under argon flow, and 250 µL (1.22 mmol) HMDS were added with a syringe before the mixture was heated to 320 °C. After reaching a constant temperature of 320 °C, 1.15 ml (11.5 µmol, 43.7 µmol and 276 µmol, respectively) of the molybdenum precursor solution was added to the flask by using a syringe pump over 30 min with a rate of 2.3 mL h^{-1}. Sulfur is present in excess with respect to molybdenum (237 eq., 62 eq. and 9.9 eq.). After the addition of a few molybdenum precursor drops, the clear yellow sulfur/HMDS solution turned black and opaque immediately. After 10 min and 30 min at 320 °C, aliquots were taken by using a syringe. The remaining reaction solution was kept at 320 °C for 30 min and was allowed to cool to room temperature afterwards.

The precipitation and redissolving of the colloidal 2D MoS_2 was performed inside a glovebox to prevent any reaction of the NPLs and NSs with oxygen. The synthesis product was precipitated by adding 16 mL hexane and centrifugation for 10 min at 3300 rcf. The clear light brown supernatant was decanted and discarded. The MoS_2 NPLs and NSs were redispersed in 5 mL hexane, ultrasonicated for 5 min, and kept under nitrogen for characterization.

Absorption

Absorption spectra were acquired by using a Varian Cary 5000 UV-Vis-NIR spectrometer. Measurements were performed on colloidal MoS_2 NPLs and NSs in hexane inside an integrating sphere to correct for scattering. Absorption measurements at cryogenic temperatures were performed by drop-casting the samples on glass slides and without using an integrating sphere.

Transmission electron microscopy (TEM)

TEM images were recorded with a Tecnai G2 G20 TMP microscope from FEI with an acceleration voltage of 200 kV. The samples were drop-casted onto a carbon coated copper grid by Quantifoil.

X-ray photoelectron spectroscopy (XPS)

XPS measurements were performed on a home-built spectrometer. A multi-chamber ultra high vacuum system with a base pressure of 2×10^{-10} mbar was used. The system is equipped with a monochromatic Al K_α radiation source (XR 50 M, Specs) and a Phoibos 150 DLD hemispherical photoelectron analyzer. Measurements were performed in fixed analyzer transmission (FAT) mode. The binding energy was calibrated with respect to the **Au***4f*$_{7/2}$ (84.0 eV) and the **Cu***2p*$_{3/2}$ (923.6 eV) peak positions. At the chosen pass energy of 30 V for detailed spectra, a resolution of about 550 meV was achieved. The peak fitting of XPS spectra was performed using the program Unifit.[75] A Voigt profile peak shape (Convolution of Gaussian and Lorentzian peaks) and a Shirley model background were used. MoS_2 NPL and NS samples were prepared by drop-casting 30 µL of a 1 mM colloidal dispersion in hexane onto a gold coated substrate. The substrates were fabricated in the LISA+ facility in Tübingen by coating a commercially available four-inch silicon wafer with 10 nm of chrome followed by 50 nm of gold. For XPS, samples were prepared on 10 x 10 mm^2 wafer cuts.

Transient absorption spectroscopy (TAS)

The colloidal NPLs and NSs were prepared in hexane in quartz cuvettes with a pathlength of 2 mm and were stirred consistently in order to prevent photocharging.[71] Ultrafast carrier dynamics were investigated by broadband pump-probe spectroscopy in a setup described previously and briefly covered here.[71, 76, 77] Laser pulses with a central wavelength of 800 nm and a pulse width of 100 fs are generated by a

Ti:sapphire amplifier system (Spectra-Physics, Spitfire ACE) and split in two parts in order to generate pump and probe (90 : 10) beam. The wavelength of the pump beam is adjustable from 300 nm to 2100 nm using nonlinear frequency mixing in an optical parametric amplifier and second harmonics generation system (TOPAS). The probe pulse is a broadband supercontinuum which is generated by using nonlinear processes in a calcium fluoride or sapphire crystal, allowing probing from 320 nm to 1600 nm (Ultrafast, Helios FIRE). Delay of the probe pulse by up to 8 ns after initial photoexcitation can be set *via* an automatic delay line. Pump and probe beam pass the sample with a maximized overlap. The attenuated probe beam is directed into a fiber-coupled detector array at different delay times to track charge carrier dynamics that cause changes in the absorption.

3.1.4 Results and Discussion

MoS_2 nanosheet morphology and crystal phase

The colloidal MoS_2 NPLs and NSs in this work are investigated with respect to the shape and the crystal phase. The shape of 2D MoS_2 NSs and NPLs is specified by their lateral dimension and their number of layers. We use TEM to characterize the shape of colloidal MoS_2 NSs in low and high resolution. **Figure 22** shows an analysis of for MoS_2 NPLs and NSs synthesized with two different molybdenum precursor concentrations (low: 10 mM and high: 240 mM). The low concentration yields NPLs and the high concentration yields intertwined NSs, respectively (see **Figure 22 a-d**). We expect the intertwining to be driven by a low surface ligand coverage as has been reported for colloidal WSe_2.[69] For WSe_2, a ligand density of 0.5 to one molecule oleic acid per nm^2 is reported, a value considerably lower than a typical surface coverage of four molecules per nm^2 found in oleic acid-stabilized spherical PbSe nanocrystals.[69, 78] In our samples, the presence of bound ligands I supported by FTIR spectroscopy (see **Figure S1**, Appendix A). Both NPLs and NSs exhibit signals between 2800 cm^{-1} and 3050 cm^{-1} originating from the oleyl group of eighter OlAm or OA.[79] The C=O stretching mode at 1708 cm^{-1} suggests monodentate OA in our samples. Vibrations at 1402 cm^{-1} and 1530 cm^{-1} attributed to a symmetric and antisymmetric COO^- stretching mode are missing, ruling out the presence of oleate acting as a bidentate ligand.[80] The lateral dimension of colloidal 2D MoS_2 is estimated by single flat-on oriented NPLs and NSs emerging next to regions of intertwined structures in HRTEM images. Flat-lying NPLs and NSs are identified by a difference in contrast to the background and by domains of lattice planes, as shown in **Figure S2**. The respective lateral size was determined by these flat-laying NPLs and NSs. We find that the low molybdenum precursor concentration (10 mM) leads to small MoS_2 NPLs with a lateral size of 7.4 ± 2.2 nm, N = 84 and the high concentration (240 mM) to laterally larger NSs with lateral sizes of 22 ± 9 nm, N = 59 (**Figure S2 a** and **b**). The growth rate after the MoS_2 nucleation step is higher for a higher precursor concentration leading to the formation of NSs.[81] Consequently, a lower growth rate for the small precursor concentration leads to the formation of small MoS_2 NPLs.

The number of layers in colloidal 2D MoS_2 is crucial for their optoelectronic properties with the band gap in monolayer MoS_2 being direct and indirect in multilayered structures.[82] The TEM analysis shows monolayers of MoS_2 (see **Figure S2 b, d** and

Figure S2 a, b) mainly.[40, 44] However, partly we find few-layered 2D MoS_2 with a molybdenum to molybdenum layer distance of 7 Å. This value is increased with respect to the bulk layer distance of 6.15 Å,[83, 84] which is caused by the colloidal NSs having a twisted shape, therefore exhibit in non-optimal stacking. In samples with high molybdenum precursor concentration (240 mM, **Figure 22 d**), few layered NSs were found more frequently than in low molybdenum precursor synthesized NPLs.

We apply four characterization methods for determining the crystal phase of MoS_2 NPLs and NSs: high-resolution TEM (HRTEM), selected area electron diffraction (SAED), powder X-ray diffraction (PXRD), and X-ray photoelectron spectroscopy (XPS). XRD and SAED provide information about the periodicity of the 2D MoS_2 crystal lattice, whereas XPS is used to determine the binding energies of the individual atomic species to quantify the 1T : 2H phase ratio. HRTEM, SAED and PXRD confirm the presence of the hexagonal lattice of MoS_2 NPLs and NSs. **Figure S2 a** and **b** show the hexagonal pattern of flat-laying MoS_2 NPLs and a single NS, respectively. In **Figure S2 c** and **d**, the FFT of a single NPL and NS are shown, confirming the presence of distinct reflexes stemming from the hexagonal lattice. We find a ring pattern between 0.27 nm and 0.28 nm corresponding to the (100) reflex for all synthesized MoS_2 samples (see **Figure S3**). These values are in agreement with the (100) reflex at a distance of 0.274 nm in bulk MoS_2 in the 2H crystal phase (ICDD 00-037-1492). SAED measurements shown as insets in **Figure 22 b** and **d**, we find a 0.283 nm radius of the (100) ring for small MoS_2 NPLs and 0.275 nm for larger NSs. Distances were obtained by radial integration of the SAED image (see **Figure S4**). With SAED, an expansion of 3% was detected in small MoS_2 NPLs, which indicates a negative surface stress induced by the edges.[85] The hexagonal crystal structure was also verified by PXRD (see **Figure S5**) for MoS_2 NPLs and NSs. The diffractograms match the reference

reflexes of bulk 2H MoS_2 and are broadened as expected for strongly confined systems.

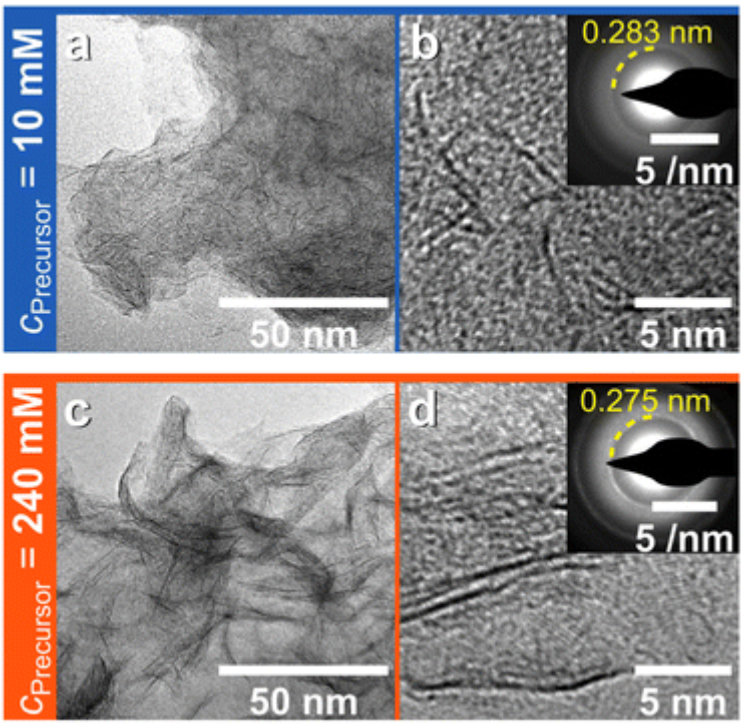

Figure 22 The size of colloidal MoS_2 NLPs and NSs depends on the molybdenum precursor concentration: (**a** and **b**) low Mo-precursor concentration (10 mM) lead to MoS_2 NPLs with smaller lateral sizes, (**c** and **d**) MoS_2 NSs synthesized with high Mo-precursor concentration (240 mM) yield larger NSs. The insets in (**b**) and (**d**) represent selected area electron diffraction patterns of the associated MoS_2 sample.

Figure 23 a and **b** show XPS data of the **Mo***3d* core levels of MoS_2 NPLs synthesized with a precursor concentration of 10 mM after 10 min, as well as after 60 min reaction time, respectively. We attribute the spin-orbit doublet between 228 eV and 234 eV to Mo^{4+}, containing $3d_{5/2}$ and $3d_{3/2}$ signals of both the 1T and 2H phase of MoS_2. The crystal-field symmetry of the MoS_2 moiety in the 1T phase (O_h) decreases the binding energy of the **Mo***3d* core level by about 1.0 eV with respect to the 2H phase with D_{3h} symmetry.[86-88] In excellent agreement with previously reported values for MoS_2, the binding energy of **Mo***3d*$_{5/2}$ peaks of the 1T (red) and 2H (green) phase is 228.7 eV and 229.7 eV, respectively.[89-91] All components were fitted using the same peak shape (Gaussian FWHM, Lorentzian FWHM). We tentatively attribute the remaining intensity around 236 eV to the presence of a Mo^{6+} species, which may originate from oxidation by the formation of water due to the condensation of oleic acid and oleylamine.[62, 91, 92]

The binding energy of the corresponding $3d_{5/2}$ component is 233.3 eV. Such unspecific oxidation is also resembled by the rather large total FWHM of 1.6 eV of the signal. Using the fitted and deconvoluted Mo^{4+} *3d* signals, we find a relative 1T phase content of 43.3% after 10 min of reaction time (**Figure 23 a**) and 14.9% after 60 min (**Figure 23 b**). An increase of the reaction time from 10 min to 60 min supports the formation of the 2H phase in MoS_2 NPLs and NSs with further examples for higher molybdenum precursor concentrations of 38 mM and 240 mM shown in **Figure S6** and summarized in **Figure 23 c**. Furthermore, a high precursor concentration leads to an increased initial 2H/1T phase ratio, which rises with reaction time.

With a high precursor concentration of 240 mM and a reaction time of 60 min, we achieve a phase purity of 94% for the semiconducting 2H phase in MoS_2 NSs.

Following the Ostwald step rule (see scheme in **Figure 23 d**), the metastable synthesis product (the MoS_2 1T phase in our case) forms first during the reaction if the free energy barrier towards the metastable product is smaller than towards the thermodynamically more stable product (here the 2H phase).[69, 93, 94] According to calculations by Qian *et al.*, 1T and 1T´ crystal phases are not separated by an energy barrier in MoS_2 monolayers which makes the slightly distorted 1T´ crystal phase the actual metastable phase.[70] However, we expect that the XPS binding energies for the 1T and 1T´phases are very similar, as the coordination of the molybdenum atoms remains the same.

In addition to the general observation that the proportion of the 1T phase vanishes over the course of the reaction, **Figure 23 c** gives information about the dependence on MoS_2 synthesis products on the Mo-precursor concentration. We find that the 1T phase fraction is lower for syntheses with high Mo-precursor reactivity with rising pressure concentration. The MoS_2 crystal growth is accelerated and crystal defects are more likely to occur.[69] A high defect concentration in turn may lead to a reduced energy barrier between the 1T and 2H phase and subsequently to a more straight-forward conversion of the 1T to the 2H crystal phase. This hypothesis is supported by the lower 1T phase fraction obtained by XPS analysis (see **Figure 23 d**). We note that a higher defect concentration in TMDC NSs synthesized at high precursor concentrations was recently also reported by Zhou *et al.* for WSe_2 NSs.[69] By combining our results of size and crystal phase control by injection and annealing time as well as precursor concentration, we are able to synthesize laterally size-tailored colloidal MoS_2 NPLs

and NSs. In the following, we compare semiconducting MoS_2 NPLs and NSs in terms of their optoelectronic characteristics.

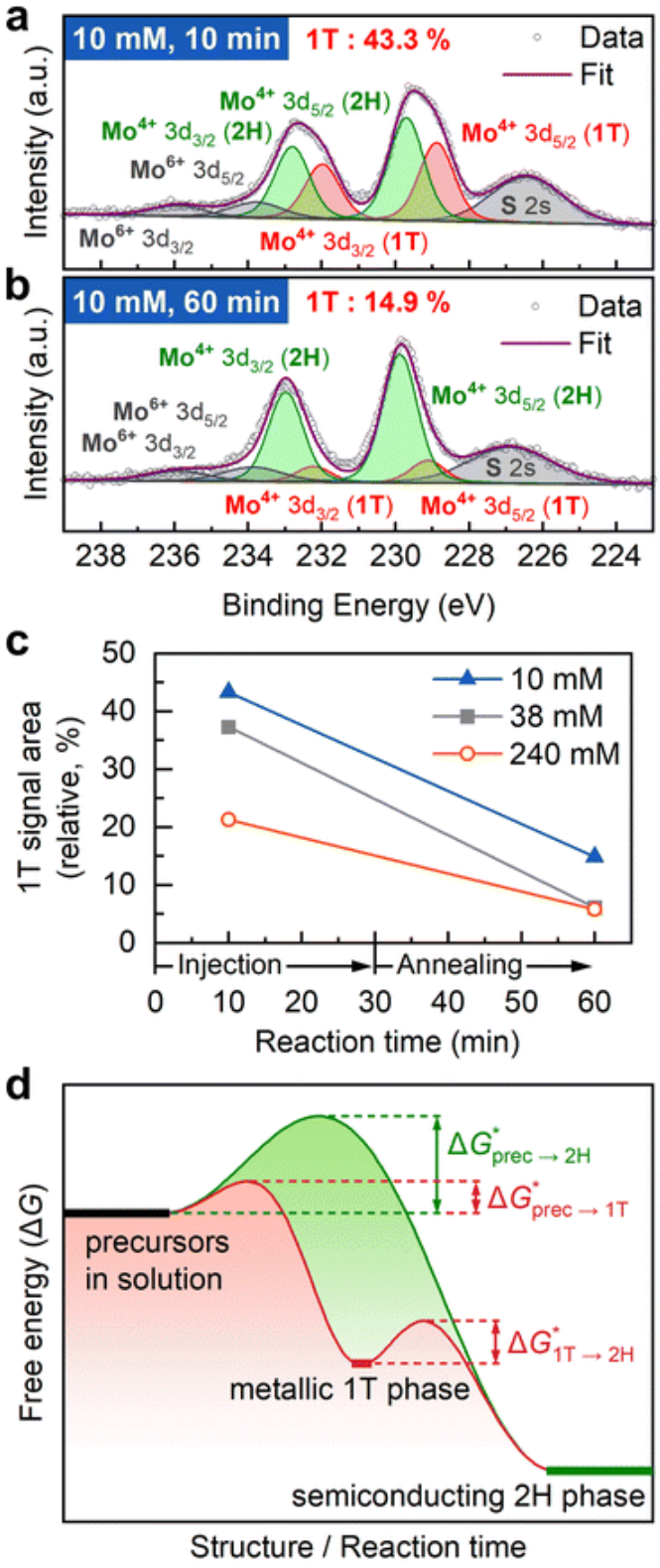

Figure 23 The 1T crystal phase fraction in colloidal 2D MoS_2 decreases over the course of the reaction. (**a** and **b**) XPS spectra of MoS_2 NPLs prepared with a low Mo-precursor concentration after reaction times of 10 and 60 min, respectively. The spectra reveal that the relative area of the 1T doublet (red) decreases from 43.3% to 14.9% with respect to the 2H signal area. (**c**) The relative 1T signal area quantified by XPS is plotted vs. the reaction time for three different Mo-precursor concentrations and shows that the 1T phase vanishes in each case. (**d**) A scheme of the Ostwald step rule applicable to colloidal 2D MoS_2 NPLs and NSs. Both, the metastable 1T phase and thermodynamically stable 2H phase, are formed initially. Subsequently, the 1T phase is transformed into the thermodynamically stable 2H phase at elevated temperatures.

Optoelectronic properties and exciton dynamics of MoS_2 nanosheets and nanoplatelets

The exciton Bohr radius r_{Bohr} in 2D MoS_2 monolayers is reported to range from 1 nm to 1.8 nm in the lateral dimension.[95-97] We therefore expect NPLs with sizes in the range (smaller or above) of 3.6 nm to exhibit photophysics different from their larger NS counterparts. The lateral size of synthesized MoS_2 NPLs and NSs range from 7.4 ± 2.2 nm to 22 ± 9 nm, respectively. To control the influence of the phase composition, we anneal MoS_2 NPLs for 5 h at 320 °C under inert gas conditions. During annealing the lateral size of the NPLs remains constant (see **Figure 24 a**). The metallic 1T phase content gradually decreases in favor of the semiconducting phase during this annealing step (see **Figure 24 b** and **Figure S7**) and the reaction ends with 100% of the 2H phase.

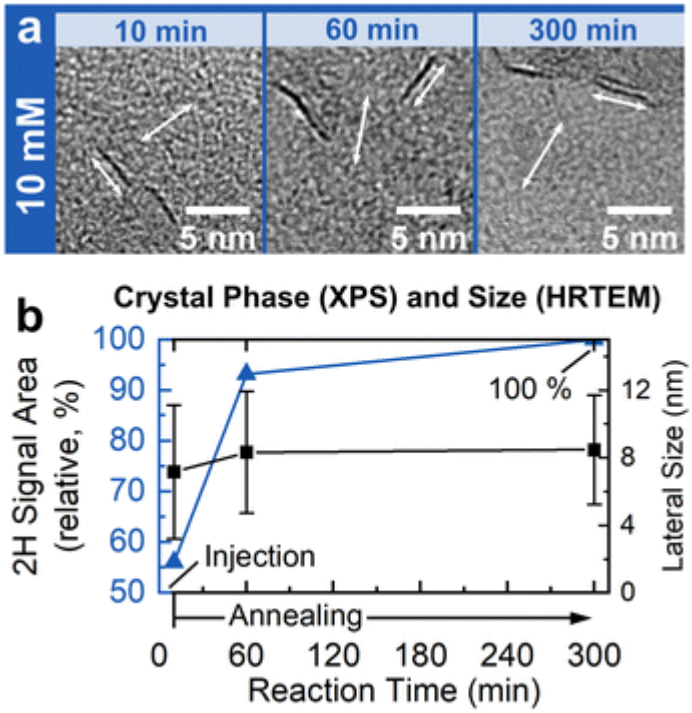

Figure 24 MoS_2 NPLs synthesized with a low 10 mM Mo-precursor concentration and annealed for 5 h. (**a**) During annealing, MoS_2 NPLs retain their lateral size. (**b**) The 1T crystal phase content is transformed to the semiconducting 2H phase during the annealing and yields pure 2H phase NPLs after 5 h (for detailed XPS spectra, see **Figure S7**)

MoS_2 NPLs exhibit an absorption feature between 2.0 and 2.3 eV (see Fig. **5 a**). For further assigning this rather broad absorption, cryogenic measurements (at 80 K) were performed. We filtered the data for noise reduction and calculated the second

derivative (see Fig. **5 b**). We find, that two distinct absorption features emerge, when lowering the temperature. At 80 K the A and B excitonic features are clearly resolved at 2.0 eV and 2.2 eV, with a FWHM of 81 meV and 201 meV, respectively. At room temperature, these features are closely spaced, resulting in a combined broader feature (FWHM of 225 meV). MoS_2 NPLs are then compared to laterally larger NSs that are dominated by the semiconducting crystal phase (94%) with respect to their absorption and transient absorption features, shown in **Figure 26** (at room temperature). The A and B excitonic transitions lead to an absorption at 1.88 eV (661 nm) and 2.03 eV (611 nm) in larger MoS_2 NSs (see Fig. **6 a**, orange, lateral sizes of 22 ± 9 nm). We determine the parameters of the absorption features using the second derivative of the absorption spectra shown in **Figure 26 b**. The energy region of the A and B exciton is fitted by Gaussian functions (see **Figure S8**). For laterally small NPLs (Fig. **6 a**, blue, lateral sizes of 8 ± 4 nm for specific synthesis), a single absorption feature is observed at 2.10 eV. We attribute this feature to the B exciton overlapped by a less pronounced A excitonic feature, as is described in **Figure 25 b**. The combined feature is hypsochromically shifted by 70 meV with respect to the B exciton when the lateral size of the MoS_2 NSs is reduced to NPLs, indicating an additional lateral confinement of the structures. Furthermore, the A, B exciton feature is broadened by a factor of 2.0 for small NPLs, which could be caused by inhomogeneous broadening (8 ± 4 nm) of the MoS_2 NPL samples with respect to lateral confinement. The intensity of the combined excitonic feature relative to the band nesting absorption at 3 eV is significantly reduced in MoS_2 NPLs. This reduced absorption might be caused by a decreased oscillator strength as argued by Ayari *et al.* for 2D CdSe NPLs.[98] The authors state the oscillator strength to be proportional to L_xL_y/r_{Bohr}^2, with L_x and L_y being the dimensions in the lateral direction in 2D CdSe NPLs. A smaller lateral size therefore lowers the oscillator strength and the intensity of the respective absorption features. Although the energetically lowest absorption features for MoS_2 NPLs and NSs are at 2.10 eV (590 nm) and 1.88 eV (659 nm), respectively, the absorption threshold of both samples is at 1.8 eV (689 nm). We determine the absorption threshold by using the Tauc plot (see **Figure S9**).

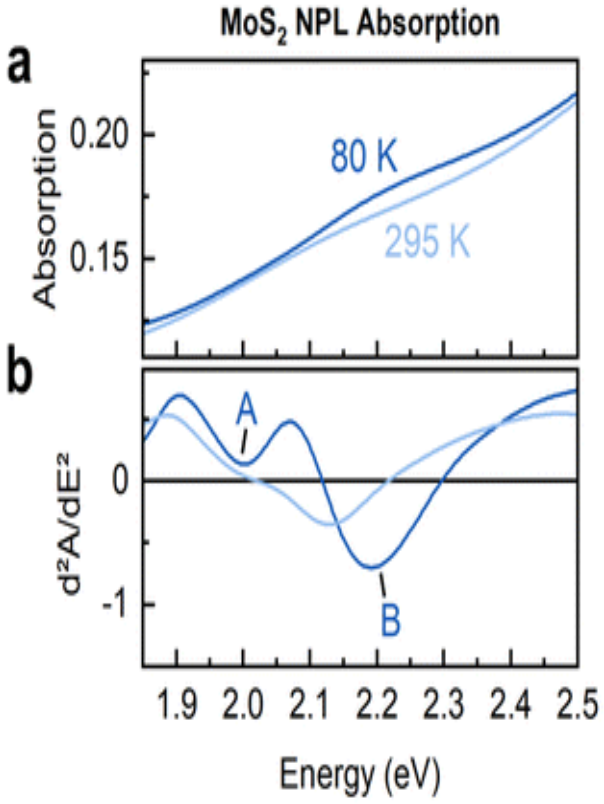

Figure 25 MoS_2 NPLs synthesized with a low 10 mM Mo-precursor concentration and annealed for 5 h at 320 °C. (**a**) Absorption at room temperature (295 K, light blue) and 80 K (blue), respectively. (**b**) Second derivative of the absorption. MoS_2 NPLs exhibit one broad absorption feature at 2.1 eV (590 nm). When lowering the temperature to 80 K, the broad feature separates into two features at 2.0 eV and 2.2 eV, corresponding to the A and B exciton, respectively.

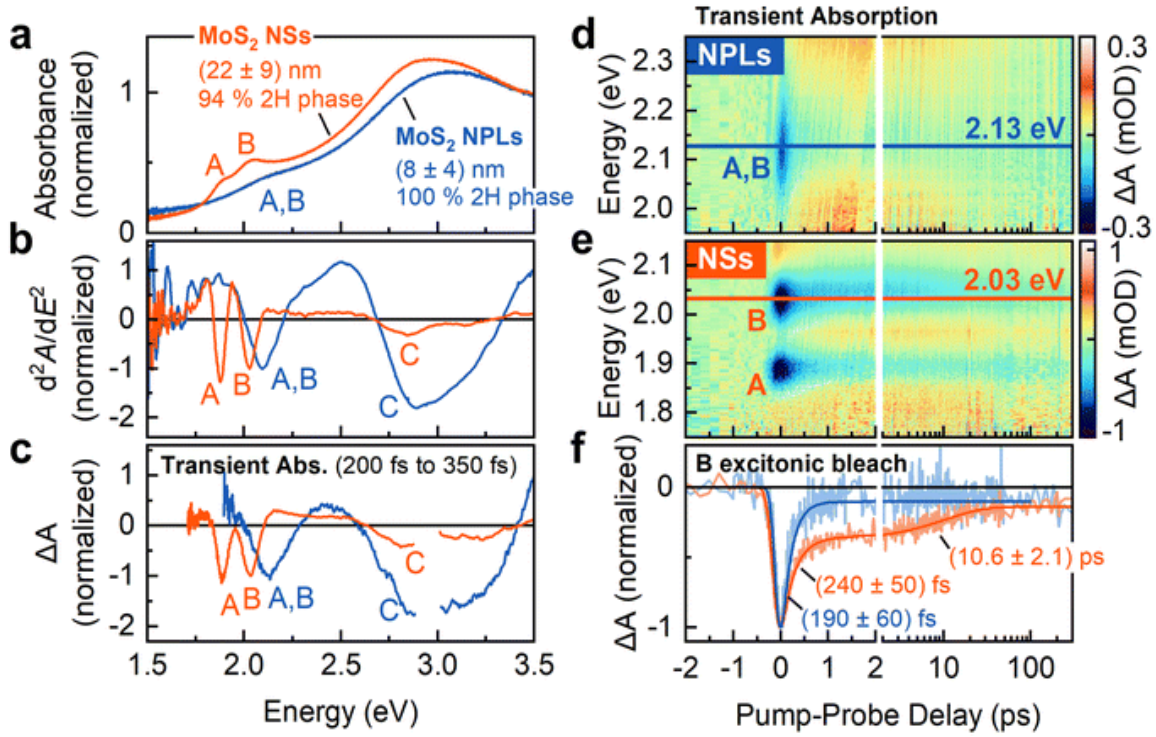

Figure 26 Optoelectronic properties and exciton dynamics of semiconducting MoS_2 NPLs and NSs at room temperature. (**a**) Steady-state absorption spectra of laterally small MoS_2 NPLs (blue) and laterally larger NSs (orange). In NSs the A, B, and C exciton are at 1.88 eV, 2.03 eV, and 2.9 eV, respectively, and appear as maxima or shoulders. (**b**) Second derivative of the smoothed steady state absorption spectra shown in (**a**). With this plot, the spectral positions of the absorption features are accurately determined. The absorption feature in MoS_2 NPLs which we attribute to both, the A and B exciton, is broadened by a factor of 2.0 with respect to the B exciton in NSs. (**c–f**) Transient absorption spectra, photoexcitation at 420 nm (2.95 eV) under 50 µJ cm^{-2} fluence. (**c**) Spectral linecut averaged from 200 to 350 fs after photoexcitation with the A, B and C excitons bleached in larger MoS_2 NSs, while smaller NPLs exhibit only the B and C exciton bleach features. (**d** and **e**) Color-coded transient absorption hyperspectra of the MoS_2 NPLs and NSs exhibiting different decay dynamics. (**f**) Laterally smaller MoS_2 NPLs exhibit a fast monoexponential B excitonic bleach decay, while in larger NSs the B exciton decays with two contributions as is discussed in the text.

Photoluminescence in the MoS_2 NPL and NS ensemble was not observed and could be a result of midgap states, excess charges leading to trions,[38] and/or strong reabsorption. However, studies on colloidal MoS_2[61] and WS_2[40] show, that by efficient

defect passivation and hBN encapsulation to prevent trion formation, photoluminescence in single colloidal MoS_2 can be obtained, which we pursue in continuation of this work. We characterize the exciton dynamics in MoS_2 NPLs and NSs with ultrafast transient absorption spectroscopy shown in **Figure 26 c–f**. MoS_2 NPLs and NSs are dispersed and photoexcited with 100 fs laser pulses at 2.95 eV (420 nm) in the C exciton region of MoS_2. **Figure 26 c** shows that each feature visible in the steady-state absorption spectrum appears as a negative bleach signal in the transients. For both, the MoS_2 NPLs and NSs, the ΔA spectra shown in **Figure 26 c** resemble the second derivative of the steady state absorption spectra shown in **Figure 26 b**. The second derivative of the steady state absorption approximating ΔA was observed by Norris et al. for CdSe nanocrystals before.[99] The authors explain this phenomenon by a trapped carrier induced stark effect resulting in a shift and broadening of the absorption spectrum after excitation. However, extensive transient absorption studies are necessary and performed currently to prove if this applies to MoS_2 NPLs and NSs. The larger MoS_2 NSs exhibit exciton dynamics similar to values previously reported for colloidal MoS_2 NSs.[36, 100] Briefly, the photoexcitation depopulates the valence band at the A, B and C transitions in the band structure, resulting in in bleach signals at the respective energies (1.88 eV, 2.03 eV, and 3 eV, see **Figure 26 b-d**) in MoS_2 NSs. Excitonic decay progresses fast by sub-picosecond hole capture due to energy states in the band gap, followed by a slow carrier-carrier recombination and capturing by the midgap states.[36] The two processes are reflected by a biexponential decay of the bleach features. The B excitonic bleach decays with time constants of 240 ± 50 fs and 10.6 ± 2.1 ps, respectively.

However, laterally small MoS_2 NPLs don’t show the slower decay process, the B excitonic bleach feature is fitted with a monoexponential decay with a time constant of 190 ± 60 fs. This value is on the time scale of hole capturing by midgap states and strongly suggests that the charge carrier dynamics in small MoS_2 NPLs is indeed determined by edge states, which are rising in relative amount with decreasing NPL size.

3.1.5 Conclusion

Colloidal synthesis represents a versatile tool for precisely tailoring the optical properties of TMDCs by a bottom-up wetchemical method, especially for lateral size and crystal phase. For the first time, we show the direct synthesis of semiconducting MoS_2 NPLs and larger NSs with the same method by simply varying the molybdenum precursor concentration and the reaction time with a higher precursor concentration leading to larger NSs. We find that at early synthesis times, a mixture of the 2H and 1T crystal phase is present in the 2D MoS_2 reaction. The 1T content decreases in favor of the formation of the 2H phase over time, following the Ostwald step rule. With the synthesis method shown here, both phasealloyed and phase pure semiconducting ultrathin 2D MoS_2 NPLs and NSs of lateral size approaching and above the exciton dimension of MoS_2 are accessible, making the additional lateral confinement of 2D excitons experimentally explorable. We use the Ostwald step rule to convert MoS_2 NPLs and NSs into phase-pure semiconductors that exhibit different excitonic decay dynamics. The confinement in the lateral plane strongly affects MoS_2 NPLs that show a significant higher number of edge states due to their small dimensions. This leads to an ultrafast exciton decay by hole trapping and in turn represents an important starting point for the synthetic design of TMDC heterostructures for further controlling and increasing emissive excitonic recombination processes.

3.1.6 Acknowledgements

The authors appreciate the Laboratory for Nano- and Quantum Engineering (LNQE) in Hannover for access to the TEM. The authors would like thank Armin Feldhoff for providing the XRD facility, Nadja C. Bigall and Dirk Dorfs for access to the UV-Vis-NIR absorption spectrometer and Jürgen Caro for access to the ATR-FTIR spectrometer. K. T. is grateful for being funded by the Hannover School for Nanotechnology (HSN). M. S. acknowledges funding by the DFG under grant SCHE1905/9-1. The authors thank Fabian Strauß for preparing wafer cuts as substrates for XPS experiments. J. L. gratefully acknowledges funding by the German Research Foundation (DFG) under the Excellence Strategy of the Cluster of Excellence PhoenixD (EXC 2122, Project ID 390833453) and access to the Ti:sapphire amplifier system (major equipment DFG, Project ID 231415720, Michael Oestreich). J. L. is grateful for funding through the Caroline Herschel Program of Leibniz Universität Hannover.

3.2 Tuning the Interfacial Electronic Structure of MoS_2 by Adsorption of Cobalt Phthalocyanine Derivatives

Philipp Haizmann[1], Eric Juriatti[1], Maren Klein[1], Katharina Greulich[1], Ruslan Ovxyannikov[3], Erika Giangrisostomi[3], Thomas Chassé[1], Heiko Peisert[1], Marcus Scheele[1,2]

[1] Institut für Theoretische und Physikalische Chemie, Universität Tübingen, 72076 Tübingen, Germany

[2] Center for Light-Matter Interaction, Sensors & Analytics LISA+, Universität Tübingen, 72076 Tübingen, Germany

[3] Institute Methods and Instrumentation for Synchrotron Radiation Research, Helmholtz-Zentrum Berlin für Materialien und Energie GmbH, 12489 Berlin, Germany

3.2.1 Abstract

We investigate the interfacial electronic structure of n-type bulk MoS_2 upon the adsorption of CoPc and $CoPcF_{16}$ mono- and few-layers using advanced spectroscopic techniques. These include X-ray photoelectron spectroscopy (XPS), X-ray absorption spectroscopy (XAS), angle-resolved photoelectron spectroscopy (ARPES), and ultraviolet photoelectron spectroscopy (UPS). Our findings indicate that the adsorption of CoPc enhances the degree of n-doping at the interface with MoS_2. In contrast, $CoPcF_{16}$ results in a nearly intrinsic position of the Fermi level. Furthermore, we note the formation of an induced gap state near the valence band maximum for monolayer $CoPcF_{16}$ on MoS_2. These observations underscore the potential to fine-tune the interfacial electronic properties of transition metal dichalcogenides through molecular functionalization for tailored electronic applications.

3.2.2 Introduction

As electronic component miniaturization progresses, innovative materials and their unique interactions become pivotal to the ongoing evolution of semiconductor devices. Transition metal dichalcogenides (TMDCs), such as molybdenum disulfide (MoS_2), have gained significant attention in this context. These materials possess a layered crystal structure, tunable bandgaps and high carrier mobilities, making them especially appealing for use in optoelectronics, photovoltaics and field-effect transistors.[101-105] To further refine these semiconductor components for targeted applications, merging TMDCs with organic semiconductors is a promising strategy, also because it preserves the structural integrity of the TMDCs.[106] Past endeavors in this direction have involved functionalization with strong electron acceptors such as (fluorinated) tetracyanoquinodimethane (TCNQ)[107-111], fluorinated fullerenes[112], and 4-nitrobenzenediazonium tetrafluoroborate (4-NBD)[113], all of which induce p-type doping of the TMDC by integer charge transfer. Similarly, n-doping has been achieved through functionalization with different organic and inorganic heterostructures.[111, 113-119] A large portion of research was dedicated to mono- and few-layer TMDCs and there are few studies that deal with bulk crystals and even less with heterostructures. Given that the number of layers is crucial for the properties of the electronic structure, expanding the research to bulk crystals is necessary to gain a deeper understanding of heterostructures from organic molecules and TMDCs.

Transition metal phthalocyanines (TPcs) are a versatile class of organic semiconductors. Their inherent chemical variability makes them especially intriguing for studies focused on organic-inorganic semiconductor heterostructures. A key aspect of TPcs is the substitutability of the central atom and the alterability of peripheral positions, like fluorination, which significantly impacts their ionization energy and affects energy level alignments in heterostructures (e.g. Ref.[120-122]) Notably, phthalocyanines are anticipated to exhibit weak interactions on van der Waals surfaces. Such interactions can be beneficial for customizing the electronic properties of TMDCs, since a strong interaction, accompanied by an integer charge transfer, would result in an undesirable localization of the charges at the interface.

By constructing such weakly interacting TMDC/TPc heterostructures, the photoresponsivity and response time in phototransistors were improved compared to the pure TMDC components.[123-127] Furthermore, TPcs could be used for defect engineering and the resulting enhancement of photoluminescence quantum yields.[128-130] In this work, we seek to modify the type and concentration of charge carriers in n-type MoS_2 by adsorption of cobalt-phthalocyanine (CoPc) and its perfluorinated derivative ($CoPcF_{16}$). While the interface between TMDCs and other TPcs has been explored previously, the effect of the cobalt derivatives has not been studied so far.[131] Moreover, this work contributes to the understanding of charge transfer processes and interface states in general which is still under investigation.[132-135]

Using synchrotron-based X-ray photoelectron spectroscopy (XPS), X-ray absorption spectroscopy (XAS), and angle-resolved photoemission spectroscopy (ArPES), complemented by ultra-violet photoelectron spectroscopy (UPS) and a laboratory-source XPS, we systematically examine the interface of these heterostructures. Our results indicate that it is possible to tune the properties of MoS_2 merely by the choice of CoPc *vs.* $CoPcF_{16}$. We find evidence for the formation of an induced gap state with $CoPcF_{16}$, which is absent with CoPc. This research provides important insights into tuning the semiconductor properties of TMDC-based devices.

3.2.3 Experimental

All experiments were conducted either at the LowDosePES endstation of the PM4 beamline (BESSY II, Helmholtz-Zentrum Berlin, Germany)[30, 136] or with our laboratory setup under ultra-high vacuum (UHV) conditions (base pressure at the LowDosePES endstation $1 \cdot 10^{-10}$ mbar and $5 \cdot 10^{-10}$ mbar at our home system). At the LowDosePES, the clean MoS_2 surface was examined with XAS, XPS and ArPES using an angle-resolved time-of-flight detector (ARTOF).[136] This detector offers high efficiency compared to conventional hemispherical analyzers, thus enabling experiments at lower photon flux, mitigating potential radiation damage to phthalocyanines in prolonged experiments with longer radiation exposure times. XAS measurements were carried out in the total electron yield mode measuring the sample current. For energy calibration we used a gold single crystal which was cleaned by repeated cycles of argon ion sputtering and annealing. After each change of the excitation energy, the **Au***4f*$_{7/2}$ (84.00 eV) binding energy was measured, and consecutive measurements calibrated to this. For photoemission experiments with excitation energies of 900, 300, 230 and 75 eV an energy resolution of 1492, 188, 133 and 69 meV was estimated, respectively. For the ArPES measurements, we utilized a photon energy of 75 eV and chose a detector acceptance angle of 30 degrees to probe with a maximum $k_{\parallel}$ value of approximately 1.16 Å^{-1}. We chose this photon energy as for a good compromise between intensity and reciprocal space resolution and extension. The calculated distances in the reciprocal space from Γ to K is 1.325 Å^{-1} and 1.147 Å^{-1} from Γ to M for the hexagonal MoS_2 lattice with a lattice constant of 3.162 Å.[137] It was possible to probe the full Brillouin zone at this energy, provided the sample is titled such that the gamma point ends up at the edge of the detector field of view (see **Figure S10**, Appendix B). Using the k_x versus k_y momentum map, we traced the path through reciprocal space from K to Γ to M and plot the energy dispersion diagrams (see red lines in **Figure 28 e** and **f**). Photoionization cross sections were taken from Yeh and Lindau[3] and employed for calculations, while the inelastic mean free path of photoelectrons was determined according to Seah and Dench.[25] For each series of experiments, a crystal was freshly cleaved. Different crystals were used for the experiments, but care was taken to ensure that specific phthalocyanines were only studied with certain crystals, preventing any cross-contamination.

3.2.4 Results and Discussion

The energy level alignment and position of the Fermi level can be, in a first approximation, indirectly monitored via the binding energy of the substrate core level peaks, assuming rigid shifts of core and valence band levels (e.g. Ref. [138]). **S***2p* and **Mo***3d* core level spectra, (measured at the LowDosePES endstation and at our home setup) are presented in **Figure 27**. We choose low excitation energies for the synchrotron experiments to ensure that the measurements are as surface-sensitive as possible. For details on the calculation of the inelastic mean free paths for all experiments and photon energies we refer to the Appendix B (**Table S 1**). Briefly, the experiments at the LowDosePES endstation probe mostly the first layer, considering an MoS_2 monolayer thickness of about 0.7 nm.[11] In contrast, the experiments at the lab spectrometer with an Al Kα source and an inelastic mean free path of the photoelectrons of about 2.4 nm are more volume-sensitive. **Figure 27 a** and **b** display the **S***2p* core-level spectra, collected at an excitation energy of 230 eV before and after the exposure of MoS_2 to CoPc and $CoPcF_{16}$, respectively. Similarly, **Figure 27 c** and **d** depict the **Mo***3d*$_{5/2}$ core-level spectra, recorded at an excitation energy of 300 eV for the same two interfaces. The layer thicknesses of 0.34 nm corresponds approximately to a monolayer coverage,[139] whereas thicker films of 1.16 nm (CoPc) and 1.71 nm ($CoPcF_{16}$) represent multilayers in the case of flat lying molecules. The spectra of the freshly cleaved surfaces which serve as reference points, are represented in black in both figures. The binding energies of the **Mo***3d*$_{5/2}$ signals (229.20 eV (**Figure 27 a**) and 229.25 eV (**Figure 27 b**)) and **S***2p*$_{3/2}$ (162.15 eV (**Figure 27 c**) and 162.20 eV (**Figure 27 d**)) are typical for 2H-MoS_2.[89, 140] Although we observe a slight difference of 50 meV between the fresh samples (e.g. due to different defect densities)[141, 142], we do not expect a great influence from this difference on the interaction between the MoS_2 and the phthalocyanines. The deposition of the first layer of CoPc and $CoPcF_{16}$ causes a binding energy shift of the MoS_2 core-level spectra. A shift of 0.3 eV towards higher binding energies (**Mo***3d*$_{5/2}$ at 229.50 eV and **S***2p*$_{3/2}$ at 162.45 eV) is observed after the deposition of the first CoPc layer (illustrated by the light green curves in the figures). Conversely, with $CoPcF_{16}$ there is a decrease of 0.3 eV (**Mo***3d*$_{5/2}$ at 228.93 eV and **S***2p*$_{3/2}$ at 161.90 eV) in binding energy (represented by the light lilac curves in the figures). The deposition of subsequent layers of the phthalocyanines has a comparably negligible effect (curves in darker shades of green and lilac). In the more volume-

sensitive experiments on the laboratory spectrometer, we obtain the same result for the CoPc/MoS_2 heterostructure (**Figure 27 e** and **f**). In contrast, with $CoPcF_{16}$ (**Figure 27 g** and **h**) no shift to lower binding energy is observed. This indicates that the interaction primarily occurs on the top layer of the molybdenum disulfide.

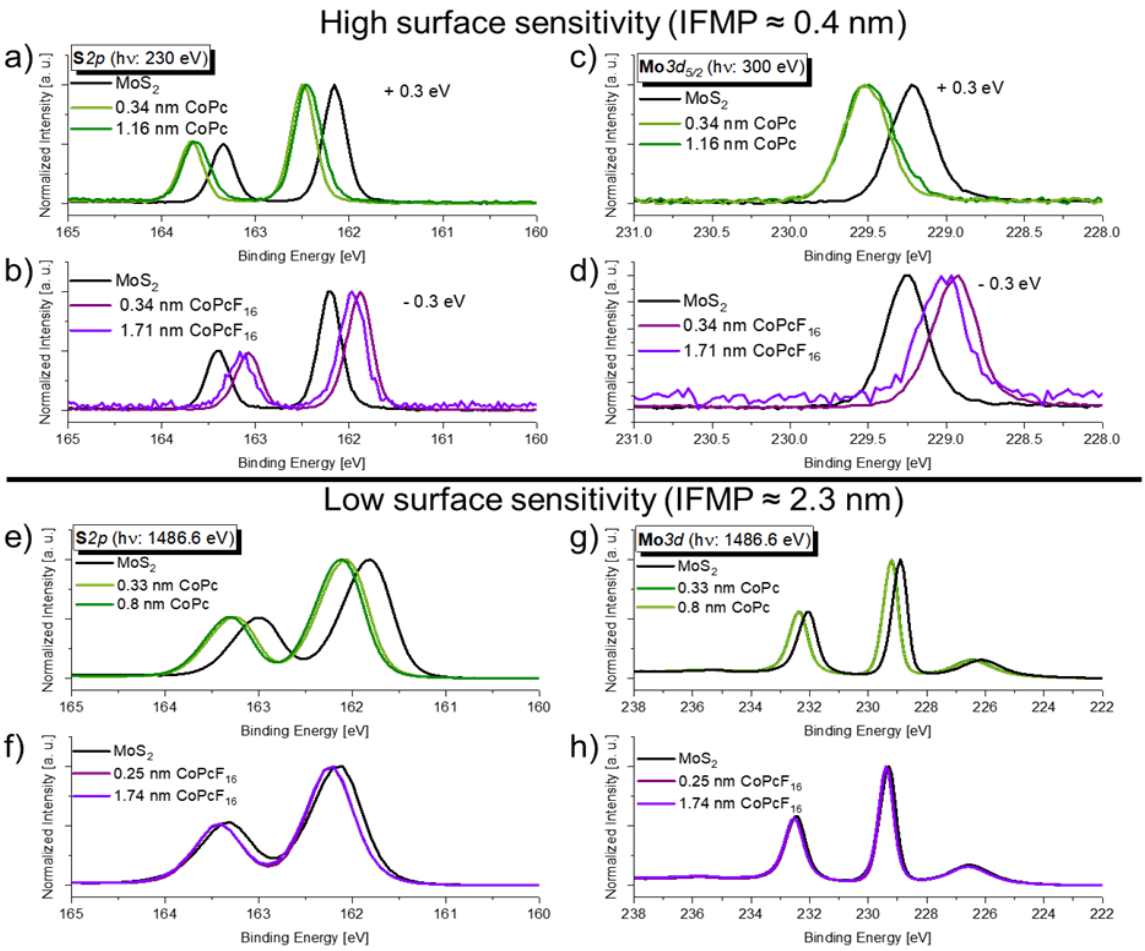

Figure 27 X-ray Photoelectron Spectroscopy (XPS) measurements of the core-levels of MoS_2 following deposition of CoPc and $CoPcF_{16}$. The spectra of the freshly cleaved surfaces appear in black. Green and lilac colors correspond to shifts in binding energy following the deposition of the CoPc and $CoPcF_{16}$ layers respectively. **S***2p* core-level spectra for MoS_2 with CoPc shown in (**a**) and (**e**) and with $CoPcF_{16}$ shown in (**b**) and (**f**). **Mo***3d* core-level spectra for MoS_2 with CoPc shown in (**c**) and (**g**) and with $CoPcF_{16}$ shown in (**d**) and (**h**). Spectra in (**a**), (**b**), (**c**) and (**d**) acquired at LowDosePES end-station, spectra in (**e**), (**f**), (**g**) and (**h**) acquired at the home setup.

Generally, shifts of core level binding energies of semiconductor materials (as probed by XPS) can be caused either by changes in the (chemical) environment of the

considered atom, or by the variation of the position of the reference level, the Fermi level. In the present case, the quantitatively identical shift of the positions of the **Mo***3d* and the **S***2p* binding energies, indicate a shift of the substrate Fermi level because of the deposition of molecules, that is, an (interface) doping. Such doping-related core level shifts are well-known: For example, for silicon the **Si***2p* binding energy of heavily n-doped silicon is found at higher values compared to heavily p-doped silicon.[143] These findings fit well to other previous investigations of doping in different heterostructured TMDCs.[112, 113, 119, 144]

To gain a deeper understanding of the origin of this doping, we map the band structure obtained by angle-resolved photoelectron spectroscopy (ARPES) in **Figure 28. Figure 28 a** and **b** display the energy dispersion diagrams for freshly cleaved MoS_2, while **Figure 28 c** and **d** depict the diagrams after deposition of monolayers (0.34 nm) of CoPc and $CoPcF_{16}$, respectively. All energy dispersion diagrams were extracted from cuts through the momentum maps shown in **Figure 28 e** and **f** and the paths are indicated by the red lines. We omit the dispersion diagrams for the thicker films here, as the method is highly surface-sensitive, and substrate-related features are no longer visible, which makes tracing a comparable momentum cut not reliable. To further illustrate changes upon deposition, **Figure 28 g** and **h** represent the integration over the imaged area of the detector for all spectra. The intensity is normalized to facilitate a comparison. The valence band maxima (VBM) at the Γ point for the two freshly cleaved substrates were found at 0.92 and 0.77 eV (**Figure 28 a** and **b**), indicating slight n-type doping, when considering a band gap of 1.23 eV.[2] We note that even in-situ cleaved samples can exhibit a slightly different position of the Fermi level, depending crucially on the number of step edges and other defects in the analyzed area. However, the careful monitoring of the measurement spot (diameter 0.1 mm) on the sample enables the analysis of the same sample region before and after the deposition of the molecules. For CoPc deposition, we observe a positive shift (+ 0.21 eV) of the Γ point to 1.13 eV, while for $CoPcF_{16}$ deposition, the Γ point moves (- 0.11 eV) to 0.66 eV. The direction of these shifts is consistent with the results obtained from XPS core-level measurements, but it is worth noting that the magnitude of these shifts is different. This shows that rigid shifts in the measured core-level provide a qualitative indication of changes in the Fermi level's position. However, for a more precise analysis, the valence band region must be examined.

The same ARPES measurements also reveal details about the electronic properties of the deposited molecular monolayers. For CoPc (**Figure 28 c**), we locate the HOMO (Highest Occupied Molecular Orbital) maximum at around 0.9 eV and the on-set at around 0.6 eV, e.g. slightly above the energy of the VBM of MoS_2. As expected for phthalocyanines, we find an intensity variation depending on the angle of emitted electrons with the highest state density around 1.5 – 1.7 $Å^{-1}$, [5, 145, 146] that is, in the vicinity of the K- and M-point of MoS_2 visible in the momentum maps at 0.8 eV shown in **Figure 28 e**. We note that for thicker CoPc films, the HOMO maximum is found at 1.05 eV (**Figure 28 g**) and the on-set at around 0.75 eV. A possible reason might be that screening effects at the interface occur in both the MoS_2 and the CoPc, which has also been observed for phthalocyanines on metal substrates.[147, 148] When fitting the HOMO peaks of the monolayer and thicker CoPc films with an Gaussian function we find two different full width half maxima (FWHM) of 0.36 and 0.4 eV respectively. Those differences can be explained by an inhomogeneous film growth but also by molecule-molecule interactions,[149, 150] which also cause energetic shifts of the HOMO.

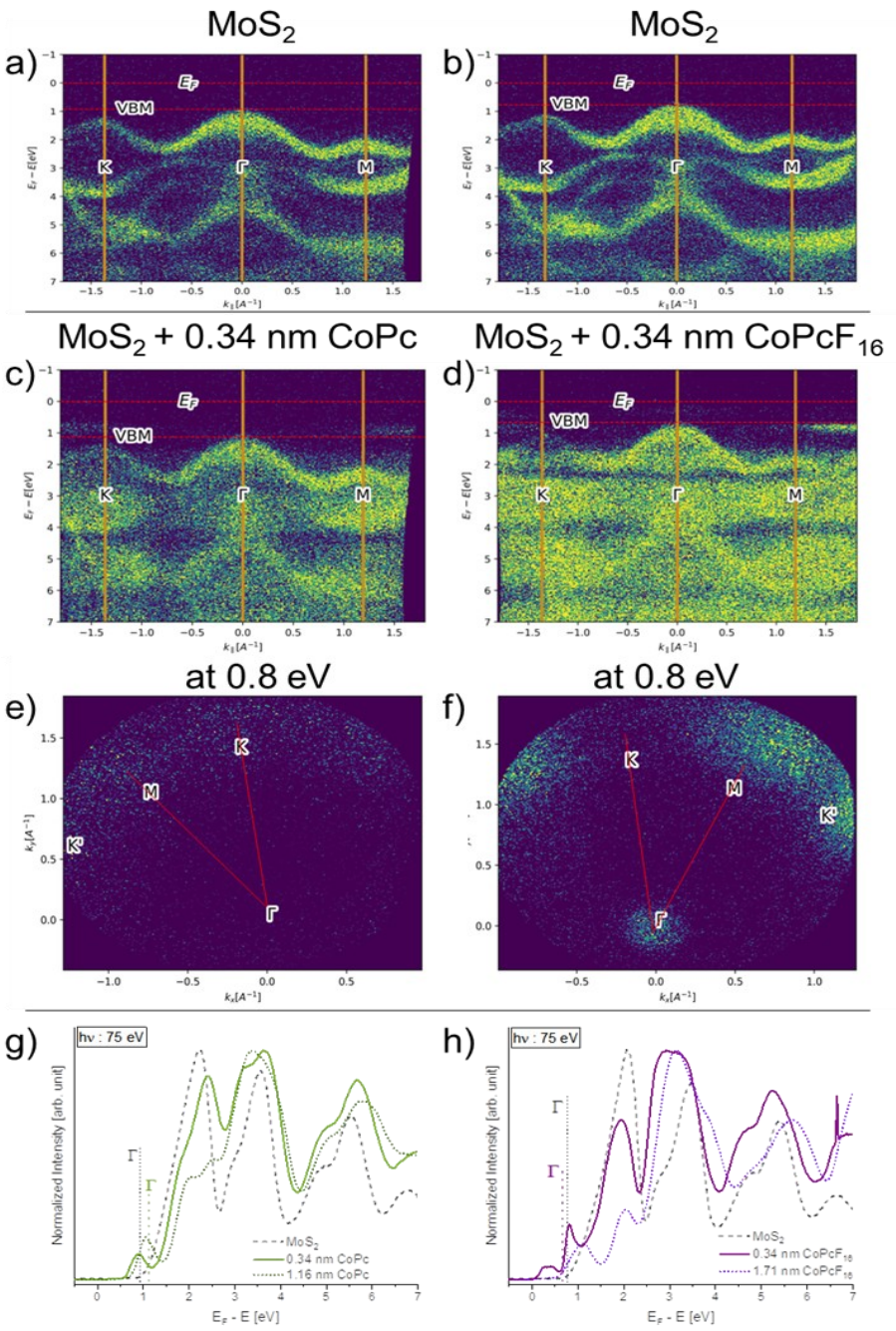

Figure 28 (**a – d**) Energy dispersion diagrams for different pathways through the Brillion zone. (**a**) and (**b**) show measurements of the clean surface while (**c**) and (**d**) show the dispersion diagrams after deposition of CoPc and $CoPcF_{16}$ respectively. In (**e**) and (**f**), momentum maps at 0.8 eV are show for the respective CoPc/MoS_2 and $CoPcF_{16}$/MoS_2 heterostructures. The red lines indicate the cuts taken to obtain the energy dispersion diagrams for (**a – d**)**.** In (**g**) and (**h**) the integrated and normalized spectra for the clean MoS_2 crystals and after deposition of the respective phthalocyanines are shown.

For $CoPcF_{16}$ (**Figure 28 d**), we locate the HOMO maximum at around 0.8 eV with the highest state density again near the K- and M-points (see momentum map in **Figure 28 f**), an on-set at 0.65 eV (**Figure 28 h**) and a FWHM of 0.3 eV. Different from CoPc, an additional, more diffuse state emerges near the Γ point with its maximum at 0.35 eV and an on-set close to the Fermi level at 0.1 eV (see also **Figure 28 h** and **Figure S10 c**, Appendix B). For thicker molecular films, this state disappears, the HOMO maximum shifts to 1.11 eV with an on-set at 0.6 eV, and the FWHM broadens to 0.55 eV. Thus, the effects displayed in **Figure 28** are confined to the interface.

We discuss the most likely provenance of this new state in the context of three established mechanisms of charge transfer (CT), namely integer charge transfer (ICT)[151-154], fractional charge transfer (FCT)[155-157], and induced gap states (IGS)[158-160]. All concepts can be used to describe CT processes at organic/inorganic interfaces of semiconductor heterostructures, and for details we refer to the Appendix B.

Based on our observation that the interaction in the $CoPcF_{16}/MoS_2$ system is limited to the first MoS_2 layer, while in the $CoPc/MoS_2$ system the interaction is more extensive, we propose that the interaction is best described by the IGS model. We will later present this in an energy level alignment (ELA) diagram summarizing all measurement results. However, it is worth noting now that the interaction in $CoPc/MoS_2$ can be explained through the formation of a macroscopic dipole, whereas the $CoPcF_{16}/MoS_2$ system needs to be described within the IGS framework, involving the formation of microscopic dipoles at the interface.

For completeness, we aim to consider the entire system and subsequently discuss our results in relation to other models. Therefore, one alternative explanation for the new state near the Fermi level could also be the occupation of the $CoPcF_{16}$ LUMO at the interface with MoS_2, similar to previous studies of diamond and F4-TCNQ, its anionic derivative,[151, 161] as well as for pentacene on copper.[162] This would be in the framework of the ICT model and could explain the observed core level shift of MoS_2 due to p-doping and a localized charge transfer, accommodated with a reduction of negative charge carriers in the MoS_2. However, for such a scenario one would expect a LUMO-like distribution in the momentum maps, that is, with zero density at the Γ-point.[5] A close examination of the momentum map at 0.35 eV (**Figure S10 c**, Appendix B) shows significant density at the Γ-point, which therefore excludes a charge transfer into the $CoPcF_{16}$ LUMO.

The formation of a gap state in the substrate for $CoPcF_{16}/MoS_2$ can cause local interfacial charge transfer and also hybridization in the context of FCT. To study if the central atom (Co) of the phthalocyanines is involved in such an interaction, we perform X-ray absorption (XAS) experiments at the Co-L_3 edge and XPS measurements of the **Co***2p*$_{5/2}$ region, presented in **Figure 29**. Metal L-edge spectra of TMPcs are in particular sensitive to changes of the configuration of d-electrons.[18] In the case of an occupation or hybridisation of particular orbitals, excitation cannels can be blocked, as shown for CoPc on Ni and grapene/Ni.[163]

The XAS results for mono- and multilayer deposition of CoPc are displayed in **Figure 29 a**, while the corresponding results for $CoPcF_{16}$ are shown in **Figure 29 b**. Most notably, there are no significant differences in the spectra for each molecule obtained after monolayer vs. multilayer deposition. This indicates that the observed induced gap state in **Figure 28** is not localized on the Co atom, as the peak shape and position would be expected to change otherwise.

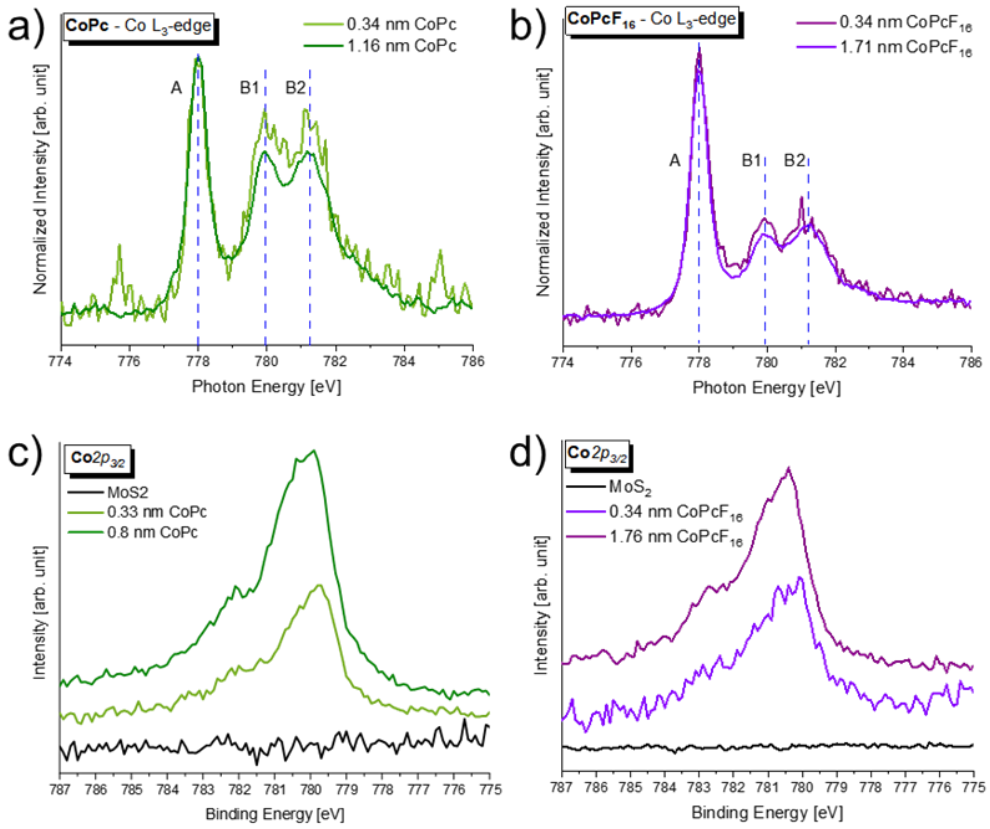

Figure 29 (**a**) and (**b**) show XAS measurements (acquired at LowDosePES) on the Co L_3-edge region after depositon of CoPc and $CoPcF_{16}$ respectively. In (**c**) and (**d**) XPS measurements (acquired at the home lab) of the **Co**$2p_{3/2}$ region are shown for similar thicknesses of CoPc and $CoPcF_{16}$ respectively.

XPS experiments of the **Co***2p*$_{3/2}$ region after CoPc or $CoPcF_{16}$ deposition (**Figure 29 c** and **d,** respectively) support our hypothesis that the Co atom does not take part in charge transfer since there are no variations in the spectral shapes after monolayer vs. multilayer deposition.

To test whether the interaction involves the organic macrocycle, we analyzed the *1s* region in more detail after CoPc or $CoPcF_{16}$ deposition (**Figure 30 a** and **b**, respectively, with fitting parameters and peak positions listed in **Table S2,** and a detailed description of the fitting procedure in the Appendix B).[104, 164] Three chemically distinct carbons can be identified marked in the chemical structure shown in **Figure 30**. Those are the ones bound to nitrogen (C1), the neighboring carbon (C2) and the peripheral carbons bound either to hydrogen or fluorine atoms depending on the

moiety under consideration (C3). We note a slight shift to higher binding energies of the CN components for multilayers vs. monolayers, indicating screening effects at the interface and/or a possible site-dependent redistribution of electrons.[147, 164] This might be a hint for a redistribution of electrons at the interface due to local interactions, but differences between the phthalocyanine monolayer in direct contact with the MoS_2 surface and the thick film are minor. Similar results were obtained for the laboratory-source measurements, although the lower energy resolution causes a broadening of the Gaussian width (see **Figure S12** and **Table S3**, Appendix B). On this basis, we can rule out hybridization in the context of an FCT. At the same time, these investigations suggest that the macrocycle has a small contribution to the formation of the IGS, and this is limited to the interface, specifically the first TPc monolayer.

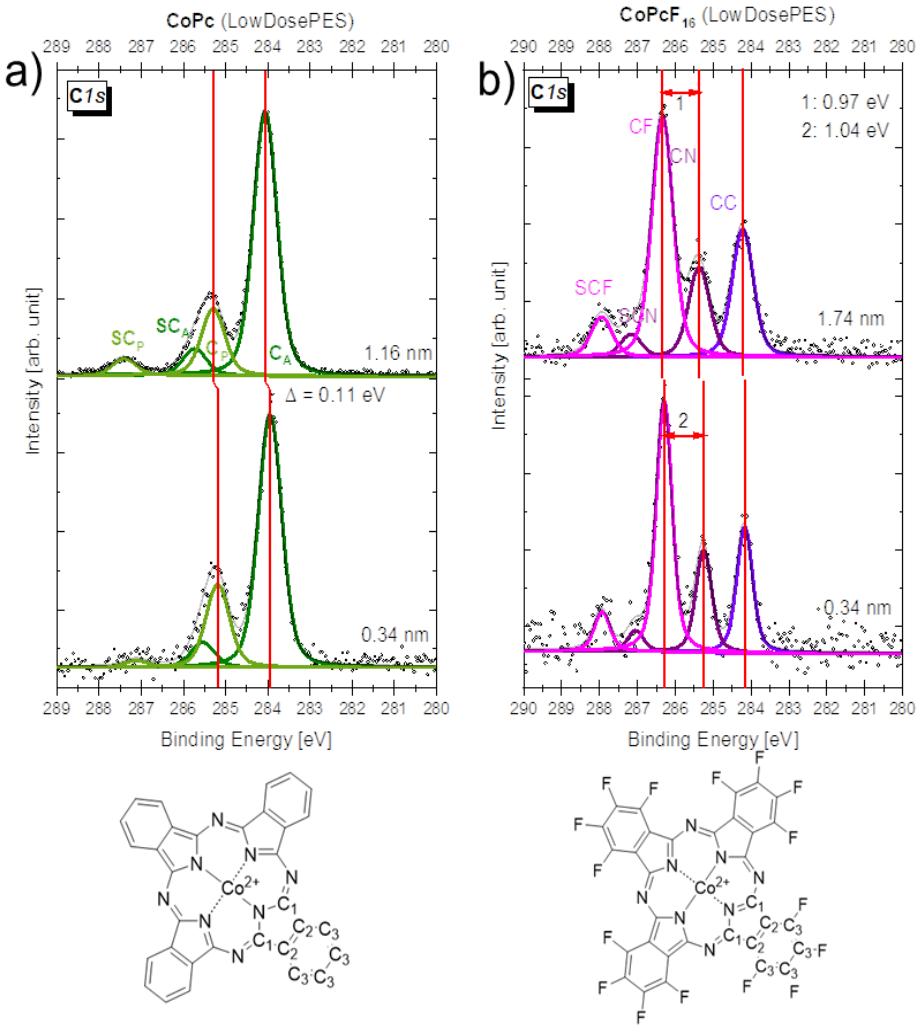

Figure 30 C*1s* core-level spectra of the phthalocyanine ML and thick film. (**a**) shows the measured data and applied fit model for CoPc (upper part for the 1.16 nm film and lower part for the phthalocyanine monolayer). Below the spectra, the chemically inequivalent carbon atoms are marked as C1 – C3. In (**b**) the results for the perfluorinated $CoPcF_{16}$ is displayed.

We combine all electronic structure information derived so far to construct the energy level alignment (ELA) diagrams in **Figure 31**. Further, we include results from the work function and UV-Vis absorption measurements shown in **Figure S13**, Appendix B. The work functions are extracted from the determination of the secondary electron cutoff in the UPS experiments. For freshly cleaved surfaces of MoS_2, we find a work function of 5.1 eV. After deposition of roughly a monolayer CoPc, the work function decreases to 4.8 eV. Depositing an even thicker film, the work function continues to decrease to 4.5 eV. In contrast, for $CoPcF_{16}$ deposition the work function increases to 5.3 eV after one monolayer, and no further changes occur for thicker films. These findings suggest

that CoPc induces a strong negative dipole change of - 0.6 eV at the MoS_2 surface. This change of the surface dipole and the accommodated band-banding observed in the core-level shifts is consistent with our previous results with iron-phthalocyanines[122] as well as for other heterostructures of MoS_2, for example with cesium carbonate.[116] In contrast, $CoPcF_{16}$ induces a weak positive dipole change of + 0.2 eV. The optical bandgaps are 1.66 eV and 1.54 eV, consistent with values for similar phthalocyanines (**Figure S13 c** and **d** respectively).[120, 165, 166] We assume that pure phthalocyanines behave identically to thick multilayers deposited on MoS_2 and compare the electronic structure of pure CoPc as well as $CoPcF_{16}$ with freshly cleaved MoS_2 in **Figure 31 a** and **c**, respectively. For the ELA construction, we neglect energy dispersions and band structure information and just evaluate the VBM (energy at the Γ point) and the CBM (based on optical band-gap measurements taken from literature).[2] The same representation is done with the phthalocyanines as we take the HOMO on-sets and the measured optical band-gap to place the LUMO accordingly. From this, we infer a staggered gap of the frontier orbitals of CoPc with the band edges of MoS_2 before contact, i.e. for vacuum level alignment. For $CoPcF_{16}$ however, we suggest that the VBM and the HOMO are roughly at the same energy before contact.

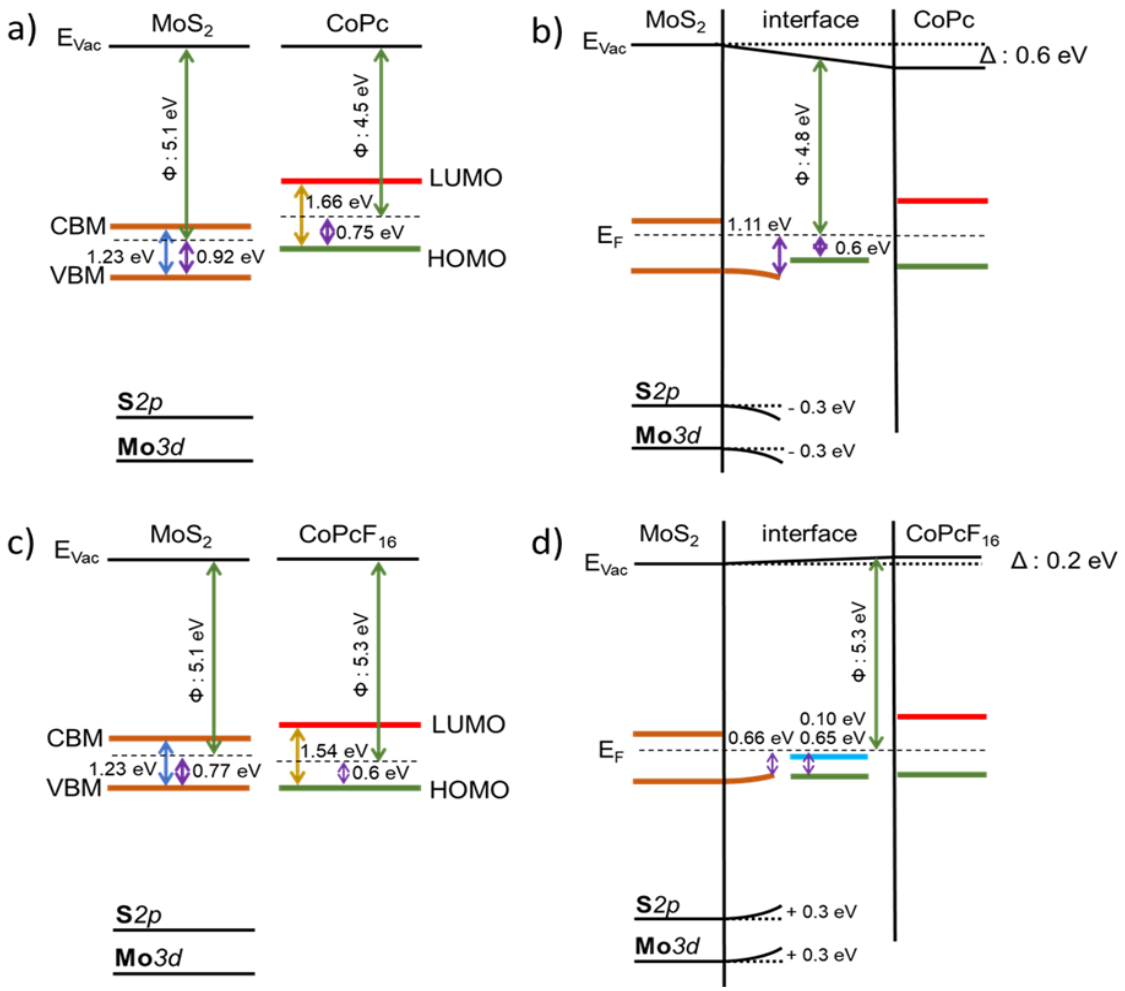

Figure 31 Energy level alignment diagrams. All arrows represent measured data, except for the band-gap of MoS_2 which is taken from literature[2]. Green arrows are obtained from UPS measurements at the lab spectrometer (**Figure S13 a** and **b**). Values for the purple arrows are taken from the integrated ARPES measurements (**Figure 28 g** and **h**). Yellow arrows represent the values taken from UV-Vis absorption measurements of the respective phthalocyanine films on glas substrates (**Figure S13 c** and **d**). (**a**) and (**c**) show MoS_2 and CoPc/$CoPcF_{16}$ before contact, respectively. The energy levels of the MoS_2 VBM (Γ-point) are represented as single values and the position of the CBM placed based on a band gap value of 1.23 eV.[2] For the HOMOs of the phthalocyanines, the measured onset values are shown in green. Since no information besides the optical band gap is measured for the LUMO of the phthalocyanines, a single energy level is shown (red). The alignment for (**a**) and (**c**) is on the vacuum niveous. (**b**) and (**d**) show MoS_2 and CoPc or $CoPcF_{16}$ in contact, i.e. with Fermi-levels aligned.

From **Figure 31 c**, no integer charge transfer from MoS_2 to $CoPcF_{16}$ is expected since the LUMO of $CoPcF_{16}$ is located above the CB of MoS_2, and compared to other electron acceptors the electron affinity is significantly lower. Nevertheless, we find p-type doping of the MoS_2. We can deduct that only a new induced gap state at the MoS_2/$CoPcF_{16}$ interface can explain the charge transfer, best described on the basis of the IGS model. We note that the formation of induced gap states at interfaces is known for several organic-metal interfaces and for organic-inorganic semiconductor interfaces.[132, 159, 167, 168]

3.2.5 Conclusion

We presented a comprehensive XPS/ARPES and XAS study on the heterostructure system of CoPc and $CoPcF_{16}$. Our findings show that CoPc and $CoPcF_{16}$ can both be used for Fermi level engineering of bulk MoS_2, however with notable differences in the mechanism of their action. CoPc induces a surface dipole and a downwards band bending, which is consistent with previous findings for other phthalocyanines. The influence of adsorbed CoPc extends into multiple layers of the MoS_2 substrate. In contrast, the n-type character of MoS_2 is reduced through interaction with $CoPcF_{16}$. The results of the study suggest the presence of an induced gap state, and the interaction is limited to only the first layer of the MoS_2 bulk crystal. While this study has focused on the interface of bulk MoS_2, the question remains open as to whether these findings can be directly transferred to heterostructures with two-dimensional MoS_2. The electronic structure of two-dimensional MoS_2 differs from that of bulk crystals. However, the effects described here are found directly at the interface, which could make them highly relevant for these materials as well.

3.2.6 Acknowledgements

This work was supported by the German Research Council (PE 546/17-1, SCHE1905/9-1 (project no. 426008387)) and the European Research Council (ERC) under the European Union's Horizon 2020 research and innovation program (Grant Agreement 802822).

3.3 Orientation of Cobalt-Phthalocyanines on Molybdenum Disulfide: Distinguishing between Single Crystals and Small Flakes

Philipp Haizmann[1,#], Eric Juriatti[1,#], Maren Klein[1], Katharina Greulich[1], Peter Nagel[2,3], Michael Merz[2,3], Stefan Schuppler[2,3] Amir Ghiami[2,3], Ruslan Ovsyannikov[4], Erika Giangrisostomi[4], Thomas Chassé[1], Marcus Scheele[1,], Heiko Peisert[1,*]*

[1] Institut für Physikalische und Theoretische Chemie, Universität Tübingen, 72076 Tübingen, Germany

[2] Institute for Quantum Materials and Technologies (IQMT), Karlsruhe Institute of Technology (KIT), 76021 Karlsruhe, Germany

[3] Karlsruhe Nano and Micro Facility (KNMFi), Karlsruhe Institute of Technology, 76344 Eggenstein-Leopoldshafen, Germany

[4] Institute for Methods and Instrumentation for Synchrotron Radiation Research, Helmholtz-Zentrum Berlin für Materialien und Energie GmbH, 12489 Berlin, Germany

[#] These authors contributed equally (P.H., E.J.).

[*] Corresponding author, heiko.peisert@uni-tuebingen.de, Tel.: (+49) 07071 / 29-76931, Fax: (+49) 07071 / 29-5490 and marcus.scheele@uni-tuebingen.de

3.3.1 Abstract

Heterostructures consisting of transition metal dichalcogenides (TMDCs) and organic molecules are currently of enormous interest for a variety of applications. Comparably weakly interacting molecules, like phthalocyanines, exhibit a high potential for tuning of electronic properties of TMDCs. Knowledge of the molecular orientation is a prerequisite for the understanding of the nature and strength of the interfacial interaction. We study the molecular orientation of cobalt phthalocyanine (CoPc) and perfluorinated cobalt phthalocyanine ($CoPcF_{16}$, also denoted $F_{16}CoPc$), on both large molybdenum disulfide (MoS_2) single crystals and small MoS_2 flakes, using synchrotron-based techniques: X-ray absorption spectroscopy (XAS) at the Co L_3 edge, and spectromicroscopy in a photoemission electron microscope (PEEM). We show that the orientation can be radically different on both substrates. Whereas on large crystals an almost flat-lying orientation is observed, significant tilt angles were found on smaller flakes. It is proposed that the orientation depends crucially on the number of MoS_2 layers and/or the smaller size of atomically flat terraces on flakes compared to bulk crystals.

3.3.2 Introduction

Due to their remarkable physical and chemical properties, layered transition metal dichalcogenides (TMDCs) are a promising class of materials for future applications in modern semiconductor devices for electronics, lighting, solar energy, and communication. In particular, it is expected that these materials will enable the further miniaturization of electronic devices according to Moore's law[169, 170] and promote the establishment of flexible electronic devices.[171] The layered structure allows for the exfoliation down to two-dimensional layers with unique electronic properties compared to their bulk counterparts; in the case of MoS_2, the nature of the band gap changes from direct to indirect.[102, 172, 173] Especially, TMDC monolayers and heterostructures are of interest for a broad variety of devices.[105, 170, 174, 175]

One approach for tuning of electronic properties is the formation of TMDC/organic semiconductor heterostructures. Recent research on conjugated organic molecule/TMDC interfaces has been mainly focused on strong molecular electron acceptors.[106-109] However, weaker interacting, physiosorbed organic molecules may also interact with TMDCs. Such systems are expected to offer new opportunities for tuning both optical and electronic characteristics.[176] For example, a quenching of the

low-temperature defect photoluminescence of MoS_2 was observed after the adsorption of metal-phthalocyanines, depending strongly on the central metal atom of the phthalocyanine.[129] The nature of such interactions is currently being increasingly discussed,[177] and one crucial parameter in this regard is the orientation of the molecules with respect to the substrate surface. For example, the coupling between nickel phthalocyanine (NiPc) and graphene is supported by the flat geometry of the NiPc complexes.[178] Especially for anisotropic organic semiconductor films, the orientation of the individual molecules at the heterostructure is of particular significance, since it influences the electronic properties of the film and, therefore the overall interaction at the interface.[179, 180]

We study the molecular orientation of cobalt phthalocyanine (CoPc) and perfluorinated cobalt phthalocyanine ($CoPcF_{16}$) on MoS_2 bulk crystals and on exfoliated pieces, often called flakes, which have fewer and even monolayer thickness — a system, where weak interactions at interfaces (i.e., the absence of an integer charge transfer) can be expected. Representatives of the family of transition metal phthalocyanines (TMPcs) were chosen due to their advantageous chemical and physical properties, including stability, film growth, and tunability of electronic parameters due to the variation of the central metal and the selection of the peripheral substituents.[181-184] Fluorination of the Pc moiety increases the ionization energy by more than 1 eV,[21, 185-187] which may significantly affect electronic interactions at interfaces, even in the case of metal surfaces passivated by graphene.[188] Numerous studies on the growth of phthalocyanines were carried out on a broad variety of substrates. On single-crystalline substrates, the almost planar phthalocyanine molecules typically prefer a predominantly flat-lying orientation (see, e.g., Refs.[18, 122, 130, 181, 189-192]), this includes also van der Waals substrates like GeS or MoS_2, and graphene-covered metal substrates.[18, 122, 130, 190, 192] In contrast, on polycrystalline substrates, the molecular orientation can be radically different, depending crucially on the substrate roughness.[189, 190] The different growth modes observed on various substrates can be understood in terms of different molecule-substrate and molecule-molecule interactions at the interface.[189, 193-195] In conclusion, higher tilt-angles for phthalocyanines on single crystals were in particular found if the molecule-substrate interaction is weaker, e.g., for van-der-Waals solids or passivated semiconductor surfaces.[130, 196]

In this study, we demonstrate that the orientation of CoPc and $CoPcF_{16}$ on molybdenum disulfide flakes can diverge from that on the bulk MoS_2 single crystal. Therefore, the prediction of the molecular orientation on thin flakes from literature data obtained with bulk crystals only could be misleading for differing structural situations.

3.3.3 Experimental

Cobalt phthalocyanine (CoPc, Sigma-Aldrich Chemie GmbH) and perfluorinated cobalt phthalocyanine ($CoPcF_{16}$, Sigma-Aldrich Chemie GmbH) were deposited on synthetic bulk 2H-phase MoS_2 (2D Semiconductors Inc. USA) by thermal evaporation under ultra-high vacuum (UHV) conditions (base pressure about $1 \cdot 10^{-9}$ mbar). The evaporation chamber was directly attached to the spectrometer chamber. The nominal film thickness was determined using a quartz crystal microbalance (QCM), setting the mass density of CoPc and $CoPcF_{16}$ at 1.6 g/cm^3 and 2.0 g/cm^3, respectively,[197, 198] and checked by the comparison of X-ray photoelectron spectroscopy (XPS) peak areas for bulk MoS_2 sample experiments.

For the studies on bulk MoS_2, the crystals were cleaved by adhesive tape in UHV. No further annealing was performed. The cleanliness was checked by XPS. These experiments were conducted at the PM4 beamline of the BESSY II electron storage ring operated by the Helmholtz-Zentrum Berlin (HZB) using the LowDosePES endstation.[30] Polarization-dependent X-ray absorption spectroscopy (XAS) measurements at the N K and Co L edges were carried out in total electron yield mode, measuring the sample drain current and orienting the sample at different polar angles with respect to the incoming beam of fixed horizontal polarization. The correction for beamline characteristics of the photon flux was carried out using the drain current from the last beamline mirror, or XAS spectra of pristine gold substrates. The XAS spectra were normalized to the same step height, well above the absorption edge.

For determining the orientation of CoPc and $CoPcF_{16}$ on MoS_2 flakes, laterally resolved spectromicroscopy experiments in a photoemission electron microscope (PEEM) were conducted at the Institute for Quantum Materials and Technologies soft x-ray beamline WERA at the KIT Light Source, Karlsruhe, Germany. The degree of linear polarization was set to nominal values between 72 and 93%, all giving sufficient orientational contrast of the Co L edge with photon energies between 770 eV – 800 eV. The energy resolution was set to 490 meV. The PEEM (FOCUS GmbH) has an integrated sample

stage (IS), an imaging energy filter (IEF) using a retarding field, and operates in a fixed geometry; the angle between the p-polarized incident photon beam and the normal of the sample was 65°. Since the fixed geometry does not allow a direct determination of the molecular orientation, the adsorption geometry was estimated from the known angular dependence of polarization dependent XAS spectra (measured, for example, on bulk MoS_2). Flat and dark field corrections were considered in the post-processing of the measured image stacks. The incident photon flux was monitored using a clean gold mesh.

Ultraviolet photoelectron spectroscopy (UPS) measurements at our laboratory spectrometer were performed inside a multichamber UHV system (base pressure of $1 \cdot 10^{-9}$ mbar) equipped with an ultraviolet source (UVS 300, Specs) and a Phoibos 150 hemispherical photoelectron analyzer (Specs). The energy calibration was performed using argon-sputtered and annealed Ag foils at the Fermi edge. The energy resolution was 150 meV.

MoS_2 flakes, containing regions with varying numbers of layers, were prepared ex-situ for PEEM measurements using the top-down scotch tape method, starting with synthetic bulk MoS_2 (2D Semiconductors Inc., USA).[199] Since MoS_2 crystals used for both exfoliation and experiments on bulk MoS_2 were purchased from the same company, we assume a similar quality of MoS_2 layers for both types of experiments. Exfoliated flakes were transferred onto a polydimethylsiloxane stamp (PF Gel Film®, Teltec GmbH). The stamp is pressed onto substrates, leaving thin-layers of TMDC on them. As substrates we used commercially available silicon wafers. Part of the silicon wafers were coated with 50 nm of titanium at an evaporation rate of 0.1 nm/s, determined by QCM, and used after exposure to environmental conditions as a substrate for the transfer of the flakes. The XPS analysis reveals that the native oxide covers the surface completely; no metallic Ti was detectable. To fit the dimensions of the PEEM sample holders, 7.5 x 7.5 mm substrates were cut from these wafers. Native titanium oxide and silicon oxide layers were found on both surfaces, as evidenced by photoemission measurements (**Figure S14** – **Figure S16**, Appendix C). The substrates were ultrasonically cleaned with a solvent cascade, starting with acetone, followed by hexane, ethyl acetate, and isopropanol. As a final cleaning step, the substrates were placed in a UV oven (Photo Surface Processor PL16-110B-1, Sen Lights Corp) for 15 minutes. Successful transfers of the MoS_2 flakes were evaluated

by optical microscope images. Those images were taken with an Olympus BHM microscope equipped with an EOS600D camera (Canon) and a NeoDPlan 50 (Olympus) objective. As this preparation method yields a large number of flakes with different thicknesses on the substrates, we selected the most promising ones based on contrast assessments. The images of the flakes selected for later experiments are shown in **Figure 33 a-c**. Prior to the deposition of phthalocyanines, the samples were annealed under UHV conditions to 250 °C for 12 h to remove contamination from preparation and ensure a clean surface, as verified by PEEM measurements (see **Figure S14** – **Figure S16**, Appendix C).

For the evaluation of the PEEM results and optical microscopy images, we used the software ImageJ/Fiji[200, 201] with the plugin FeatureJ from Erik Meijering.

3.3.4 Results and Discussion

Polarization-dependent X-ray absorption spectroscopy (XAS) offers an optimal method for studying the adsorption geometry of molecular adsorbates.[29, 189] For the planar TMPcs having D4h symmetry, both **1s**-π* or **N***1s*-π* excitations are suitable for determining molecular orientation.[189] If the electric field vector of the incoming light is oriented parallel to the atomic p_z wave functions forming the molecular π* orbital (i.e., out of the molecular plane), the absorption is maximal. In contrast, the transition is forbidden in the case of a perpendicular orientation.[29, 202] However, in our case, the analysis of N K edge absorption spectra is hindered by the overlap with features from the MoS_2 substrate. An example of a N K edge spectrum of a $CoPcF_{16}$ monolayer in superposition with Mo $M_{3,2}$, is shown in **Figure S17 a** (Appendix C) and for a thicker $CoPcF_{16}$ film in **Figure S17 b**. Also, the analysis of the C K edge is very difficult due to common carbon contaminations of beamline components and residual carbon in *ex-situ* prepared samples, especially for monolayer coverages. However, Co L edge XAS spectra also show a pronounced angular dependence (see, e.g., Refs.[18, 164]). They are determined to a large extent by multiplet effects due to the strong overlap between core level and valence wave functions.[203] Nevertheless, in-plane and out-of-plane transitions can be distinguished (for details, we refer to the literature, e.g. Refs.[204, 205]). In the following, we will use the shape of the Co L_3 XAS spectra for the estimation of the molecular orientation. We note that the shape of these spectra is almost independent on the fluorination of CoPc (see, e.g., Refs.[18, 164]).

In **Figure 32**, polarization-dependent Co L_3 edge spectra of (**Figure 32 a**) $CoPcF_{16}$ and (**Figure 32 b**) CoPc on bulk MoS_2 are shown for two different film thicknesses, measured at two different incidence angles of the p-polarized light. Transitions polarized perpendicular to the molecular plane (z-polarized) are denoted A, whereas B features are polarized within the molecular plane (xy-polarized). Consistent with the considerations above, the intensity of the out-of-plane feature A is maximal close to grazing incidence (20°), whereas the in-plane transitions B are most intense at normal incidence (90°). This indicates a preferred orientation of the molecule parallel to the substrate surface (referred to as face-on). The spectral shape of the Co L_3 edge is almost identical for the coverage in the monolayer range (0.34 nm) and the multilayer film, indicating that the orientation of the first molecular layer is maintained in the thin film. This behavior on bulk MoS_2 substrates is identical for CoPc and $CoPcF_{16}$. A more detailed comparison of the spectral shapes in **Figure 32** with literature data (e.g., Refs.[18, 164, 206]) reveals that tilt angles between the molecules and the substrate surface are rather small or even negligible. Thus, we can conclude that an orientation close to a face-on configuration of CoPc and $CoPcF_{16}$ is favored on bulk MoS_2.

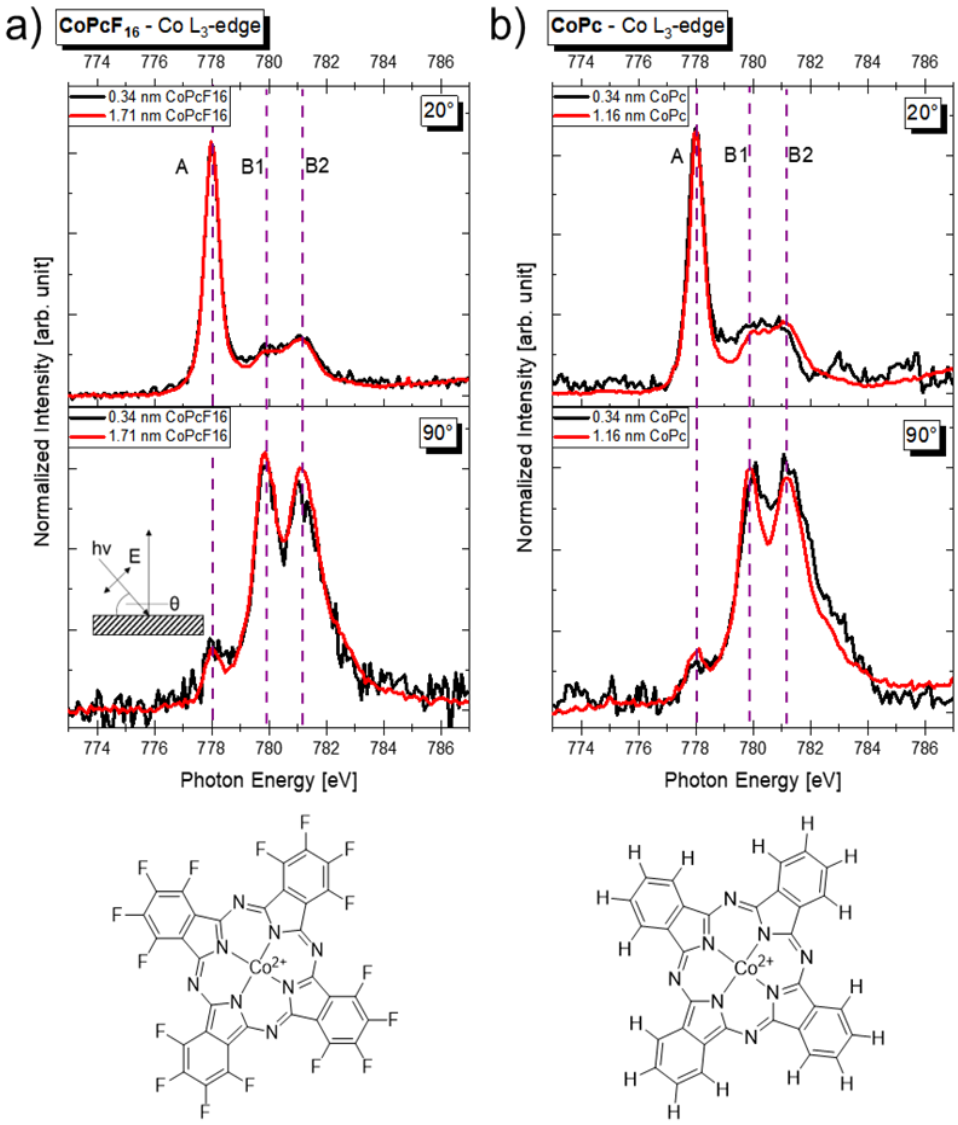

Figure 32 Angle-dependent XAS measurements in the Co L_3 region show intensity differences of features A and the two B features depending on the orientation of the electric field with respect to the sample for $CoPcF_{16}$ shown in (**a**) and CoPc shown in (**b**) on bulk MoS_2, with the respective structural formula below each spectrum.

The observed predominant face-on alignment of cobalt phthalocyanines is in good agreement with related systems, such as the previously studied $FePc(F_x)$ molecules on MoS_2.[122] However, it is essential to recognize that this orientation could be influenced by numerous factors on more frequently studied MoS_2 samples, like, e.g., 2D layers or flakes. For instance, the roughness of the substrate surface and the size of its atomically flat terraces can significantly impact the alignment of molecules.[189] This leads to the question whether the determined molecular orientation of cobalt phthalocyanines on bulk MoS_2 applies also to smaller MoS_2 flakes, which are of

particular interest for applications. Due to the small dimensions of the MoS_2 flakes, a microscopic technique is needed. A certain PEEM measurement mode, spectromicroscopy, is particularly useful here. Spectromicroscopy essentially means taking stacks of PEEM images while scanning the incoming photon energy or the kinetic energy of the emitted electrons. By tracing a pixel (or lateral region) through the image stack the former yields laterally resolved (μ-)XAS spectra, the latter laterally resolved (μ-)PES spectra. The resulting local spectra can be summed over regions of interest (RoIs) with freely defined shapes as applied on measurements discussed in the following. In particular, microscopic measurements of the work function contrast have proven to be a very sensitive method for distinguishing monolayer and few-layer regions of TMDC flakes.[207-209]

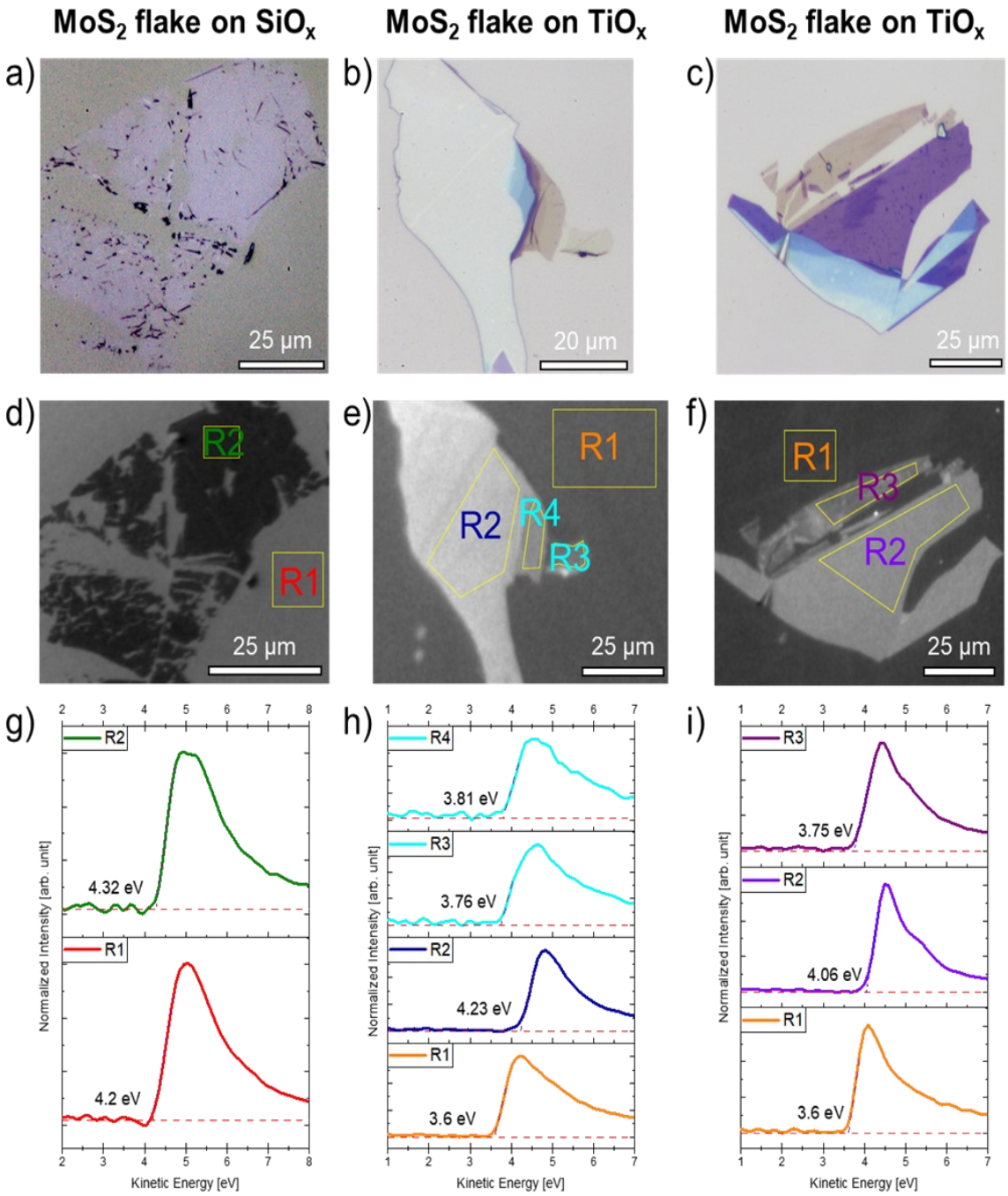

Figure 33 (**a – c**) Optical microscope images of MoS_2 flakes on SiO_x (**a**, flake 1) and on TiO_x substrates (**b**) and (**c**)**,** flake 2 and flake 3 respectively. Averaged images of the work function contrast sequence for the samples containing flake 1, flake 2 and flake 3 are shown in (**d**), (**e**) and (**f**) respectively. The grayscale is arbitrary to maximize contrast. (**g** – **i**) µ-PES spectra of the secondary electron cutoff and the calculated work functions.

In **Figure 33**, we show optical microscopy images, PEEM images, and corresponding μ-PES spectra of the secondary electron cutoff. In the following, we will refer to the flake on the oxidized silicon substrate (**Figure 33 a, d**, and **Figure S14**) as flake 1, while the two flakes on the oxidized titanium substrates are referred to as flake 2 (**Figure 33 b, e**, and **Figure S15**) and flake 3 (**Figure 33 c, f**, and **Figure S16**).

An initial indicator for estimating the number of layers can be provided by optical microscopy images. Differences in contrast between the substrate and the various layers in the flake (**Figure 33 a–c**, **Figure S18**, and **Figure S19**) can be used to estimate the number of layers.[210, 211] A detailed analysis of the red channel of optical microscope images (cf. **Figure S18**, Appendix C) reveals a distinct difference between regions R3, which is assumed to be a single MoS_2 layer based on the photoluminescence,[6, 8] and R4 in **Figure 33 e**.

Furthermore, we will discuss the work function contrast of selected MoS_2 flakes prepared on naturally oxidized silicon and titanium substrates. **Figure 33 e-i** show PEEM images (the total diameter of the field of view is 126 μm for the measured circular images; the figures shown are cutouts, and the scales are adjusted accordingly) together with the normalized μ-PES spectra of the secondary electron cutoff. Generally, differences in intensity of PEEM images are attributable to secondary electrons and, to a lesser extent, spectral features. Regions of interest (denoted R1 – R4 in **Figure 33**) were selected based on previously acquired optical microscope images and observable color variations (**Figure 33 a-c**). Average spectra in **Figure 33 g-i** were generated over all pixels in the chosen regions marked in **Figure 33 d-f**. For a better comparison of the work functions, we measured the secondary electron cutoff from the pure substrates with UPS at our laboratory spectrometer. We found a work function of 4.2 eV for the silicon and 3.6 eV for the titanium substrates, respectively (**Figure S20 g**). This difference is in good agreement with literature data and the relative differences we found in our PEEM measurements on the substrate regions (**Figure S20 d-f**), marked R1 in each experiment. Therefore, we referenced the measured work functions of the substrate regions R1 to the values measured in the UPS experiments on the bare substrates. The energy scales of the MoS_2 flake regions are based on this calibration procedure.

We find almost the same work function for the pristine titanium substrate regions (R1) for the measurements containing flake 2 and flake 3, and a higher work function for the

silicon substrate region containing flake 1. A comparably high work function F is expected for MoS_2; a value of 5.4 eV was recently reported for single-crystalline bulk substrates.[122] However, for monolayer or few-layers on oxidized silicon, significantly lower values were observed (F ~ 4.5 eV) by both PEEM and Kelvin probe force microscopy (KPFM).[208, 212-214] We note that KPFM measures relative work functions, which may complicate a direct comparison of absolute values. Furthermore, a comparison to literature data has to take into account difference in the preparation method, the influence of contaminations in the case of measurements under ambient conditions,[212] as well as the choice of the substrate, which may alter the work function of MoS_2 flakes by several tenths of eV.[213] However, and most importantly, all methods agree in that the work function increases from single to few-layer MoS_2.[208, 213, 214] Using PEEM under UHV conditions, for MoS_2 on oxidized silicon differences of 60 meV and 80 meV were observed form 1 to 2 and 2 to3 monolayers, respectively. Thus, the lower work function of regions R3 and R4 in **Figure 33 b, c** clearly indicates a lower number of MoS_2 layers.

From these investigations, we estimate that flake 1 on the oxidized silicon substrate is a bilayer, region R3 of flake 2 on oxidized titanium is a monolayer, and region R4 is a trilayer. For region R3 of flake 3, we estimate it to consist of four layers. We note that this estimation is associated with a high degree of uncertainty. However, we were able to prepare samples that exhibit regions with a few layers of MoS_2, as well as thicker, bulk-like regions (R2 in **Figure 33 e** and **f**).

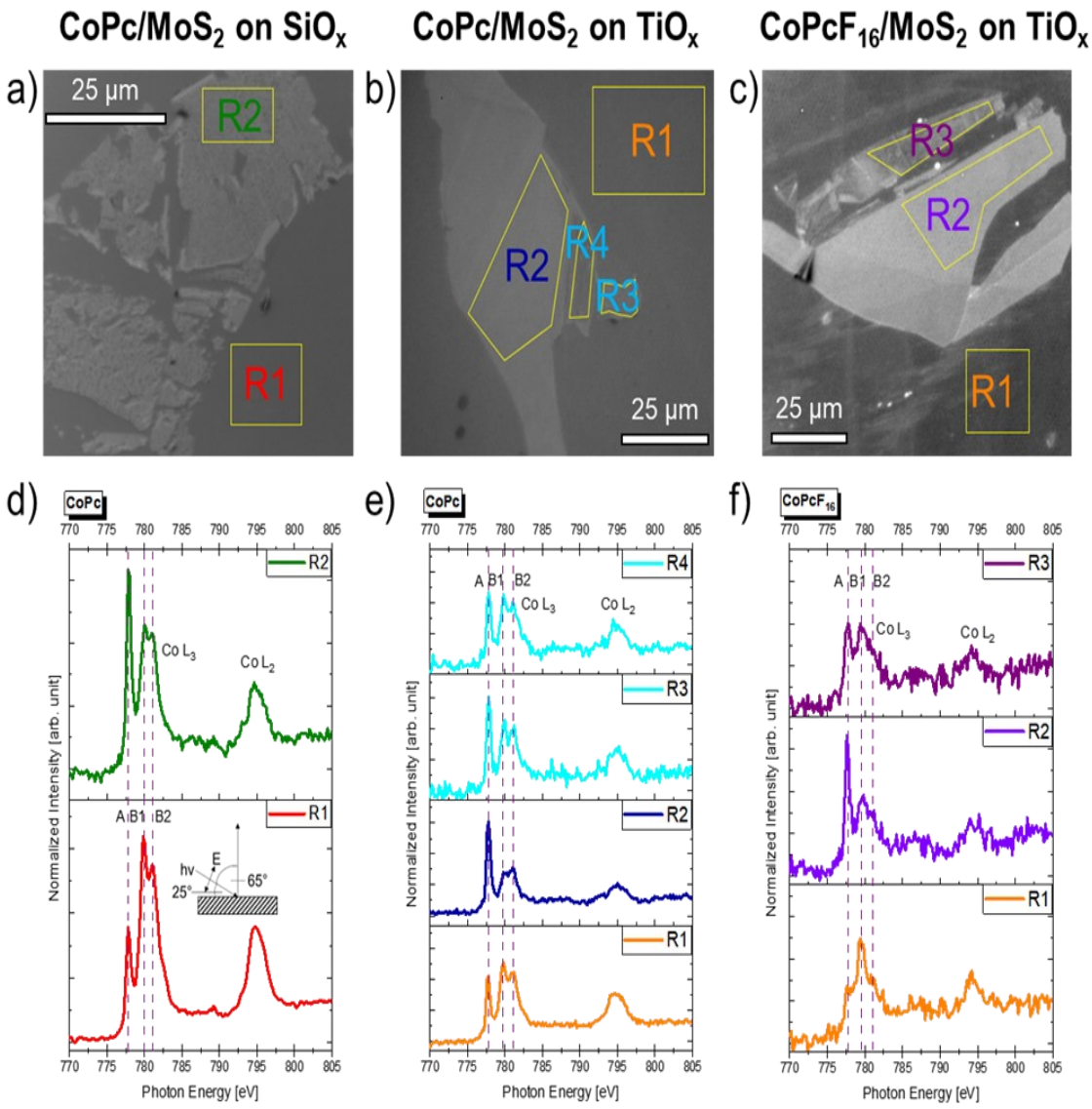

Figure 34 PEEM XAS measurements at an incident angle of 25° in the region of the Co L edge. (**a – c**) show average intensity images with an arbitrarily chosen grayscale to maximize contrast. Intensity differences are mostly based on secondary electron counts and to a lesser extent on spectral features. Selected regions of interests in these images are like those chosen for work function contrast measurements shown in **Figure 33**. (**d – f**) show the normalized spectra of the respective RoI for the flakes 1 – 3 above.

In a next step, we deposited CoPc on the samples containing flakes 1 and 2, and $CoPcF_{16}$ on the sample containing flake 3 and measured PEEM-XAS in the Co $L_{3,2}$ region. According to the QCM data, the thickness was in the monolayer range. The corresponding PEEM images, together with the averaged Co $L_{3,2}$ edge spectra of the

selected regions, are shown in **Figure 34**. The XAS spectra in **Figure 34 d-f** were obtained by the analysis of PEEM images taken at different excitation energies. Generally, the XAS features discussed in **Figure 32** are also visible in the µ-XAS spectra of **Figure 34**. Due to the fixed measurement geometry, all spectra were taken at an incident angle of 25° with respect to the surface of the sample. This is relatively close to the grazing incidence angle for the measurements of CoPc and $CoPcF_{16}$ on bulk MoS_2 single crystals (20°). Thus, for preferred predominantly flat-lying molecules only a slight increase in the relative intensity of the in-plane polarized features B1 and B2 might be expected compared to bulk MoS_2 single crystals, discussed in **Figure 32** (cf., e.g., Refs.[18, 206] for the angular dependence of Co L_3 spectra). A further reason for a slightly increased intensity of B1 and B2 could be a different degree of the polarization of the synchrotron light. Considering these minor technical limitations, the µ-XAS spectra of CoPc and $CoPcF_{16}$ on large MoS_2 terraces (R2) in **Figure 34** are very similar to the related spectra on bulk MoS_2 single crystals at grazing incidence (20°) in **Figure 32**. In both cases, the out-of-plane polarized feature A clearly dominates the spectrum. In contrast, on the oxidized silicon and titanium surfaces (regions R1 in **Figure 34**), the molecules grow obviously in a different manner: The dominating in-plane features B1 and B2 indicate a preferred standing (edge-on) adsorption geometry, which can be related to the weaker molecule-substrate interaction with increasing (micro-)roughness of the substrates (i.e., the substrates are not atomically flat). Such effects were reported for different molecules (see, e.g., Refs.[189, 193]). Most importantly, the ratio of A/B intensities of the Co L_3 spectra for the regions R3 (flake 2 and flake 3) and R4 (flake 2) deviate distinctly from the regions R2 of the MoS_2 flakes on oxidized titanium (**Figure 34 e** and **f**), indicating significant tilt angles of the molecules to the surface plane or a disordered growth. This effect is observed to some weaker extent also in the region R2 on oxidized silicon (**Figure 34 d**), where **Figure 34 a** suggests a more inhomogeneous MoS_2 layer. The regions R3 (flake 2 and flake 3) and R4 (flake 2) are characterized by i) a lower number of MoS_2 layers and ii) by a smaller size compared to regions R2. Both could affect the molecular orientation of the deposited CoPc or $CoPcF_{16}$ molecules. The lower number of MoS_2 layers may affect the surface energy of the substrate, and the flexibility of the thin-layer MoS_2 may cause a certain corrugation due to the alignment at the substrate surface. The small lateral size of the thin MoS_2 regions might limit the favorable flat-lying adsorption geometry to a certain number of molecules, and step-edge effects might become important. Another factor

that can influence the surface energy, and consequently molecule-substrate interactions, particularly in mechanically exfoliated flakes of MoS_2, is defects.[215] Further investigation is needed to understand the different adsorption geometry of Co phthalocyanines on smaller MoS_2 terraces.

3.3.5 Conclusion

In conclusion, we found that the orientation of cobalt phthalocyanines on small-sized thin-layers of MoS_2 flakes is significantly different compared to bulk MoS_2. This demonstrates that the molecular orientation on small sized (mono- to few-layers) TMDC flakes cannot be simply deduced from the orientation of organic molecules on related bulk substrates. For the understanding of electronic and optic interactions at such interfaces, different molecular orientations should be considered. From our perspective, this could also affect TMDC-based devices as the situation between electrodes with small distances could lead to a similar restricted situation, in particular if the evaporation of molecules occurs after the deposition of electrode structures. In addition, defects in the flakes and the high cleanliness of in situ cleaned substrates might be important. Although our studies are focused on monolayer coverages, more extended growth studies varying the temperature, film thickness, and deposition rate are of high interest. Also, a systematic variation of the lateral size of atomically flat MoS_2 terraces may help to understand the observations discussed in this study. Thus, further research is needed to reveal the exact underlying mechanism for the different molecular orientation on bulk MoS_2 and flakes.

3.3.6 Acknowledgments

The authors thank the Helmholtz-Zentrum Berlin (electron storage ring BESSY II) for provision of synchrotron radiation at the beamline PM4. Financial travel support by HZB is thankfully acknowledged. The authors are grateful to the KIT Light Source, Karlsruhe, Germany, for the provision of beamtime. The Center for Light-Matter Interaction, Sensors & Analytics (LISA+) at the University of Tübingen is acknowledged for technical support and Fabian Strauß for the preparation of the substrates. The work was supported by the German Research Council (PE 546/17-1, SCHE1905/9-1 (project no. 426008387)) and the European Research Council (ERC) under the European Union's Horizon 2020 research and innovation program (Grant Agreement 802822).

4 Conclusion

The studies presented in the preceding chapters investigate the interaction between organic molecules and inorganic semiconductors from various perspectives, with a particular focus on molybdenum disulfide (MoS_2) and cobalt phthalocyanines (CoPc and $CoPcF_{16}$). Collectively, they demonstrate how both the electronic properties and molecular orientation at organic–inorganic interfaces can be tailored through deliberate structural and chemical modifications. Across all studies, the targeted use of advanced analytical techniques, especially X-ray photoelectron spectroscopy (XPS) and X-ray absorption spectroscopy (XAS), together with thorough analysis of the resulting data, has been instrumental in advancing our understanding.

The studies presented in this dissertation collectively explore colloidal molybdenum disulfide and, to a greater extent, how the interaction between cobalt phthalocyanines and molybdenum disulfide can be controlled and understood at both electronic and structural levels. Although the colloidal synthesis itself was not carried out by me, my contribution focused on the in-depth characterization of the reaction products using X-ray photoelectron spectroscopy (XPS). These measurements enabled both a qualitative and quantitative assessment of the ratio between the metallic 1T and the semiconducting 2H phase of MoS_2, providing valuable insight into phase transformation mechanisms and phase control in transition metal dichalcogenides (TMDCs). Across all studies, advanced analytical techniques, including XPS, UPS, ARPES, and XAS, were applied to both molecular beam epitaxy-grown and solution-processed samples. This approach revealed how the crystal structure and excitonic properties of MoS_2, as well as the doping behavior and molecular orientation of CoPc derivatives, can be systematically tailored. Comparative studies between CoPc and its perfluorinated counterpart $CoPcF_{16}$ demonstrated that even minor chemical modifications can lead to fundamentally different interfacial electronic structures: CoPc induces band bending and n-type doping, whereas $CoPcF_{16}$ leads to the formation of localized gap states that shift the Fermi level toward p-type behavior. Additionally, it was shown that substrate morphology has a decisive impact on molecular orientation: CoPc adopts a flat-lying (face-on) configuration on bulk MoS_2, but a tilted geometry on exfoliated few-layer flakes. These results have important implications for charge transport across hybrid interfaces. Altogether, the findings contribute to a deeper

understanding of organic–inorganic heterostructures and open new pathways for tailoring interface functionality in future optoelectronic devices.

Looking ahead, several open questions remain and should be addressed in future research. While this dissertation has advanced our understanding of the interaction between cobalt phthalocyanines and molybdenum disulfide, it has also emphasized the central role of energy level alignment in determining interface properties. Here, phthalocyanines and TMDCs offer vast untapped potential for further optimization, both classes of materials can be chemically modified or combined in new ways to achieve tailored heterojunction properties. Moreover, the insights gained in this work have not yet been transferred to functional optoelectronic devices. For example, the development and investigation of optical switches based on MoS_2 heterostructures that are selectively modified with cobalt phthalocyanines is ongoing and remains an active area of research.

5 Collaborations

During my doctoral research, I specialized in photoelectron spectroscopy (PES), a technique indispensable for the comprehensive analysis of various sample types. Despite its labor-intensive nature and the requirement for extensive technical and physical knowledge for both execution and interpretation of experiments, my proficiency in PES led me to become a primary resource for related inquiries. This expertise facilitated numerous collaborative projects, resulting in several publications to which I have significantly contributed.

This thesis compiles all publications up to the present date. Given the extensive scope of each study, a detailed discussion of each is beyond the remit of this work. Therefore, I have structured the subsequent chapters to include only the abstracts and a summary of my contributions to these publications, with one notable exception. Chapter 5.1 is dedicated to an in-depth XPS study of $CsPbBrI_2$ nanocrystals, conducted in collaboration with Dr. Jan Wahl. This work represents a significant milestone in my research career, and as such, it is presented in full detail in this chapter.

5.1 Mitigating the Photodegradation of All-Inorganic Mixed-Halide Perovskite Nanocrystals by Ligand Exchange

Jan Wahl,[,1] Philipp Haizmann,[*,1] Christopher Kirsch,[1] Rene Frecot,[1] Nastasia Mukharamova,[2] Dameli Assalauova,[2] Young Yong Kim,[2] Ivan Zaluzhnyy,[3] Thomas Chasse,[1,4] Ivan A. Vartanyants,[2] Heiko Peisert[#,1] and Marcus Scheele[#,1]*

[1] Institut für physikalische und theoretische Chemie, Universität Tübingen,

Auf der Morgenstelle 18, 72076 Tübingen, Germany

[2] Deutsches Elektronen-Synchrotron DESY, Notkestraße 85, 22607 Hamburg, Germany

[3] Institut für Angewandte Physik, Universität Tübingen, Auf der Morgenstelle 10, 72076 Tübingen, Germany

[4] Center for Light-Matter Interaction, Sensors & Analytic LISA$^+$, Universität Tübingen, Auf der Morgenstelle 15, 72076 Tübingen, Germany

[*] These authors contributed equally

[#] heiko.peisert@uni-tuebingen.de, marcus.scheele@uni-tuebingen.de

5.1.1 Abstract

We show that the decomposition of caesium lead halide perovskite nanocrystals under continuous X-ray llumination depends on the surface ligand. For oleic acid/oleylamine, we observe a fast decay accompanied bythe formation of elemental lead and halogen. Upon surface functionalization with a metal porphyrin derivative, the decay is markedly slower and involves the disproportionation of lead to Pb^0 and Pb^{3+}. In both cases, the decomposition is preceded by a contraction of the atomic lattice, which appears to initiate the decay. We find that the metal porphyrin derivative induces a strong surface dipole on the nanocrystals, which we hold responsible for the altered and slower decomposition pathway. These results are important for application of lead halide perovskite nanocrystals in X-ray scintillators.

5.1.2 Introduction

Lead halide perovskites are an important class of materials for use in light harvesting and light emitting devices.[216, 217] Another promising application of perovskites is scintillators, where they have already shown good performance in X-ray detection.[218-220] However, the instability of perovskite-based materials is a significant drawback for the application in optoelectronic and scintillating devices. [219, 221-226] To address this issue, the photodegradation of methylammonium lead iodide ($MAPbI_3$) thin films has been thoroughly investigated, including the postulation of a decay mechanism.[227-229] Recently, these photodegradation studies have been extended to caesium mixed-halide perovskites ($CsPbX_3$)[230-232] in view of their improved stability against long-term light exposure.[233] However, even the most stable mixed halide perovskites, such as $CsPbBrI_2$, undergo slow photodegradation in intense visible light.[230-232] The aim of this work is to use the tunable surface chemistry of nanocrystals (NCs) to further mitigate this instability with a particular focus on photodegradation with X-ray photons to aid the application in scintillators.[223, 228] To this end, we introduce zinc-(5-monocarboxyphenyl-10,15,20-triphenylporphyrin) (mZnTPP) as surface ligand and investigate its effect on the decomposition of the NCs under X-ray illumination. As NCs, we use two model systems, namely $CsPbBrI_2$ and $CsPbBr_2Cl$, based on their light emitting properties hereafter referred to as red and blue perovskites, respectively. If not explicitly stated otherwise, these NCs are surface-functionalized with oleic acid/oleylamine, referred here to as the ‘‘native ligand’’. As previously reported, perovskites experience drastic changes under continuous X-ray exposure.[234, 235] One analytical method that utilizes X-ray irradiation is X-ray photoelectron spectroscopy (XPS). Here, a sample is continuously irradiated with X-rays, and electrons, released from the sample due to the external photoelectric effect, are detected based on their kinetic energy. The core-level binding energy of an emitted electron is directly related to the detected kinetic energy. Previous XPS experiments on perovskites reported a shift of the binding energies to higher values with ongoing measurement time. This was mostly attributed to either surface, substrate or charging effects.[222] In this work, we observe a similar shift for the red and blue perovskite NCs. However, we demonstrate by a combination of XPS and wideangle X-ray scattering (WAXS) that the core-level energy shift originates from a contraction of the atomic lattice. For the red and blue perovskite NCs with native ligands, we find a similar decay mechanism as recently postulated for thin films.[232]

While morphology and chemical composition are maintained in the red perovskites, the blue perovskites exhibit a loss of chlorine and undergo recrystallization. Most importantly, we observe a greatly altered and slower decay mechanism after surface functionalization with the porphyrin derivative mZnTPP.

5.1.3 Results and Discussion

The decomposition of both perovskite systems was analyzed under continuous X-ray illumination for at least 20 h by XPS and ultraviolet photoelectron spectroscopy (UPS). Core level and valence spectra were recorded at regular time intervals. Exemplarily, spectra of **Pb*4f*** doublet peaks recorded at the beginning and end of the illumination are shown in **Figure 35 a** and **b**. The **Pb*4f*** main peak at a binding energy of 138.25 eV in Fig. **1a** corresponds to Pb^{2+} in the red perovskites. Over the course of this investigation, all samples, independent of stoichiometry and ligand shell, developed an additional Pb species visible in the corresponding **Pb*4f*** core level spectra of **Figure 35 a** and **b**. The signal occurred at lower binding energies (~137 eV), which indicates a lowering of the oxidation state. Therefore, and in agreement with literature, we attribute this peak to the formation of elemental lead (Pb^0).[222, 227, 236] The formation of the Pb^0 component is detected after illuminating the sample for few hours. The intensity of the Pb^0 peak increases continuously with time, the relative Pb^0/Pb^{2+} content as a function of the illumination time is summarized in **Figure S23** (Appendix D). After 20 h, we observe the formation of 13.2% Pb^0 for the red perovskites (**Figure S23**, Appendix D), we find strong changes in the core level spectra of the other halides, i.e., I^- for the red perovskites (**Figure 35 c**). We observe the formation of a distinct shoulder at high binding energy in the **I*3d*** region for the red perovskites, suggesting that I^- is indeed oxidized during the reduction of Pb^{2+} (**Figure 35 c**). By tracking the stoichiometric composition, we find the iodide content to stay constant throughout the experiment (**Figure 35 d**), suggesting that the new iodine/iodide species remains in the sample during the decomposition even in ultrahigh vacuum. To calculate the amount of the newly formed species, we determined the percentages of the same element from the fits of the detailed spectra. The atomic ratio of different elements was estimated from overview spectra, considering possible time-dependent variations of the excitation intensity. The peak areas were precedingly corrected with respective photoionization cross sections as described in the Experimental section in Appendix D Section S2.

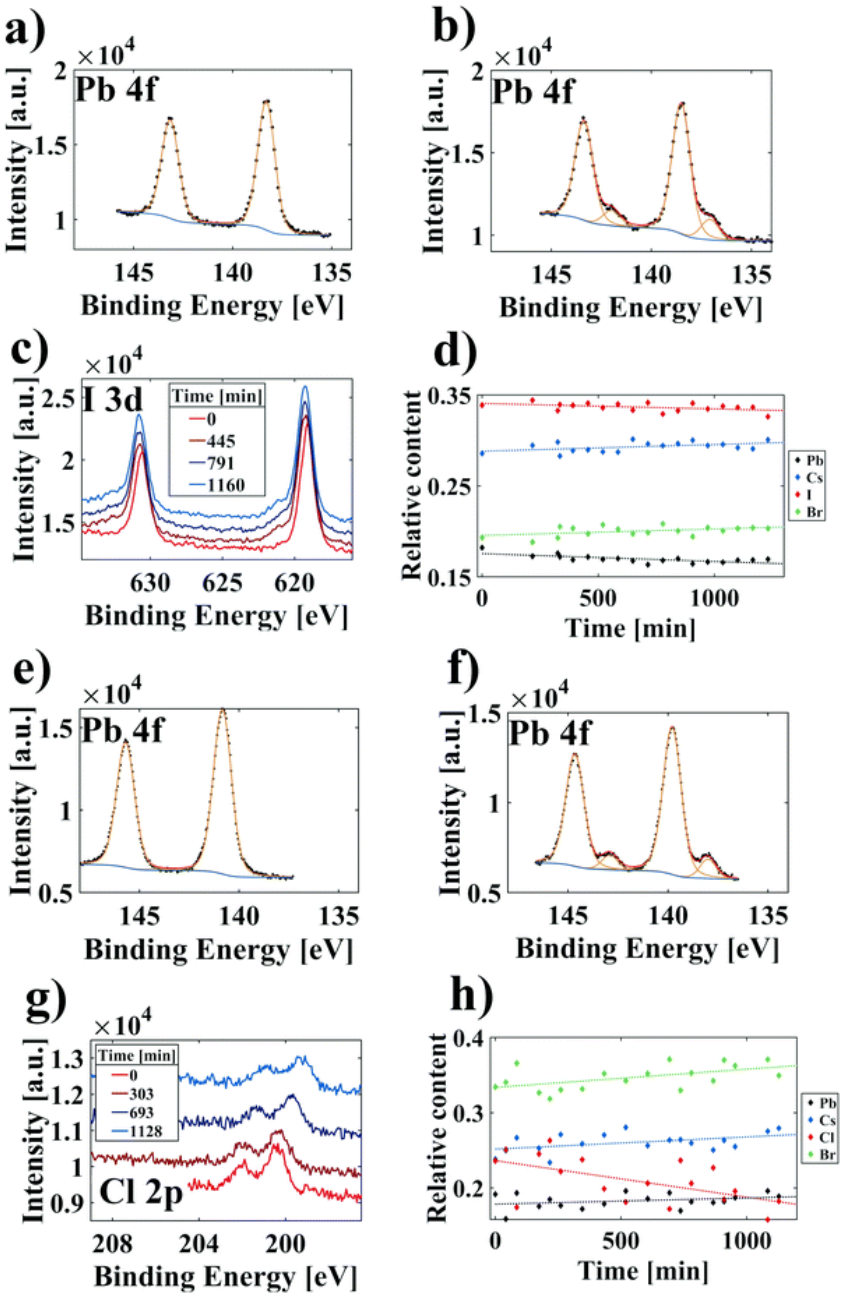

Figure 35 Pb4f core level XPS spectra of $CsPbBrI_2$ (**a**) at the start (0 min) and (**b**) after 1160 min of X-ray exposure. Fit components are shown in orange, the overall fit is depicted in red. All spectra were fitted by applying a Shirley-type background (blue). (**c**) **I***3d* spectra at different times during the illumination with the evolution of a shoulder at higher binding energy (621 eV). (**d**) Relative stoichiometric content and linear regression (dotted lines) during the exposure for $CsPbBrI_2$. **Pb***4f* spectra of $CsPbBr_2Cl$ (**e**) at the start (0 min) and (**f**) after 1128 min of exposure. (**g**) **Cl***2p* spectra (~200 eV) exhibit a decrease over time without the formation of a novel peak. (**h**) Relative stoichiometric content for $CsPbBr_2Cl$ during the experiment

We observed similar changes in the XPS core level spectra for the blue perovskites, e.g., the formation of Pb^0 (**Figure 35 e** and **f**), however to a lesser extent compared to the red perovskites. After 20 h of irradiation, a total of 10.2% Pb^0 was observed for the blue perovskites (**Figure S24**, Appendix D). Additionally, we measured a drastic decrease by ~ 20–25% (**Figure 35 h**) in the **Cl***2p* peak intensity, suggesting chloride as the redox partner for Pb^{2+} since this is roughly twice the amount of Pb^0 formed. Finally, the **Cs***4d* orbital was monitored and no formation of novel peaks could be observed (**Figure 35 d** and **h**), suggesting that Cs remains in a relatively stable environment in both cases.

We probed the morphology of both NC samples after X-ray exposure by scanning electron microscopy (SEM). While the red perovskites maintained the cubic, nanocrystalline morphology, the blue perovskites recrystallized to larger agglomerates (see **Figure S25**, Appendix D). Therefore, we determine the structure before (**Figure 36 a**) and after X-ray exposure by WAXS (**Figure 36 b**). (Note that the flux and exposure times during synchrotronbased WAXS are vastly different from those during XPS, and the cross-section is substantially higher for the XPS experiments with their lower photon energies, such that a quantitative comparison is not possible. We believe, however, that qualitative considerations may still be made.) We index the WAXS patterns observed here according to the cubic perovskite phase, although previous scattering experiments have shown a pseudocubic annotation to be more appropriate.[237, 238] However, the limited q-range and the broad reflections, which are typical for NCs, prevent such a refinement. From **Figure 36 b** one can see that one of the 200 peaks shifted to higher q values, while another remains at the same position. This indicates a contraction of this part of the sample. For further analysis, we integrate the diffraction maps over all angular coordinates to obtain an azimuthally-independent scattering pattern. In **Figure 36 c**, we display the differential intensity, obtained by subtracting the azimuthally integrated diffraction pattern after X-ray exposure from the first pattern. In this figure, positive differential intensities refer to reflections which weakened during X-ray exposure, while negative differential intensities indicate newly evolved reflections. From the differential pattern, a change of the lattice constant from 6.11 Å to 5.67 Å could be obtained (see **Figure 36 c** and Appendix D, **Figure S27**, for more details).

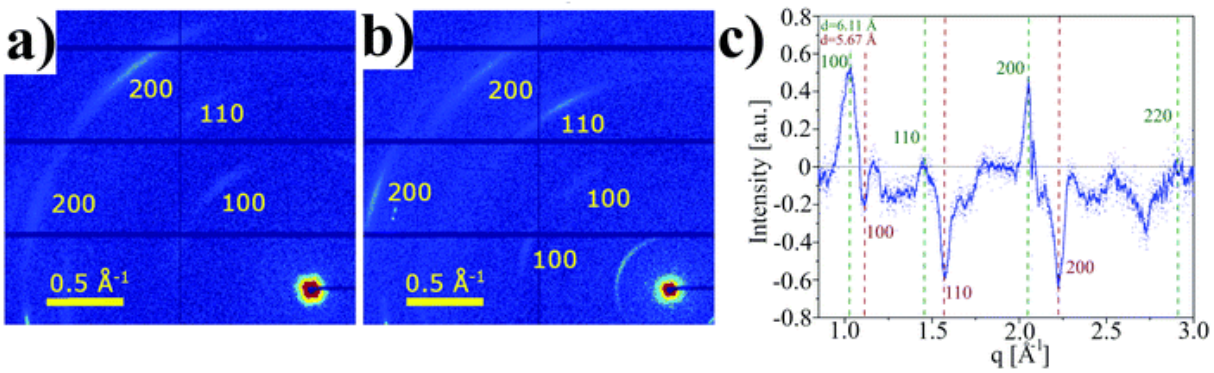

Figure 36 (**a**) First WAXS measurement of CsPbBrI2 nanocrystal superlattices and (**b**) subsequent measurement after the spot was already exposed to radiation. (**c**) Differential scattering intensity obtained by subtracting the azimuthally integrated diffraction pattern after X-ray exposure from the first pattern. Positive differential intensities refer to reflections which weakened during X-ray exposure, while negative differential intensities indicate newly evolved reflections. Indexing of old (green) and new (brown) peaks according to a cubic perovskite phase.

Upon exposing the red perovskites to X-rays during XPS, we observed a shift of all sample peaks to higher binding energies (**Figure 37**). We argue that this shift is not primarily caused by electric charging since (1) the **Au***4f* substrate peaks remain at constant energies throughout the experiment (**Figure 37 a** and **b**), (2) the perovskite films were rather thin to enable the release of a large number of secondary electrons from the Au substrate underneath to suppress charging,[239, 240] and (3) the magnitude of the shift of the sample peaks was different for different elements (**Pb***4f*: +0.63 eV, **Cs***4d*: +0.71 eV). The shifts remained constant after illumination for approximately 7 h (**Figure 37 c** and **d**).

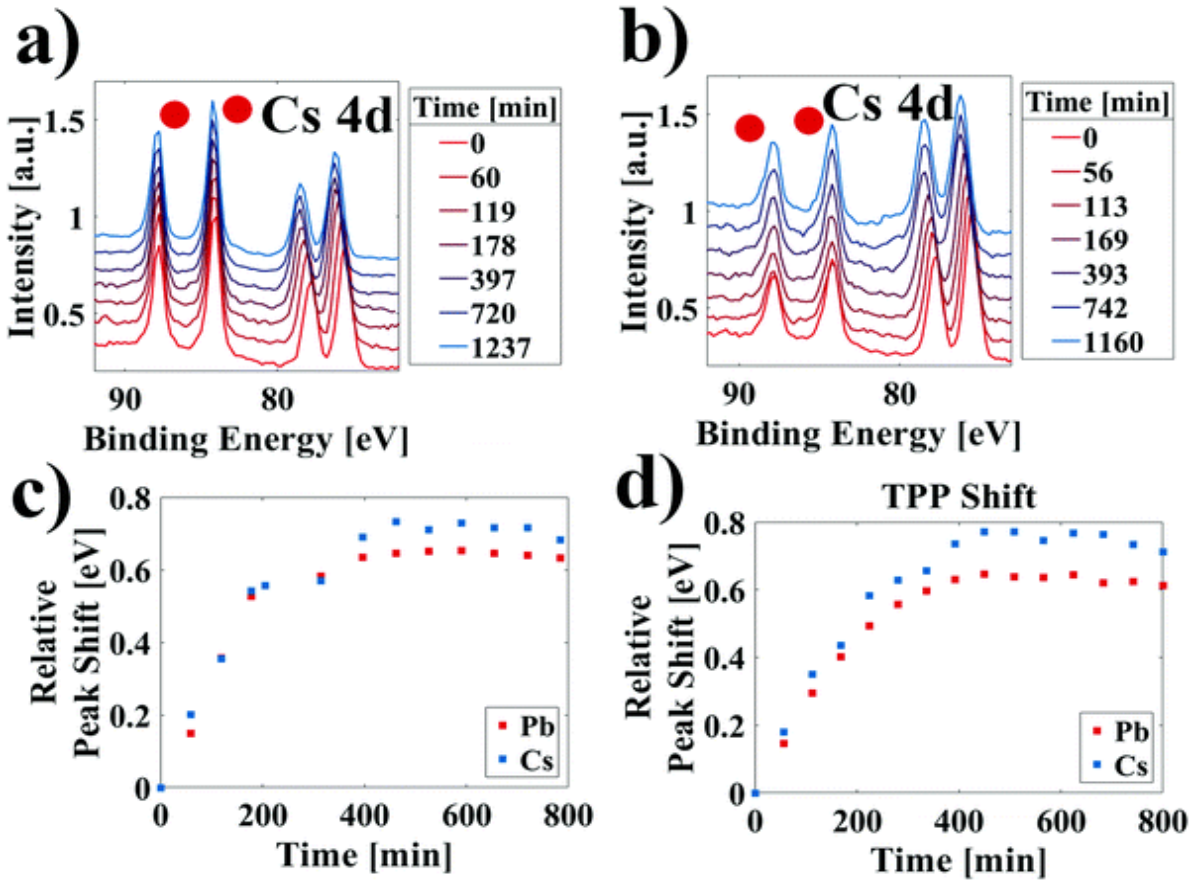

Figure 37 Cs*4d* (75 eV) and **Au***4f* (84 eV) XPS spectra for (**a**) native ligands and (**b**) mZnTPP exchanged samples after different X-ray radiation exposure times. The substrate-related Au signals are denoted by red dots and did not change throughout the experiment in both cases. Relative peak position of the **Pb***4f* and **Cs***3d* signals compared to the binding energy at the start of the experiment for (**c**) native and (**d**) mZnTPP exchanged samples.

We probed the influence of X-ray irradiation on the work function by measuring UPS before and after 20 h exposure (**Figure S26**, Appendix D). We find a shift of the high binding cutoff by 0.12 eV to higher energies, indicating a decrease of the work function. At the same time, the energy of the valence state maximum (*1s*h) referenced to the Fermi level remains constant (see **Figure S28**, Appendix D). These findings suggest that the energy levels of the nanocrystal are shifted by 0.12 eV toward the vacuum level.

Motivated by the previous finding that ligand exchange with mZnTPP can enhance the stability of red perovskites in light emitting devices,[241] we studied the effect of this ligand on the decomposition of the red perovskites under X-ray illumination. (Note: the

loss of structural integrity of the blue perovskites due to chlorine evaporation did not allow for an analogous analysis.) With the mZnTPP ligand shell, we again found the formation of Pb^0, but its formation is slower and yields only 8.1% compared to 13.2% after 20 h for the native ligand. An additional lead species occurred at higher binding energy for this ligand at ~ 140.9 eV, indicating a higher oxidation state than Pb^{2+} (**Figure 38 a** and **b**). The intensity ratio between this new peak and the evolving Pb^0 peak in the **Pb*4f*** spectrum is roughly 2 : 1 for all irradiation times, implying that their formation is correlated (**Figure 38 e**). In contrast to the sample stabilized with the native ligand (cf. **Figure 35**), we did not find a similar shoulder in the iodide signal (Appendix D, Section S7), suggesting a different decomposition mechanism as a result of the ligand exchange. Before investigating this mechanism in more detail, we verify by SEM the structural integrity of the mZnTPP stabilized red perovskites after X-ray exposure (**Figure 38 c**) and note that the stoichiometric composition remained roughly constant (**Figure 38 d**). We found the same shift in binding energies for all core-level peaks of the sample as already described for the red perovskites with the native ligand, suggesting that the shift is independent of the ligand shell and related to the NCs itself. UPS measurements before X-ray exposure revealed a shift to lower cutoff binding energies by ~ 0.5 eV compared to the NCs with native ligand stabilization (**Figure S29**, Appendix D). After X-ray exposure, the cutoff binding energies increase by 0.1 eV (**Figure S26**, Appendix D), reproducing the same effect as observed with the native ligand.

Based on the XPS and WAXS results, we now propose a mechanism for the X-ray radiation-related degradation of the red and blue perovskite NCs with their native ligands. Our findings suggest a redox reaction during which Pb^0 and molecular iodine ($CsPbBrI_2$) or chlorine ($CsPbBr_2Cl$) are formed. While iodine resides within the sample after 20 h in ultra-high vacuum, chlorine is removed. This suggests the following decomposition reaction for the red perovskites:

$$\begin{aligned} CsPbBrI_2(xl) &\rightarrow CsBr\ (s) + PbI_2\ (s) \\ PbI_2\ (s) &\rightarrow Pb^0\ (s) + I_2(s) \end{aligned} \qquad (40)$$

where (xl) refers to the crystalline and (s) to the solid state. Similar mechanisms are postulated for $MAPbI_3$ and $CsPbBrI_2$ thin films, where a comparable Pb peak was found.[221, 230-232, 235] The first reaction is facilitated by the low enthalpy of formation for $CsPbBrI_2$ as shown by calorimetry.[242] We believe that the second reaction is enabled

by the high energy radiation. In view of the high volatility of I_2, particular in ultra-high vacuum, we note that the formation of polyiodides, such as I_3^-, is possible under these conditions which greatly reduces its volatility.[232, 243]

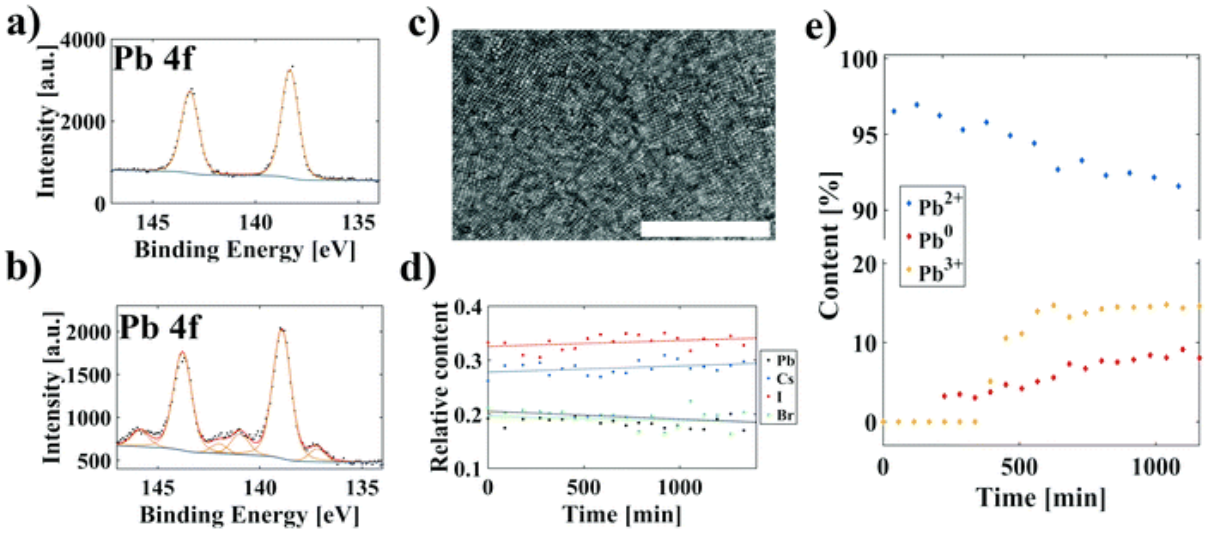

Figure 38 XPS of the **Pb*4f*** orbital for $CsPbBrI_2$ with an mZnTPP ligand shell at the (**a**) start and (**b**) end of the experiment. Two new lead species occurred, at lower and higher binding energies. (**c**) SEM micrograph of the mZnTPP exchanged sample after X-ray exposure for approximately 20 h. Scale bar corresponds to 500 nm. (**d**) Relative stoichiometric content and linear regression (dotted lines) of the exchanged $CsPbBrI_2$ sample over time. (**e**) Temporal evolution of the observed lead species, the novel formed peaks are attributed to Pb^0 (~137 eV) and Pb^{3+} (~141 eV).

We suggest a similar decay mechanism for the blue perovskites based on the analogous formation of a Pb^0 signal (**Figure 35 f**). We interpret the absence of a novel chlorine peak (**Figure 35 g**) and the strong decrease in chlorine content (**Figure 35 h**) as indirect evidence for the oxidation of chloride, since Cl_2 is highly volatile and polychlorides are less stable than polyiodides. In this scenario, chlorine would immediately evaporate and remain undetected by XPS. The crystal decomposition expected from such a loss in material is consistent with the greatly altered morphology found by SEM (**Figure S25**, Appendix D). Our finding that, in the red and blue perovskites alike, bromide is neither oxidized nor removed from the sample, can be rationalized in terms of the oxidation potentials and enthalpies of decomposition for all three halides. Firstly, the oxidation potential of bromide (E_0 = 1.087 V) is larger than that of iodide (E_0 = 0.5355 V) and triiodide (E_0 = 0.536 V), favoring the oxidation of the

latter. In contrast, the oxidation potential of chloride (E_0 = 1.396 V) is higher than for bromide. However, the enthalpy of decomposition is roughly 0.22 eV larger for $CsPbBr_3$ than for $CsPbCl_3$, which we hold responsible for the observed overall oxidation and removal of chloride.[244] We now discuss the shift of the core-levels in XPS upon X-ray illumination, for which we focus on the red-emitting perovskites since the decomposition of the blue perovskites prevents a similar analysis. A core-level shift in XPS is generally attributed to a variety of origins, such as changes in the chemical environment of specific atoms, an altered electrostatic or Madelung potential, surface effects at the sample substrate interface or charging effects.[222, 227-229] Firstly, we rule out any surface effects due to the very prominent gold substrate signal (**Figure 37**) which remains unaltered throughout the entire experiment. Secondly, charging effects are unlikely due to several reasons: the gold substrate signal is clearly visible, indicating a very thin perovskite film that can be assumed to be grounded. Closely related is the high secondary electron count, originating from the substrate that we correlate to a suppression of sample charging. Lastly, the conductivities of the native as well as the mZnTPP exchanged sample are known.[241] The electric resistance in the porphyrin-containing sample is lower and should result in a smaller shift. However, we find the same shifts independent of the ligand shell and can thus assume that the shift does not originate from charging. Therefore, only two possible explanations remain: changes in either the electrostatic potential or the chemical environment. We argue that a change of the electrostatic potential in the sample is the origin of the peak shifts, which is justified in the following. The electrostatic potential in an ionic solid for an ion i is given as:

$$V_i = \frac{e^2}{4\pi\varepsilon_0 r_0} \sum_{j=i} \frac{z_j}{r_{ij}/r_0} = \frac{e^2}{4\pi\varepsilon_0 r_0} M_i, \qquad (41)$$

with the elementary charge e, vacuum permittivity ε_0, equilibrium lattice constant r_0, effective charge z_j of the j th atom, the distance between the respective atoms r_{ij} and the Madelung constant M_i. To quantify the change in V_i for Pb and Cs according to eqn (43), we calculate the changes of the radii during the contraction of the unit cell by 0.44 Å as determined from WAXS (**Figure 36 a**) and compare the results to the core-level shifts in XPS. The excellent agreement suggests that the lattice contraction is the reason for the measured core-level shift. We attribute the remaining small

discrepancies to the inhomogeneous composition of the mixed halide system, as well as the simultaneously occurring decomposition mechanisms.

We now discuss the effect of ligand exchange with mZnTPP on the stability of the red perovskites under X-ray irradiation. Based on our XPS results, which involve the occurrence of two novel lead species (**Figure 38 b**), supposedly Pb^0 and Pb^{3+}, and a constant Pb^0 : Pb^{3+} ratio of 1 : 2 during the experiment (**Figure 38 e**), we suggest the following disproportionation reaction:

$$3CsPbBrI_2 \rightarrow Cs_3Pb_2Br_3I_6 + Pb^0 \qquad (42)$$

This disproportionation is consistent with our finding that no other iodide species occurred (**Figure S30**, Appendix D) under these conditions, that is, this degradation pathway does not involve halide oxidation. Despite the low stability of Pb^{3+}, this oxidation state has previously been postulated for perovskites.[229, 245] In addition, the specialized experimental conditions (continuous X-ray radiation in ultra-high vacuum) may facilitate its detection. Most notably, this new degradation pathway is substantially slower than the degradation with native ligand functionalization (compare **Figure S24**, Appendix D with **Figure 38 e**) and proceeds solely via the reaction of lead. To rationalize this surprising effect of the mZnTPP ligand, we note a recent work on the stabilizing effect of ligands with strong (surface) dipoles on CdSe NCs against irreversible reduction during charging.[246] During XPS, the NCs are subject to substantial charging and, while not all considerations for the reduction of Cd in CdSe may be transferable to Pb in $CsPbBrI_2$, we argue that the general rational outlined by du Fossé *et al.* is of central importance also in the present case: mZnTPP invokes a 0.5 eV increase in work function (**Figure 39 a**) and provides better dielectric screening (a higher permittivity)[241] compared to the native ligand. As du Fossé *et al.* have shown, a reduced work function affects primarily the overall crystal and only to a lesser extent a localized state, such as Pb^0.[246] This stabilizes the NCs during charging and inhibits the irreversible reduction of lead. Thus, a promising strategy to further enhance the stability of perovskite NCs is the search for ligands that induce even larger work functions.

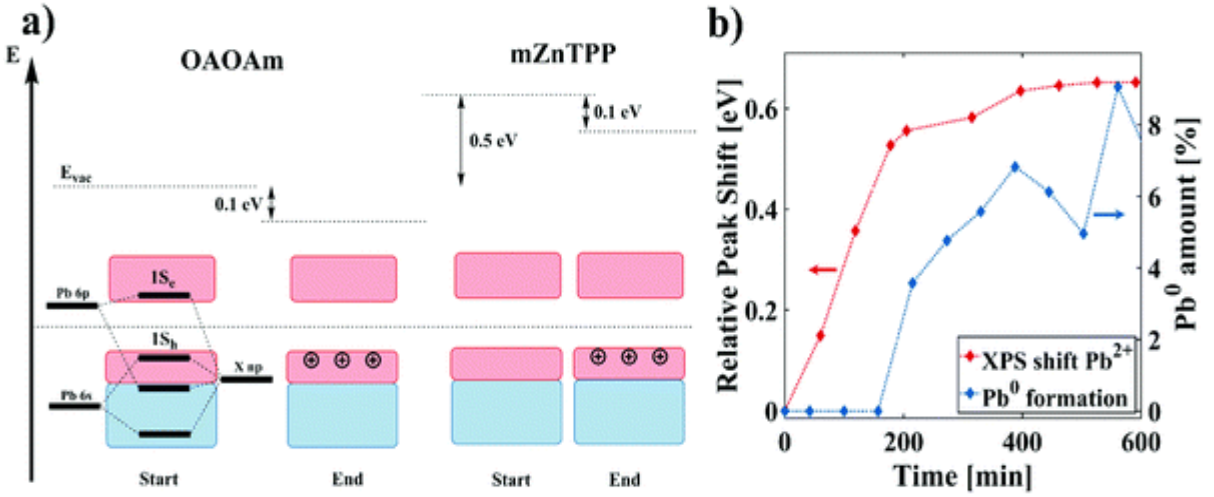

Figure 39 (**a**) Energy level scheme obtained from UPS measurements for the native shell (left) and mZnTPP functionalized nanocrystals (right), all energies are referenced against the Fermi level of the instrument. The conduction state minimum (1Se) and valence state maximum (1Sh) are indicated, respectively. The character of the states is depicted as red and blue for antibonding and bonding orbitals, respectively. The contraction of the crystal lattice resulted in a shift to higher energies by 0.1 eV for the native ligand as well as for mZnTPP. In addition, mZnTPP functionalization lowered the binding energy by 0.5 eV compared to the native functionalization. (**b**) Temporal evolution of the XPS shift induced by the lattice contraction (red) and the formation of elemental lead (blue).

Table 2 Influence of irradiation by X-rays on the lattice constants and resulting distances for the $CsPbBrI_2$ NCs. The calculated electrostatic potential for Pb and Cs as well as the difference are given, experimental value in brackets

	$CsPbBrI_2$					
	a_0 = 6.11 Å	a_1 = 5.67 Å	Difference [eV]	a_0 = 6.11 Å	a_1 = 5.67 Å	Difference [eV]
Atom	Pb			Cs		
d_{CsA} [Å]	5.2395	4.8497		n.a.	n.a.	
d_{AX} [Å]	3.025	2.8		4.2780	3.9598	
d_{PbA} [Å]	n.a.	n.a.		5.2395	4.8497	
V_{el} [Å]	7.5	8.1	0.6 (0.630)	8.9	9.6	0.7 (0.711)

We note that both degradation pathways – with and without mZnTPP – are preceded by the same core level energy shifts of Pb and Cs (Figure 37 **c** and **d**), which we were able to correlate with a lattice contraction (Figure **36 a** and Table **2**). A likely scenario for such a contraction could be either a phase transition or halide segregation.[231] The latter is a well-known phenomenon in $CsPbI_2Br$, leading to bromine-enriched crystal domains (of smaller lattice constant) with iodine-rich segregations at the boundaries.[232] Figure 39 **b** suggests that this transformation is a prerequisite for the redox reaction of Pb^{2+} to occur according to either eqn (40) or (42) as the electrostatic potential can alter the energetics inside the crystal.

We note some similarities between the X-ray induced decomposition detailed here with the behavior of mixed-halide perovskites under UV radiation. For instance, the lattice contraction observed here is reminiscent of the lattice contraction and phase segregation found for superlattices of $CsPb(Br_xI_{1-x})_3$ NCs after exposure to UV light.[247] In contrast to such studies under UV light, under X-ray exposure in ultrahigh vacuum we do not observe a fast evaporation of iodine, potentially due to the formation of triiodide. This may be rationalized with the strong dependence of iodine expulsion from the perovskite lattice on the surrounding medium,[232, 243] e.g. ultrahigh vacuum in XPS vs. ambient conditions in UV photodegradation experiments.

5.1.4 Conclusion

In conclusion, we have shown that the mechanism of photodegradation under X-ray radiation of all-inorganic mixed lead halide perovskite nanocrystals depends on the ligand shell. With the ligands oleic acid/oleylamine, we found a fast decomposition into elemental lead and halogen, similar to previous studies on bulk thin films. After ligand exchange with a metal porphyrin derivative, photodegradation was significantly slower and progressed via a disproportionation of Pb^{2+} to Pb^0 and Pb^{3+}. We hold an increase in work function of the nanocrystal film by 0.5 eV responsible for the altered photodegradation behavior, which was induced by the metal porphyrin derivative. This work highlights the advantageous tunability of the ligand shell of lead halide perovskite nanocrystals as an additional means to improve their photostability and suggests surface ligands that introduce strong dipoles as a general paradigm toward mitigating photodegradation.

5.1.5 Acknowledgements

This work was supported by the DFG under grants SCHE1905/8-1 (project no. 424708673) and SCHE1905/9-1 as well as the Carl Zeiss Stiftung (Forschungsstrukturkonzept ‘‘Interdisziplinäres nanoBCP-Lab’’). The Authors would like to thank Dmitry Lapkin and Jerome Carnis for help with the WAXS measurements. We acknowledge DESY (Hamburg, Germany), a member of the Helmholtz Association HGF, for the provision of experimental facilities. Parts of this research were carried out at PETRA III synchrotron facility and we would like to thank the beamline staff for assistance in using the Coherence Application P10 beamline.

5.2 Porphyrin Functionalization of $CsPbBrI_2/SiO_2$ Core–Shell Nanocrystals Enhances the Stability and Efficiency in Electroluminescent Devices

Jan Wahl,[1] Manuel Engelmayer,[2] Mukunda Mandal,[3] Tassilo Naujoks,[2] Philipp Haizmann,[1] Andre Maier,[1] Heiko Peisert,[1] Denis Andrienko,[3] Wolfgang Brütting,[2] Marcus Scheele[1,4]

[1] Institut für Physikalische und Theoretische Chemie, Universität Tübingen, 72076 Tübingen, Germany

[2] Institut für Physik, Universität Augsburg, 86135 Augsburg, Germany

[3] Max Planck Institute for Polymer Research, 55128 Mainz, Germany

[4] Center for Light-Matter Interaction, Sensors and Analytics (LISA+), Universität Tübingen, 72076 Tübingen, Germany

5.2.1 Abstract

Surface ligand exchange on all-inorganic perovskite nanocrystals of composition $CsPbBrI_2$ reveals improved optoelectronic properties due to strong interactions of the nanocrystal with mono-functionalized porphyrin derivatives. The interaction is verified experimentally with an array of spectroscopic measurements as well as computationally by exploiting density functional theory calculations. The enhanced current efficiency is attributed to a lowering of the charging energy by a factor of 2–3, which is determined by combining electronic and optical measurements on a selection of ligands. The coupled organic–inorganic nanostructures are successfully deployed in a light-emitting device with higher current efficacy and improved charge carrier balance, magnifying the efficiency almost fivefold compared to the native ligand.

5.2.2 Contribution

The research, primarily authored by Jan Wahl, focused on enhancing the optoelectronic properties of $CsPbBrI_2/SiO_2$ core-shell nanocrystals (NCs) by replacing the native OAOAm (Oleic Acid (OA) and Oleylamine (OAm)) ligands with porphyrin-

based ligands, specifically zinc-(5-monocarboxyphenyl-10,15,20-triphenylporphyrin) (mZnTPP). Wahl developed the synthetic route, which involved the initial growth of a thin silica shell around the perovskite core to provide the necessary stability for subsequent ligand exchange with the more polar porphyrins.

My central contribution to this work was the electronic characterization of these nanocrystal thin films using UPS. Measurements were performed on films prepared on silicon/silicon oxide or gold plated silicon substrates. These UPS measurements were critical for quantifying the electronic interaction between the NCs and the new mZnTPP ligand. Analysis revealed a significant Fermi level shift of 0.5 eV toward lower energies in the mZnTPP-functionalized NCs. This energy shift confirmed the electronic interaction of the new ligand with the nanocrystals and was attributed to the intrinsic dipole moment of the asymmetrically functionalized porphyrin, which is oriented opposite to the NC surface dipole moment, thereby partially compensating for it. Generally, a reduction in the surface dipole shifts the NC energy levels to lower energies. Notably, the onset of the valence band maximum remained constant, indicating that the valence electronic structure was preserved. These points were previously discussed in the UPS subsection of Chapter 2.3; for further orientation, I refer here again to **Figure 15**.

Broadly, my measurements and contribution to the discussion served to substantiate the reduction of the charging energy (EC) as the primary driver for the five-fold increase in current efficiency of the $CsPbBrI_2$@SiO_x@Porphyrin hybrid materials. The level modulation and surface dipole compensation identified via UPS directly correlated with a reduction in charging energy by a factor of 2.4 to 3 in the ligand-exchanged system. This facilitated an improved charge carrier balance and increased the peak current efficiency in LEDs by a factor of 4.65. Furthermore, my results supported evidence from temperature-dependent photoluminescence measurements regarding the enhanced phase stability of the ligand-exchanged perovskite nanocrystals.

5.3 Zwitterionic Carbazole Ligands Enhance the Stability and Performance of Perovskite Nanocrystals in Light-Emitting Diodes

Christopher Kirsch,[1] Tassilo Naujoks,[2] Philipp Haizmann,[1] Philipp Frech,[1] Heiko Peisert,[1] Thomas Chassé,[1] Wolfgang Brütting,[2] Marcus Scheele[1]

[1] Institut für Physikalische und Theoretische Chemie, Universität Tübingen, 72076 Tübingen, Germany

[2] Institut für Physik, Universität Augsburg, 86135 Augsburg, Germany

5.3.1 Abstract

We introduce a new carbazole-based zwitterionic ligand (DCzGPC) synthesized via Yamaguchi esterification which enhances the efficiency of lead halide perovskite (LHP) nanocrystals (NCs) in light-emitting diodes (LED). A facile ligand exchange of the native ligand shell, monitored by nuclear magnetic resonance (NMR), ultraviolet−visible (UV−vis), and photoluminescence (PL) spectroscopy, enables more stable and efficient LHP NCs. The improved stability is demonstrated in solution and solid-state LEDs, where the NCs exhibit prolonged luminescence lifetimes and improved luminance, respectively. These results represent a promising strategy to enhance the stability of LHP NCs and to tune their optoelectronic properties for further application in LEDs or solar cells.

5.3.2 Contribution

This research was led by Christopher Kirsch, who developed the concept and design, as well as the synthesis of the novel carbazole-based zwitterionic ligand 1,2-di((9H-carbazol-9-yl)propanoyl)-sn-glycero-3-phosphocholine (DCzGPC). My primary contribution involved the electronic and chemical characterization of the new ligand and the exchanged nanocrystals through UPS and XPS. The objective was to investigate the electronic properties and energy level alignment resulting from the ligand exchange.

UPS measurements were utilized to determine the work function (Φ) and the valence band maximum of both the nanocrystals and the ligand. These parameters are

essential for analyzing electronic band alignment. The measurements yielded an ionization energy of 5.8 eV for the native $CsPbBr_2Cl$ nanocrystals and 5.9 eV for the pure DCzGPC ligand. The work function was determined to be 4.0 eV for the native nanocrystals and 4.3 eV for the pure ligand. Although the energetic positions showed only minor variations between the native and exchanged nanocrystals, the analysis of band alignment is critical because it reveals whether the conjugated carbazole π-system of the DCzGPC ligand facilitates charge carrier injection. Achieving alignment for at least one carrier type, specifically the improvement of hole injection, is a requirement for enhancing LED efficiency.

Complementary XPS measurements were used to verify the chemical composition of the nanocrystals and to rule out impurities. Identifying chloride contamination was a recurring challenge in the process. My analysis helped identify these impurities, which allowed Kirsch to improve the synthetic routes and precursor selection. Specifically, XPS confirmed the absence of chloride contamination in the pure DCzGPC ligand. This finding was important because it ruled out halogen contamination as a potential explanation for the observed hypsochromic shift in the emission spectrum.

Analysis of the core-level spectra for **Cs***3d*, **Pb***4f*, **Br***3d*, and **Cl***2p* showed that the ligand exchange did not significantly alter the chemical stoichiometry of the nanocrystals. The **Pb***4f* core-level spectra remained nearly identical in shape and position for both native and exchanged nanocrystals, which suggests that the DCzGPC ligand does not induce significant doping. The presence of the new ligand on the surface after exchange was confirmed through **N***1s* and **C***1s* core-level signatures. In summary, XPS and UPS provided the necessary validation for the chemical and electronic integrity of the nanocrystals. While XPS proved that the observed optical changes were not due to halide displacement or doping, UPS provided the data required to characterize the energy band alignment and explain the improved performance in LEDs.

5.4 *Peri*-tetracene from 1,1'-bitetracene: Zipping up structurally defined graphene nanoribbons

Maren Klein,[1,2] John B. Bauer,[2] Nina Kainbacher,[3] Marie S. Wagner,[1,2] Katharina Greulich,[1] Philipp Haizmann,[1] Erika Giangrisostomi,[4] Ruslan Ovsyannikov,[4] Peter Puschnig,[3] Thomas Chassé,[1,5] Holger F. Bettinger,[2,5] and Heiko Peisert[1]

[1] Institute of Physical and Theoretical Chemistry, University of Tübingen, 72076 Tübingen,

[2] Institute of Organic Chemistry, University of Tübingen, 72076 Tübingen, Germany

[3] Institute of Physics, NAWI Graz, University of Graz, 8010 Graz, Austria

[4] Institute Methods and Instrumentation for Synchrotron Radiation Research, Helmholtz-Zentrum Berlin GmbH, 12489 Berlin, Germany

[5] Center for Light-Matter Interaction, Sensors & Analytics (LISA+) at the University of Tübingen, 72076 Tübingen, Germany

5.4.1 Abstract

Polycyclic aromatic hydrocarbons (PAH) are promising molecules for a manifold of applications in organic electronics, spintronics or energy storage devices. Among PAHs, particular attention has been focused on the synthesis and study of acenes and fused acenes – *peri*-acenes -, allowing a tuning of the HOMO – LUMO gap with the size of the conjugated system. As a starting point for surface synthesis of larger PAHs, we synthesized a 1,1'-bitetracene for the first time. This precursor molecule consists of two tetracene units connected via the 1,1'-position with a torsion angle of 70°. Interface properties of the molecule before and after annealing on a Cu (111) surface are investigated. Using X-ray photoemission spectroscopy (XPS), angle-resolved photoelectron spectroscopy (ARPES), low-energy electron diffraction (LEED), scanning-tunneling microscopy (STM), it is experimentally demonstrated that the tetracene units zip up with the help of heat forming *peri*-tetracene. These results and the exact adsorption geometry are in excellent agreement to calculations using density

functional theory (DFT). Moreover, the calculations enable the identification of newly formed valence band states at the interface to Cu (111).

5.4.2 Contribution

This research was led by Maren Klein and investigates the surface-assisted synthesis of peri-tetracene (4-PA) through the thermally induced cyclodehydrogenation of the precursor molecule 1,1′-bitetracene (Bi4A) on a Cu(111) surface.

My primary contribution to this publication involved the execution of extensive experimental series during synchrotron beam time sessions. These experiments were conducted at the PM4 beamline of the BESSY II electron storage ring in Berlin. Performing these measurements within strictly limited beamtime necessitated high intensity and precision to maintain the required data quality across a wide range of sample states, particularly before and after annealing at 250 °C.

The resulting PES and XAS data were essential for the interpretation and discussion of the subsequent electronic and chemical modifications. Through the successful execution of these spectroscopic measurements and my involvement in the interpretation of the spectra, the central conclusion of the work was confirmed, which states that a surface- and temperature-controlled zipping-up reaction of Bi4A to peri-tetracene occurs.

5.5 Direct laser induced writing of high precision gold nanosphere SERS patterns

Olympia Geladari,[1,2] Philipp Haizmann,[1] Andre Maier,[1,2] Markus Strienz,[3] *Martin Eberle,[1] Marcus Scheele,[1,2] Heiko Peisert,[1,2] Andreas Schnepf,[3] Thomas Chassé,[1,2] Kai Braun,[1,2] and Alfred J. Meixner[1,2]*

[1] Institute of Physical and Theoretical Chemistry, University of Tübingen, 72076 Tübingen,

[2] Center for Light-Matter Interaction, Sensors & Analytics (LISA+) at the University of Tübingen, 72076 Tübingen, Germany

[3] Institute of Organic Chemistry, University of Tübingen, 72076 Tübingen, Germany

5.5.1 Abstract

The high sensitivity and molecular fingerprint capability of Surface-Enhanced Raman Spectroscopy (SERS) have lead to a wide variety of applications ranging from classical physics, chemistry over biology to medicine. Equally, there are numerous methods to fabricate samples owing to the desired properties and to create the localized surface plasmon resonances (LSPRS). However, for many applications the LSPRs must be specifically localized on micrometer sized areas and multiple steps of lithography are needed to achieve the desired substrates. Here we present a fast and reliable direct laser induced writing (DIW) method to produce SERS substrates with active areas of interest in any desired size and shape in the micrometer regime. Afterwards, the SERS substrates have been functionalized with phthalocyanines. The DIW fabricated samples realize sub-monolayer sensitivity and an almost uniform enhancement over the entire area, which make this production method suitable for many sensing applications.

5.5.2 Contribution

This research was led by Olympia Geladari. My primary contribution to this work was the conceptualization and utilization of $CoPcF_{16}$ as a probe molecule, which was essential for the validation and characterization of the SERS substrates developed in this study.

I performed the physical vapor deposition of $CoPcF_{16}$ with the objective of depositing a precise monolayer. Following the deposition, I conducted XPS measurements to provide the experimental basis for validating and measuring the thickness of the evaporated $CoPcF_{16}$ film. A strategic reason for selecting this perfluorinated phthalocyanine was the ability to track the **F*1s*** signal in the XPS spectra, which allowed for the accurate quantification and verification of molecular coverage.

As $CoPcF_{16}$ was employed as a probe molecule to investigate the optical properties and SERS performance of the printed gold nanostructure (Au-NS) architectures. The choice of $CoPcF_{16}$ is highly advantageous due to its characteristic Raman fingerprint, particularly in the 1340 – 1550 cm^{-1} region. This distinctive signature provides a reliable benchmark for evaluating the enhancement capabilities of the fabricated substrates.

6 Appendix

6.1 Appendix A

Supporting Information: Untangling the Intertwined: Metallic to Semiconducting Phase Transition of Colloidal MoS_2 Nanoplatelets and Nanosheets

André Niebur,[*,1,2] Aljoscha Söll,[*,1] Philipp Haizmann,[3] Onno Strolka,[1,2,3] Dominik Rudolph,[1,2] Kevin Tran,[4,5] Franz Renz,[4,5] André Philipp Fauendorf,[6] Jens Hübner,[5,6] Heiko Peisert,[3] Marcus Scheele[3] and Jannika Lauth[#,1,2,3,5]

[1] Institute of Physical Chemistry and Electrochemistry, Leibniz University Hannover, Callinstr. 3a, D-30167 Hannover, Germany

[2] Cluster of Excellence PhoenixD (Photonics, Optics, and Engineering – Innovation Across Disciplines), Hannover, Germany

[3] Institute of Physical and Theoretical Chemistry, University of Tübingen, Auf der Morgenstelle 18, D-72076 Tübingen, Germany

[4] Institute of Inorganic Chemistry, Leibniz University Hannover, Callinstr. 9, D-30167 Hannover, Germany

[5] Laboratory of Nano and Quantum Engineering (LNQE), Leibniz University Hannover, Schneiderberg 39, D-30167 Hannover, Germany

[6] Institute of Solid State Physics, Leibniz University Hannover, Appelstr. 2, D-30167 Hannover, Germany

[*] Equal contribution

[#] jannika.lauth@uni-tuebingen.de

Stabilization of Colloidal MoS_2 NPLs and NSs by Oleic Acid and Oleylamine

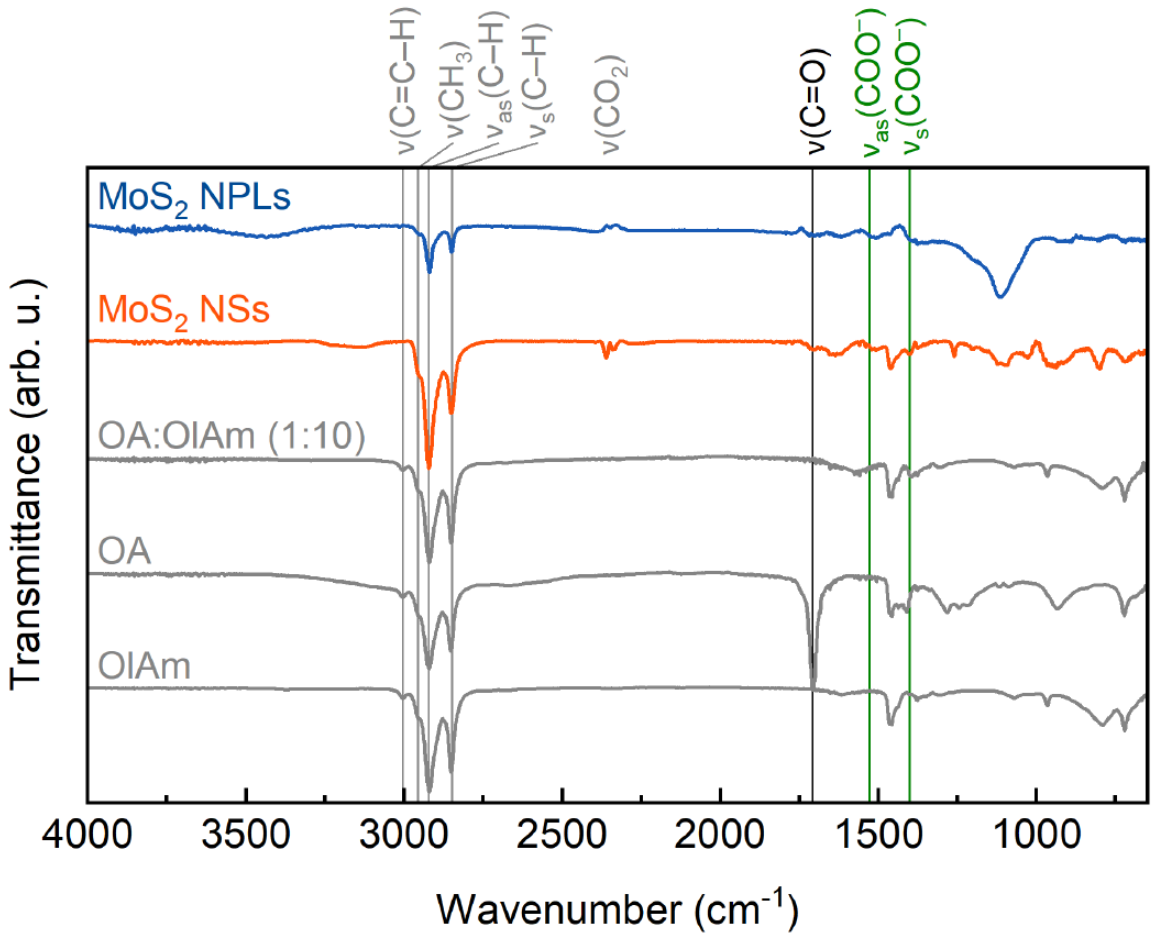

Figure S1 FTIR spectra of MoS_2 NPLs and NSs, pure oleic acid, oleylamine and a 1 : 10 -mixture of oleic acid and oleylamine used to dissolve the Mo precursor. s = symmetric, as = antisymmetric.

Fourier-Transform Infrared (FTIR) transmission spectra of MoS_2 NPLs and NSs were obtained using a Tensor 27 spectrometer from Bruker. Washed samples were added to KBr and were subsequently dried at 110 °C for 24 h. Discs were pressed out of the KBr/MoS_2 mixture. FTIR spectra of OA, OlAm and an OA:OlAm (1 : 10) mixture were measured using a Cary 630 FTIR spectrometer by Agilent Technologies, utilizing Attenuated Total Reflection (ATR).

The vibration modes between 2800 cm^{-1} and 3050 cm^{-1} present in all samples are caused by the oleyl group in OA or OlAm. In detail, the modes are attributed to the C=C–H stretching (3004 cm^{-1})[79], the antisymmetric stretching of CH_3 (2958 cm^{-1})[248], and the antisymmetric and symmetric stretching of non-terminal C–H (2922 cm^{-1} and 2850 cm^{-1})[79]. These signals suggest that OA or OlAm is present in the washed

samples. In pure oleic acid C=O stretching appears at 1708 cm^{-1} (black line) and is replaced by two modes of the COO^- group at 1402 cm^{-1} and 1530 cm^{-1} if the OA is present as oleate (green lines)[79, 80]. Both samples, MoS_2 NPLs and NSs, show a low intensity C=O stretching signal, suggesting that OA acts as a monodentate ligand. The characteristic symmetric and antisymmetric COO^- stretch modes at 1402 cm^{-1} and 1530 cm^{-1} are not clearly visible in the samples.

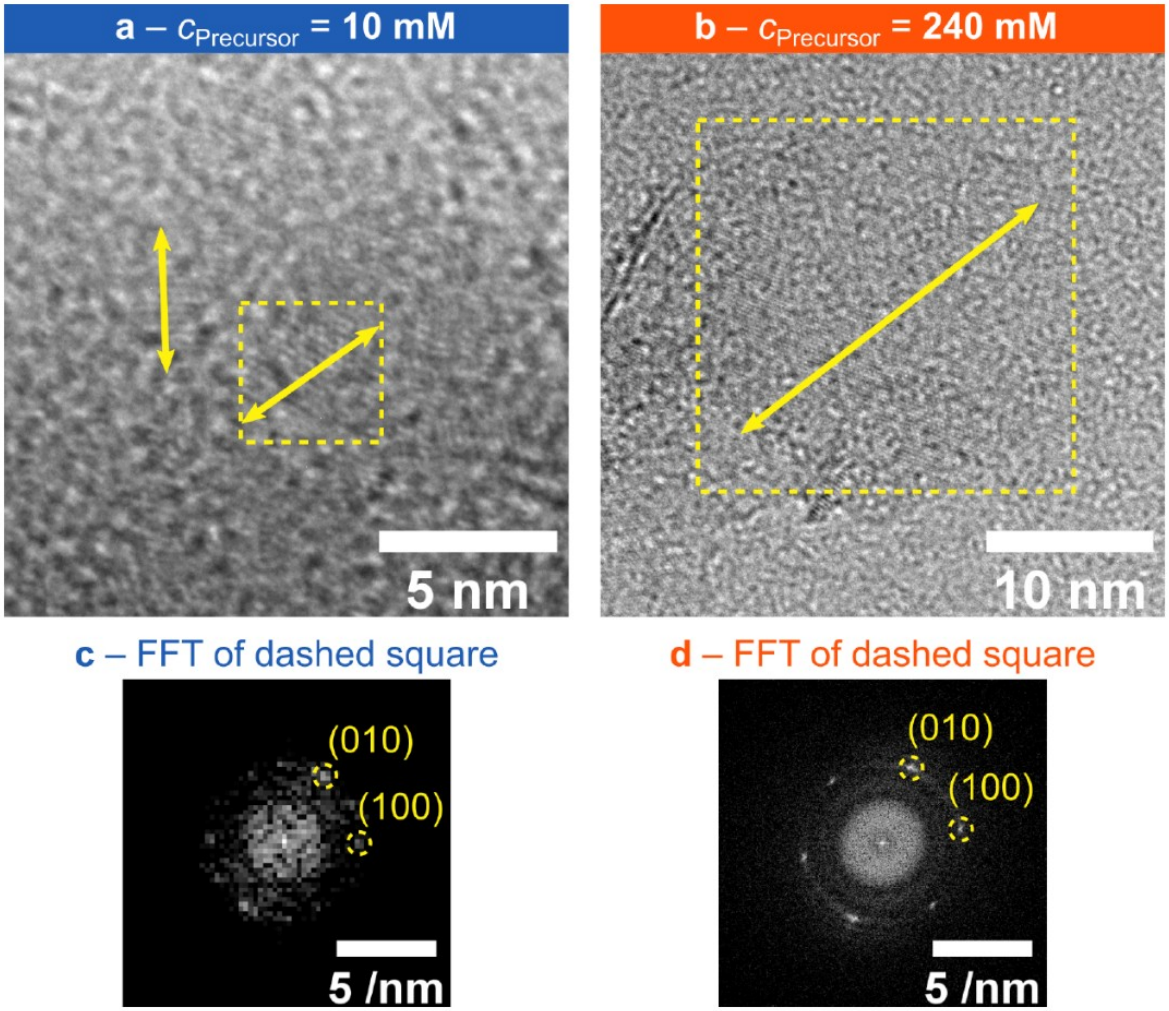

Figure S2 HRTEM images of flat-on oriented 2D MoS_2 NPLs and NSs synthesized with Mo-precursor concentrations of (**a**) 10 mM and (**b**) 240 mM. NPL and NS sizes are identified by a difference in contrast to the background and by domains of lattice planes (indicated by yellow arrows). (**c**) and (**d**) are FFT of the area in dashed squares in (**a**) and (**b**), respectively. Both images show the hexagonal pattern of the 2H MoS_2 crystal phase for NPLs and NSs.

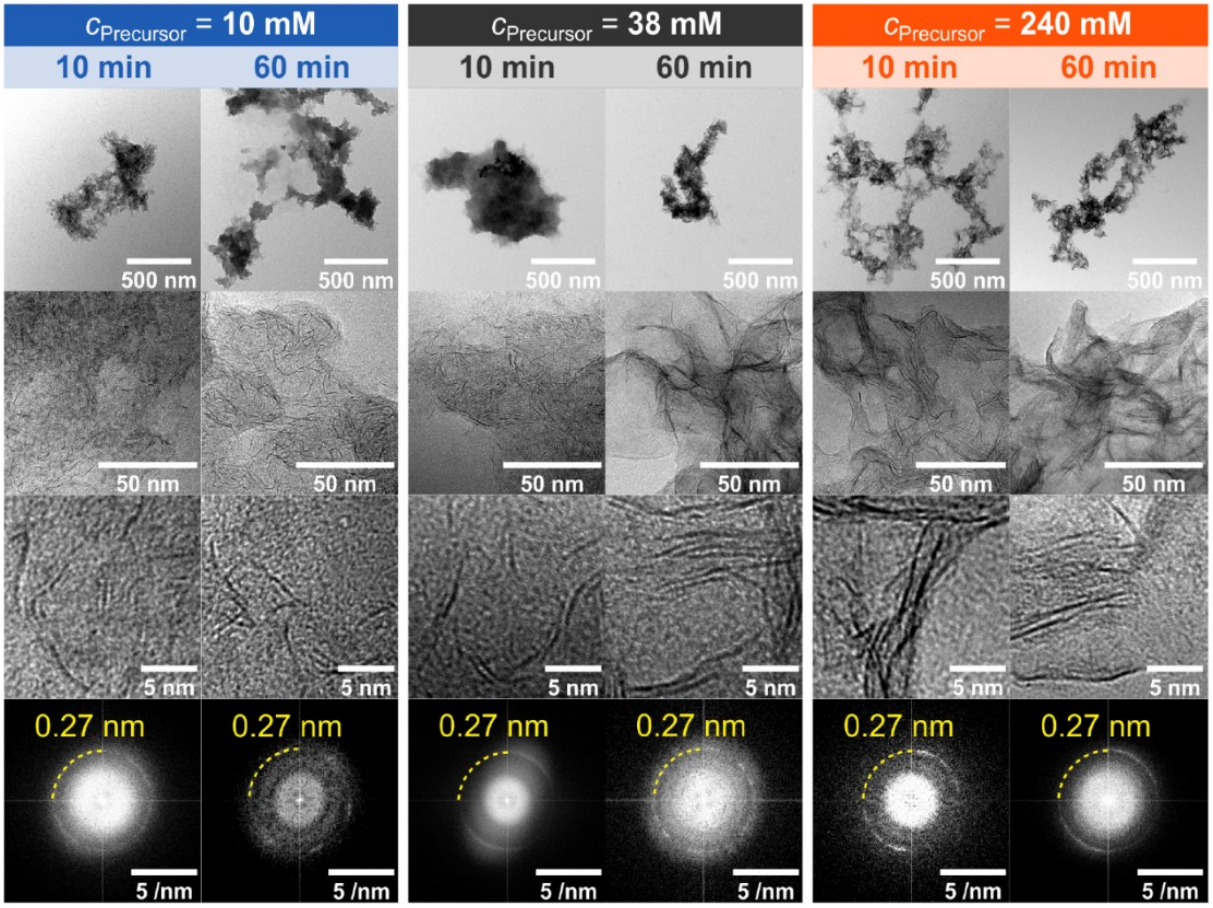

Figure S3 TEM and HRTEM images of MoS_2 NPLs and NSs synthesized by using different precursor concentrations: 10 mM (blue), 38 mM (grey), and 240 mM (orange). For each precursor concentration TEM images are shown after 10 min and 60 min of reaction time. The last row shows a Fourier-transformed HRTEM image exhibiting the same lattice constant of 0.27 nm for all MoS_2 samples.

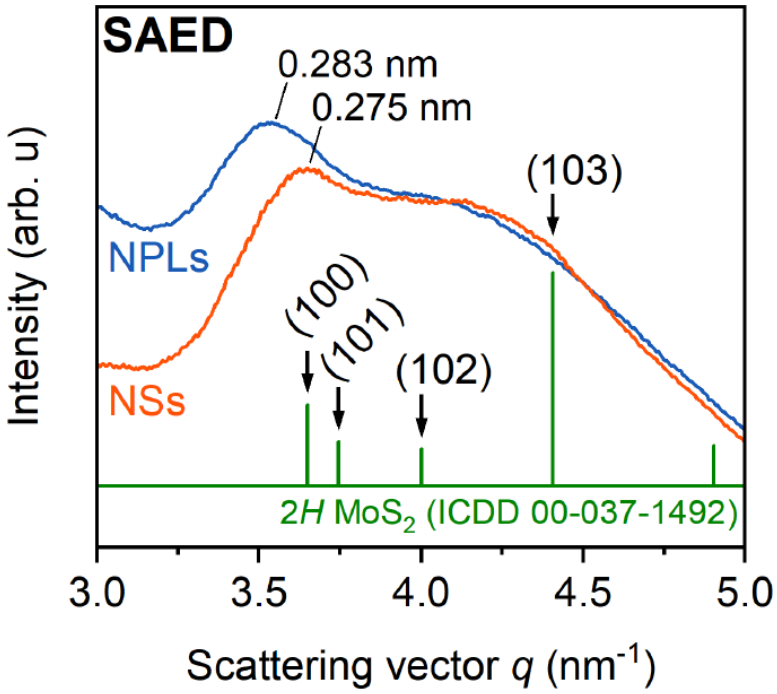

Figure S4 SAED measurements of single MoS_2 NPLs and NSs shown in **Figure 22 a** and **b**. Both samples show the typical (100) reflex overlapped by a broad (103) reflex. The (100) reflex of the MoS_2 NSs matches the literature value of 0.274 nm for bulk 2H MoS_2 (ICDD 00 037-1492). For NPLs the (100) reflex is shifted to 0.283 nm corresponding to a lattice expansion of 3%.

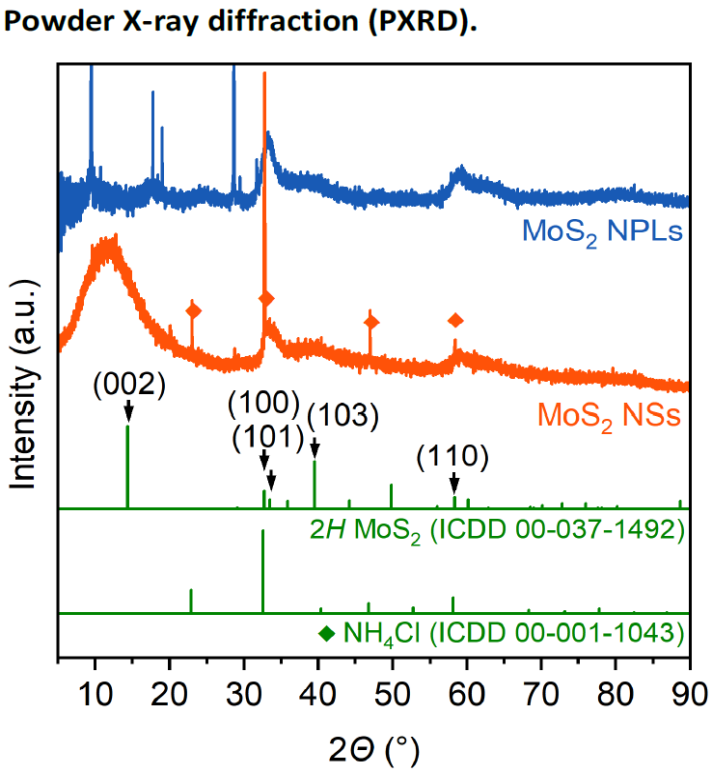

Figure S5 XRD patterns are associated with the 2H crystal phase of MoS_2. The dominant reflexes are the (002), (100), (101), (103) and (110) lattice planes and are broadened due to the spatial confinement of the NPLs and NSs. Most of the narrow reflexes are attributed to in situ formed impurities such as NH_4Cl.

Powder X-ray diffractograms were recorded with a Bruker D8 ADVANCE diffractometer with a Cu Kα1 source (40 kV, 30 mA). Samples were prepared on a silicon single crystal by drop casting. **Figure S5** shows XRD patterns for 10 mM and 240 mM Mo-precursor concentrations respectively with a comparison to bulk MoS_2 in the 2H crystal phase. The (002) reflex has a special significance for the estimation of the MoS_2 layer thickness due to repeating (002) lattice planes which correspond to formation of MoS_2 multilayers. Fewer MoS_2 layers lead to a broadening of the (002) reflex. MoS_2 NSs synthesized by a low 10 mM Mo-precursor concentration lack the (002) reflex, implying the presence of mainly monolayers.[44] In contrast, the XRD pattern of high 240 mM Mo precursor MoS_2 NSs exhibit a (002) reflex. This reflex is broadened as is expected for multilayer NS and shifted to 11.72° compared to the bulk reflex at 14.38°. This shift corresponds to an enlarged Mo-to-Mo layer distance of 0.75 nm (0.615 nm in bulk[83,84]) and is caused by the colloidal NSs having a twisted shape and are therefore not optimally stacked. **Figure S5** shows that the most prominent reflexes are attributed to

the lattice planes (100), (101), (103) and (110) of MoS_2 in the 2H crystal phase. These reflexes are strongly broadened, which is expected for confined systems and usually observed in TMDC NS diffractograms in the literature.[44, 62] Due to the similarity of both crystal phases combined with the strong broadening, a distinction between the 2H and the 1T phase cannot be made with absolute certainty by XRD.

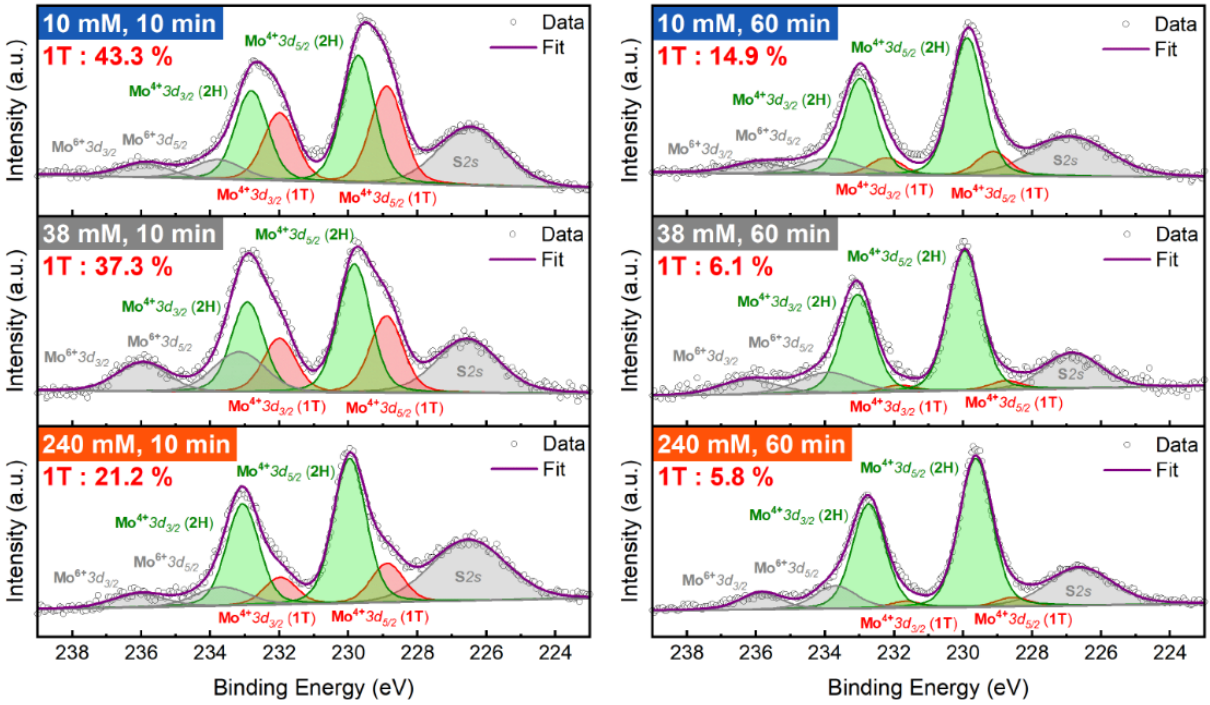

Figure S6 XPS spectra of NPLs and NSs synthesized with different Mo-precursor concentrations. The synthesis parameters (precursor concentration and synthesis time) are indicated in the upper left corner. The fraction of the signal area associated with the 1T phase in the total Mo^{4+} signal area is given.

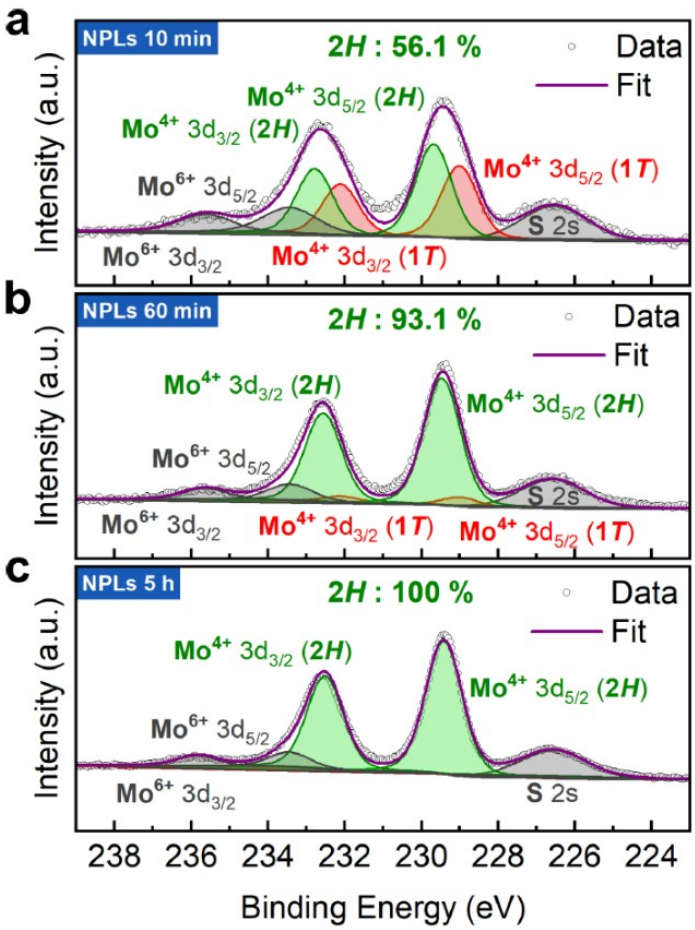

Figure S7 XPS spectra of MoS_2 NPLs synthesized with a 10 mM Mo-precursor concentration for reaction. Aliquots were taken after the injection of 10 min (**a**), 60 min of reaction (**b**) and 5 h of reaction at 320 °C (**c**). After the injection, NPLs are 2H/1T phase mixed (56:44) and transformed into the semiconducting 2H phase during the reaction.

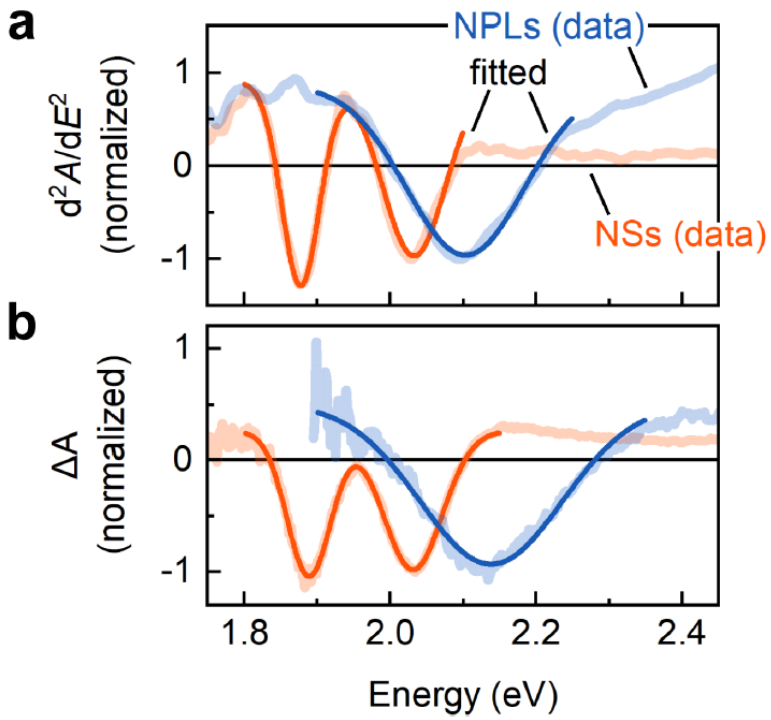

Figure S8 Fitting of **a** – d²A/dE² and **b** – ΔA data: The measured spectra are normalized and fitted with one or two Gaussian functions to get information about the energetic position and FWHM of the respective A and B excitonic feature.

Fitting of the absorption spectroscopy data

Derivative absorbance spectra and transient absorbance spectra were normalized to the B exciton feature between 2 eV and 2.2 eV. The normalized data were fitted with the sum of a constant background and one or two Gaussian curves for MoS_2 NPLs or NSs, respectively.

$$A_{fit} = A_0 + g_A + g_B \qquad (43)$$

$$= A_0 + \sqrt{\frac{2}{\pi}}\left(\frac{Amp_A}{w_A} e^{-2\frac{(x-x_{c,A})^2}{w_A^2}} + \frac{Amp_B}{w_B} e^{-2\frac{(x-x_{c,B})^2}{w_B^2}}\right) \qquad (44)$$

With A_0 being a constant offset and – with indices *A* and *B*, referring to the respective exciton – *g* the Gaussian function, *Amp* the amplitude, *w* the width, and x_c the energetic

center of the Gaussian function. The fitted parameters are *Amp*, *w*, and x_c, and subsequently the full width at half maximum (FWHM) is calculated by

$$FWHM = \sqrt{2\ln(2)} \cdot w \qquad (45)$$

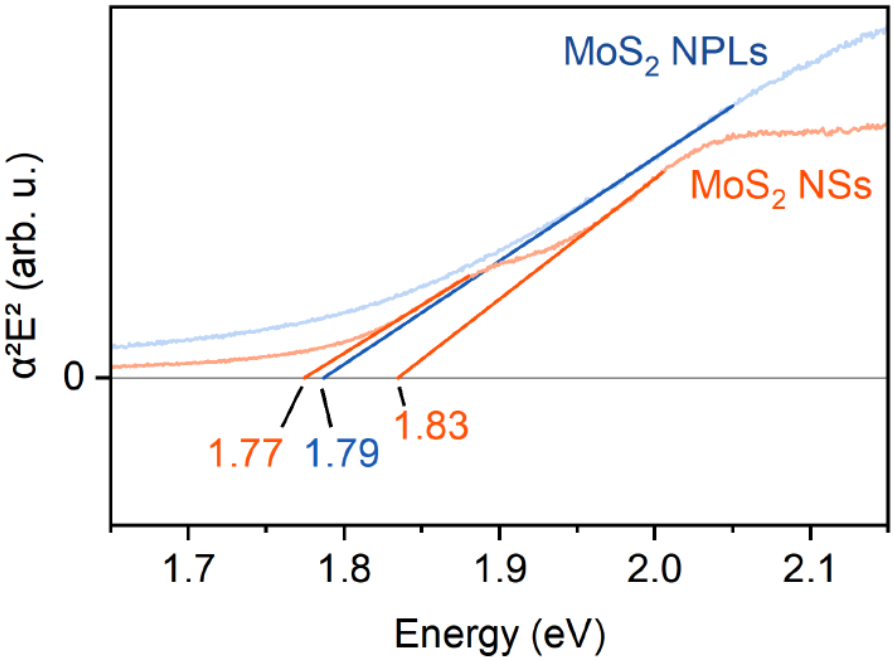

Figure S9 Tauc plot of MoS_2 NPLs and NSs (blue and orange, respectively). The lateral size of the sample does not affect the absorption threshold, which is 1.8 eV in both cases. Note, that the determined threshold corresponds to the band gap subtracted by the exciton binding energy and a broadening parameter.

6.2 Appendix B

Supporting Information: Tuning the Interfacial Electronic Structure of MoS_2 by Adsorption of Cobalt Phthalocyanine Derivatives

Philipp Haizmann[1], Eric Juriatti[1], Maren Klein[1], Katharina Greulich[1], Ruslan Ovsyannikov[3], Erika Giangrisostomi[3], Thomas Chassé[1], Heiko Peisert[1,], Marcus Scheele[1,2,*]*

1 Institut für Theoretische und Physikalische Chemie, Universität Tübingen, 72076 Tübingen, Germany

2 Center for Light-Matter Interaction, Sensors & Analytics LISA+, Universität Tübingen, 72076 Tübingen, Germany

3 Institute Methods and Instrumentation for Synchrotron Radiation Research, Helmholtz-Zentrum Berlin für Materialien und Energie GmbH, 12489 Berlin, Germany

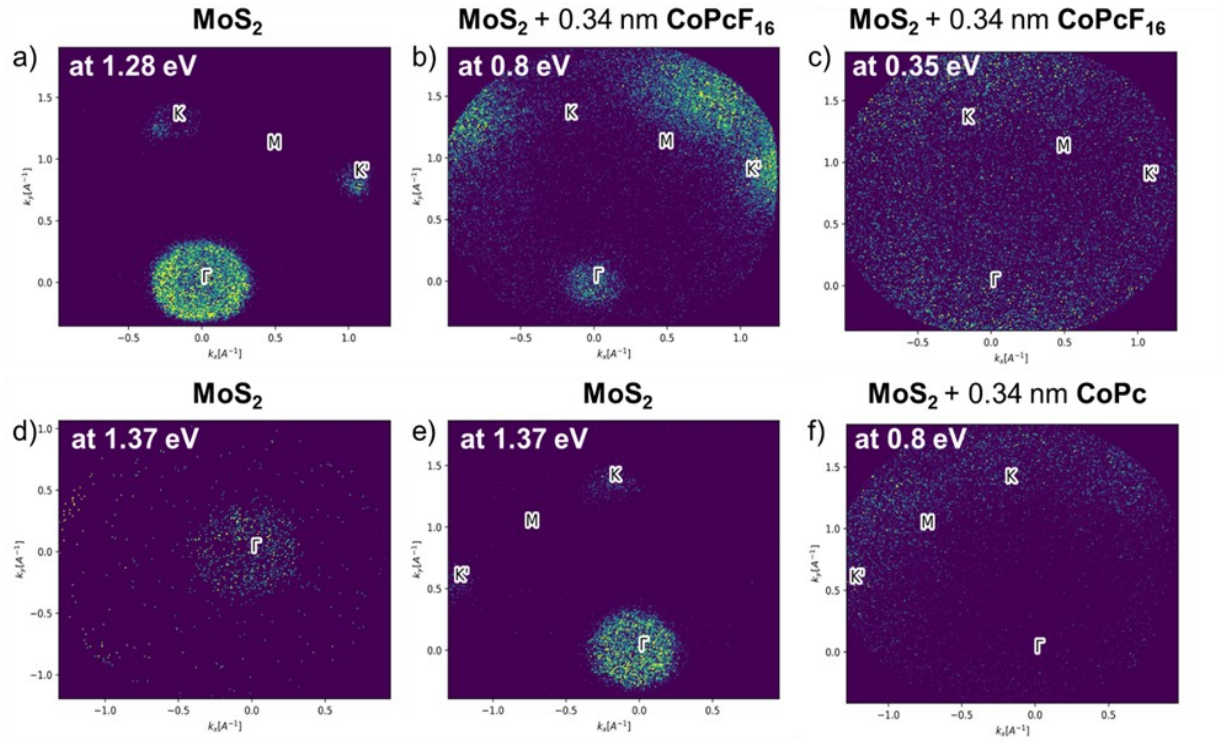

Figure S10 Momentum maps measured with the angle resolved time of flight analyzer at the LowDosePES endstation. The top row (**a – c**) shows the results for the experiments with $CoPcF_{16}$. In (**a**) the momentum map at 1.28 eV is shown, where the Γ and K points are visible. The Γ point is already near the edge and no further optimization of the measurement geometry was needed. In (**b**) the momentum map at 0.8 eV and in (**c**) at 0.35 eV is shown for the measurements with 0.34 nm $CoPcF_{16}$. In (**d**) and (**e**) the momentum map at 1.37 eV before and after the strategic tilting of the MoS_2 crystal is shown. By changing the angle, the whole Brillouin zone can be probed. (**f**) shows the momentum map at 0.8 eV after deposition of CoPc. The intensity distribution matches the expected symmetry of the $CoPcF_{16}$ HOMO in both cases.

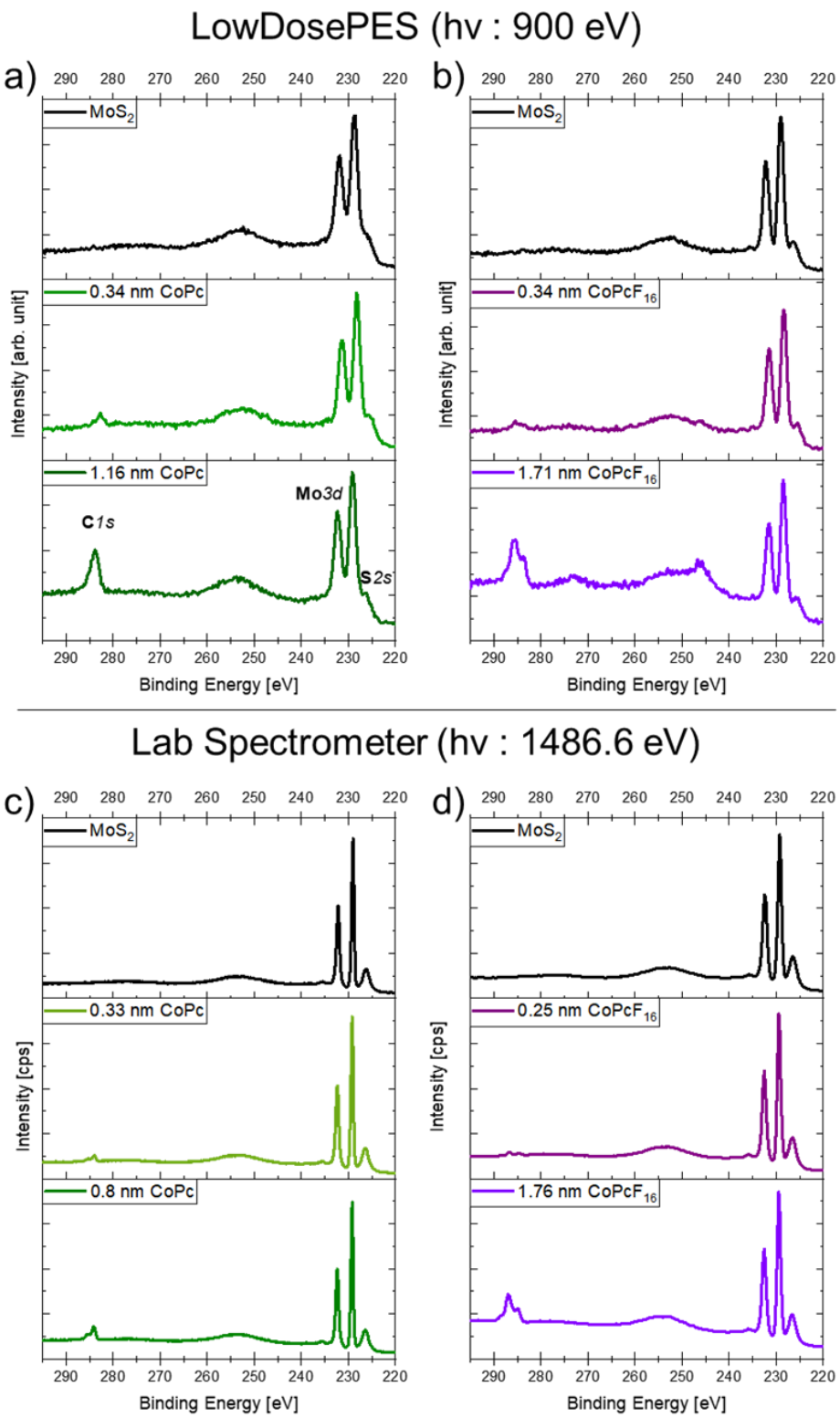

Figure S11 Overview spectra of the freshly cleaved MoS_2 crystals (shown in black (**a – d)**) and after deposition of the respective phthalocyanines CoPc shown in shades of green (**a** and **c**) and $CoPcF_{16}$ represented in lilac in the figures (**b** and **d**). For the measurements at the LowDosePES endstation (**a** and **b**) an excitation energy of 900 eV was used. For the spectra obtained at the lab setup (**c** and **d**) a monochromated Al-Kα source (1486.6 eV) was used.

Concerning the peak fit model for the CoPc, we distinguish between aromatic (C2 and C3, marked as CA in the peak fit) and pyrrolic carbon (C1, marked CP) both with their satellites from π→π*. Fixed convoluted Gaussian- and Lorentz-function (Voigt profile) are applied and iterated for position and intensity. With this, we are able to fit the data with an expected ratio of CA+SCA:CP+SCP of 3:1. For $CoPcF_{16}$, as the C3 position is fluorinated and therefore appears at a much higher binding energy, we can apply a model with three components and their satellites. The differentiation between C1 (marked as CN), C2 (marked as CC) and C3 (marked as CF) with the high resolution at the LowDosePES for an excitation of 300 eV allows for a six-component fit for each of the chemically different carbons and their satellites. The fits also mirror the relative stoichiometric intensities CC+SCC:CN+SCN:CF+SCF of 1:1:2 .

Table S 1 Calculated inelastic mean free paths for photoelectrons emitted from specific core-levels of MoS_2 with different excitation energies. For the calculations we used the density of MoS_2 of 5.06 g cm^{-3}, a molar mass of 160.07 g mol^{-1} and a bandgap of 1.23 eV. For the TPP-2M[26] equation, based on the work of Tanuma, Penn, and Powell, the number of valence electrons is 18. Further values for the S1[27] equation of Seah, are Z(Mo): 42 and Z(S):18 from which the average Z was calculated.

Core-Level (hv)	**E_{Kin}**	**λ (TPP-2M) [nm]**	**λ (S1) [nm]**
S*2p* (230 eV)	62.5	0.47	0.40
S*2p* (1486.6 eV)	1319.6	2.44	2.41
Mo*3d* (300 eV)	65.5	0.47	0.40
Mo*3d* (1486.6 eV)	1252.1	2.38	2.31

Table S2 Fit parameters for the **C*1s*** spectra shown in **Figure 30**. Satellite positions are given relative to respective carbon signals.

CoPc (**LowDosePES**) (1.16 nm)	C_A	SC_A	C_P	SC_P
Position [eV]	284.06	1.67	285.29	2.10
GP [eV]	0.55	0.55	0.55	0.55

LP [eV]	0.20	0.20	0.20	0.20
Rel Area [%]	70.67	7.07	17.83	4.40

CoPc (**LowDosePES**) (0.34 nm)	C_A	SC_A	C_P	SC_P
Position [eV]	283.95	1.6	285.19	1.93
GP [eV]	0.55	0.55	0.55	0.55
LP [eV]	0.20	0.20	0.20	0.20
Rel Area [%]	68.72	6.85	22.56	1.88

$CoPcF_{16}$ (**LowDosePES**) (1.74 nm)	CC	SCC	CN	SCN	CF	SCF
Position [eV]	284.22	1.8	285.37	1.8	286.34	1.67
GP [eV]	0.55	0.55	0.55	0.55	0.55	0.55
LP [eV]	0.20	0.20	0.20	0.20	0.20	0.20
Rel Area [%]	24.57	0.25	17.18	4.28	46.13	7.58

$CoPcF_{16}$ (**LowDosePES**) (0.34 nm)	CC	SCC	CN	SCN	CF	SCF
Position [eV]	284.17	1.7	285.25	1.8	286.29	1.64
GP [eV]	0.38	0.38	0.38	0.38	0.38	0.38
LP [eV]	0.20	0.20	0.20	0.20	0.20	0.20
Rel Area [%]	23.34	0.23	19.05	3.82	46.37	7.18

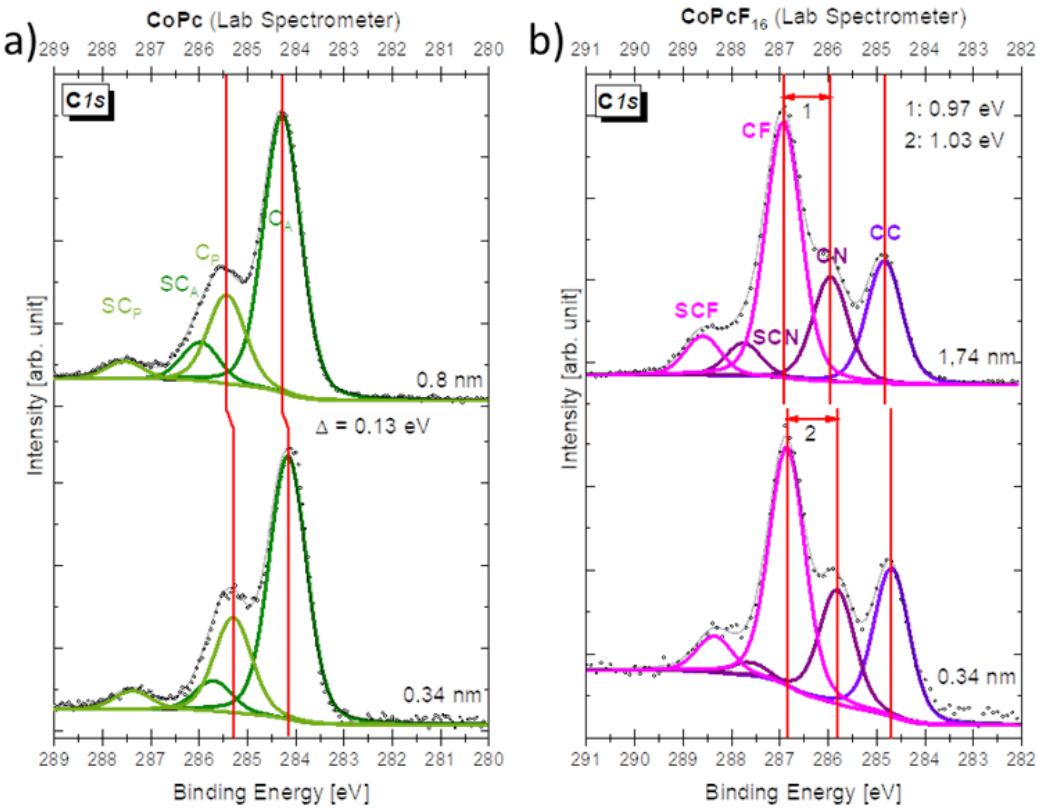

Figure S12 Measurement and fit of the **C***1s* XPS spectra collected at our home setup.

Table S3 Fit parameters for the **C***1s* spectra shown in **Figure S12**. Satellite positions are given relative to respective carbon signals.

CoPc (Lab Spectometer) (0.8 nm)	C_A	SC_A	C_P	SC_P
Position [eV]	284.28	1.70	285.43	2.10
GP [eV]	0.80	0.80	0.80	0.80
LP [eV]	0.20	0.20	0.20	0.20
Rel Area [%]	65.72	9.13	21.00	4.15

CoPc (Lab Spectometer) (0.38 nm)	C_A	SC_A	C_P	SC_P
Position [eV]	284.16	1.60	285.30	2.08

GP [eV]	0.80	0.80	0.80	0.80	
LP [eV]	0.20	0.20	0.20	0.20	
Rel Area [%]	64.66	7.46	23.32	4.55	

$CoPcF_{16}$ (Lab Spectometer) (1.74 nm)	CC	SCC	CN	SCN	CF	SCF
Position [eV]	284.84	1.8	285.96	1.8	286.93	1.67
GP [eV]	0.75	0.75	0.75	0.75	0.75	0.75
LP [eV]	0.20	0.20	0.20	0.20	0.20	0.20
Rel Area [%]	21.97	0.45	18.73	5.88	45.97	7.01

$CoPcF_{16}$ (Lab Spectometer) (0.25 nm)	CC	SCC	CN	SCN	CF	SCF
Position [eV]	284.69	1.8	285.82	1.8	286.85	1.67
GP [eV]	0.75	0.75	0.75	0.75	0.75	0.75
LP [eV]	0.20	0.20	0.20	0.20	0.20	0.20
Rel Area [%]	26.88	0.27	20.61	2.39	43.13	6.56

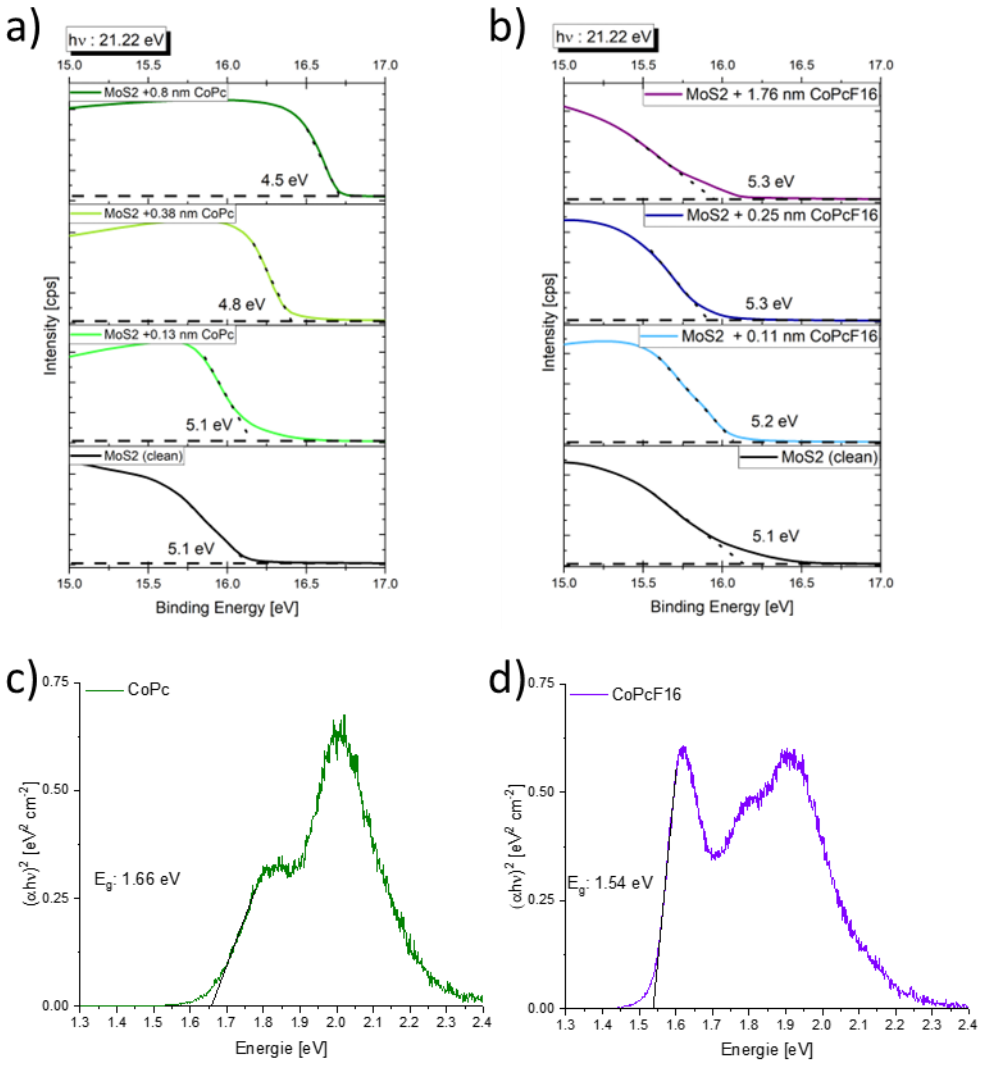

Figure S13 Work function measurements for CoPc (green color code) and $CoPcF_{16}$ (lilac/blue color code) on MoS_2 (black) and the clean MoS_2 substrates are shown in (**a** and **b**). Measurements are done with an applied BIAS voltage between sample and analyzer of 15 V, which was considered in the calculation of the binding energies. In (**c**) (CoPc) and (**d**) ($CoPcF_{16}$) UV-Vis absorbance measurements of the phthalocyanine films, evaporated on glass slides, are shown. The measurements were performed in transmission with a Maya 200 Pro (Ocean Insight).

A brief discussion of common models to describe charge transfer processes at organic/inorganic interfaces

In the ICT model, compared to the FCT model, the transfer of integer charge carriers is described. This is often observed at interfaces of passivated, oxidic semiconductor surfaces with organic molecules. The reason for this is that the charge transfer must take place through tunneling, which in turn only allows the transfer of integer charge carriers. In the molecular film, a situation then prevails in which charged and uncharged molecules are adjacent to each other. Compared to this, FCT often leads to a rehybridization of the molecular states at the surface. For rehybridization, it is essential that the wave functions of the molecules overlap with the wave functions of the substrate. Also, a sufficient number of free charge carriers must be present, therefore FCT is often observed at the interfaces with reactive metals. Lastly, ICT describes the presence of charge neutrality levels (CNLs). Here, the occurrence of macroscopic and microscopic dipoles due to CT at the interfaces plays a major role. Macroscopic dipoles occur when the Fermi levels of the considered semiconductors are misaligned. Charge equalization leads to band bending in the semiconductors. CNLs play no role in this but are the decisive factor in the formation of microscopic dipoles. These microscopic dipoles form when the CT includes CNLs. Compared to macroscopic dipoles, microscopic dipoles are a pure phenomenon of the interface.

6.3 Appendix C

Supporting Information: Orientation of Cobalt-Phthalocyanines on Molybdenum Disulfide: Distinguishing between Single Crystals and Small Flakes

Philipp Haizmann[1,#], Eric Juriatti[1,#], Maren Klein[1], Katharina Greulich[1], Peter Nagel[2,3], Michael Merz[2,3], Stefan Schuppler[2,3] Amir Ghiami[2,3], Ruslan Ovsyannikov[4], Erika Giangrisostomi[4], Thomas Chassé[1], Marcus Scheele[1,], Heiko Peisert[1,*]*

1 Institut für Physikalische und Theoretische Chemie, Universität Tübingen, 72076 Tübingen, Germany

2 Institute for Quantum Materials and Technologies (IQMT), Karlsruhe Institute of Technology (KIT), 76021 Karlsruhe, Germany

3 Karlsruhe Nano and Micro Facility (KNMFi), Karlsruhe Institute of Technology, 76344 Eggenstein-Leopoldshafen, Germany

4 Institute for Methods and Instrumentation for Synchrotron Radiation Research, Helmholtz-Zentrum Berlin für Materialien und Energie GmbH, 12489 Berlin, Germany

[#] These authors contributed equally (P.H., E.J.).

* Corresponding author, heiko.peisert@uni-tuebingen.de, Tel.: (+49) 07071 / 29-76931, Fax: (+49) 07071 / 29-5490 and marcus.scheele@uni-tuebingen.de

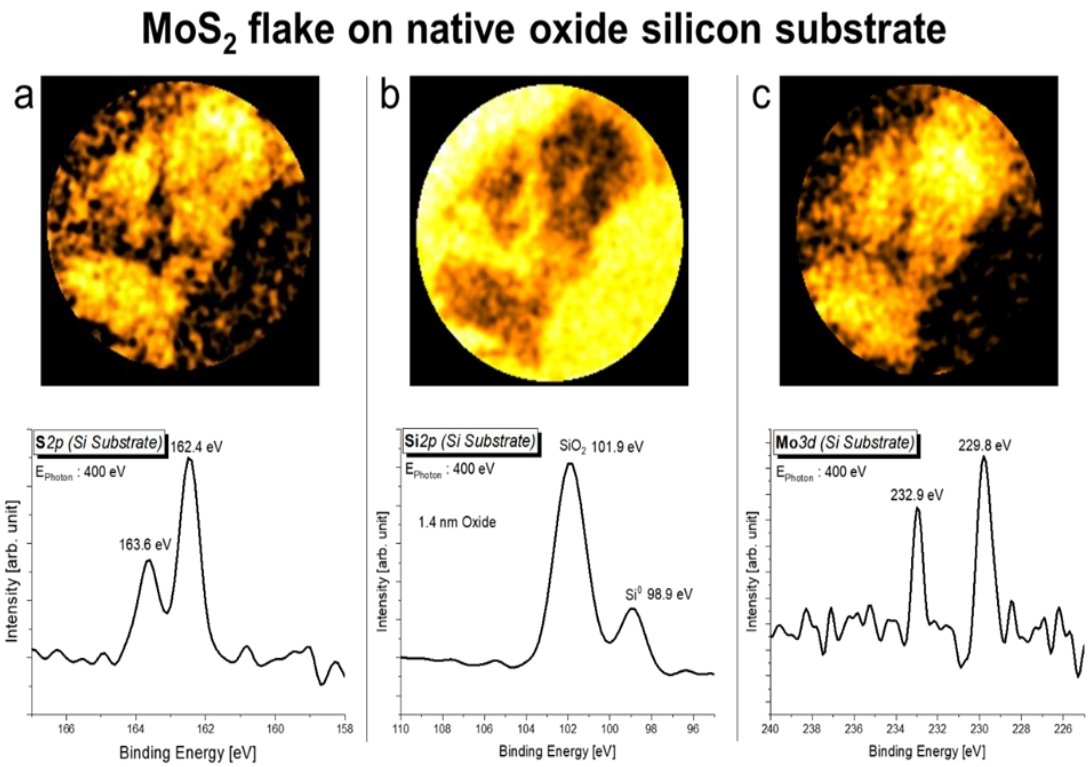

Figure S14 Micro-XPS measurements on a MoS_2 flake on native oxide silicon substrate, referred to as flake 1 in the main text. The intensity maps show the summed intensity measured over the **S***2p* region (**a**), the **Si***2p* region (**b**) and the **Mo***3d* region (**c**). The bright pixels have an overall high intensity while the intensity in darker areas is low. Below each image the average spectra, integrated over the total detector area is shown.

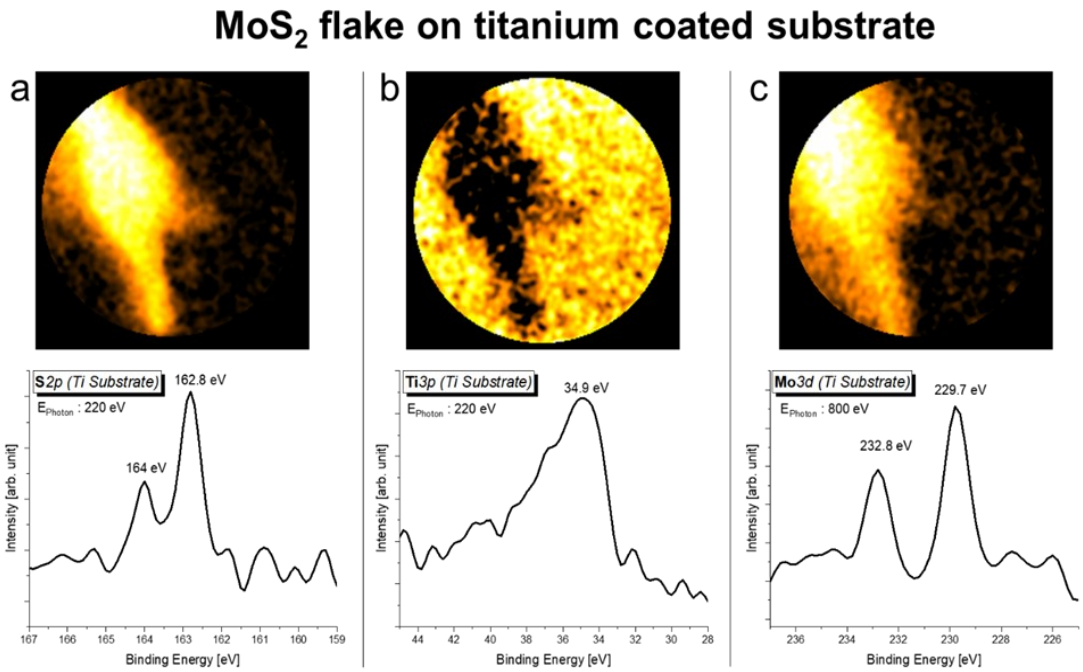

Figure S15 Micro-XPS measurements on a MoS_2 flake on a titanium coated substrate, referred to as flake 2 in the main text. The intensity maps show the summed intensity measured over the **S***2p* region (**a**), the **Ti***3p* region (**b**) and the **Mo***3d* region (**c**). The bright pixels have an overall high intensity while the intensity in darker areas is low. Below each image the average spectra, integrated over the total detector area is shown.

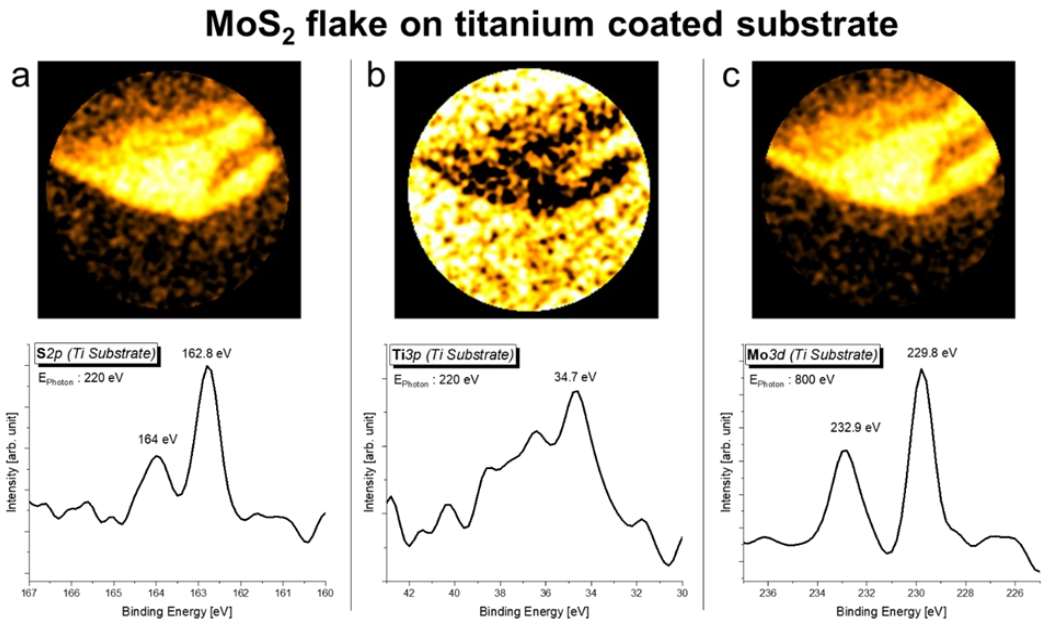

Figure S16 Micro-XPS measurements on a MoS_2 flake on a titanium coated substrate, referred to as flake 3 in the main text. The intensity maps show the summed intensity measured over the **S***2p* region (**a**), the **Ti***3p* region (**b**) and the **Mo***3d* region (**c**). The bright pixels have an overall high intensity while the intensity in darker areas is low. Below each image the average spectra, integrated over the total detector area is shown.

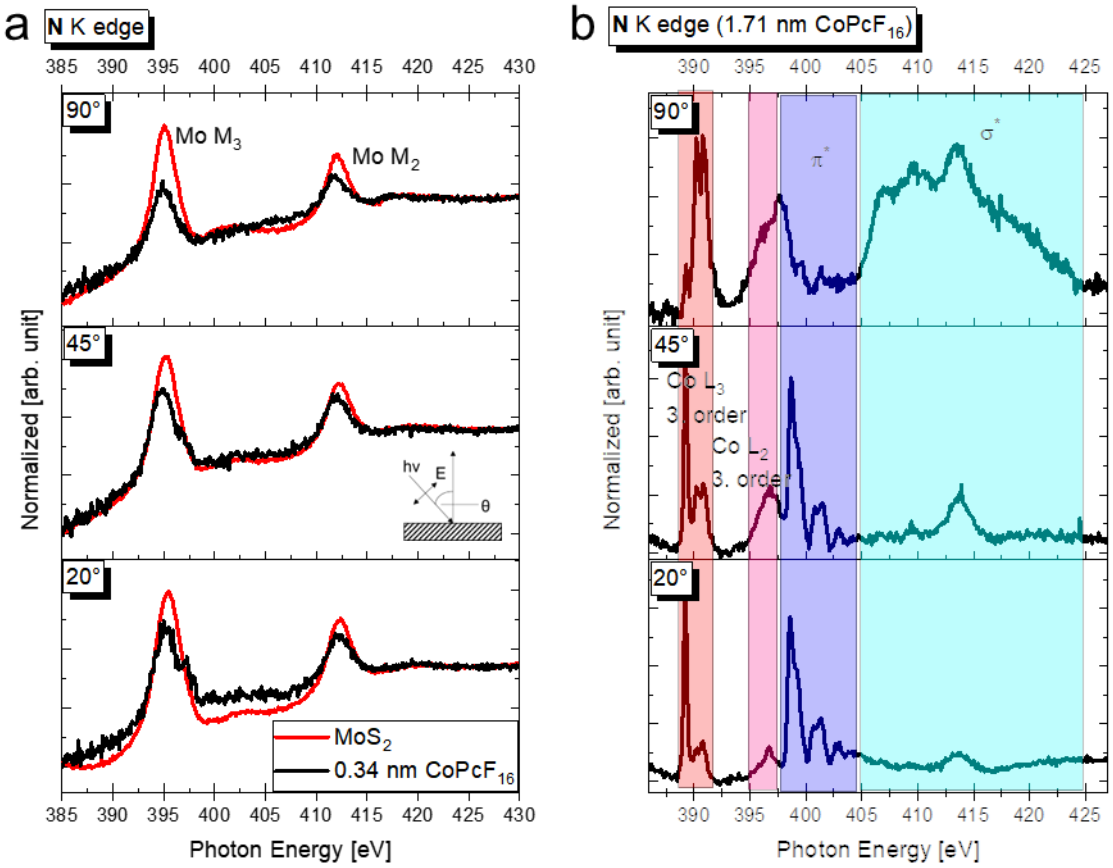

Figure S17 Angle dependent XAS measurements of (**a**) N K edge region of clean bulk MoS_2 (red) and bulk MoS_2 with an overlayer of $CoPcF_{16}$ (black). (**b**) N K edge region after the second deposition of $CoPcF_{16}$.

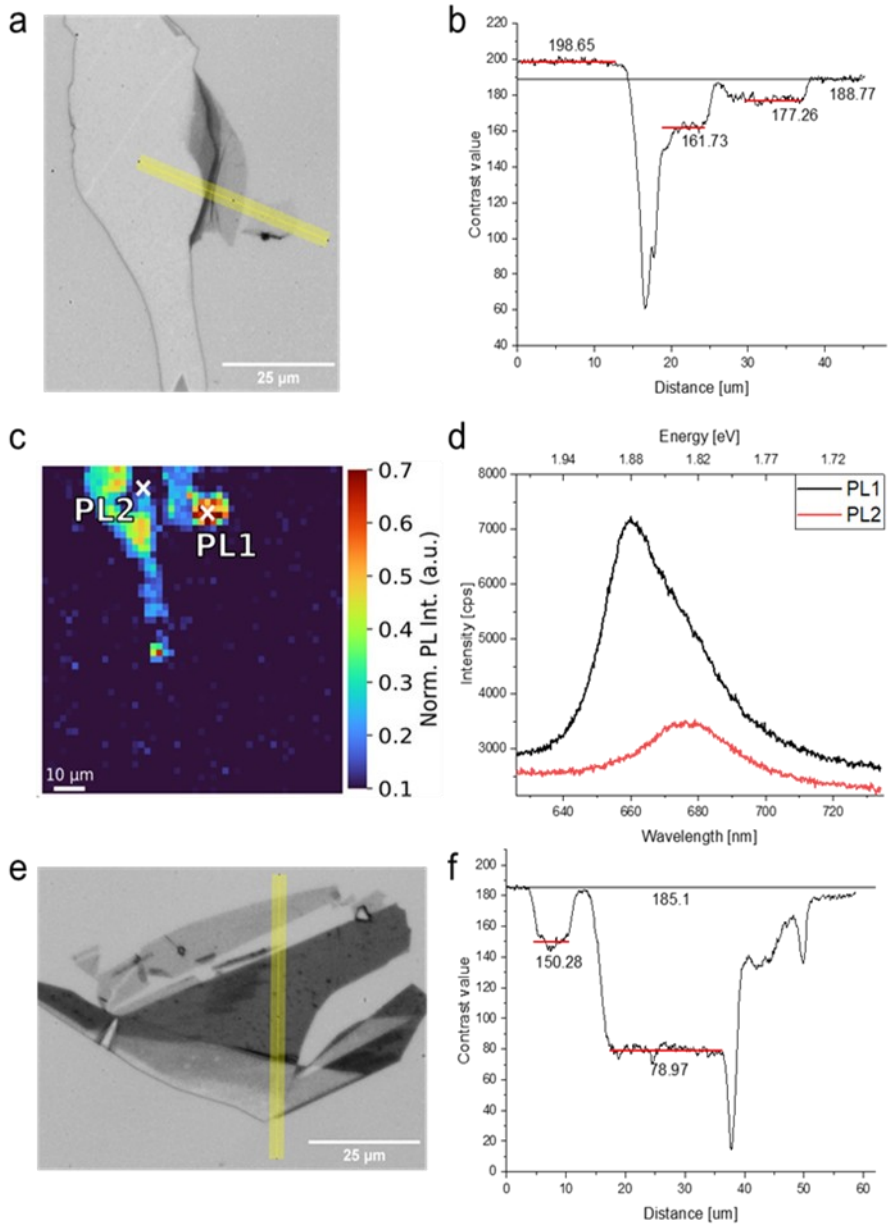

Figure S18 (**a**) and (**e**) display the red channel of the RGB optical microscope images of the samples referred to as flake 2 and 3 in the main text. The contrast profiles produced in (**b**) and (**f**) were generated using ImageJ and correspond to the values along the yellow line shown in (**a**) and (**e**). (**c**) presents a photoluminescence (PL) map of the flake shown in (**a**). Strong PL is observed in the monolayer areas, where direct band transitions occur. (**d**) shows the PL spectra of the monolayer (black) and the bulk (red) region. The peak maximum at an energy of 1.88 eV is typical for structures with two or less layers.[6] In addition, the increased photoluminescence in comparison to the bulk area is characteristic for such thin structures.[8]

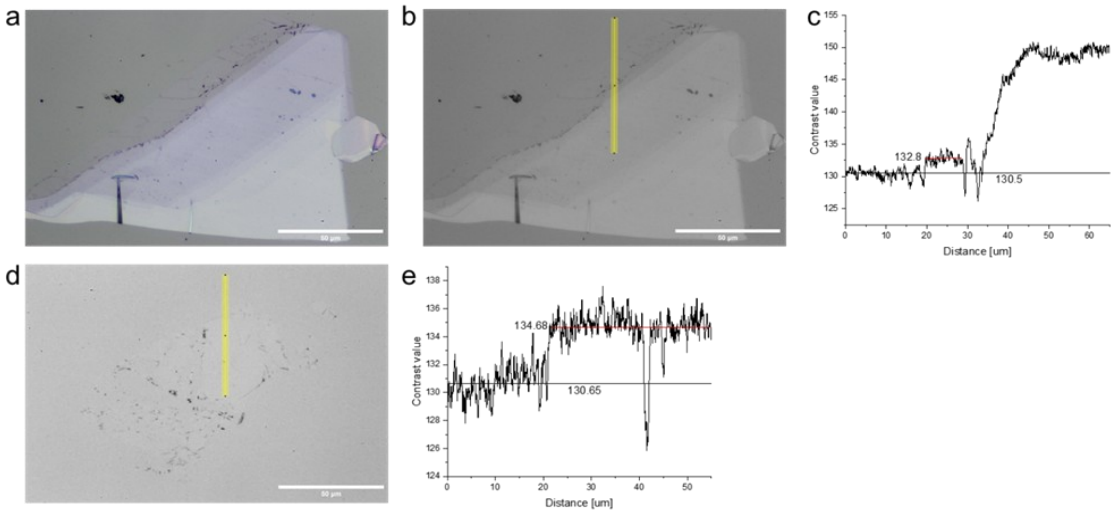

Figure S19 (**a**) displays the optical microscope image of an exfoliated flake on a silicon substrate with a native oxide layer. (**b**) and (**d**) show the red channel of the RGB optical microscope image of the flake presented in (**a**), as well as of flake 1 discussed in the main text. (**c**) and (**e**) depict the contrast values along the lines drawn in (**b**) and (**d**), which were generated using ImageJ.

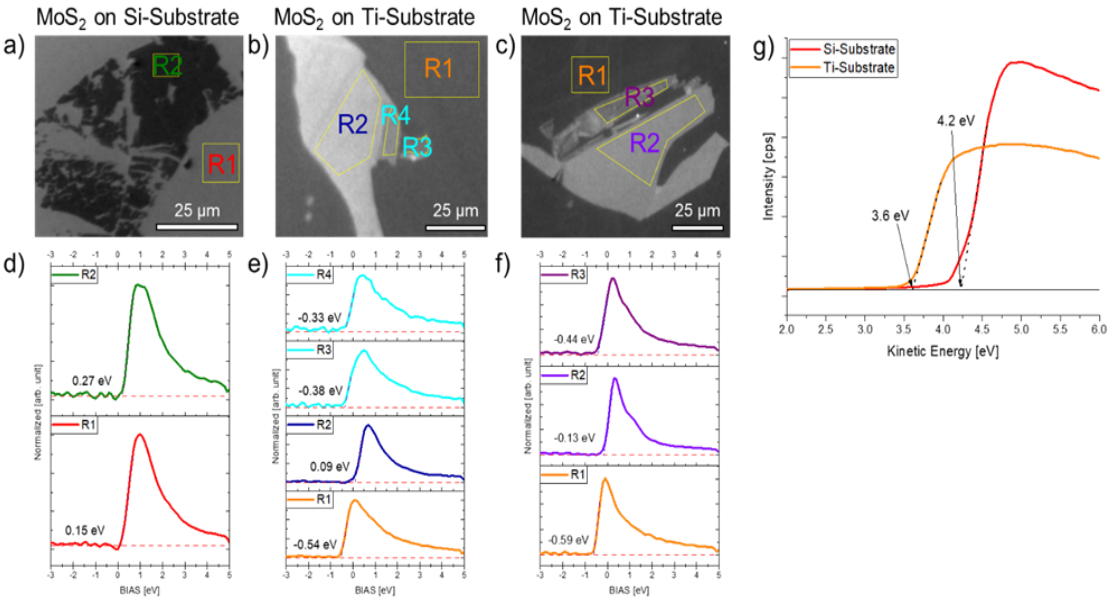

Figure S20 Measured BIAS voltages for flakes 1-3 (**a** – **c**) and the averaged spectra from the marked region of interest (**d** – **f**). (**g**) measured secondary electron cut-off for the clean substrates.

6.4 Appendix D

Supporting Information: Mitigating the Photodegradation of All-Inorganic Mixed-Halide Perovskite Nanocrystals by Ligand Exchange

Jan Wahl,[*,1] Philipp Haizmann,[*,1] Christopher Kirsch,[1] Rene Frecot,[1] Nastasia Mukharamova,[2] Dameli Assalauova,[2] Young Yong Kim,[2] Ivan Zaluzhnyy,[3] Thomas Chasse,[1,4] Ivan A. Vartanyants,[2] Heiko Peisert[#,1] and Marcus Scheele[#,1]

[1] Institut für physikalische und theoretische Chemie, Universität Tübingen,

Auf der Morgenstelle 18, 72076 Tübingen, Germany

[2] Deutsches Elektronen-Synchrotron DESY, Notkestraße 85, 22607 Hamburg, Germany

[3] Institut für Angewante Physik, Universität Tübingen, Auf der Morgenstelle 10, 72076 Tübingen, Germany

[4] Center for Light-Matter Interaction, Sensors & Analytic LISA$^+$, Universität Tübingen, Auf der Morgenstelle 15, 72076 Tübingen, Germany

[*] These authors contributed equally

[#] heiko.peisert@uni-tuebingen.de, marcus.scheele@uni-tuebingen.de

Materials and methods Materials

1-Octadecene (ODE), technical grade, 90%, Sigma Aldrich; Oleic acid (OA), 97%, Acros Organics; Oleylamine (OAm), 80-90%, Acros Organics; Caesium carbonate (Cs_2CO_3), 99.99% (trace metal basis), Acros Organics; Lead(II)iodide (PbI2), 99.999% (trace metal basis), Sigma Aldrich; Lead(II)bromide ($PbBr_2$), ≥98%, Sigma Aldrich; Lead(II)chloride ($PbCl_2$), PuratronicTM, 99.999% (metal trace), Crystalline, Alfa Aesar; Toluene, HPLC grade, 99.8%; Toluene, 99.8%, extra dry, AcroSeal, Acros Organics; zinc-(5-monocarboxyphenyl-10,15,20-triphenylporphyrin) (mZnTPP), TriPorTech; Tetrachloroethylene (TCE), ≥99%, Acros Organics; Kapton® polyimide membranes (125 µm thickness), DuPont

$CsPbX_3$ nanocrystal synthesis

The used nanocrystals were synthesized with two different stoichiometries, namely CsPbBrI2 and CsPbBr2Cl, following the published synthesis route by Krieg et al.[223]

with slight adjustments. For CsPbBrI2 a 20 ml glass reaction vial was used which could be heated to the reaction temperature of 160°C in a custom-made aluminum heating block. Generally, the syntheses were carried out with twice the concentration of precursors compared to literature.

Ligand exchange and thin film preparation

Following the purification, the nanocrystals (NC) were either used as obtained or post-synthetically modified by ligand exchange with zinc-(5-monocarboxyphenyl-10,15,20-triphenylporphyrin) (mZnTPP). The exchange was effectively carried out in solution by adding 0.25 stoichiometric equivalents of mZnTPP to the NC solution. An immediate color change was observed upon addition. The ligand exchange procedure and corresponding analysis is given in more detail in another paper.[241]

The as-synthesized and exchanged NCs were subsequently spin-coated onto custom-made gold substrates under nitrogen atmosphere to prepare thin films. The coating parameters were chosen to be 10 rps for 30 s with a 3 s ramp.

The used substrates were custom made at the LISA+ center Tübingen. A commercially available four-inch silicon wafer with native oxide layer was coated with 10 nm chromium in an evaporation chamber, followed by deposition of a 50 nm gold layer.

Self-assembly into superlattices

To prepare superlattices for the X-ray scattering measurements, the perovskite samples were prepared as 1-3 mM solutions in toluene ($CsPbBrI_2$) or tetrachloroethylene ($CsPbBr_2Cl$) and drop-casted onto Kapton® substrates under inert atmosphere. The substrates were placed inside a petri dish with an additional reservoir of solvent (1 – 2 ml) to slow down the evaporation process and covered with a lid. The samples were allowed to dry for 24 h before the lid was removed and an additional drying process for 5 – 6 h was allowed.

Scanning electron microscopy (SEM)

SEM was carried out at a HITACHI SU8030 electron microscope, utilizing an acceleration voltage of 30 kV. SEM micrographs were taken of thin film samples.

X-ray photoelectron spectroscopy and ultraviolet photoelectron spectroscopy

The thin film samples were analyzed inside an ultrahigh vacuum chamber (base pressure: 2×10^{-10} mbar) with a XR-50M X-ray source from SPECS utilizing monochromatic Al Kα radiation (hv = 1486.6 eV) with a flux of $8.3 \cdot 10^{10}$ photons/s onto a ~ 2 mm^2 area. For photoelectron detection a Phoibos 150 DLD hemispherical photoelectron energy analyzer (SPECS) was used. The spectrometer was calibrated to reproduce the binding energy of **Au***4f*$_{7/2}$ (84.0 eV) and **Cu***2p*$_{3/2}$ (932.6 eV) signals, with photoionization cross sections of 0.2511 and 0.3438, respectively.[3] Measurements were performed under fixed analyzer transmission mode, with an energy resolution of 400 meV and 150 meV for XPS and Ultraviolet photoelectron spectroscopy (UPS), respectively. Custom written scripts were used to measure overview and detailed spectra at specified times during the experiment. Peak fitting was done using the Unifit software package.[249] Peaks are expected to show Voigt profile, meaning a convolution of Lorentzian and Gaussian peaks. The background was modeled with an iterative algorithm to apply Shirley background.

UPS was carried out with similar conditions as XPS measurements. A helium ultraviolet source with an energy of 21.22 eV was used in combination with a Phoibos 150 DLD electron analyzer.

XPS and UPS experiments were conducted on thin film samples.

Small- and wide-angle X-ray scattering

The small- and wide-angle X-ray scattering (SAXS and WAXS) were carried out at the Coherence Applications beamline P10 of the PETRA III synchrotron source at the Deutsche Elektronen-Synchrotron (DESY). The X-ray source provided a beam with a wavelength of λ = 0.0898 nm or an energy of 13.8 keV, the beam was focused on a spot size of roughly 400 x 400 nm^2 with a focal depth of 0.5 mm. A two-dimensional EIGER X4M (Dectris) detector with 2070 x 2167 pixels of size 75 x 75 μm^2 was used, it was located 412 mm away from the sample plane. The detector was positioned in a way to allow simultaneous measurements of SAXS and WAXS. The exposure time of the samples was 0.5 s. The obtained diffraction patterns were analyzed by Bragg peak assignment and radial profiles could be achieved by averaging over the angular coordinates. For SAXS and WAXS measurements superlattice samples were used.

Low Binding energy survey from XPS

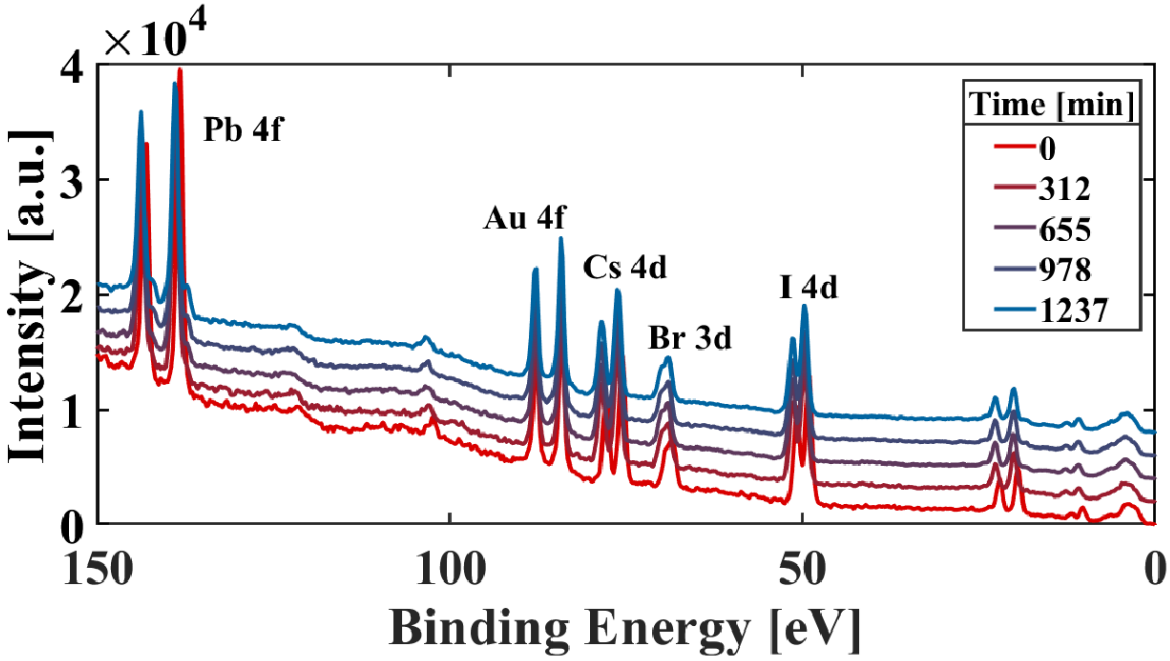

Figure S21 Survey spectra at different times during the X-ray illumination. A shift in peak position for all elements associated with the perovskites can be observed. As the perovskites were deposited on a gold substrate, the **Au***4f* core level peak serves as a reference for the binding energies. Another interesting feature is the occurrence of an additional novel peak in the **Pb***4f* region, visible at lower binding energies after illumination, indicating the decomposition of the nanocrystals (cf. **Figure 35** of the manuscript). Beside of the energetic shift of the **Br***3d* peak no further change could be observed, i.e., it was not possible to detect an additional species for this element arising from the degradation.

Calculation of the I:Pb ratio and temporal evolution of novel lead species

As detail XPS spectra are generally not comparable, the ratio of formed elemental lead and iodine was calculated as follows. The percentages were taken from the ratio of the areas fitted to the detail spectra as shown in **Figure S22**. Subsequently, the areas from the survey spectra were fitted as described in the methods section. The as obtained areas were then multiplied with the percentages from the detail spectra, resulting in areas that are quantitatively comparable.

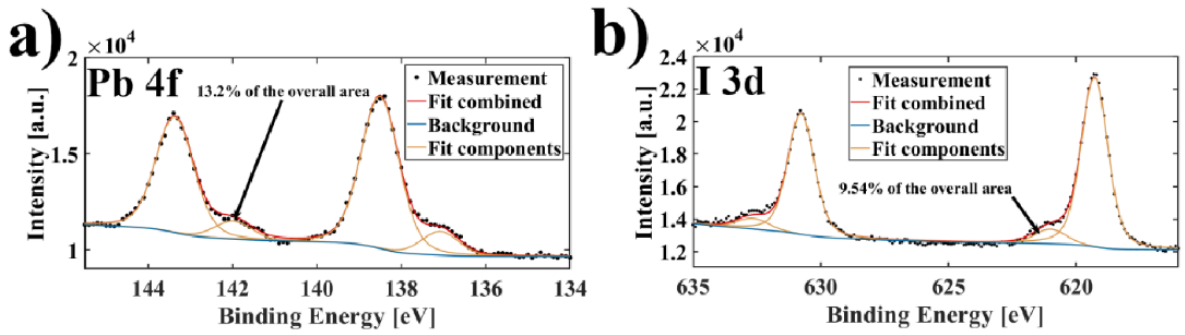

Figure S23 Percentages of the novel formed species after illuminating the native sample for ~ 20 h for (**a**) lead and (**b**) iodide. The amount of newly formed species is given as a percentage of the overall peak area in both cases.

Generally, an error of 10% per fitted peak area is assumed.[250] Additionally, a Gaussian error propagation was carried out since multiple calculations were done with the measured values.

The precise error calculation is given by:

$$\Delta\left(\frac{I_2}{Pb^0}\right) = \Delta R = \sqrt{\left(\frac{\partial R}{\partial A_{I_2}} * \Delta A_{I_2}\right)^2 + \left(\frac{\partial R}{\partial A_{Pb^0}} * \Delta A_{Pb^0}\right)^2} \qquad (46)$$

With the ratio of formed iodine to elemental lead R, the area of iodine A_{I2} and elemental lead A_{Pb0} as well as the corresponding uncertainties denoted by Δ. The error calculation resulted in an error of the ratio of 0.23.

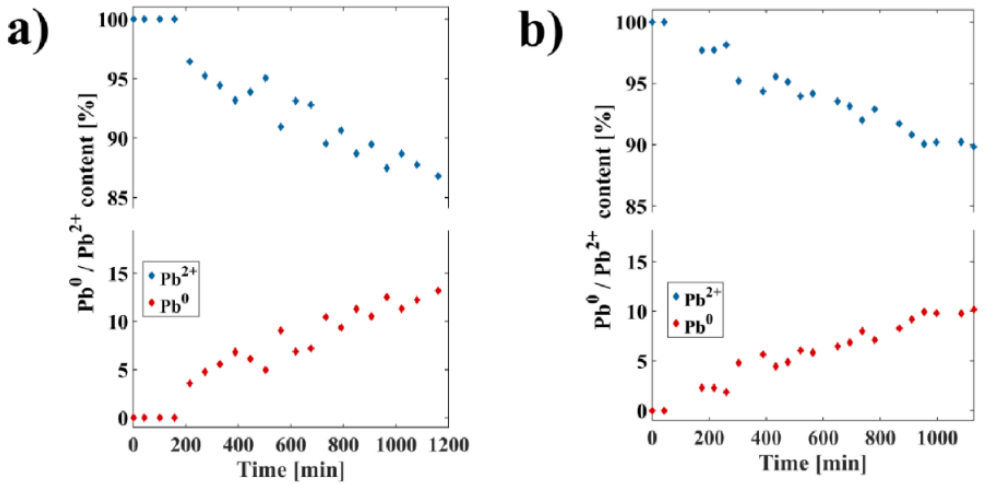

Figure S24 Temporal evolution of elemental lead (Pb^0) for (**a**) $CsPbBrI_2$ and (**b**) $CsPbBr_2Cl$ obtained by fitting the **Pb***4f* XPS spectra in **Figure 35** of the manuscript.

Structural integrity probed by SEM for $CsPbBrI_2$ and $CsPbBr_2Cl$

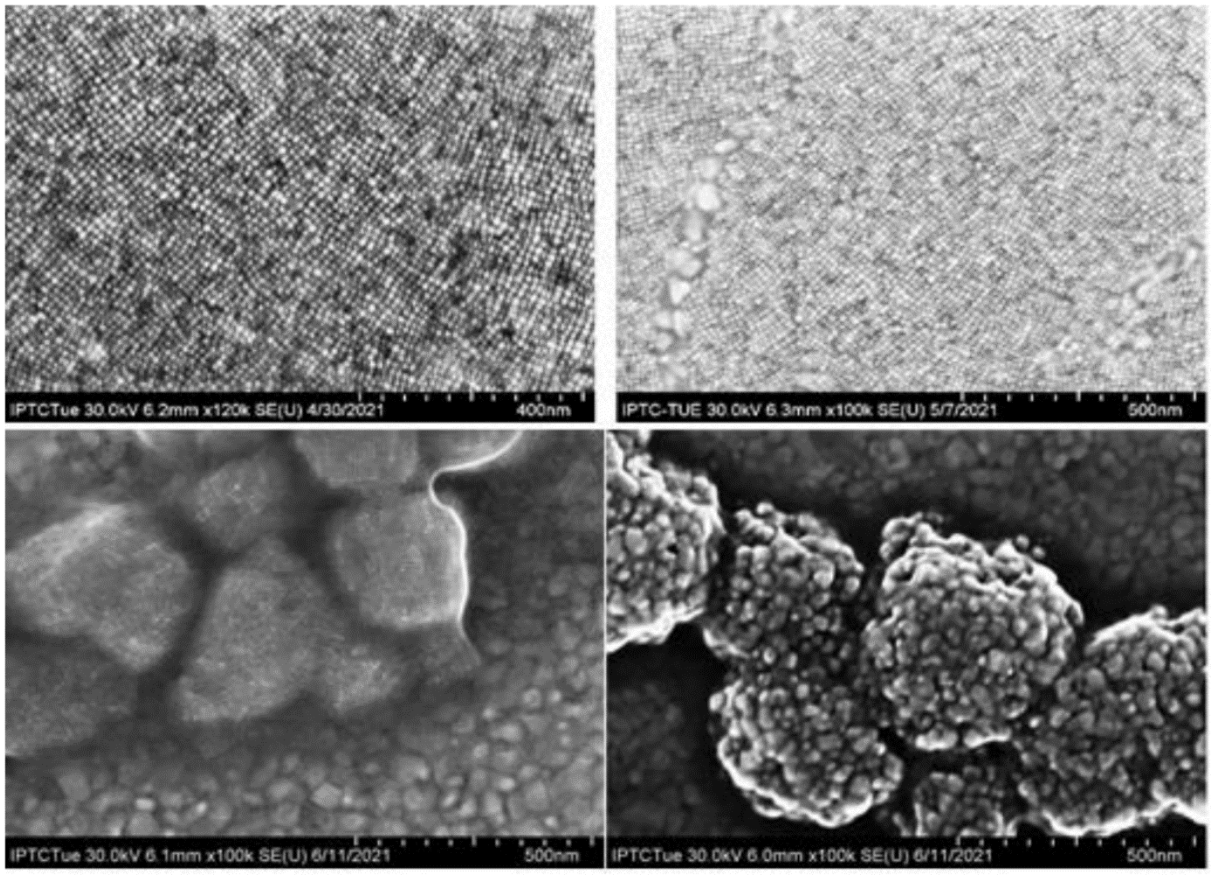

Figure S25 SEM of $CsPbBrI_2$ (top) and $CsPbBr_2Cl$ (bottom) before (left) and after (right) X-ray exposure.

UPS of native and exchanged CsPbBrI2 before and after X-ray illumination

The shifts of the UPS onset were found to be $\Delta native$ = 0.12 eV and ΔTPP = 0.10 eV from fitting. However, as UPS has a resolution limit of one decimal, the value for both shifts was taken to be ~ 0.1 eV.

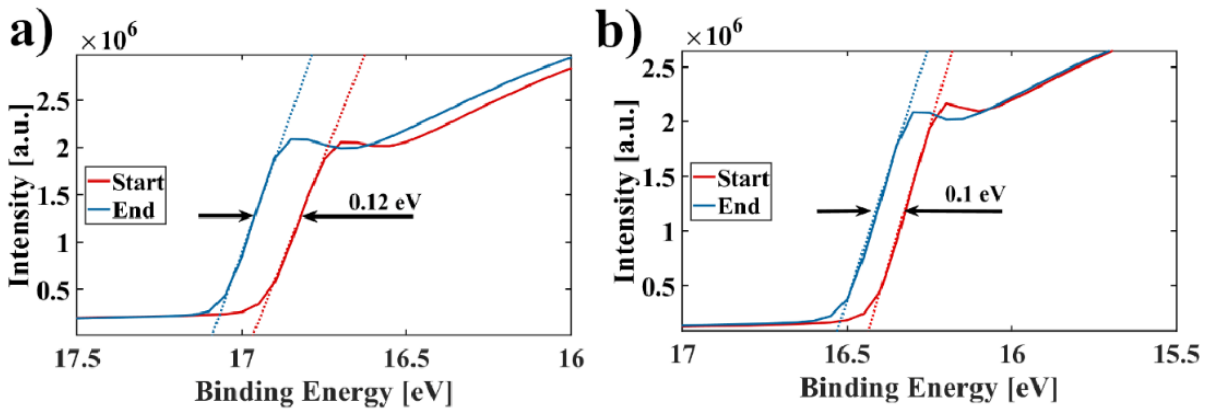

Figure S26 UPS cut-off energies of (**a**) native and (**b**) exchanged $CsPbBrI_2$. The shift in the cut-off energy of ~ 0.1 eV in both cases is found from a linear extrapolation, the shift indicates a reduction of the work function by the same amount. The fits are indicated as dotted lines.

Further example of the lattice contraction

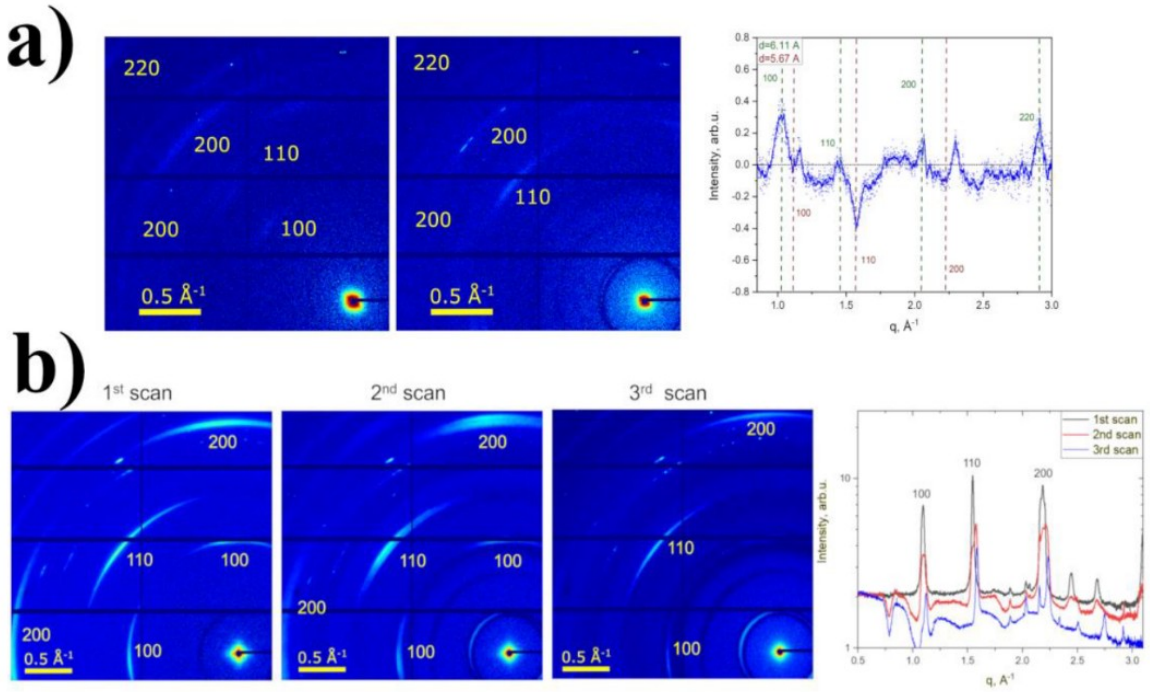

Figure S27 More examples of the isotropic lattice contraction for (**a**) $CsPbBrI_2$ and (**b**) $CsPbBr_2Cl$

UPS overview spectra and onset

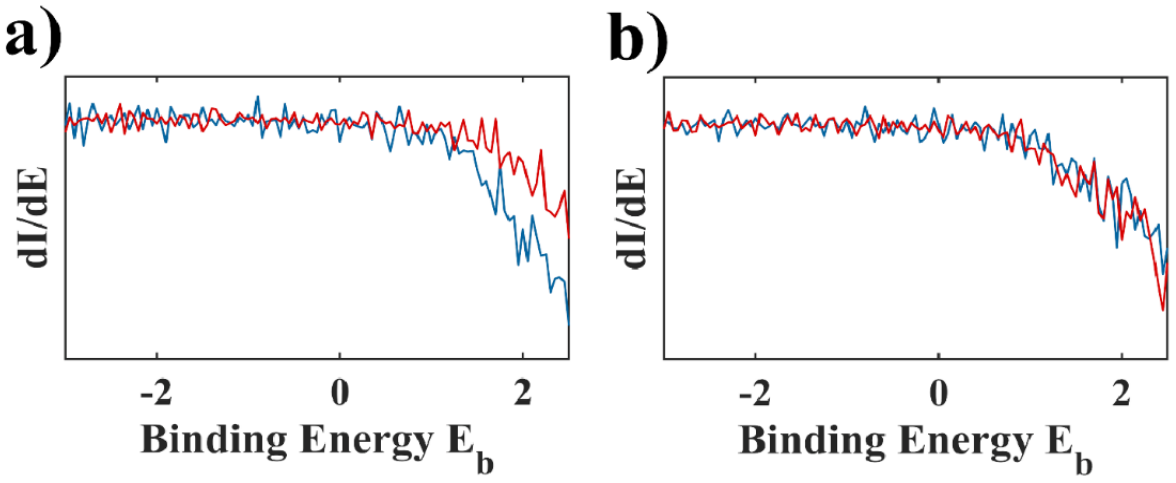

Figure S28 The onset remained constant at ~ 1 eV, shown by the derivative of the UPS spectrum for (**a**) native and (**b**) mZnTPP functionalized $CsPbBrI_2$. The constant onset refers to the Fermi level being located in the middle of the band gap before and after the illumination. Therefore, a shift of the energy states in their entirety is at hand.

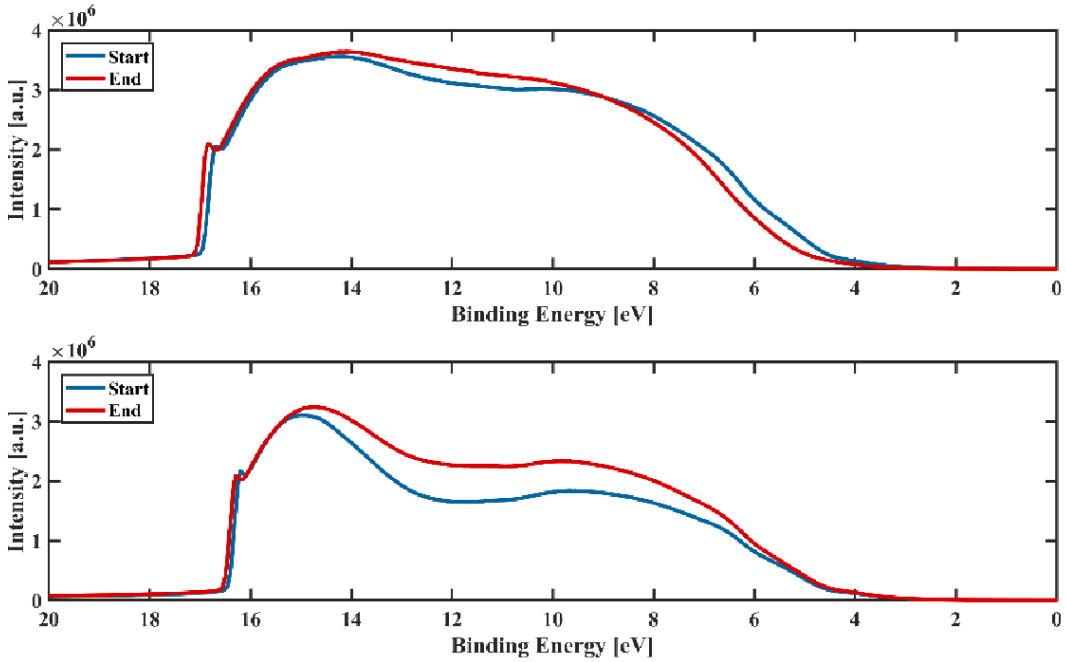

Figure S29 UPS overview spectra of the native $CsPbBrI_2$ sample (top) and the mZnTPP exchanges sample (bottom). The cutoff energies are shifted by ~ 0.5 eV.

Iodide preservation for $CsPbBrI_2$ functionalized with mZnTPP

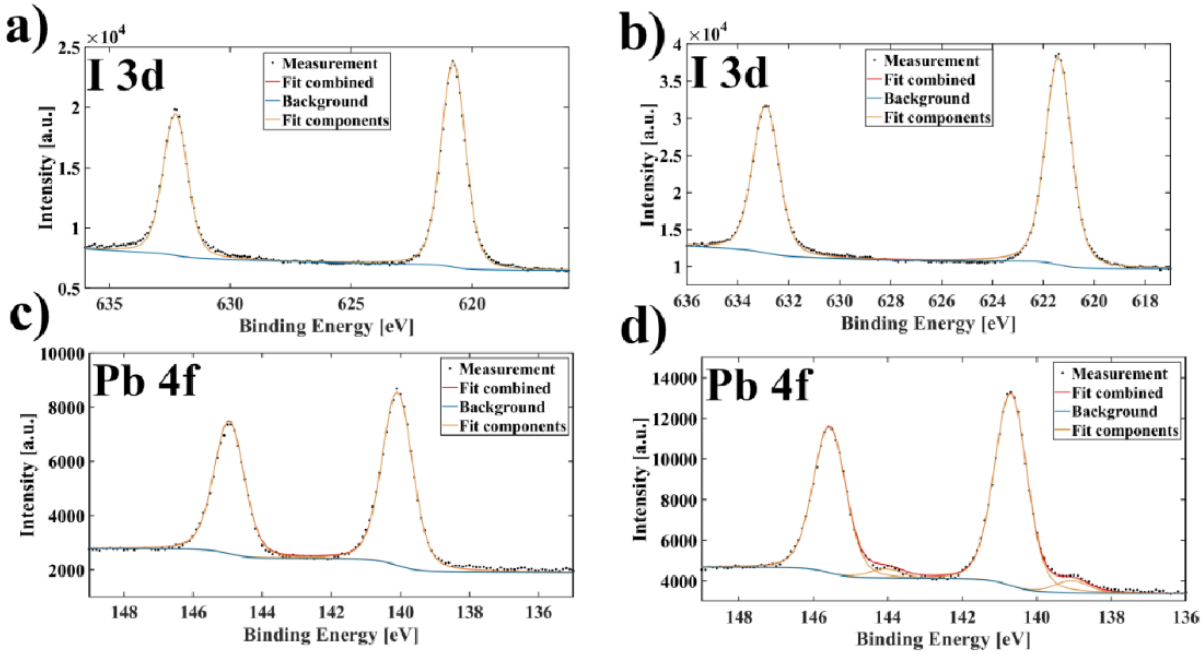

Figure S30 I 3d (**a** + **b**) and Pb 4f (**c** + **d**) XPS detail spectra for the mZnTPP exchanged sample. The decomposition of the NCs started as indicated by the formation of elemental lead. However, there are no novel peaks for the iodide signal.

Photoluminescence loss after X-ray illumination

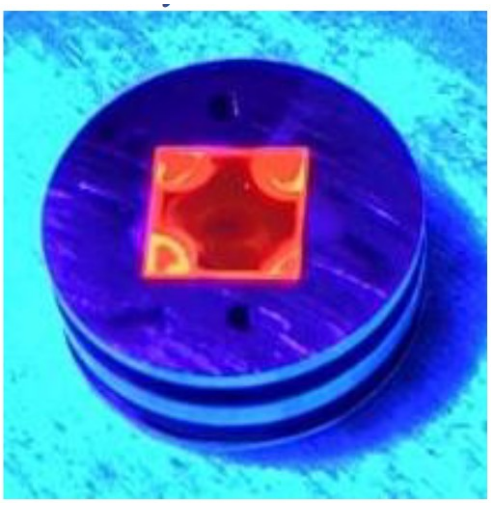

Figure S31 $CsPbBrI_2$ sample after exposure to X-ray radiation for ~ 21 h. The middle of the sample was illuminated, the area exhibits a darker spot corresponding to a loss of PL response.

7 Register of Symbols and Abbreviations

1T / 2H / 3R	Polytypes of MoS_2 (metallic, semiconducting, rhombohedral)
2D	Two Dimensional
4-NBD	4-nitrobenzenediazonium tetrafluoroborate
Å	Angstrom
ARPES	Angle-Resolved Photoemission Spectroscopy
ARTOF	Angle-Resolved Time-of-Flight (detector)
a.u.	Arbitrary Units
CBM	Conduction Band Minimum
COINFLIP	Coupled Organic Inorganic Nanostructures for Fast, Light-induced Data Processing
CoPc	Cobalt Phthalocyanine
CoPcF16	Perfluorinated Cobalt Phthalocyanine
CS_2	Carbon disulfide
CT	Charge Transfer
CuPc	Copper Phthalocyanine
°C	Degree Celcius
DFT	Density Functional Theory
DIW	Direct Laser Induced Writing
EA	Electron Affinity
E_B	Binding Energy
E_F	Fermi Level
E_g	Band Gap
E_{kin}/E_k	Kinetic Energy
ERC	European Research Council

ELA	Energy Level Alignment
E_{vac}	Vacuum Level
eV	Electron Volt (1.602×10^{-19} C)
eq	Equivalent
ε_0	Vacuum Permittivity (8.854×10^{-12} F/m)
F	Farad
FAT	Fixed Analyzer Transmission
FCT	Fractional Charge Transfer
FFT	Fast Fourier Transform
FTIR	Fourier-Transform Infrared
FWHM	Full Width at Half Maximum
Γ,M,K,Q	High-symmetry points of the Brillouin zone
g	Gram
hBN	Hexagonal Boron Nitride
hv	Photon Energy
HRTEM	High-Resolution Transmission Electron Microscopy
HMDS	1,1,1,3,3,3-Hexamethyldisilazane
HOMO	Highest Occupied Molecular Orbital
ICDD	International Centre for Diffraction Data
ICT	Integer Charge Transfer
IE	Ionization Energy
IGS	Induced Gap States
IMFP	Inelastic Mean Free Path
J	Joule

j	Total angular momentum quantum number
K	Kelvin
K	Wave vector / Momentum
kV	Kilovolt
l	Azimuthal quantum number
λ	Mean Free Path
LED	Light-Emitting Diode
LEED	Low-Energy Electron Diffraction
LHP	Lead Halide Perovskite
LSPRs	Localized Surface Plasmon Resonances
LUMO	Lowest Unoccupied Molecular Orbital
m	Meter
min	Minute
M/mM	Molar/Millimolar
m_e	Electron Mass (9.109×10^{-31} kg)
μ_0	Magnetic Constant (1.2566×10^{-6} N/A^2)
mol	Mole
MoS_2	Molybdenum disulfide
$MoCl_5$	Molybdenum(V) chloride
$([Mo(Ac)_2]_2)$	Molybdenum(II) acetate
mZnTPP	Zinc-(5-monocarboxyphenyl-10,15,20-triphenylporphyrin)
NEXAFS	Near Edge X-ray Absorption Fine Structure
NCs	Nanocrystals
N/m^2	Newton per Square Meter

nm	Nanometer
NS	Nanosheet
NPLs	Nanoplatelets
OA	Oleic acid
OlAm	Oleylamine
PEEM	Photoemission Electron Microscopy
PES	Photoelectron Spectroscopy
PL	Photoluminescence
Φ	Work Function
PXRD	Powder X-ray Diffraction
rcf	Relative Centrifugal Field
s	Spin quantum number
SAED	Selected Area Electron Diffraction
SAXS	Small-Angle X-ray Scattering
SECO	Secondary Electron Cutoff
SEM	Scanning Electron Microscopy
SERS	Surface-Enhanced Raman Spectroscopy
STM	Scanning Tunneling Microscopy
TAA	Thioacetamide
TAS	Transient absorption spectroscopy
TCNQ	Tetracyanoquinodimethane
TEM	Transmission Electron Microscopy
TEY	Total Electron Yield
TMDC/TMD	Transition metal dichalcogenide

TPcs	Transition metal phthalocyanines
UHV	Ultra-High Vacuum
UPS	Ultraviolet Photoelectron Spectroscopy
VBM	Valence Band Maximum
WAXS	Wide-Angle X-ray Scattering
WS_2	Tungsten disulfide
XAS	X-ray Absorption Spectroscopy
XPS	X-ray Photoelectron Spectroscopy
XRD	X-ray Diffraction
Z	Atomic Number

8 List of Figures

9 List of Tables

10 Bibliography

1. P. van der Heide, *X-Ray Photoelectron Spectroscopy*, John Wiley & Sons, Inc., 2011.
2. K. K. Kam and B. A. Parkinson, *The Journal of Physical Chemistry*, 2002, **86**, 463-467.
3. J. J. Yeh and I. Lindau, *Atomic Data and Nuclear Data Tables*, 1985, **32**, 1-155.
4. R. Roldán, J. A. Silva-Guillén, M. P. López-Sancho, F. Guinea, E. Cappelluti and P. Ordejón, *Annalen der Physik*, 2014, **526**, 347-357.
5. K. Schönauer, S. Weiss, V. Feyer, D. Lüftner, B. Stadtmüller, D. Schwarz, T. Sueyoshi, C. Kumpf, P. Puschnig, M. G. Ramsey, F. S. Tautz and S. Soubatch, *Physical Review B*, 2016, **94**, 205144.
6. S. Golovynskyi, I. Irfan, M. Bosi, L. Seravalli, O. I. Datsenko, I. Golovynska, B. Li, D. Lin and J. Qu, *Applied Surface Science*, 2020, **515**, 146033.
7. V. V. Maslyuk, V. Y. Aristov, O. V. Molodtsova, D. V. Vyalikh, V. M. Zhilin, Y. A. Ossipyan, T. Bredow, I. Mertig and M. Knupfer, *Applied Physics A*, 2009, **94**, 485-489.
8. A. Splendiani, L. Sun, Y. Zhang, T. Li, J. Kim, C. Y. Chim, G. Galli and F. Wang, *Nano Lett*, 2010, **10**, 1271-1275.
9. K. S. Novoselov, A. K. Geim, S. V. Morozov, D. Jiang, M. I. Katsnelson, I. V. Grigorieva, S. V. Dubonos and A. A. Firsov, *Nature*, 2005, **438**, 197-200.
10. D. Voiry, A. Mohite and M. Chhowalla, *Chem Soc Rev*, 2015, **44**, 2702-2712.
11. D. J. Late, B. Liu, H. S. Matte, V. P. Dravid and C. N. Rao, *ACS Nano*, 2012, **6**, 5635-5641.
12. Y. Liang, H. D. Yoo, Y. Li, J. Shuai, H. A. Calderon, F. C. Robles Hernandez, L. C. Grabow and Y. Yao, *Nano Lett*, 2015, **15**, 2194-2202.
13. J. Brivio, D. T. Alexander and A. Kis, *Nano Lett*, 2011, **11**, 5148-5153.
14. J. T. Alexander V. Kolobov, *Two-Dimensional Transition-Metal Dichalcogenides*, Springer Cham, 2016.
15. T. Böker, R. Severin, A. Müller, C. Janowitz, R. Manzke, D. Voß, P. Krüger, A. Mazur and J. Pollmann, *Physical Review B*, 2001, **64**.
16. T. M. Willey, M. Bagge-Hansen, J. R. I. Lee, R. Call, L. Landt, T. van Buuren, C. Colesniuc, C. Monton, I. Valmianski and I. K. Schuller, *The Journal of Chemical Physics*, 2013, **139**, 034701.
17. C. C. L. a. A. B. P. Lever, *Phthalocyanines: Properties and Applications*, VCH Publishers, Inc., 1989.
18. H. Peisert, J. Uihlein, F. Petraki and T. Chassé, *Journal of Electron Spectroscopy and Related Phenomena*, 2015, **204**, 49-60.
19. F. Petraki, H. Peisert, J. Uihlein, U. Aygul and T. Chasse, *Beilstein J Nanotechnol*, 2014, **5**, 524-531.
20. T. Kroll, R. Kraus, R. Schonfelder, V. Y. Aristov, O. V. Molodtsova, P. Hoffmann and M. Knupfer, *J Chem Phys*, 2012, **137**, 054306.

21. Q. Zhou, Z. F. Liu, T. J. Marks and P. Darancet, *J Phys Chem A*, 2021, **125**, 4055-4061.
22. D. Cahen and A. Kahn, *Advanced Materials*, 2003, **15**, 271-277.
23. T. Fließbach, *Quantenmechanik – Lehrbuch zur Theoretischen Physik III*, Spektrum Akademischer Verlag, 2005.
24. C. N. Berglund and W. E. Spicer, *Physical Review*, 1964, **136**, A1030-A1044.
25. M. P. Seah and W. A. Dench, *Surface and Interface Analysis*, 1979, **1**, 2-11.
26. H. Shinotsuka, S. Tanuma, C. J. Powell and D. R. Penn, *Surf Interface Anal*, 2018, **51**, 427-457.
27. M. P. Seah, *Surface and Interface Analysis*, 2011, **44**, 497-503.
28. A. Kahn, *Materials Horizons*, 2016, **3**, 7-10.
29. J. Stöhr, *NEXAFS Spectroscopy*, 1992.
30. E. Giangrisostomi, R. Ovsyannikov, F. Sorgenfrei, T. Zhang, A. Lindblad, Y. Sassa, U. B. Cappel, T. Leitner, R. Mitzner, S. Svensson, N. Mårtensson and A. Föhlisch, *Journal of Electron Spectroscopy and Related Phenomena*, 2018, **224**, 68-78.
31. P. Tonndorf, R. Schmidt, R. Schneider, J. Kern, M. Buscema, G. A. Steele, A. Castellanos-Gomez, H. S. J. van der Zant, S. Michaelis de Vasconcellos and R. Bratschitsch, *Optica*, 2015, **2**, 347-352.
32. Y. M. He, G. Clark, J. R. Schaibley, Y. He, M. C. Chen, Y. J. Wei, X. Ding, Q. Zhang, W. Yao, X. Xu, C. Y. Lu and J. W. Pan, *Nat Nanotechnol*, 2015, **10**, 497-502.
33. T. Mueller and E. Malic, *npj 2D Materials and Applications*, 2018, **2**, 29.
34. M. Druppel, T. Deilmann, P. Kruger and M. Rohlfing, *Nat Commun*, 2017, **8**, 2117.
35. A. Chernikov, T. C. Berkelbach, H. M. Hill, A. Rigosi, Y. Li, O. B. Aslan, D. R. Reichman, M. S. Hybertsen and T. F. Heinz, *Phys Rev Lett*, 2014, **113**, 076802.
36. P. Schiettecatte, P. Geiregat and Z. Hens, *The Journal of Physical Chemistry C*, 2019, **123**, 10571-10577.
37. M. Amani, D. H. Lien, D. Kiriya, J. Xiao, A. Azcatl, J. Noh, S. R. Madhvapathy, R. Addou, S. Kc, M. Dubey, K. Cho, R. M. Wallace, S. C. Lee, J. H. He, J. W. Ager, 3rd, X. Zhang, E. Yablonovitch and A. Javey, *Science*, 2015, **350**, 1065-1068.
38. D. H. Lien, S. Z. Uddin, M. Yeh, M. Amani, H. Kim, J. W. Ager, 3rd, E. Yablonovitch and A. Javey, *Science*, 2019, **364**, 468-471.
39. A. O. A. Tanoh, J. Alexander-Webber, J. Xiao, G. Delport, C. A. Williams, H. Bretscher, N. Gauriot, J. Allardice, R. Pandya, Y. Fan, Z. Li, S. Vignolini, S. D. Stranks, S. Hofmann and A. Rao, *Nano Lett*, 2019, **19**, 6299-6307.
40. A. P. Frauendorf, A. Niebur, L. Harms, S. Shree, B. Urbaszek, M. Oestreich, J. Hübner and J. Lauth, *The Journal of Physical Chemistry C*, 2021, **125**, 18841-18848.
41. D. Xiao, G. B. Liu, W. Feng, X. Xu and W. Yao, *Phys Rev Lett*, 2012, **108**, 196802.

42. F. Bussolotti, H. Kawai, Z. E. Ooi, V. Chellappan, D. Thian, A. L. C. Pang and K. E. J. Goh, *Nano Futures*, 2018, **2**, 032001.
43. L. Li, L. Shao, X. Liu, A. Gao, H. Wang, B. Zheng, G. Hou, K. Shehzad, L. Yu, F. Miao, Y. Shi, Y. Xu and X. Wang, *Nat Nanotechnol*, 2020, **15**, 743-749.
44. M. Zhou, Z. Zhang, K. Huang, Z. Shi, R. Xie and W. Yang, *Nanoscale*, 2016, **8**, 15262-15272.
45. A. Thomas and K. B. Jinesh, *ACS Omega*, 2022, **7**, 6531-6538.
46. A. Niebur, T. Lorenz, M. Schreiber, G. Seifert, S. Gemming and J.-O. Joswig, *Physical Review Materials*, 2021, **5**, 064001.
47. K. Wu, X. Li, W. Wang, Y. Huang, Q. Jiang, W. Li, Y. Chen, Y. Yang and C. Li, *ACS Catalysis*, 2021, **12**, 8-17.
48. B.-H. Kim, M.-H. Jang, H. Yoon, H. J. Kim, Y.-H. Cho, S. Jeon and S.-H. Song, *NPG Asia Materials*, 2021, **13**, 41.
49. C. Meerbach, B. Klemmed, D. Spittel, C. Bauer, Y. J. Park, R. Hubner, H. Y. Jeong, D. Erb, H. S. Shin, V. Lesnyak and A. Eychmuller, *ACS Appl Mater Interfaces*, 2020, **12**, 13148-13155.
50. S. V. Sivaram, A. T. Hanbicki, M. R. Rosenberger, G. G. Jernigan, H. J. Chuang, K. M. McCreary and B. T. Jonker, *ACS Appl Mater Interfaces*, 2019, **11**, 16147-16155.
51. Z. X. Gan, L. Z. Liu, H. Y. Wu, Y. L. Hao, Y. Shan, X. L. Wu and P. K. Chu, *Applied Physics Letters*, 2015, **106**, 233113.
52. T. P. Nguyen, W. Sohn, J. H. Oh, H. W. Jang and S. Y. Kim, *The Journal of Physical Chemistry C*, 2016, **120**, 10078-10085.
53. J. Fouladi-Oskouei, S. Shojaei and Z. Liu, *J Phys Condens Matter*, 2018, **30**, 145301.
54. Q. Zhao, T. Wang, Y. K. Ryu, R. Frisenda and A. Castellanos-Gomez, *Journal of Physics: Materials*, 2020, **3**, 016001.
55. H. Kim, D. Ovchinnikov, D. Deiana, D. Unuchek and A. Kis, *Nano Lett*, 2017, **17**, 5056-5063.
56. X. Fan, P. Xu, D. Zhou, Y. Sun, Y. C. Li, M. A. Nguyen, M. Terrones and T. E. Mallouk, *Nano Lett*, 2015, **15**, 5956-5960.
57. S. S. Chou, Y. K. Huang, J. Kim, B. Kaehr, B. M. Foley, P. Lu, C. Dykstra, P. E. Hopkins, C. J. Brinker, J. Huang and V. P. Dravid, *J Am Chem Soc*, 2015, **137**, 1742-1745.
58. C. Backes, D. Campi, B. M. Szydlowska, K. Synnatschke, E. Ojala, F. Rashvand, A. Harvey, A. Griffin, Z. Sofer, N. Marzari, J. N. Coleman and D. D. O'Regan, *ACS Nano*, 2019, **13**, 7050-7061.
59. J. N. Coleman, M. Lotya, A. O'Neill, S. D. Bergin, P. J. King, U. Khan, K. Young, A. Gaucher, S. De, R. J. Smith, I. V. Shvets, S. K. Arora, G. Stanton, H. Y. Kim, K. Lee, G. T. Kim, G. S. Duesberg, T. Hallam, J. J. Boland, J. J. Wang, J. F. Donegan, J. C. Grunlan, G. Moriarty, A. Shmeliov, R. J. Nicholls, J. M. Perkins, E. M. Grieveson, K. Theuwissen, D. W. McComb, P. D. Nellist and V. Nicolosi, *Science*, 2011, **331**, 568-571.
60. A. Jawaid, D. Nepal, K. Park, M. Jespersen, A. Qualley, P. Mirau, L. F. Drummy and R. A. Vaia, *Chemistry of Materials*, 2015, **28**, 337-348.

61. G. Pippia, A. Rousaki, M. Barbone, J. Billet, R. Brescia, A. Polovitsyn, B. Martín-García, M. Prato, F. De Boni, M. M. Petrić, A. Ben Mhenni, I. Van Driessche, P. Vandenabeele, K. Müller and I. Moreels, *ACS Applied Nano Materials*, 2022, **5**, 10311-10320.
62. B. Mahler, V. Hoepfner, K. Liao and G. A. Ozin, *J Am Chem Soc*, 2014, **136**, 14121-14127.
63. D. Son, S. I. Chae, M. Kim, M. K. Choi, J. Yang, K. Park, V. S. Kale, J. H. Koo, C. Choi, M. Lee, J. H. Kim, T. Hyeon and D. H. Kim, *Adv Mater*, 2016, **28**, 9326-9332.
64. N. Savjani, E. A. Lewis, M. A. Bissett, J. R. Brent, R. A. W. Dryfe, S. J. Haigh and P. O'Brien, *Chemistry of Materials*, 2016, **28**, 657-664.
65. Y. Pang, M. N. Uddin, W. Chen, S. Javaid, E. Barker, Y. Li, A. Suvorova, M. Saunders, Z. Yin and G. Jia, *Adv Mater*, 2019, **31**, e1905540.
66. G. Almeida, L. Goldoni, Q. Akkerman, Z. Dang, A. H. Khan, S. Marras, I. Moreels and L. Manna, *ACS Nano*, 2018, **12**, 1704-1711.
67. B. G. Kumar and K. Muralidharan, *RSC Adv.*, 2014, **4**, 28219-28224.
68. Q. Liu, X. Li, Q. He, A. Khalil, D. Liu, T. Xiang, X. Wu and L. Song, *Small*, 2015, **11**, 5556-5564.
69. P. Zhou, P. Schiettecatte, M. Vandichel, A. Rousaki, P. Vandenabeele, Z. Hens and S. Singh, *Crystal Growth & Design*, 2021, **21**, 1451-1460.
70. X. Qian, J. Liu, L. Fu and J. Li, *Science*, 2014, **346**, 1344-1347.
71. F. Manteiga Vazquez, Q. Yu, L. F. Klepzig, L. D. A. Siebbeles, R. W. Crisp and J. Lauth, *J Phys Chem Lett*, 2021, **12**, 680-685.
72. M. S. Sokolikova and C. Mattevi, *Chem Soc Rev*, 2020, **49**, 3952-3980.
73. Z. Liu, K. Nie, X. Qu, X. Li, B. Li, Y. Yuan, S. Chong, P. Liu, Y. Li, Z. Yin and W. Huang, *J Am Chem Soc*, 2022, **144**, 4863-4873.
74. G. Pippia, D. Van Hamme, B. Martin-Garcia, M. Prato and I. Moreels, *Nanoscale*, 2022, **14**, 15859-15868.
75. R. Hesse, T. Chassé, P. Streubel and R. Szargan, *Surface and Interface Analysis*, 2004, **36**, 1373-1383.
76. F. C. Spoor, L. T. Kunneman, W. H. Evers, N. Renaud, F. C. Grozema, A. J. Houtepen and L. D. Siebbeles, *ACS Nano*, 2016, **10**, 695-703.
77. L. F. Klepzig, L. Biesterfeld, M. Romain, A. Niebur, A. Schlosser, J. Hubner and J. Lauth, *Nanoscale Adv*, 2022, **4**, 590-599.
78. B. Fritzinger, I. Moreels, P. Lommens, R. Koole, Z. Hens and J. C. Martins, *J Am Chem Soc*, 2009, **131**, 3024-3032.
79. J. M. Luther, M. Law, Q. Song, C. L. Perkins, M. C. Beard and A. J. Nozik, *ACS Nano*, 2008, **2**, 271-280.
80. D. M. Kroupa, M. Voros, N. P. Brawand, B. W. McNichols, E. M. Miller, J. Gu, A. J. Nozik, A. Sellinger, G. Galli and M. C. Beard, *Nat Commun*, 2017, **8**, 15257.
81. M. A. Lovette, A. R. Browning, D. W. Griffin, J. P. Sizemore, R. C. Snyder and M. F. Doherty, *Industrial & Engineering Chemistry Research*, 2008, **47**, 9812-9833.
82. K. F. Mak, C. Lee, J. Hone, J. Shan and T. F. Heinz, *Phys Rev Lett*, 2010, **105**, 136805.

83. N. Wakabayashi, H. G. Smith and R. M. Nicklow, *Physical Review B*, 1975, **12**, 659-663.
84. S. K. Srivastava, B. N. Avasthi and B. K. Mathur, *Journal of Materials Science Letters*, 1984, **3**, 671-673.
85. P. M. Diehm, P. Agoston and K. Albe, *Chemphyschem*, 2012, **13**, 2443-2454.
86. W. Xu, S. Yan and W. Qiao, *RSC Adv*, 2018, **8**, 8435-8441.
87. Y. Kang, S. Najmaei, Z. Liu, Y. Bao, Y. Wang, X. Zhu, N. J. Halas, P. Nordlander, P. M. Ajayan, J. Lou and Z. Fang, *Adv Mater*, 2014, **26**, 6467-6471.
88. A. N. Enyashin, L. Yadgarov, L. Houben, I. Popov, M. Weidenbach, R. Tenne, M. Bar-Sadan and G. Seifert, *The Journal of Physical Chemistry C*, 2011, **115**, 24586-24591.
89. G. Eda, H. Yamaguchi, D. Voiry, T. Fujita, M. Chen and M. Chhowalla, *Nano Lett*, 2011, **11**, 5111-5116.
90. E. Er, H.-L. Hou, A. Criado, J. Langer, M. Möller, N. Erk, L. M. Liz-Marzán and M. Prato, *Chemistry of Materials*, 2019, **31**, 5725-5734.
91. K. C. Knirsch, N. C. Berner, H. C. Nerl, C. S. Cucinotta, Z. Gholamvand, N. McEvoy, Z. Wang, I. Abramovic, P. Vecera, M. Halik, S. Sanvito, G. S. Duesberg, V. Nicolosi, F. Hauke, A. Hirsch, J. N. Coleman and C. Backes, *ACS Nano*, 2015, **9**, 6018-6030.
92. D. Ganta, S. Sinha and R. T. Haasch, *Surface Science Spectra*, 2014, **21**, 19-27.
93. A. L. Washington, 2nd, M. E. Foley, S. Cheong, L. Quffa, C. J. Breshike, J. Watt, R. D. Tilley and G. F. Strouse, *J Am Chem Soc*, 2012, **134**, 17046-17052.
94. R. Van Santen, *The Journal of Physical Chemistry*, 1984, **88**, 5768-5769.
95. A. Molina-Sánchez, D. Sangalli, K. Hummer, A. Marini and L. Wirtz, *Physical Review B*, 2013, **88**, 045412.
96. R. Gillen and J. Maultzsch, *IEEE Journal of Selected Topics in Quantum Electronics*, 2017, **23**, 219-230.
97. D. Y. Qiu, F. H. da Jornada and S. G. Louie, *Phys Rev Lett*, 2013, **111**, 216805.
98. S. Ayari, M. T. Quick, N. Owschimikow, S. Christodoulou, G. H. V. Bertrand, M. Artemyev, I. Moreels, U. Woggon, S. Jaziri and A. W. Achtstein, *Nanoscale*, 2020, **12**, 14448-14458.
99. D. J. Norris, A. Sacra, C. B. Murray and M. G. Bawendi, *Phys Rev Lett*, 1994, **72**, 2612-2615.
100. E. A. Pogna, M. Marsili, D. De Fazio, S. Dal Conte, C. Manzoni, D. Sangalli, D. Yoon, A. Lombardo, A. C. Ferrari, A. Marini, G. Cerullo and D. Prezzi, *ACS Nano*, 2016, **10**, 1182-1188.
101. D. Jariwala, V. K. Sangwan, L. J. Lauhon, T. J. Marks and M. C. Hersam, *ACS Nano*, 2014, **8**, 1102-1120.
102. Q. H. Wang, K. Kalantar-Zadeh, A. Kis, J. N. Coleman and M. S. Strano, *Nat Nanotechnol*, 2012, **7**, 699-712.

103. H. Wang, C. Li, P. Fang, Z. Zhang and J. Z. Zhang, *Chem Soc Rev*, 2018, **47**, 6101-6127.
104. H. Schmidt, F. Giustiniano and G. Eda, *Chem Soc Rev*, 2015, **44**, 7715-7736.
105. B. Radisavljevic, A. Radenovic, J. Brivio, V. Giacometti and A. Kis, *Nat Nanotechnol*, 2011, **6**, 147-150.
106. Y. L. Huang, Y. J. Zheng, Z. Song, D. Chi, A. T. S. Wee and S. Y. Quek, *Chem Soc Rev*, 2018, **47**, 3241-3264.
107. D. Nevola, B. C. Hoffman, A. Bataller, H. Ade, K. Gundogdu and D. B. Dougherty, *Surface Science*, 2019, **679**, 254-258.
108. S. Park, T. Schultz, X. Xu, B. Wegner, A. Aljarb, A. Han, L.-J. Li, V. C. Tung, P. Amsalem and N. Koch, *Communications Physics*, 2019, **2**, 109.
109. Y. Jing, X. Tan, Z. Zhou and P. Shen, *J. Mater. Chem. A*, 2014, **2**, 16892-16897.
110. J. Wang, Z. Ji, G. Yang, X. Chuai, F. Liu, Z. Zhou, C. Lu, W. Wei, X. Shi, J. Niu, L. Wang, H. Wang, J. Chen, N. Lu, C. Jiang, L. Li and M. Liu, *Advanced Functional Materials*, 2018, **28**, 1806244.
111. S. Mouri, Y. Miyauchi and K. Matsuda, *Nano Lett*, 2013, **13**, 5944-5948.
112. Z. Song, T. Schultz, Z. Ding, B. Lei, C. Han, P. Amsalem, T. Lin, D. Chi, S. L. Wong, Y. J. Zheng, M. Y. Li, L. J. Li, W. Chen, N. Koch, Y. L. Huang and A. T. S. Wee, *ACS Nano*, 2017, **11**, 9128-9135.
113. H. G. Ji, P. Solis-Fernandez, D. Yoshimura, M. Maruyama, T. Endo, Y. Miyata, S. Okada and H. Ago, *Adv Mater*, 2019, **31**, e1903613.
114. D. Kiriya, M. Tosun, P. Zhao, J. S. Kang and A. Javey, *J Am Chem Soc*, 2014, **136**, 7853-7856.
115. B. Chamlagain, S. S. Withanage, A. C. Johnston and S. I. Khondaker, *Sci Rep*, 2020, **10**, 12970.
116. J. D. Lin, C. Han, F. Wang, R. Wang, D. Xiang, S. Qin, X. A. Zhang, L. Wang, H. Zhang, A. T. Wee and W. Chen, *ACS Nano*, 2014, **8**, 5323-5329.
117. L. Yang, K. Majumdar, H. Liu, Y. Du, H. Wu, M. Hatzistergos, P. Y. Hung, R. Tieckelmann, W. Tsai, C. Hobbs and P. D. Ye, *Nano Lett*, 2014, **14**, 6275-6280.
118. H. Fang, M. Tosun, G. Seol, T. C. Chang, K. Takei, J. Guo and A. Javey, *Nano Lett*, 2013, **13**, 1991-1995.
119. I. Jeong, K. Cho, S. Yun, J. Shin, J. Kim, G. T. Kim, T. Lee and S. Chung, *ACS Nano*, 2022, **16**, 6215-6223.
120. H. Brinkmann, C. Kelting, S. Makarov, O. Tsaryova, G. Schnurpfeil, D. Wöhrle and D. Schlettwein, *physica status solidi (a)*, 2008, **205**, 409-420.
121. S. Lindner, U. Treske, M. Grobosch and M. Knupfer, *Applied Physics A*, 2011, **105**, 921-925.
122. K. Greulich, A. Belser, S. Bölke, P. Grüninger, R. Karstens, M. S. Sättele, R. Ovsyannikov, E. Giangrisostomi, T. V. Basova, D. Klyamer, T. Chassé and H. Peisert, *The Journal of Physical Chemistry C*, 2020, **124**, 16990-16999.
123. J. Pak, J. Jang, K. Cho, T. Y. Kim, J. K. Kim, Y. Song, W. K. Hong, M. Min, H. Lee and T. Lee, *Nanoscale*, 2015, **7**, 18780-18788.

124. J. Pak, M. Min, K. Cho, D.-H. Lien, G. H. Ahn, J. Jang, D. Yoo, S. Chung, A. Javey and T. Lee, *Applied Physics Letters*, 2016, **109**, 183502.
125. S. Andleeb, X. Wang, H. Dong, S. Valligatla, C. N. Saggau, L. Ma, O. G. Schmidt and F. Zhu, *Journal*, 2023, **13**.
126. Y. Huang, F. Zhuge, J. Hou, L. Lv, P. Luo, N. Zhou, L. Gan and T. Zhai, *ACS Nano*, 2018, **12**, 4062-4073.
127. N. Mutz, S. Park, T. Schultz, S. Sadofev, S. Dalgleish, L. Reissig, N. Koch, E. J. W. List-Kratochvil and S. Blumstengel, *The Journal of Physical Chemistry C*, 2020, **124**, 2837-2843.
128. J. H. Park, A. Sanne, Y. Guo, M. Amani, K. Zhang, H. C. P. Movva, J. A. Robinson, A. Javey, J. Robertson, S. K. Banerjee and A. C. Kummel, *Sci Adv*, 2017, **3**, e1701661.
129. S. H. Amsterdam, T. K. Stanev, L. Wang, Q. Zhou, S. Irgen-Gioro, S. Padgaonkar, A. A. Murthy, V. K. Sangwan, V. P. Dravid, E. A. Weiss, P. Darancet, M. K. Y. Chan, M. C. Hersam, N. P. Stern and T. J. Marks, *J Am Chem Soc*, 2021, **143**, 17153-17161.
130. S. Padgaonkar, S. H. Amsterdam, H. Bergeron, K. Su, T. J. Marks, M. C. Hersam and E. A. Weiss, *The Journal of Physical Chemistry C*, 2019, **123**, 13337-13343.
131. C. J. Benjamin, S. Zhang and Z. Chen, *Nanoscale*, 2018, **10**, 5148-5153.
132. Y. Kong, S. M. Obaidulla, M. R. Habib, Z. Wang, R. Wang, Y. Khan, H. Zhu, M. Xu and D. Yang, *Mater Horiz*, 2022, **9**, 1253-1263.
133. A. Banerjee, B. Kundu and A. J. Pal, *Phys Chem Chem Phys*, 2017, **19**, 28450-28457.
134. T. R. Kafle, B. Kattel, P. Yao, P. Zereshki, H. Zhao and W. L. Chan, *J Am Chem Soc*, 2019, **141**, 11328-11336.
135. X. Y. Liu, X. Y. Xie, W. H. Fang and G. Cui, *J Phys Chem A*, 2018, **122**, 9587-9596.
136. A. Vollmer, R. Ovsyannikov, M. Gorgoi, S. Krause, M. Oehzelt, A. Lindblad, N. Mårtensson, S. Svensson, P. Karlsson, M. Lundvuist, T. Schmeiler, J. Pflaum and N. Koch, *Journal of Electron Spectroscopy and Related Phenomena*, 2012, **185**, 55-60.
137. G. Lucovsky, R. M. White, J. A. Benda and J. F. Revelli, *Physical Review B*, 1973, **7**, 3859-3870.
138. U. Aygül, H. Hintz, H.-J. Egelhaaf, A. Distler, S. Abb, H. Peisert and T. Chassé, *The Journal of Physical Chemistry C*, 2013, **117**, 4992-4998.
139. R. D. Gould, *Coordination Chemistry Reviews*, 1996, **156**, 237-274.
140. A. Niebur, A. Soll, P. Haizmann, O. Strolka, D. Rudolph, K. Tran, F. Renz, A. P. Frauendorf, J. Hubner, H. Peisert, M. Scheele and J. Lauth, *Nanoscale*, 2023, **15**, 5679-5688.
141. C. P. Lu, G. Li, J. Mao, L. M. Wang and E. Y. Andrei, *Nano Lett*, 2014, **14**, 4628-4633.
142. E. Giangrisostomi, R. Ovsyannikov, R. Haverkamp, N. L. A. N. Sorgenfrei, S. Neppl, H. Sezen, F. O. L. Johansson, S. Svensson and A. Föhlisch, *Advanced Materials Interfaces*, 2023, **10**, 2300392.

143. T. He, H. Ding, N. Peor, M. Lu, D. A. Corley, B. Chen, Y. Ofir, Y. Gao, S. Yitzchaik and J. M. Tour, *J Am Chem Soc*, 2008, **130**, 1699-1710.
144. F. Rückerl, T. Klaproth, R. Schuster, B. Büchner and M. Knupfer, *physica status solidi (b)*, 2016, **254**, 1600656.
145. N. Ueno and S. Kera, *Progress in Surface Science*, 2008, **83**, 490-557.
146. M.-H. Shang, M. Nagaosa, S.-i. Nagamatsu, S. Hosoumi, S. Kera, T. Fujikawa and N. Ueno, *Journal of Electron Spectroscopy and Related Phenomena*, 2011, **184**, 261-264.
147. H. Peisert, D. Kolacyak and T. Chassé, *The Journal of Physical Chemistry C*, 2009, **113**, 19244-19250.
148. T. Chiang, G. Kaindl and T. Mandel, *Phys Rev B Condens Matter*, 1986, **33**, 695-711.
149. N. Ueno, S. Kera, K. Sakamoto and K. K. Okudaira, *Applied Physics A*, 2008, **92**, 495-504.
150. H. Peisert, M. Knupfer, T. Schwieger, J. M. Auerhammer, M. S. Golden and J. Fink, *Journal of Applied Physics*, 2002, **91**, 4872-4878.
151. S. Braun and W. R. Salaneck, *Chemical Physics Letters*, 2007, **438**, 259-262.
152. S. Braun, W. R. Salaneck and M. Fahlman, *Advanced Materials*, 2009, **21**, 1450-1472.
153. S. Braun, X. Liu, W. R. Salaneck and M. Fahlman, *Organic Electronics*, 2010, **11**, 212-217.
154. M. Gruenewald, L. K. Schirra, P. Winget, M. Kozlik, P. F. Ndione, A. K. Sigdel, J. J. Berry, R. Forker, J.-L. Brédas, T. Fritz and O. L. A. Monti, *The Journal of Physical Chemistry C*, 2015, **119**, 4865-4873.
155. O. T. Hofmann, P. Rinke, M. Scheffler and G. Heimel, *ACS Nano*, 2015, **9**, 5391-5404.
156. O. T. Hofmann, J. C. Deinert, Y. Xu, P. Rinke, J. Stahler, M. Wolf and M. Scheffler, *J Chem Phys*, 2013, **139**, 174701.
157. S. Erker and O. T. Hofmann, *J Phys Chem Lett*, 2019, **10**, 848-854.
158. H. Vázquez, R. Oszwaldowski, P. Pou, J. Ortega, R. Pérez, F. Flores and A. Kahn, *Europhysics Letters (EPL)*, 2004, **65**, 802-808.
159. H. Vázquez, F. Flores, R. Oszwaldowski, J. Ortega, R. Pérez and A. Kahn, *Applied Surface Science*, 2004, **234**, 107-112.
160. J. F. Wager and K. Kuhn, *Critical Reviews in Solid State and Materials Sciences*, 2016, **42**, 373-415.
161. W. Chen, D. Qi, X. Gao and A. T. S. Wee, *Progress in Surface Science*, 2009, **84**, 279-321.
162. T. Ules, D. Lüftner, E. M. Reinisch, G. Koller, P. Puschnig and M. G. Ramsey, *Physical Review B*, 2014, **90**, 155430.
163. J. Uihlein, M. Polek, M. Glaser, H. Adler, R. Ovsyannikov, M. Bauer, M. Ivanovic, A. B. Preobrajenski, A. V. Generalov, T. Chassé and H. Peisert, *The Journal of Physical Chemistry C*, 2015, **119**, 15240-15247.
164. A. Belser, K. Greulich, P. Grüninger, R. Karstens, R. Ovsyannikov, E. Giangrisostomi, P. Nagel, M. Merz, S. Schuppler, T. Chassé and H. Peisert, *The Journal of Physical Chemistry C*, 2021, **125**, 8803-8814.

165. J. Vlček, I. A. Kühne, D. Zákutná, E. Marešová, L. Fekete, J. Otta, P. Fitl and M. Vrňata, *CrystEngComm*, 2021, **23**, 7237-7244.
166. M. Brendel, S. Krause, A. Steindamm, A. K. Topczak, S. Sundarraj, P. Erk, S. Höhla, N. Fruehauf, N. Koch and J. Pflaum, *Advanced Functional Materials*, 2015, **25**, 1565-1573.
167. W. Chen, A. Kahn, P. S. Mangat, P. Soukiassian, L. T. Florez, J. P. Harbison and C. J. Palmstrom, *Journal of Vacuum Science & Technology B: Microelectronics and Nanometer Structures Processing, Measurement, and Phenomena*, 1993, **11**, 1571-1574.
168. C. Shen and A. Kahn, *Organic Electronics*, 2001, **2**, 89-95.
169. S. Zeng, Z. Tang, C. Liu and P. Zhou, *Nano Research*, 2020, **14**, 1752-1767.
170. G. Fiori, F. Bonaccorso, G. Iannaccone, T. Palacios, D. Neumaier, A. Seabaugh, S. K. Banerjee and L. Colombo, *Nat Nanotechnol*, 2014, **9**, 768-779.
171. L. Zheng, X. Wang, H. Jiang, M. Xu, W. Huang and Z. Liu, *Nano Research*, 2021, **15**, 2413-2432.
172. K. S. Novoselov, D. Jiang, F. Schedin, T. J. Booth, V. V. Khotkevich, S. V. Morozov and A. K. Geim, *Proc Natl Acad Sci U S A*, 2005, **102**, 10451-10453.
173. S. Manzeli, D. Ovchinnikov, D. Pasquier, O. V. Yazyev and A. Kis, *Nature Reviews Materials*, 2017, **2**, 17033.
174. Y. Liu, N. O. Weiss, X. Duan, H.-C. Cheng, Y. Huang and X. Duan, *Nature Reviews Materials*, 2016, **1**, 16042.
175. P. V. Pham, S. C. Bodepudi, K. Shehzad, Y. Liu, Y. Xu, B. Yu and X. Duan, *Chem Rev*, 2022, **122**, 6514-6613.
176. S. H. Amsterdam, T. J. Marks and M. C. Hersam, *J Phys Chem Lett*, 2021, **12**, 4543-4557.
177. J. Krumland and C. Cocchi, *Electronic Structure*, 2021, **3**, 044003.
178. A. Casotto, G. Drera, D. Perilli, S. Freddi, S. Pagliara, M. Zanotti, L. Schio, A. Verdini, L. Floreano, C. Di Valentin and L. Sangaletti, *Nanoscale*, 2022, **14**, 13166-13177.
179. N. Koch, *Applied Physics Letters*, 2021, **119**, 260501.
180. S. Duhm, G. Heimel, I. Salzmann, H. Glowatzki, R. L. Johnson, A. Vollmer, J. P. Rabe and N. Koch, *Nat Mater*, 2008, **7**, 326-332.
181. S. R. Forrest, *Chem Rev*, 1997, **97**, 1793-1896.
182. K. Kudo, D. Xing Wang, M. Iizuka, S. Kuniyoshi and K. Tanaka, *Thin Solid Films*, 1998, **331**, 51-54.
183. Z. Bao, A. J. Lovinger and A. Dodabalapur, *Applied Physics Letters*, 1996, **69**, 3066-3068.
184. O. A. Melville, B. H. Lessard and T. P. Bender, *ACS Appl Mater Interfaces*, 2015, **7**, 13105-13118.
185. K. Greulich, A. Belser, T. Basova, T. Chassé and H. Peisert, *The Journal of Physical Chemistry C*, 2021, **126**, 716-727.
186. M. Toader, T. G. Gopakumar, P. Shukrynau and M. Hietschold, *The Journal of Physical Chemistry C*, 2010, **114**, 21548-21554.

187. H. Peisert, M. Knupfer, T. Schwieger, G. G. Fuentes, D. Olligs, J. Fink and T. Schmidt, *Journal of Applied Physics*, 2003, **93**, 9683-9692.
188. D. Balle, H. Adler, P. Grüninger, R. Karstens, R. Ovsyannikov, E. Giangrisostomi, T. Chassé and H. Peisert, *The Journal of Physical Chemistry C*, 2017, **121**, 18564-18574.
189. H. Peisert, I. Biswas, M. Knupfer and T. Chassé, *physica status solidi (b)*, 2009, **246**, 1529-1545.
190. H. Peisert, T. Schwieger, J. M. Auerhammer, M. Knupfer, M. S. Golden, J. Fink, P. R. Bressler and M. Mast, *Journal of Applied Physics*, 2001, **90**, 466-469.
191. S. Kera, M. B. Casu, K. R. Bauchspieß, D. Batchelor, T. Schmidt and E. Umbach, *Surface Science*, 2006, **600**, 1077-1084.
192. M. Scardamaglia, C. Struzzi, S. Lizzit, M. Dalmiglio, P. Lacovig, A. Baraldi, C. Mariani and M. G. Betti, *Langmuir*, 2013, **29**, 10440-10447.
193. T. Breuer, I. Salzmann, J. Götzen, M. Oehzelt, A. Morherr, N. Koch and G. Witte, *Crystal Growth & Design*, 2011, **11**, 4996-5001.
194. T. Schmidt, T. Wilkens and J. Falta, *Surface Science*, 2022, **725**, 122127.
195. R. R. Cranston and B. H. Lessard, *RSC Adv*, 2021, **11**, 21716-21737.
196. D. A. Evans, H. J. Steiner, A. R. Vearey-Roberts, A. Bushell, G. Cabailh, S. O'Brien, J. W. Wells, I. T. McGovern, V. R. Dhanak, T. U. Kampen, D. R. T. Zahn and D. Batchelor, *Nuclear Instruments and Methods in Physics Research Section B: Beam Interactions with Materials and Atoms*, 2003, **199**, 475-480.
197. P. Ballirano, R. Caminiti, C. Ercolani, A. Maras and M. A. Orrù, *Journal of the American Chemical Society*, 1998, **120**, 12798-12807.
198. D. G. de Oteyza, E. Barrena, Y. Zhang, T. N. Krauss, A. Turak, A. Vorobiev and H. Dosch, *The Journal of Physical Chemistry C*, 2009, **113**, 4234-4239.
199. K. S. Novoselov and A. H. Castro Neto, *Physica Scripta*, 2012, **T146**, 014006.
200. C. A. Schneider, W. S. Rasband and K. W. Eliceiri, *Nat Methods*, 2012, **9**, 671-675.
201. J. Schindelin, I. Arganda-Carreras, E. Frise, V. Kaynig, M. Longair, T. Pietzsch, S. Preibisch, C. Rueden, S. Saalfeld, B. Schmid, J. Y. Tinevez, D. J. White, V. Hartenstein, K. Eliceiri, P. Tomancak and A. Cardona, *Nat Methods*, 2012, **9**, 676-682.
202. J. Stohr and D. A. Outka, *Phys Rev B Condens Matter*, 1987, **36**, 7891-7905.
203. F. d. Groot, *Coordination Chemistry Reviews*, 2005, **249**, 31-63.
204. T. Zhang, I. E. Brumboiu, V. Lanzilotto, J. Lüder, C. Grazioli, E. Giangrisostomi, R. Ovsyannikov, Y. Sassa, I. Bidermane, M. Stupar, M. de Simone, M. Coreno, B. Ressel, M. Pedio, P. Rudolf, B. Brena and C. Puglia, *The Journal of Physical Chemistry C*, 2017, **121**, 26372-26378.
205. I. E. Brumboiu, S. Haldar, J. Luder, O. Eriksson, H. C. Herper, B. Brena and B. Sanyal, *J Chem Theory Comput*, 2016, **12**, 1772-1785.

206. T. Kroll, V. Y. Aristov, O. V. Molodtsova, Y. A. Ossipyan, D. V. Vyalikh, B. Buchner and M. Knupfer, *J Phys Chem A*, 2009, **113**, 8917-8922.
207. K. Keyshar, M. Berg, X. Zhang, R. Vajtai, G. Gupta, C. K. Chan, T. E. Beechem, P. M. Ajayan, A. D. Mohite and T. Ohta, *ACS Nano*, 2017, **11**, 8223-8230.
208. M. Berg, K. Keyshar, I. Bilgin, F. Liu, H. Yamaguchi, R. Vajtai, C. Chan, G. Gupta, S. Kar, P. Ajayan, T. Ohta and A. D. Mohite, *Physical Review B*, 2017, **95**, 235406.
209. M. Frégnaux, H. Kim, D. Rouchon, V. Derycke, J. Bleuse, D. Voiry, M. Chhowalla and O. Renault, *Surface and Interface Analysis*, 2016, **48**, 465-469.
210. H. Li, J. Wu, X. Huang, G. Lu, J. Yang, X. Lu, Q. Xiong and H. Zhang, *ACS Nano*, 2013, **7**, 10344-10353.
211. D. J. Late, B. Liu, H. S. S. R. Matte, C. N. R. Rao and V. P. Dravid, *Advanced Functional Materials*, 2012, **22**, 1894-1905.
212. O. Ochedowski, K. Marinov, N. Scheuschner, A. Poloczek, B. K. Bussmann, J. Maultzsch and M. Schleberger, *Beilstein Journal of Nanotechnology*, 2014, **5**, 291-297.
213. C. Lattyak, K. Gehrke and M. Vehse, *The Journal of Physical Chemistry C*, 2022, **126**, 13929-13935.
214. M. Tamulewicz, J. Kutrowska-Girzycka, K. Gajewski, J. Serafinczuk, A. Sierakowski, J. Jadczak, L. Bryja and T. P. Gotszalk, *Nanotechnology*, 2019, **30**, 245708.
215. Y. Liang, B.-H. Li, Z. Li, G. Zhang, J. Sun, C. Zhou, Y. Tao, Y. Ye, Z. Ren and X. Yang, *Materials Today Physics*, 2021, **21**, 100506.
216. L. Chouhan, S. Ghimire, C. Subrahmanyam, T. Miyasaka and V. Biju, *Chem Soc Rev*, 2020, **49**, 2869-2885.
217. L. N. Quan, B. P. Rand, R. H. Friend, S. G. Mhaisalkar, T. W. Lee and E. H. Sargent, *Chem Rev*, 2019, **119**, 7444-7477.
218. Q. Chen, J. Wu, X. Ou, B. Huang, J. Almutlaq, A. A. Zhumekenov, X. Guan, S. Han, L. Liang, Z. Yi, J. Li, X. Xie, Y. Wang, Y. Li, D. Fan, D. B. L. Teh, A. H. All, O. F. Mohammed, O. M. Bakr, T. Wu, M. Bettinelli, H. Yang, W. Huang and X. Liu, *Nature*, 2018, **561**, 88-93.
219. F. Zhou, Z. Li, W. Lan, Q. Wang, L. Ding and Z. Jin, *Small Methods*, 2020, **4**.
220. Y. Zhou, J. Chen, O. M. Bakr and O. F. Mohammed, *ACS Energy Letters*, 2021, **6**, 739-768.
221. B. Conings, J. Drijkoningen, N. Gauquelin, A. Babayigit, J. D'Haen, L. D'Olieslaeger, A. Ethirajan, J. Verbeeck, J. Manca, E. Mosconi, F. D. Angelis and H. G. Boyen, *Advanced Energy Materials*, 2015, **5**.
222. W. Xiang, S. Liu and W. Tress, *Energy & Environmental Science*, 2021, **14**, 2090-2113.
223. F. Krieg, Q. K. Ong, M. Burian, G. Raino, D. Naumenko, H. Amenitsch, A. Suess, M. J. Grotevent, F. Krumeich, M. I. Bodnarchuk, I. Shorubalko, F. Stellacci and M. V. Kovalenko, *J Am Chem Soc*, 2019, **141**, 19839-19849.
224. S. Mazumdar, Y. Zhao and X. Zhang, *Frontiers in Electronics*, 2021, **2**.

225. A. Xie, C. Hettiarachchi, F. Maddalena, M. E. Witkowski, M. Makowski, W. Drozdowski, A. Arramel, A. T. S. Wee, S. V. Springham, P. Q. Vuong, H. J. Kim, C. Dujardin, P. Coquet, M. D. Birowosuto and C. Dang, *Communications Materials*, 2020, **1**, 37.
226. S. Kishimoto, K. Shibuya, F. Nishikido, M. Koshimizu, R. Haruki and Y. Yoda, *Applied Physics Letters*, 2008, **93**, 261901.
227. J. Endres, M. Kulbak, L. Zhao, B. P. Rand, D. Cahen, G. Hodes and A. Kahn, *Journal of Applied Physics*, 2017, **121**.
228. M. Scheele, W. Brutting and F. Schreiber, *Phys Chem Chem Phys*, 2015, **17**, 97-111.
229. S. Colella, M. Todaro, S. Masi, A. Listorti, D. Altamura, R. Caliandro, C. Giannini, E. Carignani, M. Geppi, D. Meggiolaro, G. Buscarino, F. De Angelis and A. Rizzo, *ACS Energy Letters*, 2018, **3**, 1840-1847.
230. A. F. Akbulatov, L. A. Frolova, N. N. Dremova, I. Zhidkov, V. M. Martynenko, S. A. Tsarev, S. Y. Luchkin, E. Z. Kurmaev, S. M. Aldoshin, K. J. Stevenson and P. A. Troshin, *J Phys Chem Lett*, 2020, **11**, 333-339.
231. L. A. Frolova, Q. Chang, S. Y. Luchkin, D. Zhao, A. F. Akbulatov, N. N. Dremova, A. V. Ivanov, E. E. M. Chia, K. J. Stevenson and P. A. Troshin, *Journal of Materials Chemistry C*, 2019, **7**, 5314-5323.
232. L. A. Frolova, S. Y. Luchkin, Y. Lekina, L. G. Gutsev, S. A. Tsarev, I. S. Zhidkov, E. Z. Kurmaev, Z. X. Shen, K. J. Stevenson, S. M. Aldoshin and P. A. Troshin, *Advanced Energy Materials*, 2021, **11**, 2002934.
233. R. E. Beal, D. J. Slotcavage, T. Leijtens, A. R. Bowring, R. A. Belisle, W. H. Nguyen, G. F. Burkhard, E. T. Hoke and M. D. McGehee, *J Phys Chem Lett*, 2016, **7**, 746-751.
234. C. Das, M. Wussler, T. Hellmann, T. Mayer and W. Jaegermann, *Phys Chem Chem Phys*, 2018, **20**, 17180-17187.
235. J. D. McGettrick, K. Hooper, A. Pockett, J. Baker, J. Troughton, M. Carnie and T. Watson, *Materials Letters*, 2019, **251**, 98-101.
236. S. Tao, I. Schmidt, G. Brocks, J. Jiang, I. Tranca, K. Meerholz and S. Olthof, *Nat Commun*, 2019, **10**, 2560.
237. F. Bertolotti, L. Protesescu, M. V. Kovalenko, S. Yakunin, A. Cervellino, S. J. L. Billinge, M. W. Terban, J. S. Pedersen, N. Masciocchi and A. Guagliardi, *ACS Nano*, 2017, **11**, 3819-3831.
238. P. Cottingham and R. L. Brutchey, *Chem Commun (Camb)*, 2016, **52**, 5246-5249.
239. D. R. Baer, K. Artyushkova, H. Cohen, C. D. Easton, M. Engelhard, T. R. Gengenbach, G. Greczynski, P. Mack, D. J. Morgan and A. Roberts, *Journal of Vacuum Science & Technology A: Vacuum, Surfaces, and Films*, 2020, **38**, 031204.
240. J. Cazaux, *Journal of Electron Spectroscopy and Related Phenomena*, 2000, **113**, 15-33.
241. J. Wahl, M. Engelmayer, M. Mandal, T. Naujoks, P. Haizmann, A. Maier, H. Peisert, D. Andrienko, W. Brütting and M. Scheele, *Advanced Optical Materials*, 2021, **10**, 2101945.

242. B. Wang and A. Navrotsky, *The Journal of Physical Chemistry C*, 2020, **124**, 8639-8642.
243. P. S. Mathew, G. F. Samu, C. Janáky and P. V. Kamat, *ACS Energy Letters*, 2020, **5**, 1872-1880.
244. R. A. Evarestov, E. A. Kotomin, A. Senocrate, R. K. Kremer and J. Maier, *Phys Chem Chem Phys*, 2020, **22**, 3914-3920.
245. D. Cortecchia, J. Yin, A. Bruno, S.-Z. A. Lo, G. G. Gurzadyan, S. Mhaisalkar, J.-L. Brédas and C. Soci, *Journal of Materials Chemistry C*, 2017, **5**, 2771-2780.
246. I. du Fosse, S. Lal, A. N. Hossaini, I. Infante and A. J. Houtepen, *J Phys Chem C Nanomater Interfaces*, 2021, **125**, 23968-23975.
247. M. C. Brennan, S. Toso, I. M. Pavlovetc, M. Zhukovskyi, S. Marras, M. Kuno, L. Manna and D. Baranov, *ACS Energy Letters*, 2020, **5**, 1465-1473.
248. C. N. Dibenedetto, T. Sibillano, R. Brescia, M. Prato, L. Triggiani, C. Giannini, A. Panniello, M. Corricelli, R. Comparelli, C. Ingrosso, N. Depalo, A. Agostiano, M. L. Curri, M. Striccoli and E. Fanizza, *Journal*, 2020, **25**.
249. R. Hesse, M. Weiß, R. Szargan, P. Streubel and R. Denecke, *Journal of Electron Spectroscopy and Related Phenomena*, 2013, **186**, 44-53.
250. K. Harrison and L. B. Hazell, *Surface and Interface Analysis*, 2004, **18**, 368-376.

12 List of Publications

12.1 First Author

1. Tuning the Interfacial Electronic Structure of MoS_2 by Adsorption of Cobalt Phthalocyanine Derivatives
2. Orientation of Cobalt Phthalocyanine on Molybdenum Disulfide: Distinguishing between Single Crystals and Small Flakes
3. Mitigating the Photodegradation of All-Inorganic Mixed-Halide Perovskite Nanocrystals by Ligand Exchange

12.2 Contributions

1. Untangling the Intertwined: Metallic to Semiconducting Phase Transition of Colloidal MoS_2 Nanoplatelets and Nanosheets
2. Porphyrin Functionalization of $CsPbBrI_2/SiO_2$ Core-Shell Nanocrystals Enhances the Stability and Efficiency in Electroluminescent Devices
3. Zwitterionic Carbazole Ligands Enhance the Stability and Performance of Perovskite Nanocrystals in Light-Emitting Diodes
4. Peri-tetracene from 1,1’-bitetracene: Zipping up structurally defined graphene nanoribbons
5. Direct laser induced writing of high precision gold nanosphere SERS patterns

13 Acknowledgments

Throughout the course of my doctoral studies, interactions with others play a pivotal role, and it is these very exchanges that make the journey and such an ambitious project truly special and ultimately successful. I am profoundly grateful to all those who supported and guided me both professionally and personally during this time.

First and foremost, I want to thank my research mentor, **Prof. Dr. Marcus Scheele**, who welcomed me into his group and made this work possible. Beyond the scientific and financial support, I received as part of his highly motivated team of researchers, I am particularly grateful for the interpersonal aspects. Even during challenging times, I was met with open ears, respect, and genuine encouragement, which helped me persevere and stay motivated. From a scientific perspective, I must highlight the open-door policy and the opportunity to critically and openly discuss results, which were invaluable in achieving high-quality publications.

I am also profoundly grateful to **Prof. Dr. Thomas Chassé** for his scientific exchange and financial support for my work. The seminars he led, and the overall guidance of the group fostered a productive environment where I truly enjoyed working.

I would like to express my gratitude to **apl. Prof. Dr. Heiko Peisert** for his expert guidance. His patience in answering my numerous questions and his support in writing proposals for synchrotron beamtime contributed significantly to the success of this dissertation. His hands-on assistance during these labor-intensive yet exciting measurement periods was particularly invaluable.

I look back with much gratitude and fondness at the wonderful time I spent with the members of the research groups. I would like to thank my colleagues: **Dr. Christopher Kirsch, Dr. Krishan Kumar, Dr. Björn Märker, Dr. Andre Maier, Dr. Christine Schedel, Dr. Jan Wahl, Dr. Fabian Strauß, Kai Wurst, Robert Thalwitzer, Eric Juriatti, Philipp Frech, Theresa Hettiger, Patrick Michel, Jonas Hiller, Sophia Westendorf, Pia Kohlschreiber, Dr. Sven Bölke, Katharina Greulich, Maren Zirwick, Dr. Dustin Quinones, Dr. Marie-Sophie Wagner, Ivana Mršić, Dr. Kai Braun**, and, of course, the administrative and technical staff who provided crucial support, especially **Ms. Alexa and Ms. Nadler**.

In addition to the work conducted in the laboratories at the University of Tübingen, I received significant support during synchrotron beamtime experiments. I would like to thank the administrative staff at **BESSY in Berlin** for ensuring smooth measurement sessions, with special thanks to **Dr. Ruslan Ovsyannikov** and **Dr. Erika Giangrisostomi** from the LowDosePES beamline. Similarly, I am grateful to the staff at the synchrotron facility at **KIT North Campus**, particularly **Dr. Peter Nagel, Dr. Michael Merz, Dr. Stefan Schuppler**, and **Amir Ghiami** from the WERA beamline.

I am also thankful for the inquisitive and open-minded students I had the opportunity to work with during my time at the University of Tübingen. Their collaboration brought fresh perspectives and valuable support to my work. I would especially like to thank **Benjamin Weber, Rene Frecot, Adrian Jenner**, and **Rebecca Pamies**.

Lastly, I want to express my gratitude to the many people outside the scientific community who supported me and motivated me to complete this work successfully. Foremost among them are my dear wife, **Lilly**, and my daughter, **Emma**. This work is as much for them as it is for our shared future and represents an important part of my life. My heartfelt thanks also go to my parents, **Iris** and **Wolfgang**, for everything they have done to help me get to this point. Their unwavering support and love are a gift I deeply cherish. To my sister, **Sandra**, I also extend my thanks for her love and encouragement.